Hadronic light-by-light scattering contribution to the anomalous magnetic moment of the muon from Lattice Quantum Chromodynamics

Dissertation
zur Erlangung des Grades
"Doktor der Naturwissenschaften"

am Fachbereich Physik, Mathematik, Informatik
der Johannes Gutenberg-Universität Mainz

vorgelegt von

En-Hung CHAO

geboren in Kaohsiung (Taiwan)

Mainz, den 28. Oktober 2021

Date of the exam: 17.01.2022

List of publications

Part of the work presented in this thesis has led to the following publications

- **E. H. Chao**, A. Gérardin, J. R. Green, R. J. Hudspith and H. B. Meyer, *"Hadronic light-by-light contribution to $(g-2)_\mu$ from lattice QCD with SU(3) flavor symmetry,"* Eur. Phys. J. C **80** (2020) no.9, 869

  Personal contribution: cross-checks for the lattice data and the implementation of the finite-size-effect corrections, computation of the $\pi^{\pm}$-loop contribution to a_μ^{hlbl} and the development of the diagram matching between the π^0-exchange and different Wick-contraction classes.

- **E. H. Chao**, R. J. Hudspith, A. Gérardin, J. R. Green, H. B. Meyer and K. Ottnad, *"Hadronic light-by-light contribution to $(g-2)_\mu$ from lattice QCD: a complete calculation,"* Eur. Phys. J. C **81** (2021) no.7, 651

  Personal contribution: the development of the codes for computing the sub-leading topologies (part of which has been merged with the codes for the leading topologies to avoid computational overhead) utilizing the existing position-space disconnected-loop data, the analysis of the sub-leading-topology results and the diagram matching between the light-meson contributions and different Wick-contraction classes.

and conference proceeding

- N. Asmussen, **E. H. Chao**, A. Gérardin, J. R. Green, R. J. Hudspith, H. B. Meyer and A. Nyffeler, *"Developments in the position-space approach to the HLbL contribution to the muon $g-2$ on the lattice,"* PoS **LATTICE2019** (2019), 195

  Personal contribution: co-author for being part of the current working group of the subject presented at the 37th International Symposium on Lattice Field Theory.

This page is intentionally left blank.

Abstract

The anomalous magnetic moment of the muon, a_μ, provides a stringent test for the Standard Model of particle physics, as it is so far one of the most precisely measured quantities. On the theory side, the Standard Model prediction has reached the same level of precision as experiment. However, a long-standing discrepancy between the Standard Model theory prediction and the experimental result exists. In order for the tension to potentially reach the critical level of five standard deviations, it is essential to further reduce the errors. The uncertainty on the theory side is dominated by the hadronic contributions.

The main purpose of this thesis is to calculate the Hadronic Light-by-Light scattering contribution a_μ^{hlbl}, which makes one of the single largest contributions to the error budget of the Standard Model prediction. The calculation is based on Lattice Quantum Chromodynamics (LQCD), a Monte-Carlo based technique that gives access to non-perturbative hadronic physics from first-principles. In particular, we adopt a position-space formalism which handles the Quantum Electrodynamics (QED) effects semi-analytically in the continuum and infinite-volume. In this thesis, along with additional unpublished material, I present the results of a series of publications related to our determination of a_μ^{hlbl}. I discuss several techniques that have been applied to our a_μ^{hlbl} calculations in order to have better control over different artifacts introduced by the simulations. After showing how our position-space method can be applied, by considering as an example the scalar-meson contribution to a_μ^{hlbl}, and how one estimates the finite-size effects under our formalism with several models, I explain how to make the connection between different calculable contributions in LQCD and low-energy effective models. With all the building blocks introduced, the analyses leading to our published results are reviewed at the end of this thesis.

This page is intentionally left blank.

This page is intentionally left blank.

This page is intentionally left blank.

Contents

Introduction **1**

1 Hadronic contributions to the anomalous magnetic moment of the muon **4**
1.1 Hadronic Vacuum Polarization contribution to a_μ . . . 5
1.1.1 Data-driven approach . . . 5
1.1.2 Lattice approach . . . 6
1.2 Hadronic light-by-light contribution to a_μ . . . 7
1.2.1 Data-driven method . . . 8
1.2.2 Status of lattice computation of a_μ^{hlbl} . . . 11

2 Lattice Quantum Chromodynamics **12**
2.1 Theoretical aspects . . . 13
2.1.1 The Wilson-Dirac action . . . 13
2.1.2 Boundary conditions . . . 15
2.1.3 Improvement of the action . . . 16
2.2 Algorithms for ensemble generation . . . 21
2.2.1 Markov Chain Monte Carlo and generation of pure gauge ensembles . . . 21
2.2.2 Pseudo-fermions and Hybrid Monte Carlo . . . 23
2.2.3 Gauge field generation algorithms for the CLS $N_f = 2+1$ simulations . . . 25
2.3 Computing observables . . . 28
2.3.1 Wick-contraction . . . 28
2.3.2 Propagator solve and `openQCD` solvers . . . 28
2.3.3 Scale-setting for the CLS $N_f = 2+1$ ensembles . . . 31

3 Position-space method and the QED-kernel **35**
3.1 a_μ^{hlbl} and the QED-kernel . . . 35
3.2 Scalar-meson-exchange contribution to a_μ^{HLbL} . . . 38
3.2.1 Analytic calculation of the hadronic function for the scalar-meson exchange . . . 41
3.2.2 Gegenbauer polynomial technique and implementation of the scalar integrals . . . 44
3.2.3 Details of the numerical implementation . . . 52
3.2.4 Result for the integrand for large $|y|$ . . . 53

4 Techniques for finite-size-effect correction **56**
4.1 Finite-size effects from a lepton loop . . . 57
4.1.1 The first term in the brackets of Eq. (4.8) . . . 59
4.1.2 The second term in the brackets of Eq. (4.8) . . . 66
4.1.3 Implication of the distributional nature of the scalar propagator 67
4.1.4 Comparison with free theory on the lattice . . . 67
4.2 Finite-size effects from scalar QED . . . 68

4.2.1 Notations and analytic expressions . . . 69
4.2.2 Charged-pion-loop contribution to a_μ^{hlbl} with different mass and in different integral representation in finite-volume . . . 71

5 Partially-Quenched Chiral Perturbation Theory and applications 74
5.1 Brief review on Chiral Perturbation Theory . . . 75
5.1.1 SU(3) Chiral Perturbation Theory . . . 76
5.1.2 U(3) Chiral Perturbation Theory . . . 78
5.2 Partially-Quenched Chiral Perturbation Theory . . . 80
5.2.1 Graded Lie groups . . . 81
5.2.2 The kinetic part of the chiral SU$(N|M)$ Lagrangian . . . 84
5.2.3 The kinetic part of the chiral U$(N|M)$ Lagrangian . . . 86
5.2.4 Interaction vertices in Partially-Quenched Chiral Perturbation Theory . . . 91
5.3 Wick-contraction topologies in LQCD and the leading pseudoscalar meson contributions to a_μ^{hlbl} . . . 93
5.3.1 Charged-pseudoscalar-meson loop . . . 93
5.3.2 Neutral-pseudoscalar-meson exchange . . . 94

6 Lattice results on a_μ^{hlbl} 98
6.1 Vector current on the lattice and its renormalization . . . 98
6.2 Calculating a_μ^{hlbl} on the lattice . . . 101
6.2.1 The leading topologies . . . 103
6.2.2 The sub-leading topologies . . . 105
6.2.3 Numerical implementation . . . 106
6.3 Analysis of the SU$(3)_f$ study . . . 107
6.3.1 Modelling the integrand . . . 108
6.3.2 Correction for the finite-size effects . . . 110
6.3.3 Continuum extrapolation . . . 112
6.4 Analysis of the approach to the physical point . . . 114
6.4.1 Calculation of the disconnected loops . . . 115
6.4.2 The leading topologies at the physical point . . . 115
6.4.3 The sub-leading topologies . . . 119
6.4.4 The total a_μ^{hlbl} . . . 124

7 Summary and outlook 125

A Data analysis 128
A.1 Analysis of data from Monte Carlo simulations . . . 128
A.1.1 Auto-correlation time . . . 128
A.1.2 Resampling methods . . . 129
A.2 χ^2-fitting . . . 130

B Complements for Chap. 2 132
B.1 Convention for the γ-matrices . . . 132
B.2 Discrete symmetries on the lattice . . . 132

C Complements for Sect. 3.2 134
C.1 Computational details of $i\hat{\Pi}^{\mathrm{I}}$ . . . 134
C.2 Useful recurrence relations . . . 137
C.2.1 Modified Bessel functions . . . 137
C.2.2 Chebyshev polynomial of the second kind . . . 138

D Complements for Sect. 4.1 **139**
D.1 Derivatives of the functions J_α's and related quantities . . . 139
D.2 Numerical treatment of $J_{\frac{1}{2}}(a,b)$ and $\partial_a J_{\frac{1}{2}}(a,b)$ . . . 142
D.3 Expressions for the C^i's . . . 143
D.3.1 The usual part . . . 144
D.3.2 The additional part . . . 145
D.4 Case with anti-periodic boundary condition in the time-direction . . . 148

E Complements for Sect. 4.2 **150**
E.1 List of functions for the box class . . . 150
E.1.1 $\tilde{I}_4$ . . . 150
E.1.2 $i\hat{\Pi}^{4,1}$ . . . 151
E.1.3 $\tilde{N}$ . . . 151
E.2 List of functions for the triangle class . . . 152
E.2.1 $\tilde{I}_3$ . . . 152
E.2.2 $i\hat{\Pi}^{3,j}$ . . . 152

F Supplementary material for Chap. 6 **154**
F.1 Results from individual ensembles for Sect. 6.3 . . . 154
F.1.1 The connected contribution . . . 154
F.1.2 The (2+2)-disconnected contribution . . . 154
F.2 Results from individual ensembles for Sect. 6.4 . . . 154
F.2.1 Purely light-quark contribution to the leading topologies . . . 155
F.2.2 Strange quark contribution to the leading topologies . . . 155
F.2.3 The $(3+1)_{\text{light}}$ contribution . . . 155
F.3 Fitting results for the (3+1)-contribution . . . 155

Acronyms **159**

Bibliography **161**

This page is intentionally left blank.

Introduction

The Standard Model (SM) of particle physics, a model which unifies three of the fundamental interactions, namely the electromagnetic, weak and strong interactions, was constructed in the 1960's and has led to tremendous success in various predictions of physical observables. Notably, the discovery of the Higgs boson in 2012 at the Large Hadron Collider (LHC) further corroborates the model. However, besides conceptual problems such as the hierarchy problem associated with the Higgs boson mass, it is clear that the SM itself is not complete, because it fails in explaining the mass of neutrinos and the abundance of dark matter in the Universe. Over years, efforts have been made to push the precision frontier on both the theory and the experimental sides to verify the validity of the SM on a wide range of observables for which SM predictions appeared consistent early with the experimental measurements. However, as the precision improves, we see that some discrepancies between the SM predictions and experiments gradually show up.

A very recently reported example of this kind of tension is the discovery of lepton universality violation in the B-meson semi-leptonic decay at the LHCb [Aai+21]. The 3 charged leptons in the SM, the electron e^-, the muon μ^- and the tau τ^-, are expected to interact almost in the same way with the quarks up to processes suppressed by their mass due to the mass hierarchy between them. The LHCb experiment shows that the branching ratio for $B^+ \to K^+\mu^+\mu^-$ to $B \to K^+e^+e^-$ measured in the kinematic region of the dilepton mass-squared ranging from 1.1 to 6.0 GeV^2/c^4 is 3.1σ away from unity. Another famous example is the search for unitarity violation of the Cabibbo-Kobayashi-Maskawa (CKM) matrix. The CKM matrix provides a way to realize CP-violating processes in nature by mixing the quark flavors. The violation of unitarity of the CKM matrix would be another failure of the SM in providing a consistent mechanism to describe the CP-violation, which is one of the Sakharov necessary conditions for baryogenesis to happen in the history of Universe [Sak91]. Even though tensions between predictions from different processes still exist, theorists have been working hard in sharpening the theory prediction on this quantity, which requires good handling of the non-perturbative effects [Gam+20].

The *anomalous magnetic moment of the muon* (a_μ), also commonly called $g-2$ of the muon, is quantified by the deviation of the g-factor of the muon from its classical value of 2 due to quantum corrections. Historically, the success in predicting the quantum correction to $g-2$ for the electron, first by Julian Schwinger [Sch48] and then followed by other higher order computations, provides a strong proof for the validity of Quantum Electrodynamics (QED). However, to test the validity of the SM, merely considering the $g-2$ of the electron is not sufficient, because the electron is quite light and not very sensitive to the strong interaction described by Quantum Chromodynamics (QCD), which is more difficult to handle because perturbative methods can not be applied in the relevant energy region. The muon, being about 200 times heavier than the electron, is a good candidate to explore the realm where QCD effects really kick in. For the same reasons, the sensitivity to the physics at an energy scale beyond the SM is proportional to the mass-squared of the lepton.

On the experimental side, the most recent result for a_μ is the one from the first run of the E989 experiment at Fermi National Accelerator Laboratory (FNAL) released in April 2021 [Abi+21], with a 0.46 ppm-level precision. The technology is based on its predecessor, the completed E821 experiment at Brookhaven National Laboratory (BNL) [Ben+06], with a 0.54 ppm-level precision. On the theory side, a consensus on a_μ has been reached and published in the 2020 muon $(g-2)$ White Paper [Aoy+20], with comparable precision to the experiments. Comparing these results, one finds that the theory prediction is 4.2σ smaller than the experimental world-average.

The on-going experimental efforts at FNAL and the planned E34 experiment at J-PARC [Abe+19] are expected to reduce the experimental uncertainty by a factor of 4. On the theory side, the major error budget comes from the hadronic contributions. At the time of writing of this thesis, the community has put great efforts in two key not-so-well determined hadronic contributions: the Hadronic Vacuum Polarization (HVP) and the Hadronic Light-by-Light (HLbL) scattering. The former makes a much larger contribution and therefore requires going to higher relative accuracy. The latter is small in magnitude but has been determined with sizeable relative uncertainty.

Challenges on the theory side come from the non-perturbative nature of QCD at low energies, the scale of hadronic physics. Many methods used in the calculation of a_μ are based on low-energy effective field theories of QCD with experimental data as input. Independently of data-driven methods, it is possible to directly numerically simulate QCD from first-principles. Lattice Quantum Chromodynamics (LQCD), developed from a formulation proposed by Ken Wilson in 1974 [Wil74], provides a systematically improvable way of studying non-perturbative QCD. With the progress of modern computing technology, LQCD has become a competitive method even in precision physics. After it being successfully applied to the HVP calculation, proposals of applying LQCD for the HLbL have been made [Hay+06; Blu+15; Gre+16]. Nonetheless, this is not a trivial task. First, due to the more complex structure of the function which has to be evaluated non-perturbatively on the lattice, it is computationally more demanding. Second, one expects large finite-volume corrections from the lattice computation because of the effects of massless photons. This aspect is also relevant for the HVP computation, but the propagating light mesonic intermediate states, rendered possible because of chiral anomaly, could make this issue a bigger concern in the HLbL calculation. In the Mainz group, a lattice approach based on position-space formalism has been developed in the past years [Asm+19]. The finite-size effects are expected to be much milder in this framework.

This thesis includes work concerning different aspects of the Mainz determination for a_μ^{hlbl}. Especially, it covers several technical aspects of our published papers on this topic [Cha+20; Cha+21], either directly or indirectly but illustrated with applications to different examples. This thesis is organized in the following way. We will start with a review on the current research status on a_μ in Chapter 1 in full generality including different theoretical approaches. In Chapter 2, a brief general review of LQCD and other field-theoretical background knowledge will be given, with a special focus on the formalism employed by the Mainz group. In Chapter 3, we give the general formulation of the Mainz position-space approach for calculating the HLbL contribution to the muon $g-2$ on the lattice. As an example of how the position-space technique is applied, we compute the scalar-meson-exchange contribution to a_μ^{hlbl} based on the position-space method. This computation illustrates in

part how Gegenbauer Polynomials, which is extensively employed for the QED kernel function, can be used in a diagrammatic approach to scattering amplitudes. In Chapter 4, we discuss the techniques used for finite-size-effect correction adopted in Ref. [Cha+20] and illustrate them with two different examples. In Chapter 5, we first briefly review some fundamental properties of Chiral Perturbation Theory and discuss how to extend it to a Partially Quenched Chiral Perturbation Theory, which is particularly useful in the study of the contributions of different intermediate components from an LQCD computation. With all these tools introduced, we will come back to our lattice calculations of a_μ^{hlbl} [Cha+20; Cha+21] in Chapter 6, with comments on the specific LQCD techniques involved in the calculations. Finally, we conclude the thesis with a summary of relevant work done for this thesis and give an outlook of the presented work in Chapter 7.

The results presented in following parts of the thesis are my independent work: Sect. 3.2, Chap. 4, Chap. 5. The work presented in Chap. 6 are done in collaboration, where my main contribution is on the data generation and analysis for the sub-leading topologies.

Chapter 1

Hadronic contributions to the anomalous magnetic moment of the muon

The anomalous magnetic moment of a lepton l is defined via the second Pauli form factor, F_2, of the process $l\gamma \to l$ at on-shell photon kinematics. Formally, the matrix element $\mathcal{M}^\mu \equiv \langle \mu^-(q_2)|j^\mu|\mu^-(q_1)\rangle$ of this process at arbitrary momenta before being contracted with the polarization vector of the external photon can be parametrized as (c.f. e.g. Ref. [Sch14])

$$i\mathcal{M}^\mu = (-ie)\bar{u}(q_2)\left[\gamma^\mu F_1(p^2) + \frac{i\sigma^{\mu\nu}}{2m_l}p_\nu F_2(p^2)\right]u(q_1)\,, \tag{1.1}$$

where $\bar{u}$ and u are the spinor fields of the incoming and the outgoing lepton, the q_i's are the momenta of the leptons, $\sigma^{\mu\nu} \equiv \frac{i}{2}[\gamma^\mu, \gamma^\nu]$ and $p \equiv q_2 - q_1$. At tree-level, we have, for all momenta,

$$F_1 = 1\,, \quad F_2 = 0\,. \tag{1.2}$$

When putting the photon on-shell, the form factor $F_1(0)$ is a measure of the electric charge of the lepton, so its value does not change when higher order quantum corrections are included. On the contrary, the form factor $F_2(0)$ does receive higher order corrections, which provides a way of probing the quantum effects that can not be described by classical theories. The non-vanishing deviation of $F_2(0)$ from zero defines the anomalous magnetic moment,

$$a_l = F_2(0)\,. \tag{1.3}$$

An equivalent definition of this quantity involving the *Landé g-factor*, g_l, which has a classical value of 2, is

$$a_l = \frac{1}{2}(g_l - 2)\,. \tag{1.4}$$

One can prove that in the non-relativistic limit, the Landé g-factor enters in the definition of the magnetic moment $\vec{\mathfrak{m}}$ of the lepton l as

$$\vec{\mathfrak{m}} = g_l \frac{e}{2m_l}\vec{S}\,, \tag{1.5}$$

where $\vec{S}$ is the spin of the lepton l.

Experimentally, the anomalous magnetic moment of the muon a_μ can be determined from the difference between the cyclotron frequency and the spin precession frequency of the muon in presence of an external electromagnetic field, as done in

the BNL E821 experiment and the FNAL E989 experiment [Ben+06; Abi+21], with a very high precision. The accuracy of the combination of the BNL and the first run of the FNAL experiment is 0.35 ppm. Therefore, the prediction of a_μ can be used as a strong check for the validity of models of particle physics. Due to the mass difference between the electron and the muon, they are sensitive to physics from different scales. In particular, the muon is more sensitive to hadronic physics. Within the Standard Model, a_μ receives contributions from 3 different sources: QED, electroweak interaction and QCD. The non-perturbative nature of QCD at low energies renders it difficult to make theoretical predictions. As of the White Paper from the Muon g-2 Theory Initiative[1] published in 2020 [Aoy+20], the averaged theory prediction, taking into account all 3 sources of the SM contributions, is

$$a_\mu^{\mathrm{SM}} = 116\,591\,810(43) \times 10^{-11}\,, \tag{1.6}$$

with an error entirely dominated by the hadronic contributions; whereas the averaged result from the BNL E821 and the FNAL E989 reads

$$a_\mu^{\mathrm{exp}} = 116\,592\,061(41) \times 10^{-11}\,, \tag{1.7}$$

i.e. there is currently a 4.2σ-level tension between theory and experiment. Nonetheless, scientific consensus for confirming a discrepancy requires at least a 5σ-level significance. On both the theory and the experimental side, further efforts are being made in order to reduce the uncertainties.

In the rest of this chapter, we will review the status of the theory calculations of the hadronic contributions to a_μ following the White Paper [Aoy+20]. The latter focuses on the two first categories of hadronic contributions one encounters by expanding in α_{QED}: the *Hadronic Vacuum Polarization* contribution at $\mathrm{O}(\alpha_{\mathrm{QED}}^2)$ and the *Hadronic Light-by-Light* contribution at $\mathrm{O}(\alpha_{\mathrm{QED}}^3)$ (see Fig. 1.1). In terms of order of magnitude, at leading order, a_μ^{hvp} is about 7000×10^{-11} and a_μ^{hlbl} is about 100×10^{-11}. Therefore, to reach the required accuracy to confirm the discrepancy, a_μ^{hvp} has to be determined to sub-percent precision, while a mere 10%-level precision for a_μ^{hlbl} is desired. For each of them, there are two accepted approaches in the 2020 White Paper. The first one is a data-driven one, which relates the relevant contributions to other physical processes, for which experimental data are available, based on unitarity and analyticity of matrix elements as a consequence of Quantum Field Theory. The second approach is to calculate directly the hadronic processes from first-principles, using Lattice QCD.

1.1 Hadronic Vacuum Polarization contribution to a_μ

1.1.1 Data-driven approach

The leading hadronic contribution to a_μ comes from the Hadronic Vacuum Polarization, which enters in $\mathrm{O}(\alpha_{\mathrm{QED}}^2)$ at leading order. It admits an integral representation [LR68; BR68]

$$a_\mu^{\mathrm{HVP,LO}} = \frac{\alpha^2}{3\pi^2} \int_{m_\pi^2}^{\infty} \frac{K(s)}{s} R(s) ds\,, \tag{1.8}$$

where m_π is the mass of the pion, K is a kernel function containing the QED information and R is called the *R-ratio*, which is directly related to the $e^+e^- \to$ hadrons

[1] `https://muon-gm2-theory.illinois.edu/`

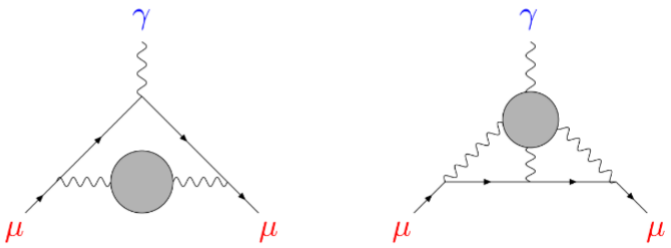

FIGURE 1.1: The first two hadronic contributions to a_μ in power-counting of α_{QED}: the hadronic vacuum polarization (left) and the hadronic light-by-light scattering (right). The plain lines with arrow are the muons, the wavy lines represent the photons and the blobs in the middle are the hadronic contributions. Plot taken from Ref. [MW19].

cross-section. Therefore, one can take the experimental input for the latter and compute a_μ^{hvp}. The most detailed cross-section analyses for different hadronic final states from the e^+e^--collision have been carried out by two different groups [Dav+17; Dav+20a; KNT18; KNT20], supplemented with advanced perturbative-QCD calculations, valid in the high-momentum regime. These analyses also include the next-to-leading order HVP contribution (with different kernel function). Another mature analysis is based on the constraints due to unitarity and analyticity of scattering amplitudes, providing parametrizations for the relevant form factors for the 2- and 3-pion scattering channels [CHS19; HHK19]. The above approaches lead to values in the same ballpark for the specific pion contributions. As for the next-to-next-to-leading order, an estimate based on a cross-section analysis is given in Ref. [Kur+14]. In these analyses, it turns out that the uncertainties from the higher-order contributions are well under control for the required precision. The improvement for the HVP contribution solely requires the improvement on the leading order contribution.

1.1.2 Lattice approach

During the past decades, systematic ways of computing a_μ^{hvp} on the lattice have been established and the achieved accuracy is being progressively improved. One early formalism is based on a representation involving spacelike momenta, which is convenient for a calculation on the lattice [LPd72; Blu03]

$$a_\mu^{\text{hvp}} = \left(\frac{\alpha}{\pi}\right)^2 \int_0^\infty dQ^2 f(Q^2)\hat{\Pi}(Q^2)\,, \tag{1.9}$$

where $f(Q^2)$ is a kernel function incorporating the QED information and $\hat{\Pi}(Q^2)$ is related to the vacuum polarization tensor, which one can obtain from the electromagnetic current 2-point function calculated on the lattice.

A caveat of the above formalism is that the vacuum polarization tensor becomes hard to measure precisely at small Q^2 on the lattice. This region is nonetheless important because of the long-range nature of the QED effects. A method to handle this region is to first compute the trace of the vacuum polarization tensor $\sum_k \Pi_{kk}(Q^2)$ at vanishing spatial momenta, and then deduce the value of $\hat{\Pi}$ at small momenta from

its series expansion in terms of the derivatives of $Q^2 \sum_k \Pi_{kk}(Q^2)$ with respect to Q^2. Such a method is known as the *time-moment method* [Cha+14]. Another popular alternative, the *time-momentum representation* of a_μ^{hvp}, is proposed in Ref. [BM11], under which [MW19]

$$a_\mu^{\text{hvp}} = \left(\frac{\alpha}{\pi}\right)^2 \int_0^\infty dx_0 w(x_0) G(x_0)\,, \quad G(x_0)\delta_{kl} = -\int d^3\vec{x}\,\langle J_k(x) J_l(0)\rangle\,, \tag{1.10}$$

where $w(x_0)$ is a kernel function in the Euclidean time x_0 and the J_i's are the hadronic components of the electromagnetic current.

Although not yet totally lining up with the precision level achieved by the data-driven approaches, the lattice results on a_μ^{hvp} from different collaborations are being systematically improved. More complete programs, including the strong-isospin breaking due to the mass difference between the up- and down-quarks, the dynamical charm-quark and further radiative corrections have been envisaged and proceeded in the community [Cha+18; Bor+18; Blu+18; Giu+19a; SK19; Dav+20b; Gérardin+19; Aub+20; GS19] .

Remarkably, the current most accurate lattice determination of a_μ^{hvp}, coming from the published result of the Budapest-Marseille-Wuppertal (BMW) collaboration in 2021 [Bor+21], has achieved a very competitive precision compared to the White Paper average, which only accounts for the results obtained with data-driven approaches due to the large errors of the available lattice results by the time of its publication. This lattice result is much closer to the current experimental determination from the average of the Brookhaven E821 experiment and the FNAL E989 experiment of a_μ with only a 1.5σ-level deviation. As the lattice community is now more or less adopting the same methodologies in computing a_μ^{hvp}, it is interesting to see if other lattice collaborations could confirm the finding of the BMW collaboration, which might lead the research on the muon $g-2$ to another direction.

1.2 Hadronic light-by-light contribution to a_μ

Although starting at $\mathrm{O}(\alpha_{\text{QED}}^3)$ at its leading order, relatively large relative error of a_μ^{hlbl} makes a more precise determination thereof necessary to reduce the overall theory error on a_μ. As of the 2020 Theory White Paper, the most accurate determinations of a_μ^{hlbl} also came from data-driven methods [MV04; MSP17; Col+17; Hof+18a; GMN19; BHTRS19; Col+20; PV14; DV17; Jeg17; Kne+18; EFW20; RSP20; Col+14b], although formalisms suitable for LQCD calculations have been developed and the progress is catching up with data-driven methods rapidly [Blu+20; Cha+21].

The light-by-light scattering process itself has actually been observed in a certain energy range experimentally for (quasi-)real photons. Among recent developments, it is worth mentioning the extraction from the data measured at ATLAS at the Large Hadron Collider (LHC) [Aab+17; Aad+19]. Different from other previously established methods, such as the ones based on Delbrück scattering [MK33], which describes the positron-electron pair production in a Coulomb field background[2], the ATLAS collaboration focuses on the *ultra-peripheral collisions* of relativistic lead ions [BB88; NRC02]. The principle behind this method is that, in the relativistic regime, the perturbation of the electromagnetic field due to a moving heavy ion

[2] See Ref. [Aab+17] for further references for measurements using this method.

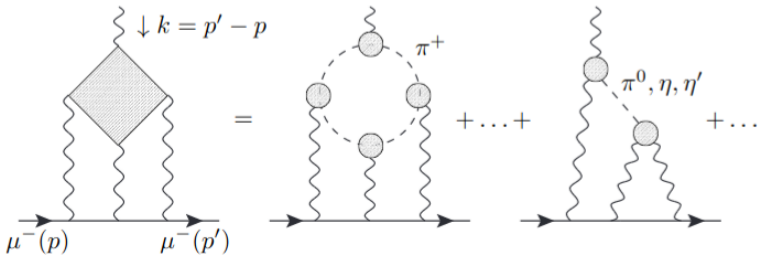

FIGURE 1.2: Contributions to a_μ^{hlbl} from light pseudoscalar mesons: the charged-pion loop (first term on the right-hand side) and the neutral-pseudoscalar pole (second term on the right-hand side). Plot adapted from Ref. [Nyf19].

leads to the production of quasi-real photons with small virtualities [Fer25]. In particular, this effect is enhanced by the proton number of the incident ion. By keeping the impact factor of the collision large enough, the process becomes much less sensitive to the strong interaction between the ions. Instead, hadronic processes are triggered by the scattering of the quasi-real photons.

However, a_μ^{hlbl} is a much harder quantity for data-driven methods compared to a_μ^{hvp} due to the fact that one is now concerned with the virtual process $\gamma^*\gamma^* \to \gamma^*\gamma$, which results in extra complications in handling the possible intermediate states created by the $\gamma^*\gamma^* \to$ hadrons processes.

1.2.1 Data-driven method

The most popular and successful data-driven approaches for a_μ^{hlbl} deal with the off-shell hadronic four point function of electromagnetic currents directly

$$\Pi^{\mu\nu\lambda\sigma}(q_1, q_2, q_3) = -i \int_{x,y,z} e^{-i(q_1 x + q_2 y + q_3 z)} \left\langle 0 \left| T \left\{ j^\mu(x) j^\nu(y) j^\lambda(z) j^\sigma(0) \right\} \right| 0 \right\rangle . \quad (1.11)$$

We will not give the explicit connection between $\Pi^{\mu\nu\lambda\sigma}$ and a_μ^{hlbl} here as it will be covered in Sect. 3.1 when we discuss the position-space QED kernel that we use for our lattice computation.

One can expand the HLbL scattering process in the way described in Fig. 1.2 in Chiral Perturbation Theory (see Sect. 5.1), where only the lightest degrees of freedom are shown. Note that for the interaction vertices, one has to include properly the form factors due to the internal structure of the pseudoscalar mesons. The most long-ranged contribution stems from the neutral-pion (π^0) exchange (*pion-pole contribution*). It also turns out to be numerically dominant compared to the charged-pion loop, even though the charged-pion loop is of order $O(p^2)$ and therefore parametrically larger in chiral counting [Nyf19].

Early attempts to compute a_μ^{hlbl} were based on models, which also provided a description of the form factors. Examples of such are the Hidden Local Symmetry approach supplemented with Vector-Meson-Dominance (VMD) [HKS95; KNO85] and the extended Nambu-Jona-Lasinio (ENJL) model [BPP95]. Note that both calculations made a sign mistake for the pion-pole and have been corrected in subsequent publications. Also, in the ellipsis on the right-hand side of Fig. 1.2 are hidden short-distance contributions that can not be captured by low-energy effective field

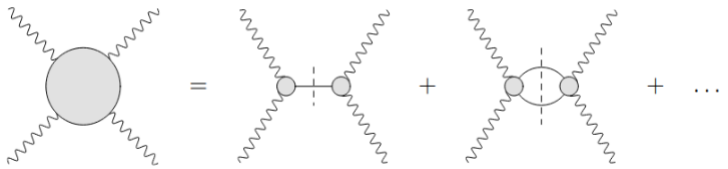

FIGURE 1.3: Unitarity cuts applied to the HLbL diagram. Plot taken from Ref. [Col+17].

theories of QCD. Those were often estimated using constituent quark models in the early days, which in fact might introduce unwanted double-counting [Nyf19].

In modern model-independent approaches [Col+15], the tensor structure of the rank-4 tensor $\Pi^{\mu\nu\lambda\sigma}$ has been analyzed in detail and it is found that it can be decomposed in a basis composed of 7 genuinely independent tensors plus quantities that are related to these independent tensors under crossing symmetry [BT68; Tar75]. At the end of the day, a_μ^{hlbl} can be reduced to a sum of integrals of 12 scalar functions from the tensor decomposition with different weight factors [Col+15]. The dispersive data-driven approach classifies a_μ^{hlbl} into different topologies in a rigorous way based on analyticity and unitarity of the light-by-light scattering amplitude. The topologies reveal the behavior of different parts of the amplitude under one- or multi-particle cuts (see Fig. 1.3). The light-by-light scattering amplitude can be reconstructed from these various cuts using inputs from experiment to parametrize the relevant form factors in each channel based on partial wave analysis.

Pion-pole contribution

At leading order in Chiral Perturbation Theory, the $\pi^0\gamma\gamma$ vertex is described by the Wess-Zumino-Witten term [WZ71; Wit83] as a point-like interaction. This is obviously not realistic due to the internal structure of π^0. Therefore, the knowledge of the transition form factor (TFF) for the $\pi^0 \to \gamma^*\gamma^*$ process in the space-like kinematic region, denoted by $\mathcal{F}_{\pi^0\gamma^*\gamma^*}(-Q_1^2, -Q_2^2)$, is crucial for the determination of the pion-pole contribution to a_μ^{hlbl} (the middle diagram of Fig. 1.3). A trustworthy parametrization should satisfy short-distance constraints from perturbative QCD at large momenta such as the Brodsky-Lepage limit [PB79; LB80] for a single virtual photon and the one from Operator Product Expansion [NR83; Nov+84] for two virtual photons. Also, the Adler-Bell-Jackiw (ABJ) anomaly [Adl69; BJ69] should be reproduced when both momenta are zero. Among the simplest phenomenological inspired TFF parametrizations are the VMD and the low-meson-dominance (LMD) [PPR98] ones. It was pointed out in Ref. [KN02] that the VMD parametrization in fact fails to satisfy both short-distance constraints listed above. So does the TFF that one deduces from the ENJL model that was used in the earlier model calculation of a_μ^{hlbl}.

Among recent work on the parametrizations of the pion TFF of the data-driven approach, we can mention two of them. The first one again utilizes a dispersive analysis to interpret the dependence of the pion TFF on other intermediate processes [Hof+18b; Hof+18a]. Under such a framework, the pion TFF is expressed as a double spectral integral, with the pion electromagnetic form factor and certain partial-wave amplitudes as input. The second approach [MSP17] consists in using

Canterbury approximants [Chi73; CMK74; Jon76], an extension of the Padé approximants, to approximate the momenta dependence of the pion TFF. This parametrization is motivated by the expectation that the true TFF would belong to some special class of functions [MSP15].

Also, the short-distance constraints can be easily imposed to such approximants. The final values for the pion-pole contribution obtained from these two methods are in good agreement with competitive errors [Aoy+20].

Experimental input for the pion-pole contribution

It is worth mentioning the available experimental inputs for the study of the pion TFF. As stated earlier, the pion TFF is a key element for the data-driven approach. As of the 2020 theory White Paper [Aoy+20], methods for extracting the TFF from experimental data are established for 3 kinematic regimes: double-real photon, singly-virtual photon at space-like region and singly-virtual photon at time-like region. For the case of double-real photon, the form factor $\mathcal{F}_{\pi^0\gamma^*\gamma^*}(0,0)$ can be extracted from the radiative decay width. The most accurate result comes from the PrimEX experiments [Lar+11; Lar+20]. Their experimental setup is based on the Primakoff effect [Pri51]. The latter states that, when a photon enters in collision with a nucleon via static Coulomb potential, a pion can be subsequently produced. When it comes to the pion TFF in the singly-virtual spacelike region, there is a wide range of available data from e^+e^--collisions. More precisely, experiments try to identify the process $e^+e^- \to e^+e^-X$ with X different possible hadronic final states. To really target the singly-virtual space-like kinematic region, exactly one of the scattered electron should be "tagged" (i.e. not collinear to the incoming one). Finally, for the singly-virtual case in the time-like region, one can reconstruct the TFF from the π^0 Dalitz decay [Dal51]. In this decay mode, after the pion decays into a real and a virtual photon, the virtual one, at a virtuality above the threshold for the dilepton pair production, will then produce a pair of lepton and anti-lepton. Using this process, the kinematic region between the dilepton threshold and the invariant mass of the pion can be probed.

Two-pion, heavier intermediate states and the short-distance contributions

Beside the pion-pole, another important contribution from the pion that has been analyzed is the two-pion contribution, i.e. when two intermediate pion lines are cut (the right-most case of Fig. 1.3). This can be separate into the pion-box contribution, which is characterized by the existence of the left-hand cut in the helicity amplitude[3] and completed to a gauge-invariant object with some other diagrams, and the rest [Col+14a]. It is proven that the pion-box contribution is equivalent to that of a charged-pion loop with an appropriate form factor for the $\gamma \to \pi^+\pi^-$ process [Col+17]. Once this part isolated, the remaining contribution can be computed in a partial wave decomposition, where, for instance, the $\pi\pi$-rescattering effect comes in.

Beyond the pseudoscalar meson contributions, other possible contributions with non-negligible size should enter via the $\gamma\gamma \to$ hadronic process. The lightest scalar,

[3] i.e. existence of poles in the $s < 0$ region, where s is the usual Mandelstem variable, in a two-to-two scattering.

tensor and axial resonances have been studied with different approaches. Usually, the widths of the resonances are assumed to be narrow. Under such a framework, the main difficulty consists in the parametrization of the transition form factors [RSP20; Kne+18], while the treatments with different tensor structures are well-understood [PV14]. In particular, sum rules from unitarity and analyticity of the light-by-light amplitude can be used as a constraint between form factors and the decay width of a resonance state to two photons [PPV12; DV17].

Lastly, at high energies, where QCD becomes perturbative, contributions coming from short-distance physics should be taken into account properly. A set of constraints have to be respected in some particular kinematic regions based on the Operator Product Expansion [MV04; BHTRS19; Col+20].

1.2.2 Status of lattice computation of a_μ^{hlbl}

The first determination of a_μ^{hlbl} at physical quark masses from Lattice QCD is done in a full QED+QCD setup on the lattice by the RBC/UKQCD collaboration [Blu+20]. It utilizes the $\mathrm{QED_L}$ formulation of QED on the lattice [HU08].[4] One important computational strategy that has been used in RBC/UKQCD's $\mathrm{QED_L}$ formulation is the sampling of the electromagnetic field with a stochastic method to perform the complicated integrations on the lattice efficiently [Blu+16]. However, a severe problem with QED on the lattice is the finite-size effects due to the photon zero-mode. Often, a power-law volume dependence in $1/L$, where L is the spatial extent of the box of the lattice simulation, is observed in such a setup.

To have a better control over the finite-volume effects, an alternative consisting in computing the QED part in the continuum and infinite-volume and the QCD part on the lattice has been initiated by both the Mainz group and the RBC/UKQCD [Asm+16; Asm+18; Blu+17]. This is called position-space method by the Mainz group and $\mathrm{QED_\infty}$ by RBC/UKQCD. With this method, one expects an exponentially suppressed volume effect due to the fast decay of the QCD 4-point function at large distances. However, it requires to evaluate a semi-analytic QED kernel function which contains multiple multivariate integrals. The formalism and the numerical methods involved in the computation of the QED kernel will be reviewed a bit more in detail in Sect. 3.1 of this thesis. In the Mainz group, significant effort has been devoted to the numerical optimization of the kernel function and to the verification of the correctness. Based on the previously established work on the position-space method, part of the work presented in this thesis leads to the determination of a_μ^{hlbl} at the physical point of the Mainz group [Cha+21], which is a complete calculation including all possible diagrammatic topologies at the physical point. The Mainz results obtained in Refs. [Cha+20; Cha+21] during my doctoral studies will be reviewed in Chap. 6 of this thesis.

[4] A review of different attempts in putting QED on the lattice can be found in Ref. [Pat17]. In the reference, some caveats of $\mathrm{QED_L}$ are discussed.

Chapter 2

Lattice Quantum Chromodynamics

Lattice Quantum Chromodynamics (LQCD) is a tool that enables studies of the strong-interaction physics in the non-perturbative regime of QCD from first-principles. One starts with a formulation of the QCD action in discretized Euclidean space-time. The space-time discretization with a finite lattice spacing is similar to setting a UV cut-off in momentum-space. Similarly, the finite extent of the lattice introduces an IR-regulator. Such a regularized formulation will give finite results and the discretized space-time is suitable for computer simulations. In particular, Euclidean field theory can be seen as a statistical physics system if the path integral measure of the field space is real and positive. Certain physical observables can thus be computed by carrying out Markov Chain Monte Carlo (MCMC) simulations in Euclidean space-time and traced back to their counterparts in Minkowskian space-time if the simulated lattice theory verifies certain conditions [OS73]. After all, upon Wick rotation, the QCD action in Minkowski space-time is translated into a theory in Euclidean space-time.

The goal of this chapter is to cover the essential theoretical and technical notions of LQCD related to the computation of our observable a_μ^{hlbl}. In particular, we will focus on the formalism and techniques used for the $N_f = 2+1$ gauge field ensembles, with two mass-degenerate dynamical light-quarks and one dynamical strange-quark, generated by the Coordinated Lattice Simulations (CLS) consortium [Bru+15], in which the Mainz group takes part. In Sect. 2.1, we will review the theoretical aspects. We begin with some generalities about LQCD. Then, we will shift our attention to the specific lattice action used by the CLS collaboration, the O(a)-improved Wilson-clover fermion action. In Sect. 2.2, we will focus on the algorithmic aspects of gauge field generation. Again, after introducing general concepts, we will turn to some details of the CLS $N_f = 2+1$ simulations. Lastly, in Sect. 2.3, we will discuss the measurement of physical observables on the lattice. We will dedicate a sub-section to the Dirac operator solver routines existing in the `openQCD` package[1] [LS13] used for our simulations. At the end of the section, we will review the scale setting of our lattice ensembles.

Convention and notations Unless otherwise mentioned, we always refer to Euclidean space-time and actions. The symbol a denotes the lattice spacing. The set of lattice points is represented by Λ and indexed by 4 positive integers. For notational simplicity, color and spin indices are omitted in many cases. They remain open if not traced. Einstein summation convention is used for repeated Lorentz indices. The Lorentz index 0 indicates the temporal direction. The spatial extent of the lattice will be denoted by L and the temporal one by T.

[1] `http://cern.ch/luscher/openQCD`

2.1 Theoretical aspects

2.1.1 The Wilson-Dirac action

The QCD action comprises two parts: a fermionic part and a gluonic part. In continuous Euclidean space-time, the fermionic part of the QCD action reads [GL10]

$$S_F^{\text{cont.}}[\psi, \bar{\psi}, A] = \sum_{f \in \text{flavors}} \int d^4x \bar{\psi}^f(x) \left[\gamma_\mu \left(\partial_\mu + iA_\mu(x)\right) + m^f\right] \psi^f(x). \tag{2.1}$$

where ψ^f is the quark field of flavor f, A_μ is an SU(3)-valued gluonic field, m_f is the quark mass for the quark of flavor f, and the γ_μ's are the γ-matrices in Euclidean space-time (see Appendix B.1 for an explicit choice of representation) which satisfy the anti-commutation relation

$$\{\gamma_\mu, \gamma_\nu\} = 2\delta_{\mu\nu}\mathbb{I}. \tag{2.2}$$

The quark field ψ carries a Dirac (spinor) index and a color index. The $\text{SU}(3)_c$-gauge invariance of the QCD action is achieved by requiring the quark and gluon fields to transform as

$$\begin{aligned} &\psi(x) \to \Omega(x)\psi(x), \\ &\bar{\psi}(x) \to \bar{\psi}(x)\Omega^\dagger(x), \\ &A_\mu(x) \to \Omega(x)A_\mu(x)\Omega^\dagger(x) + i(\partial_\mu\Omega(x))\Omega^\dagger(x). \end{aligned} \tag{2.3}$$

for $\Omega(x) \in \text{SU}(3)$.

On the other hand, the gluonic part of the QCD action is given by

$$S_G^{\text{cont.}}[A] = \frac{1}{2g_0^2} \int d^4x \text{Tr}[F_{\mu\nu}(x)F_{\mu\nu}(x)]. \tag{2.4}$$

where g_0 is the bare coupling constant of the gluon fields and $F_{\mu\nu}$ is the gluonic field strength, defined with the covariant derivative

$$D_\mu(x) = \partial_\mu + iA_\mu(x), \tag{2.5}$$

$$F_{\mu\nu} = -i[D_\mu(x), D_\nu(x)]. \tag{2.6}$$

Let us now put the Euclidean version of QCD on the lattice. Due to the finite extent of the lattice, one has to impose boundary conditions to have a well-defined system. A common choice is to make gluon and quark fields periodic in the spatial directions. However, as the choice of boundary condition should account for the Fermi-Dirac spin statistics for fermions correctly, one has to impose the boundary condition in the time direction with care. More details on boundary conditions will be discussed in a later section.

On the lattice, derivatives are replaced by finite differences. This makes a big difference compared to the theory in the continuum because some terms in the Lagrangian become non-local. To guarantee gauge-invariance of the action, we introduce the *link variable* $U_\mu(n)$, which transforms under gauge transformation as

$$U_\mu(n) \to \Omega(n)U_\mu(n)\Omega^\dagger(n + \hat{\mu}). \tag{2.7}$$

where $n \in \Lambda$, $\Omega(n) \in \mathrm{SU}(3)$ and $\hat{\mu}$ is the unit vector in the μ-direction. For convenience, we use the notation

$$U_{-\mu}(n) = U_\mu^\dagger(n - \hat{\mu}). \tag{2.8}$$

Link variables are closely related to the *gauge transporter* in the continuum. With the help of link variables, we can write down the lattice version of the gluonic part of the QCD action [Wil74]

$$S_G[U] = \frac{\beta}{3} \sum_{n\in\Lambda} \sum_{\mu<\nu} \Re\mathrm{Tr}[\mathbb{I} - U_{\mu\nu}(n)], \tag{2.9}$$

where

$$U_{\mu\nu}(n) = U_\mu(n) U_\nu(n + \hat{\mu}) U_\mu^\dagger(n + \hat{\nu}) U_\nu^\dagger(n). \tag{2.10}$$

is called *plaquette* and

$$\beta = 6/g_0^2 . \tag{2.11}$$

Using the Baker-Campbell-Hausdorf formula, one can prove that the continuum action Eq. (2.4) is recovered at the $a \to 0$ limit.

Unlike the gluonic part, the discretization of the fermionic action contains some subtleties. One severe problem stems from *doublers*, i.e. extra zero modes in the first Brillouin zone, when one tries to write down the Dirac operator of the action naïvely. A way to circumvent this issue is to introduce a Laplacian term, in a way that the Dirac operator can be expressed as [Lus+96]

$$D_\mathrm{W} = \frac{1}{2}\left(\gamma_\mu(\nabla_\mu^* + \nabla_\mu) - a\nabla_\mu^*\nabla_\mu\right), \tag{2.12}$$

where the forward covariant derivative ∇ and the backward covariant derivative ∇^* are defined with action on the quark fields by

$$\begin{aligned} a\nabla_\mu\psi(x) &= U_\mu(x)\psi(x + \hat{\mu}) - \psi(x), \\ a\nabla_\mu^*\psi(x) &= \psi(x) - U_\mu^\dagger(x - \hat{\mu})\psi(x - \hat{\mu}). \end{aligned} \tag{2.13}$$

D_W is called *Wilson-Dirac operator* and the corresponding fermion action is given by

$$S_F[\bar{\psi}, \psi, U] = a^4 \sum_{f\in\text{flavor}} \sum_{n,n'\in\Lambda} \bar{\psi}^f(n)\left(D_\mathrm{W}(n, n') + m^f\right)\psi^f(n'). \tag{2.14}$$

In the above construction, the link variables guarantee gauge-invariance of the action. The extra Laplacian term $\bar{\psi}\nabla_\mu^*\nabla_\mu\psi$ is of dimension 5 and its effect on low modes disappears in the continuum limit. One can verify that the total lattice action $S_F + S_G$ gives the QCD action in the naïve continuum and infinite-volume limit. Furthermore, each part of the action is gauge-invariant and also admits the discrete C, P and T (Euclidean time reflection) symmetries (see Appendix B.2).

Also remarkable is the γ_5-*Hermiticity* satisfied by the Wilson-Dirac operator

$$D_\mathrm{W}^\dagger = \gamma_5 D_\mathrm{W} \gamma_5. \tag{2.15}$$

where $\gamma_5 = \gamma_0\gamma_1\gamma_2\gamma_3$. Note that for most of the popular lattice Dirac operators, this property also holds.

Nonetheless, the Wilson-Dirac formulation suffers from another notorious problem due to the introduction of the extra dimension-five Laplacian term in the action.

In the limit of vanishing quark mass, the QCD action in the continuum and infinite-volume limit admits chiral symmetry, i.e. the action is invariant under the chiral rotation of the quark fields

$$\psi(x) \to e^{i\alpha\gamma_5}\psi(x)\,, \quad \bar{\psi}(x) \to \bar{\psi}(x)e^{i\alpha\gamma_5}\,. \tag{2.16}$$

This is explicitly broken for Wilson-Dirac fermion. Although many attempts in remedying the problem have been tried out, a no-go theorem due to Nielsen and Ninomiya [NN81a; NN81b; NN81c] concludes that it is impossible to put a theory with fermions on the lattice such that chiral symmetry is preserved without doublers under some commonly imposed conditions. More precisely, it can be shown that for a fermionic theory on the lattice with a local Hamiltonian in $(d+1)$-dimension where d is odd, if chiral symmetry is exact, then there will be an equal amount of left-handed and right-handed states for a given energy [Fri82].

Note that one can address the issue of chiral symmetry breaking by requiring the Dirac operator to satisfy a lattice version of chiral symmetry. One lattice version of chiral symmetry is defined by the Ginsparg-Wilson equation [GW82]. There exist fermion discretizations for which this property holds, for instance the *overlap fermion* [Neu98a; Neu98b]. This subject is however out of the scope of this thesis.

The breaking of chiral symmetry by the action has an impact on the renormalization of certain operators. Within the Mainz group and the CLS collaboration, we adopt an extended version of Wilson fermion — the *Wilson-clover* fermion — for our simulations. Although chiral symmetry is again explicitly broken by the action, extra terms in the formulation allow one to mitigate the violation of some particular Ward identities with improved scaling behavior towards the continuum limit. We will give details about the Wilson-clover fermion and the tuning for the scaling improvement in Sect. 2.1.3.

2.1.2 Boundary conditions

Because of the finite extent of the lattice, we have to impose boundary conditions to have a well-defined system. Eligible ones are required to guarantee the discrete space-time symmetries already established in the bulk part. The simplest choice that one can come up with is that of *periodic boundary conditions*, where the gauge fields are periodic in all space-time directions, while the fermionic fields are periodic in the spatial directions and anti-periodic in time to keep the correct Fermi-Dirac statistics. One big advantage of periodic boundary conditions is that one can exploit translational invariance in all directions while computing observables.

A unique feature of the CLS $N_f = 2+1$ simulations is the use of *open boundary condition* [LS11] for a large amount of ensembles, in addition to the ones with periodic boundary condition. This boundary condition is motivated by the decreasing tunnelling rate between different topological sectors of the vacuum while approaching the continuum limit, known as *topological freezing*.

For an SU(N) gauge theory, the *topological charge* in the continuum is defined as[2] [GL10]

$$Q_{\text{top}} = \frac{1}{32\pi^2}\int d^4x\,\varepsilon_{\mu\nu\rho\sigma}\text{Tr}[F_{\mu\nu}F_{\rho\sigma}]\,, \tag{2.17}$$

where $\varepsilon_{\mu\nu\rho\sigma}$ is the Levi-Civita tensor. The topological charge provides a classification of topological sectors of an SU(N)-theory as it is related to the second Chern

[2]Note that there exists different conventions for the field strength $F_{\mu\nu}$ so there might be a sign difference in the continuum expression that we give. Here we stick to the convention of Ref. [GL10].

class [Bel+75]. In particular, the topological charge is an integer. The discretization of the topological charge on the lattice can be done by the standard procedure by respecting the correct limit in the continuum. It has been shown that, under some conditions on the smoothness of the field with periodic boundary conditions in all directions, the space of gauge fields on the lattice is also divided into different topological sectors [Lus82; PS86] and the transition between sectors is shown to be less likely as the lattice spacing diminishes [LÏ0]. This leads to a much longer auto-correlation time for many observables [DDPV02; SSV11]. A long auto-correlation time reduces the effective number of samples of a Monte-Carlo chain because of its implication to the error estimation (cf. Appendix A). The problem is called *critical slowing-down*.

An attempt at mitigating the problem proposed in Ref. [LS11] is to adopt a different boundary condition in the time direction. It consists in requiring

$$F_{0k}(x)|_{x_0=0} = F_{0k}(x)|_{x_0=T} = 0\,, \tag{2.18}$$

for all spatial directions k for the gauge field, and

$$P_+\psi(x)|_{x_0=0} = P_-\psi(x)|_{x_0=T} = 0\,, \quad \bar{\psi}(x)P_-|_{x_0=0} = \bar{\psi}(x)P_+|_{x_0=T} = 0\,, \tag{2.19}$$

where

$$P_\pm \equiv \frac{1}{2}(1 \pm \gamma_0)\,, \tag{2.20}$$

for the quark fields. These conditions are also seen in the *Schrödinger functional* boundary condition, which will be discussed later in Sect. 2.1.3. Note that the boundary condition for the quark fields guarantees the discrete symmetries of the theory. The lack of topological barrier between different sectors for this boundary condition is due to the fact that the boundary condition on the gauge fields Eq. (2.18) allows one to deform smoothly a field configuration satisfying the boundary condition to another one by passing through the trivial one. In other words, the field configuration space is connected under this boundary condition and the topological charge is not quantized in the continuum.

A drawback of open boundary condition is that one loses translational invariance in the temporal direction. Consequently, the boundary effects might appear considerable for some observables and one should stay away from the regions close to the temporal boundaries in practice, if one wants to compute vacuum correlators.

2.1.3 Improvement of the action

The non-vanishing lattice spacing a introduces discretization errors in many ways, for instance, the derivatives are replaced by finite differences. In Refs. [Sym83a; Sym83b], Symanzik proposed a program to improve the discretization error of physical observables computed on the lattice. It consists in modifying the Lagrangian of a theory by adding terms composed of higher dimensional irrelevant operators, which vanish in the continuum limit. For a given n, there exist a finite number of n-dimensional gauge-invariant operators that one can write down with quark and gluon fields. These higher-dimensional operators can enter in the Lagrangian linearly without changing it in the continuum limit. One can tune the coefficients perturbatively or non-perturbatively such that the observables that one is interested in follow desired scaling behaviors while approaching the continuum limit. A way

to shorten the list of additional irrelevant operators is to use the equations of motion of the original Lagrangian. This condition restricts the number of linearly independent operators. We will give details specific to the CLS $N_f = 2+1$ simulations, which utilize a non-perturbatively $O(a)$-improved Wilson-clover fermion action with Lüscher-Weisz tree-level $O(a^2)$-improved gauge action.

Tree-level O(a^2)-improvement of the gauge action

Let us start with the improvement of the gauge action. Recall that the Wilson gauge action Eq. (2.9) is constructed in a way that it recovers the purely glonic part of the QCD action in the continuum. This is done with a plaquette sum. One can visualize the plaquette Eq. (2.10) as an elementary square made of link variables surrounding a given point on the lattice according to an orientation. The plaquette sum amounts to covering the whole space-time with these elementary squares composed of link variables. Besides the elementary square, there exist also other contours of link variables which one can use to cover the whole space-time with and give the correct continuum limit (see Fig. 2.1). By combining gauge actions constructed with different choices of link variable contour and the Wilson gauge action Eq. (2.9), it is possible to cancel unwanted discretization effects by keeping the difference between the resulting action and the one in the continuum at higher order in the lattice spacing a.

In Ref. [LW85], Lüscher and Weisz derived a set of conditions on the coefficients for the linear combination of gauge actions with different link variable contours and the Wilson plaquette action, such that the discretization effects of the energy spectrum are milder than O(a^2) in perturbation theory. The authors call this *on-shell improvement*. Following the improvement conditions, the choice made by the CLS collaboration for the $N_f = 2+1$ simulations is to modify the bulk Wilson plaquette action Eq. (2.9) to[3]

$$S_G^{\text{impr.}}[U] = \frac{\beta}{6}\Big(c_0 \sum_p \text{Tr}[\mathbb{I} - U(p)] + c_1 \sum_r \text{Tr}[\mathbb{I} - U(r)]\Big)\,, \tag{2.21}$$

where $c_0 = 5/3$, $c_1 = -1/12$ and the sums run over the plaquette p and the 1×2 planar rectangles r covering the entire space-time. Note that there are other improvement schemes for the gauge action with different criteria, e.g. the Iwasaki action [Iwa83] which utilizes the behavior of the renormalization group as argument.

Non-perturbative O(a)-improvement of the fermion action

As for the fermionic part, the improvement is done by including the dimension-5 purely gluonic Sheikholeslami-Wohlert term (or *clover term*) in the action [SW85], which enters in the improved action with a coefficient c_{SW} and modifies the fermionic action Eq. (2.14) to [Lus+96]

$$S_F^{\text{impr.}}[U,\bar\psi,\psi] = S_F[U,\bar\psi,\psi] + a^5 \sum_{n\in\Lambda} c_{\text{SW}}\bar\psi(n)\frac{i}{4}\sigma_{\mu\nu}\hat F_{\mu\nu}(n)\psi(n)\,, \tag{2.22}$$

where

$$\sigma_{\mu\nu} = \frac{i}{2}[\gamma_\mu,\gamma_\nu]\,, \tag{2.23}$$

[3] In fact, extra improvement terms are put on the boundaries due to technical complications, which will not be discussed in detail here.

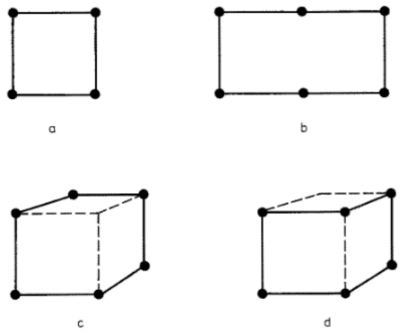

FIGURE 2.1: Examples of possible elementary contours of link variables which one can use to cover up the whole space-time with the correct continuum limit for the gauge action. Figure taken from Ref. [LW85].

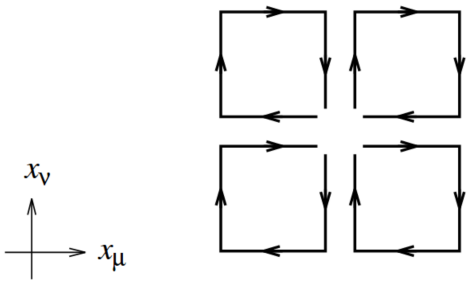

FIGURE 2.2: Graphic representation of the plaquettes appearing in Eq. (2.25). Figure taken from Ref. [Lus+96].

$$\hat{F}_{\mu\nu}(n) = \frac{1}{8a^2}\Big(Q_{\mu\nu}(n) - Q_{\nu\mu}(n)\Big)\,, \tag{2.24}$$

with $Q_{\mu\nu}(n)$ defined with the sum of the plaquettes forming the shape of a clover leaf around the site n (see Fig. 2.2),

$$Q_{\mu\nu}(n) \equiv U_{\mu,\nu}(n) + U_{\nu,-\mu}(n) + U_{-\mu,-\nu}(n) + U_{-\nu,\mu}(n)\,. \tag{2.25}$$

Note that c_{SW} depends only on the bare gluon field coupling constant g_0.

The non-perturbative determination of c_{SW} for the CLS $N_f = 2+1$ ensembles has been done in Ref. [BS13] with a similar prescription as in Ref. [Lus+97]. The starting point is the *Partially Conserved Axial Current* (PCAC) relation. Before introducing it, let us consider the axial Ward identity for isovector axial current in the continuum limit.

In the continuum, the QCD quark field path integral measure is anomalous under chiral rotation Eq. (2.16) in the massless limit. However, the QCD action in the massless limit also admit $\mathrm{SU}(N_f)$-flavor symmetry generated by the infinitesimal transformations

$$\begin{aligned} \psi(x) &\to \Big(1 + i\alpha T\gamma_5\Big)\psi(x)\,, \\ \bar{\psi}(x) &\to \bar{\psi}(x)\Big(1 + i\alpha T\gamma_5\Big)\,, \end{aligned} \tag{2.26}$$

where T is an element of $\mathfrak{su}(N_f)$ and acts only on the flavor space.

Using

$$\det A = \exp(\mathrm{Tr} \ln A)\,, \tag{2.27}$$

one can show that the QCD quark field path integral measure is not anomalous under this transformation due to the tracelessness of T.

Let us now focus on the $N_f = 3$ case. Define the isovector axial current

$$A^a_\mu = \frac{1}{2}\bar{\psi}\gamma_\mu\gamma_5\lambda^a\psi\,, \tag{2.28}$$

and the isovector pseudo-scalar

$$P^a = \frac{1}{2}\bar{\psi}\gamma_5\lambda^a\psi\,, \tag{2.29}$$

where λ^a is a Gell-Mann matrix acting on the flavor space only. Then, it can be shown that, in the continuum limit, we have the following Ward identity in the degenerate quark mass limit

$$\partial_\mu A^a_\mu = 2mP^a\,. \tag{2.30}$$

This identity is called the PCAC relation and holds also for renormalized quantities.

On the lattice, especially with an action which breaks chiral symmetry explicitly, one would expect that the PCAC relation holds only up to O(a) effects. Nonetheless, one can tune c_{SW} such that the O(a)-discretization effects are removed. Upon Symanzik improvement of the action, there might be extra O(a) corrections to correlation functions. In that regard, one has to take into account the corrections coming from higher dimensional operators which can mix with the operator that we are interested in. From parity and charge-conjugation symmetry properties of A^a and P^a, we introduce the *improved axial current* $(A_{\mathrm{I}})^a$ defined by

$$(A_{\mathrm{I}})^a_\mu = A^a_\mu + ac_A\frac{1}{2}(\partial_\mu + \partial^*_\mu)P^a\,, \tag{2.31}$$

where ∂_μ and ∂^*_μ are the forward and backward finite difference and c_A is a coefficient to be determined. We do not have to change the definition of P^a to account for the improvement because it can be shown that this can be hidden in the renormalization constant for P^a. Then, the PCAC relation that we want to restore up to O(a) is

$$\frac{1}{2}(\partial_\mu + \partial^*_\mu)\langle(A_{\mathrm{I}})^a_\mu(x)\mathcal{O}\rangle = 2m\langle P^a(x)\mathcal{O}\rangle\,, \tag{2.32}$$

where $\mathcal{O}$ is a generic operator.

A choice made in Ref. [Lus+96] for the operator $\mathcal{O}$ makes use of the *Schrödinger functional* [LW96]. The idea is to introduce extra fields which live only on the temporal boundaries and can naturally be coupled to the bulk while respecting the symmetries of the action. One of the advantages and reasons why this choice is made is due to the renormalization of the strong coupling constant. In fact, we would like to find a mass-independent scheme such that the renormalization conditions can be imposed in the zero quark mass limit, and run up to the scale that we are interested in. Under the breaking of chiral symmetry, it is expected that the physical, renormalized quark mass vanishes when the bare mass m_0 equals a critical mass m_c which depends on the bare strong coupling constant g_0 in a mass-independent renormalization scheme.

Introduce the subtracted bare mass

$$m_q = m_0 - m_c \,. \tag{2.33}$$

The renormalization patterns of the strong coupling constant and the quark mass are

$$\begin{aligned} g_R^2 &= g_0^2 Z_g(g_0^2, a\mu)\,, \\ m_R &= m_q Z_m(g_0^2, a\mu)\,, \end{aligned} \tag{2.34}$$

where μ is a renormalization scale. Therefore, a mass-independent scale for the renormalization has to be introduced. On the lattice, the finite extent provides a natural good choice of scale for this purpose: the spatial extent L. The running of the strong coupling constant has been studied in Ref. [SS96] using the Schrödinger functional approach by looking at the response of the functional to a change of the gauge field at the temporal boundaries. The inclusion of boundary fields in the lattice action can also be improved with the help of perturbation theory at one-loop [LW96]. We will give neither the technical details, nor the explicit expression for the Schrödinger functional. We refer the reader to the original references.

The Schrödinger functional extends the action naturally by including boundary quark fields ρ, $\bar{\rho}$, ρ' and $\bar{\rho}'$, which are related to the chiral projections of the bulk quark fields on the temporal boundaries. The un-primed quantities sit on time slice 0 and the primed ones sit on time slice T, where T is the time extent of the lattice. If one wants to get the correlation function in the original action, one simply sets these fields to zero at the end. Now define the boundary sources

$$\begin{aligned} \zeta(\mathbf{x}) &= \frac{\delta}{\delta\bar{\rho}(\mathbf{x})}\,, \quad \bar{\zeta}(\mathbf{x}) = -\frac{\delta}{\delta\rho(\mathbf{x})} \\ \zeta'(\mathbf{x}) &= \frac{\delta}{\delta\bar{\rho}'(\mathbf{x})}\,, \quad \bar{\zeta}'(\mathbf{x}) = -\frac{\delta}{\delta\rho'(\mathbf{x})}\,. \end{aligned} \tag{2.35}$$

We then feed the boundary operators

$$\mathcal{O}^a = a^6 \sum_{\mathbf{y},\mathbf{z}} \bar{\zeta}(\mathbf{y})\gamma_5 \frac{\lambda^a}{2} \zeta(\mathbf{z})\,, \quad \mathcal{O}'^a = a^6 \sum_{\mathbf{y},\mathbf{z}} \bar{\zeta}'(\mathbf{y})\gamma_5 \frac{\lambda^a}{2} \zeta'(\mathbf{z})\,, \tag{2.36}$$

to the PCAC relation Eq. (2.30). Note that the operators and the mass entering in Eq. (2.30) should be renormalized. For an O(a)-improvement of the PCAC relation, let us define a "mass" parameter at a given time coordinate x_0

$$m(x_0) \equiv r(x_0) + c_A s(x_0)\,, \tag{2.37}$$

where

$$r(x_0) = \frac{1}{4f_P(x)}(\partial_0^* + \partial_0) f_A(x_0)\,, \tag{2.38}$$

$$s(x_0) = \frac{1}{2f_P(x_0)} a\partial_0^*\partial_0 f_P(x_0)\,, \tag{2.39}$$

$$\begin{aligned} f_A(x_0) &= -\frac{1}{3}\langle A_0^a(x)\mathcal{O}^a\rangle\,, \quad f_P(x_0) = -\frac{1}{3}\langle P^a(x)\mathcal{O}^a\rangle\,, \\ f_A'(T-x_0) &= \frac{1}{3}\langle A_0^a(x)\mathcal{O}'^a\rangle\,, \quad f_P'(T-x_0) = -\frac{1}{3}\langle P^a(x)\mathcal{O}'^a\rangle\,. \end{aligned} \tag{2.40}$$

To get rid of the c_A dependence for the tuning of c_{SW}, one can tune the "effective mass"

$$M(x_0, y_0) = m(x_0) - s(x_0)\frac{m(y_0) - m'(y_0)}{s(y_0) - s'(y_0)}\,, \tag{2.41}$$

instead, where the primed quantities are obtained by using only other primed quantities. It can be shown that the definitions of $M(x_0, y_0)$, $m(x_0)$ and the renormalized quark mass agree up to $\mathrm{O}(a^2)$. Similarly, we define $M'(x_0, y_0)$ by replacing the quantities in the above definition by their primed/un-primed counterpart. If the improvement is done correctly, we should expect $M(x_0, y_0)$ and $M'(x_0, y_0)$ to be equal up to $\mathrm{O}(a^2)$. The strategy of the recent c_{SW} determination of the CLS $N_f = 2+1$ ensembles [BS13] consists in matching the following difference

$$\Delta M \equiv M(3T/4, T/4) - M'(3T/4, T/4)\,, \tag{2.42}$$

to its analytically calculable tree-level value $\Delta M^{(0)}$ obtained from Ref. [LW96]. In Ref. [BS13] the calculations were performed at fixed volume $L/a = 8$ but it has been checked that finite-volume effects are small.

2.2 Algorithms for ensemble generation

In this section, we will discuss different algorithms for gauge ensemble generation. It is of pedagogical interest to review the pure gauge case first. It will also serve as an explanation of the principle of *importance sampling* in Markov Chain Monte Carlo simulations. We will then come to the case with dynamical fermions with two mass-degenerate light-quarks and a strange-quark. As we will see, the inclusion of the strange-quark causes additional technical difficulty and has to be handled with care.

2.2.1 Markov Chain Monte Carlo and generation of pure gauge ensembles

We will consider pure gauge theories and their simulations using Monte Carlo method in this sub-section following closely Chap. 4 of Ref. [GL10].

A quantum field theory in Euclidean space-time can be considered as a statistical physics system if the path integral measure is positive semi-definite in the configuration space comprised of field U. The Boltzmann weight of a field configuration is proportional to $e^{-S[U]}$, where S is the action of the theory. If the probability measure is normalizable, we can then compute the expectation value of a physical observable using importance sampling. More precisely, we use the Law of Large Number to write

$$\langle \mathcal{O} \rangle \equiv \int \mathcal{D}[U] e^{-S[U]} \mathcal{O}[U] \approx \lim_{N\to\infty} \frac{1}{N} \sum_{n=1}^{N} \mathcal{O}[U_n]\,, \tag{2.43}$$

where $\{U_n\}$ forms a set of N samples drawn according to the probability distribution density (the *Gibbs measure*):

$$\mathrm{d}P(U) = \frac{e^{-S[U]}\mathcal{D}[U]}{\int \mathcal{D}[U] e^{-S[U]}}\,. \tag{2.44}$$

The error of this estimate decreases with $1/\sqrt{N}$ as a result of the Central Limit Theorem. This is the basis of Monte Carlo simulation. Note that for a configuration space

of fields taking value in a continuous compact group (so is the case for the special unitary group $\mathrm{SU}(N)$), the measure $\mathcal{D}[U]$ is well defined and normalizable and leads to the *Haar measure*, which is itself also gauge invariant (cf. Chap. 3 of Ref. [GL10] for details).

To exploit the method, we need to generate many gauge configurations according to the probability distribution of the underlying theory to have a reliable estimate of the physical quantity that we are interested in. More importantly, with a large but finite set of configurations, we would like to explore the phase space as much as possible, and make sure that we are at statistical equilibrium, only under which it makes sense to talk about statistical weights. The idea of constructing a stochastic sequence which reaches the distribution at equilibrium such that each simulated event depends only on the previous one is called *Markov chain*.

Denote the transition probability from a configuration U to U' at simulation time n by

$$T(U'|U) \equiv P(U_n = U'|U_{n-1} = U)\,. \tag{2.45}$$

At equilibrium, the probability of coming into a configuration at time n should be the same as the probability of going out from it. This amounts to requiring

$$\sum_U T(U'|U)P(U) \stackrel{!}{=} \sum_U T(U|U')P(U')\,. \tag{2.46}$$

A sufficient condition for the above, known as *detailed balance*, is given by

$$T(U'|U)P(U) = T(U|U')P(U')\,. \tag{2.47}$$

Most MCMC algorithms aim at fulfilling detailed balance, such as the *Metropolis-Hasting algorithm* [Met+53; Has70]. As it is an important building block, we will give a bit more details about this algorithm, following Ref. [GL10].

Metropolis-Hasting algorithm

Assuming that a configuration $U_{n-1} = U$ has been constructed at time n. To draw a configuration U_n following the wanted distribution with Boltzmann weight $\propto e^{-S[U_n]}$ with detailed balance fulfilled, we follow the steps:

- **Step 1**: pick up some candidate U' following the *a priori* selection probability $T_0(U'|U)$.
- **Step 2**: accept the candidate U' with the acceptance probability

$$T_A(U'|U) = \min\left(1, \frac{T_0(U|U')\exp(-S[U'])}{T_0(U'|U)\exp(-S[U])}\right)\,. \tag{2.48}$$

  If the candidate is not accepted, then go back to Step 1. Repeat until a proposed candidate is accepted.

The acceptance Eq. (2.48) is further simplified if a symmetric selection probability, i.e. $T_0(U|U') = T_0(U'|U)$, is considered, in which case

$$T_A(U'|U) = \min\left(1, \exp(-\Delta S)\right)\,, \quad \Delta S \equiv S[U'] - S[U]\,. \tag{2.49}$$

The latter condition is widely used in LQCD simulations in practice.

SU(N) pure gauge simulations with Wilson gauge action

Consider an SU(N)-theory. As already discussed previously, we can write down the pure gauge action on the lattice with the help of plaquette sum in a gauge-invariant way. For a generic N, the action Eq. (2.9) is simply modified with the denominator 3 replaced by N. However, Eq. (2.9) or its SU(N) version is expensive to compute. If one only does a local update on the site n, one only needs to know how much this changes the action in order to decide whether to keep the new configuration [Eq. (2.49)]. This amounts to computing

$$\Delta S = -\frac{\beta}{N}\Re\mathrm{Tr}\left[\left(U'_\mu(n) - U_\mu(n)\right) A\right] , \tag{2.50}$$

where

$$A = \sum_{\nu\neq\mu}\left(U_\nu(n+\hat{\mu})U_{-\mu}(n+\hat{\mu}+\hat{\nu})U_{-\nu}(n+\hat{\nu}) + U_{-\nu}(n+\hat{\mu})U_{-\mu}(n+\hat{\mu}-\hat{\nu})U_\nu(n-\hat{\nu})\right) , \tag{2.51}$$

is called *staple*, and feeding back ΔS to the Metropolis-Hasting algorithm.

For $N = 2$, an efficient algorithm called *heatbath* has been proposed [Cre80; KP85]. As for $N \geq 3$, generally it is done with the *pseudo-heatbath* algorithm [CM82], which consists in updating all the SU(2) sub-blocks embedded in an SU(N) group. Note that heatbath based algorithms do only smooth and local updates. They are in general inefficient in exploring the whole configuration space. Usually, one combines heatbath with a microcanoical update called *over-relaxation* [Adl81; Whi84] to have more "effective" MCMC samples. As already mentioned for the choice of open boundary condition and explained in Appendix A, one serious problem that one might encounter in an MCMC simulation is that the generated samples are auto-correlated. A possible cause of this is that one is stuck in a corner of the phase space instead of exploring the whole space, and thus the obtained finite number of samples is not representative enough for describing the underlying probability distribution. Over-relaxation is an approach to fix the problem in the case of pure gauge simulations. The issue of auto-correlation becomes severe especially when we approach the continuum limit. A comprehensive review for SU(N) simulations can also be found in Ref. [FJ05].

2.2.2 Pseudo-fermions and Hybrid Monte Carlo

Our total action is the sum of Eq. (2.21) and Eq. (2.22). The part with only gauge fields, Eq. (2.21), is not a problem and can be implemented numerically directly. However, the fermion fields in Eq. (2.22) are Grassmann numbers due to the required spin statistics. If we write Eq. (2.22) as a bilinear in the quark fields $\sum_{f\in\text{flavor}} \bar{\psi}^f D_f[U]\psi^f$, after the fermion fields being integrated out, the partition function is modified to:[4]

$$Z = \int \mathcal{D}[U] e^{-S_G[U]} \prod_{f\in\text{flavor}} \det[D_f] . \tag{2.52}$$

[4] We will omit the super-script "impr." from now on for simplicity.

On the other hand, the expectation value of a purely fermionic composite operator can be written as

$$\begin{aligned}\langle\prod_n \psi_{i_n}\bar{\psi}_{j_n}\rangle =& \frac{1}{Z}\int \mathcal{D}[U]\Big(\prod_n \frac{\partial}{\partial\eta_{j_n}}\frac{\partial}{\partial\bar{\eta}_{i_n}}\Big)W[U,\eta,\bar{\eta}]\Big|_{\eta=\bar{\eta}=0}\\ =& \frac{1}{Z}\int \mathcal{D}[U]\Big(e^{-S_G[U]}\prod_{f\in\text{flavor}}\det[D_f]\Big)\\ &\times\Big\{\Big(\prod_n \frac{\partial}{\partial\eta_{j_n}}\frac{\partial}{\partial\bar{\eta}_{i_n}}\Big)\Big[\prod_{f\in\text{flavor}}\exp\Big(\sum_{f\in\text{flavor}}\bar{\eta}_f D_f^{-1}\eta_f\Big)\Big]\Big\}\Big|_{\eta=\eta'=0},\end{aligned} \tag{2.53}$$

where the relation for the generating functional

$$\begin{aligned}W[U,\eta,\bar{\eta}] =& \int\mathcal{D}[\psi,\bar{\psi}]\exp\Big(-S_G[U]-S_F[U,\psi,\bar{\psi}]+\sum_{f\in\text{flavor}}\bar{\eta}_f\psi_f+\sum_{f\in\text{flavor}}\bar{\psi}_f\eta_f\Big)\\ =& e^{-S_G[U]}\prod_{f\in\text{flavor}}\Big\{\det[D_f]\exp\Big(\sum_{f\in\text{flavor}}\bar{\eta}_f D_f^{-1}\eta_f\Big)\Big\},\end{aligned} \tag{2.54}$$

has been used. Note that the spin and color indices of Eq. (2.53) remain open. Hence, the expectation value of a purely fermionic operator is equivalent to the average over gluonic fields of the quantity in the last line of the right-hand side of Eq. (2.53) with a Boltzmann weight proportional to $e^{-S_G[U]}\prod_{f\in\text{flavor}}\det[D_f]$. We will explain how this quantity is computed in practice in Sect. 2.3. As far as the MCMC simulation is concerned, the task now is to create samples with the aforementioned Boltzmann weight. Note that this is possible only when the product of the determinants of the Dirac operators is real and positive. In our case, the reality is guaranteed because of the γ_5-Hermiticity of the Dirac operator,

$$\det[D]^* = \det[D^\dagger] = \det[\gamma_5 D\gamma_5] = \det[D] \tag{2.55}$$

As for the positivity, it is also guaranteed if we have only two mass-degenerate light-quarks. However, as will be commented later, the positivity of the lone strange-quark determinant is not clear for an action which breaks chiral symmetry and is currently under investigation [MS20]. Hereunder we will assume the positivity of the strange-quark determinant to simplify the discussion.

A direct evaluation of the fermion determinant is computationally-daunting. People used to do simulations in omitting the fermion determinant by setting it to unity. This kind of simulation is called *quenched*, contrary to *dynamical*.

A possible way of evaluating the fermion determinant is to introduce extra degrees of freedom called *pseudo-fermions* [WP81]. Concretely, we would like to write the fermion determinant as a Gaussian integral of some bosonic fields ϕ and $\phi^\dagger$,

$$\prod_{f\in\text{flavor}}\det[D_f] = \int\mathcal{D}[\phi,\phi^\dagger]\exp\Big(-S_{\text{PF}}[U,\phi,\phi^\dagger]\Big) \propto \int\mathcal{D}[\phi,\phi^\dagger]\exp\Big(-\phi^\dagger A\phi\Big), \tag{2.56}$$

where A is a matrix. Assume that it is possible to arrange the product of fermion determinants as above, we can then update an MC sample with *molecular dynamics* (MD). Write the expectation value of an observable $\mathcal{O}$ as

$$\langle\mathcal{O}\rangle = \frac{\int\mathcal{D}[\pi,U,\phi,\phi^\dagger]\exp\left(-\frac{1}{2}(\pi,\pi)-S_G[U]-S_{\text{PF}}[U,\phi,\phi^\dagger]\right)\mathcal{O}[U]}{\int\mathcal{D}[\pi,U,\phi,\phi^\dagger]\exp\left(-\frac{1}{2}(\pi,\pi)-S_G[U]-S_{\text{PF}}[U,\phi,\phi^\dagger]\right)}, \tag{2.57}$$

where π is an auxiliary momentum field. From Eq. (2.57), π and U evolve following a canonical ensemble of a classical system with Hamiltonian

$$H[\pi, U] = \frac{1}{2}(\pi, \pi) + S_{\text{G+PF}}[U, \phi, \phi^\dagger], \quad S_{\text{G+PF}}[U, \phi, \phi^\dagger] \equiv S_{\text{G}}[U] + S_{\text{PF}}[U, \phi, \phi^\dagger] \tag{2.58}$$

of which the evolution equations are[5]

$$\begin{aligned} \partial_\tau \pi(x, \mu) &= -T^a \partial^a_{x,\mu} S_{\text{G+PF}}, \\ \partial_\tau U(x, \mu) &= \pi(x, \mu) U(x, \mu), \end{aligned} \tag{2.59}$$

where τ is a fictitious time which can be chosen as the simulation time.

Now, let us introduce the *Hybrid Monte Carlo* (HMC) algorithm [Dua+87]. HMC combines the molecular dynamics update and the Metropolis-Hasting accept/reject step. In each HMC trajectory, we start by alternatively updating ϕ and U. The update of ϕ can be easily achieved if we can write $S_{\text{PF}}[U, \phi, \phi^\dagger]$ as

$$S_{\text{PF}}[U, \phi, \phi^\dagger] = (M^{-1}\phi, M^{-1}\phi), \tag{2.60}$$

in which case we can simply generate a random Gaussian field χ with probability weight $\propto \exp(-\chi^\dagger \chi)$ and build $\phi = M\chi$. With a given pseudofermion field, we then let π, initially drawn from a Gaussian distribution, and the field U evolve on a hyper-surface of constant Hamiltonian in the configuration space according to the MD evolution equation Eq. (2.59). As we want the distribution to fulfill the detailed balance condition Eq. (2.47), we have to guarantee that

1. The integration measure $\mathcal{D}[\pi]\mathcal{D}[U]$ is area-preserving ;
2. The process is reversible, in the sense that the transition probability for $(\pi, U) \to (\pi', U')$ should be equal to the transition probability for $(-\pi', U') \to (-\pi, U)$.

These requirements are important criteria for choosing a scheme to integrate the molecular dynamics evolution equations Eq. (2.59) numerically. In the limit of perfect arithmetic precision, the MD updates are microcanonical, so each new configuration has to be accepted. However, this is not the case anymore in reality because of the step-size error introduced in a numerical integration. The second half of HMC consists in correcting this numerical imprecision with a Metropolis accept/reject step, with an acceptance of

$$T_A(\pi', U' | \pi, U) = \min\left(1, \frac{\exp(-H[\pi', U'])}{\exp(-H[\pi, U])}\right). \tag{2.61}$$

In practice, it is more efficient to adopt a multi-level integration scheme that takes into account the different sizes and computational cost difference of the force terms [SW92]. This point will be elaborated later while we talk about numerical integrators.

2.2.3 Gauge field generation algorithms for the CLS $N_f = 2 + 1$ simulations

The main strategy of the CLS $N_f = 2 + 1$ simulations can be found in detail in Ref. [LS13]. We will go through the most relevant aspects of the reference. This

[5] The notations of Ref. [LS13] are used here. Contrary to our previous notations, the Lorentz indices are given in the argument of the fields.

sub-section will contain quite some specific technical details. Firstly, we introduce the twisted-mass determinant reweighting for the light-quark sector [Has01; HJ03; Urb+06]. It helps regularize the quark determinant which can have very small eigenvalues and hence behave numerically badly. Secondly, we will talk about the Rational Hybrid Monte Carlo (RHMC) algorithm used for the strange-quark sector [KHS99; CK07]. Lastly, the numerical integration schemes of the MD equations will be reviewed and discussed.

Twisted mass determinant reweighting

Due to the γ_5-Hermiticity and the mass-degeneracy of the u- and d-quarks, we can conveniently write the product of the light-quark determinants as

$$\det[D_u]\det[D_d] = \det[D_l^\dagger D_l]\,. \tag{2.62}$$

In this way, the light-quark component of the pseudofermion action Eq. (2.56) can be written in the form of Eq. (2.60) with $M = D_l$. The pseudofermion field can be easily built from a Gaussian random variable in the way that we described previously in this case.

However, because of the near-zero eigenmodes of D_l, it is numerically more stable to regularize the light-quark determinant and work under this modified theory. Once a Markov chain is generated using a regularized light-quark determinant, one has to correct posteriorly the Boltzmann weight for each MC sample to account for the modification. This correcting process is called *reweighting*. The reweighting factors can be obtained using stochastic methods with modest computing cost.

In Ref. [LP08], two regularization schemes are proposed with the help of a regularizing mass parameter μ:

1.
$$\det[D_l^\dagger D_l] \to \det[w_1]\,, \quad w_1 \equiv D_l^\dagger D_l + \mu^2\,, \tag{2.63}$$
with reweighting factor
$$W_1 = \det\left[D_l^\dagger D_l (D_l^\dagger D_l + \mu^2)^{-1}\right]\,. \tag{2.64}$$

2.
$$\det[D_l^\dagger D_l] \to \det[w_2]\,, \quad w_2 \equiv (D_l^\dagger D_l + \mu^2)^2 (D_l^\dagger D_l + 2\mu^2)^{-1}\,, \tag{2.65}$$
with reweighting factor
$$W_2 = \det\left[D_l^\dagger D_l (D_l^\dagger D_l + 2\mu^2)(D_l^\dagger D_l + \mu^2)^{-2}\right]\,. \tag{2.66}$$

Denote $\langle\cdot\rangle_{\mathrm{m}}$ the expectation value in the theory with a modified quark determinant. Then, the expectation value of an observable $\mathcal{O}$ in the original theory can be expressed as

$$\langle\mathcal{O}\rangle = \frac{\langle\mathcal{O}W_i\rangle_{\mathrm{m}}}{\langle W_i\rangle_{\mathrm{m}}}\,, \tag{2.67}$$

where W_i is the reweighting factor listed above. To determine the reweighting factor, one can use the same idea as the pseudo-fermion. With a set of N independent and

identically distributed Gaussian variables $\{\eta_k\}$, we have a stochastic estimate for W_i:

$$W_{i,N} = \frac{1}{N}\sum_{k=1}^{N} \exp\left((\eta_k, [1 - w_i^{-1}]\eta_k)\right). \tag{2.68}$$

Rational Hybrid Monte Carlo

The strange-quark being non-degenerate, a way to arrive at a bilinear form as Eq. (2.60) is to take M to be the "square-root" of the strange part of the Dirac operator D_s. A rational approximation of $y \mapsto 1/\sqrt{y}$ is given by Zolotarev (relevant references can be found in Ref. [Lus10a]). We can re-write the strange determinant as

$$\det[D_s] = W_s \det[R^{-1}], \tag{2.69}$$

where R approximates $\sqrt{D_s^\dagger D_s}$ and W_s is the strange-quark reweighting factor

$$W_s = \det[D_s R]. \tag{2.70}$$

The strange reweighting factor works in the same way as the light reweighting factor and enters multiplicatively. Again, the strange reweighting factor can be stochastically estimated.

Finally, it is worth it to add a word of caution from a recent work concerning the strange-quark reweighting [MS20]. It should be noted that the working hypothesis of RHMC is that the strange determinant is positive. This is guaranteed if the Dirac operator is γ_5-Hermitian and preserves chiral symmetry. Nonetheless, the latter is not fulfilled for Wilson fermion. Ref. [MS20] shows that the gauge fluctuation might bring configurations into a region with negative strange determinant. The authors of Ref. [MS20] studied the eigenmodes of the Dirac operators for a wide range of the CLS $N_f = 2+1$ ensembles and found correlations between the numerical integrators (see next sub-section) and the negativity of the strange determinant. It is not yet clear how this occurs. One has to take care of including a minus sign for the strange reweighting factor for some configurations.

Numerical integration of the molecular dynamics evolution equations

As stated before, an admissible numerical integrator for our problem should preserve the measure and should be time-reversible. The CLS $N_f = 2+1$ simulations use different integrators satisfying these conditions: leapfrog (see e.g. Ref. [GL10]), the second and the fourth order Omelyan-Mryglod-Fold integrators [OMF03]. All these schemes are comprised of sequences of elementary updates with time step ϵ on the momentum field π and the field U according to the MD evolution equations Eq.(2.59):

$$\begin{aligned} \mathcal{I}_\pi &: \pi \to \pi - \epsilon F, \\ \mathcal{I}_U &: U \to e^{\epsilon\pi} U, \end{aligned} \tag{2.71}$$

where

$$F \equiv T^a \partial^a_{x,\mu} S(U), \tag{2.72}$$

is the molecular dynamics force.

The discretization error and the cost of each integrator are different in each integration scheme. One might find it advantageous to decompose the Hamiltonian into different parts according to the eigenmodes and update each of them with an

adequate choice of integrator. As mentioned earlier, because one has to correct for numerical imprecision happening during the MD updates at the end of an HMC trajectory with a Metropolis accept/reject step, it is advantageous to find a compromise between the computing cost for the MD updates and the acceptance, such that the efficiency of the update is reasonably good [SW92].

2.3 Computing observables

In this section, we will discuss how to compute fermionic observables on the lattice. The measurement of such observables requires to compute the inverse of the Dirac operator by solving the Dirac equation in the gluonic background. We will give an overview on the available solvers within the `openQCD` package [LS13] that we use in the lattice study of the project. Finally, we will deal with the scale-setting of gauge ensembles, which will allow us to interpret lattice results in physical units.

2.3.1 Wick-contraction

As explained in the previous section, gauge configurations are generated and stored according to the probability distribution imposed by the action. For the physics that we are interested in, we then build observables using these gauge configurations as our MCMC samples. In the case of gluonic quantities, it is straightforward to build the observables from the gauge fields. As for the fermionic quantities, we shall make use of the expression Eq. (2.53) where the fermionic degrees of freedom are integrated out. The braced term in the last line of Eq. (2.53) is nothing but the common object that one encounters in statistical field theory: *Wick-contraction*. To compute it, one puts all the quark/anti-quark fields ψ and $\bar{\psi}$ on a plane and draws all possible diagrams by drawing lines from a point x with a quark $\psi(x)$ to another point y with an anti-quark field $\bar{\psi}(y)$. In our case where the Dirac operator is flavor-diagonal, there is no flavor-mixing between quark fields, so a legitimate line should link a quark field to an anti-quark field with the same flavor. Note that it is allowed to have “disconnected diagrams" here, which contain lines going from and back to the same point. In fact, they are still “connected" in the QFT sense because of the presence of gluonic background. Mathematically, each line linking a quark field to an anti-quark field with flavor f represents the inverse of the Dirac operator in the corresponding flavor sector, $D_f^{-1}(x,y)$, with open spin and color indices.

In practice, same diagrams with opposite quark flow can be conveniently treated together thanks to the γ_5-Hermiticity [Eq. (2.15)] of the Dirac operator.

2.3.2 Propagator solve and `openQCD` solvers

Solving the propagator, i.e. finding the inverse of the Dirac operator D, is often the most computationally expensive part due to the scaling in complexity with regard to the size of the lattice. For a point-to-all propagator, i.e. a propagator $S(x,y)$ with a source at y to any point x on the lattice, this amounts to solving the linear equation

$$D\psi(x) = \eta(x)\,, \tag{2.73}$$

where

$$\eta(x) = \delta_{x,y}\,, \tag{2.74}$$

is a *point-source*. The propagator $S(x,y)$ is then the solution $\psi(x)$ of Eq. (2.73) for fixed y.

Note that in the above, there are some different choices for the color and spin dependence of the source η. In theory the point-source η is a delta function in color and spin; however, in practice, it might be advantageous to impose a different spin-color dependence[6] or even to use other types of source instead of point-source for computing certain observables. Regardless, the methods for solving propagator that we are going to discuss remain valid for solving the linear system Eq. (2.73).

In the `openQCD` package [LS13], which has been used for the CLS gauge ensemble generations and observable measurements, an efficient scheme consisting of deflated Schwarz alternating procedure (SAP) preconditioning and generalized conjugate residual (GCR) algorithm is available. We will give some technical details and its physical motivations in the following sub-sections. A pedagogical review of these details can be found in Ref. [Lus10a].

Generalized conjugate residual algorithm

Most modern solvers used for LQCD are based on *Krylov space* methods. Krylov space is a vector space spanned by a field χ and those obtained by applying $n \in \mathbb{N}$ times the Dirac operator to it, $D^n\chi$. The GCR algorithm solves the linear system Eq. (2.73) iteratively with a target error tolerance. The method is valid for generic matrices. With a linear system like Eq. (2.73), we start with a vector $\rho_0 = \eta$ and construct recursively an orthogonal basis $\{\chi_l\}$ such that, at the k-th iteration, we minimize the residual [Lus10a]

$$\rho_k = \eta - \sum_{l=0}^{k-1} c_l \chi_l \,, \quad c_l \equiv (\chi_l, \eta) \,, \tag{2.75}$$

in a direction orthogonal to all the existing vectors in the orthogonal basis. The stopping condition is when the residual at the end of n iterations, ρ_n, is smaller than a given tolerance in norm. By construction, the solution is a linear combination of the computed residuals. For a pseudo-code of the algorithm, see e.g. Ref. [Saa03].

Schwarz alternating procedure preconditioning

When the condition number of D in Eq. (2.73) is large, it will take an iterative solver such as GCR more iterations to converge. A way to improve this situation is to rewrite the linear system in an equivalent form with a much lower condition number for the problem. This is called *preconditioning*. For instance, if one rewrites Eq. (2.73) as

$$LDR\phi = L\eta \,, \tag{2.76}$$

with two matrices L and R, then the solution is obtained by setting $\psi = R\phi$. If the matrix LDR on the left-hand side has a lower condition number, the algorithm will then be more efficient. A widely used preconditioning in LQCD is the *even-odd preconditioning*, which consists in re-arranging the matrix D into blocks according to the parity of the coordinate sum of a site (see e.g. Ref. [Lus10a]):

$$D = \begin{pmatrix} D_{ee} & D_{eo} \\ D_{oe} & D_{oo} \end{pmatrix} \,, \tag{2.77}$$

where “e" stands for even and “o" stands for odd. Since the odd sites and the even sites do not couple within themselves, D_{ee} and D_{oo} can be inverted easily. We can

[6] An example, the *dilution* method, is discussed in Sect. 6.3.1.

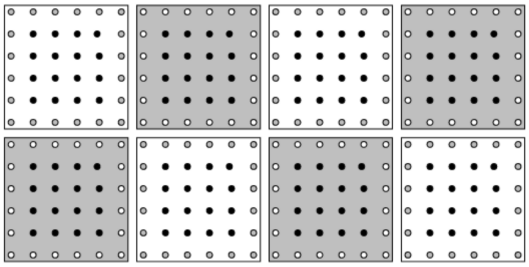

FIGURE 2.3: Illustration of the domain decomposition for the SAP procedure. Figure taken from Ref. [Lus04].

then precondition the matrix D via its Schur complement decomposition

$$LDR = \begin{pmatrix} \hat{D} & 0 \\ 0 & D_{oo} \end{pmatrix}, \quad \hat{D} \equiv D_{ee} - D_{eo} D_{oo}^{-1} D_{oe}, \tag{2.78}$$

where

$$L = \begin{pmatrix} 1 & -D_{eo} D_{oo}^{-1} \\ 0 & 1 \end{pmatrix}, \quad R = \begin{pmatrix} 1 & 0 \\ -D_{oo}^{-1} D_{oe} & 1 \end{pmatrix}. \tag{2.79}$$

Preconditioning the Dirac operator in this way effectively reduces the condition number. However, in a large-scale computation, such a decomposition might contain a high communication overhead while passing information from one node to another.

A domain decomposition precondition scheme inspired by the Schwarz alternating procedure [Sch90] was proposed in Ref. [Lus04]. This consists in checkerboarding the lattice into two categories of blocks, black and white, as shown in Fig. 2.3. We define 4 different sets of points: Ω the union of the filled points inside a black block, $\partial\Omega^*$ union of the open (gray) points inside a white block, Ω^* the union of the filled points inside a white block and $\partial\Omega$ the union of the open points inside a black block. The Dirac operator can then be expressed as

$$D = \begin{pmatrix} D_{\Omega} & D_{\partial\Omega} \\ D_{\partial\Omega^*} & D_{\Omega^*} \end{pmatrix}, \tag{2.80}$$

where D_A is the restriction of the Dirac operator to the subset A.

The proposal of Ref. [Lus04] is to precondition Eq. (2.73) as

$$D M_{\mathrm{SAP}} \phi = \eta, \tag{2.81}$$

where

$$M_{\mathrm{SAP}} \equiv K \sum_{\nu=0}^{n_{\mathrm{cy}}-1} (1 - DK)^{\nu}, \quad K \equiv D_{\Omega}^{-1} + D_{\Omega^*}^{-1} - D_{\Omega^*}^{-1} D_{\partial\Omega^*} D_{\Omega}^{-1}. \tag{2.82}$$

The solution of the original system becomes $\psi = M_{\mathrm{SAP}}\phi$. It is clear that, the preconditioning operator M_{SAP} becomes D^{-1} when $n_{\mathrm{cy}} \to \infty$. However, the SAP itself is often not efficient enough as a solver, so it is only used as a preconditioner and the GCR algorithm is applied to solve the preconditioned system. In practice, successive update of the field is used instead of a direct computation of M_{SAP}. Note that an exact SAP is not necessary in this case.

Low-mode deflation

In order to approach the physical point, one has to reduce the bare mass of the light-quarks. A direct impact of this is that the Dirac operator becomes more ill-conditioned due to the increase in the number of low modes of the Dirac operator. The idea of low-mode deflation is to treat the low modes separately ("deflating") and solve the Dirac operator with low modes projected out using Krylov solvers. Ref. [Lus07] suggests an inexact scheme for the deflation subspace generation accompanying the block decomposition described previously. To access the space generated by the low modes, we start with an arbitrary set of fields $\{\psi_l^\Lambda\}_{l\in[1,N_s]}$ with a support on a sub-block Λ of the lattice. We can suppress the high-modes by applying D^{-1} several times to these fields. Note that at this stage, D^{-1} does not need to be computed exactly and it suffices to apply several cycles of SAP. Then, a basis of the deflation subspace $\{\phi_l^\Lambda\}$ can be obtained by orthogonalizing $\{\psi_l^\Lambda\}$.

Collecting all these different orthogonal fields from all the N_b sub-blocks to cover the whole lattice, the full quark propagator is given by

$$S(x,y) = P_R S(x,y) + \sum_{k,l=1}^{N_b N_s} \phi_k(x)(A^{-1})_{kl}\phi_l^\dagger(y)\,, \tag{2.83}$$

where

$$A_{kl} = (\phi_k, D\phi_l)\,, \tag{2.84}$$

is the restriction of the Dirac operator to the deflation subspace and the first term on the right-hand side of Eq. (2.83) corresponds to the solution of the deflated system:

$$P_L D\chi = P_L\eta\,, \tag{2.85}$$

$$P_L\psi(x) \equiv \psi(x) - \sum_{k,l=1}^{N} D\phi_k(x)(A^{-1})_{kl}(\phi_l,\psi)\,. \tag{2.86}$$

The efficiency of this method comes from the fact that low-modes are in general locally well approximated by a small number of fields (referred as "local coherence" in Ref. [Lus07]), so that the deficit from the deflation subspace projection can be fairly small under modest computing cost.

2.3.3 Scale-setting for the CLS $N_f = 2+1$ ensembles

Dimensionful observables measured on the lattice are obtained in units of the lattice spacing. To convert to physical units, one has to determine the physical value of the lattice spacing for each ensemble used in the calculation. The determination of the lattice spacing usually relies on the calculation of a certain dimensionful observable which we know experimentally. To this end, one needs to perform calculation on several different ensembles in order to take a combined continuum, infinite-volume and chiral — i.e. to the physical pion mass — extrapolation, after which the reference physical scale can be determined.

Examples of common choices for the reference physical scale are stable baryon masses (e.g. the Ω^- [TD05]) and the Sommer scale r_0 determined from the static quark potential [Som94]. These examples reflect some desired criteria for setting the scale: the former takes as reference a quantity that is very well known experimentally, while the latter can be determined very precisely on the lattice. In this

sub-section, we will review some methods used in the most recent scale-setting paper for the CLS $N_f = 2+1$ simulations [BKS17]. It utilizes as intermediate scale the dimension-2 Wilson flow time parameter t_0 introduced in Ref. [LÏ10]. We will first describe briefly some basic properties of t_0 and then move on to the scale-setting strategy of Ref. [BKS17].

The Wilson flow

The idea of the Wilson flow is to evolve continuously the gauge link variables U in an extra dimension parametrized by the "flow time" t. Prior to Ref. [LÏ10], the author of the article had considered it as an approach to realize *trivializing map* [Nic80b; Nic80a] which aimed at handling the long auto-correlation time between gauge configurations close to the physical point [Lus10b].

The lattice Wilson flow $V_t(x,\mu)$ is defined by the equations

$$\frac{\mathrm{d}}{\mathrm{d}t}V_t(x,\mu) = -g_0^2[\partial_{x,\mu}S_G(V_t)]V_t(x,\mu)\,, \quad V_t(x,\mu)|_{t=0} = U(x,\mu)\,, \tag{2.87}$$

where S_G is the Wilson-plaquette action.

In the continuum, we define the energy density E of the Wilson flow as

$$E = \frac{1}{4}G^a_{\mu\nu}G^a_{\mu\nu}\,, \tag{2.88}$$

where $G_{\mu\nu}$ is the field strength of the flow V_t. There are some different choices for the discretization of the energy density on the lattice. In particular, a clover-type discretized version is used in Ref. [Bru+15].

The Wilson flow can be considered as a *smearing* process [MP04], in that the ultraviolet divergence is waived away and the energy density is proven to be already renormalized at one-loop. Based on the relation between the observable $t^2\langle E\rangle$ and the strong coupling constant and the QCD scale Λ [Cap+99; RVL97], it was proposed to defined the flow parameter t_0 such that

$$\{t^2\langle E\rangle\}_{t=t_0} = 0.3\,. \tag{2.89}$$

Scale setting strategies

Now let us come back to the scale-setting of the CLS $N_f = 2+1$ ensembles. In Ref. [BKS17] are defined the following quantities:

$$f_{\pi K} = \frac{2}{3}(f_K + \frac{1}{2}f_\pi)\,, \tag{2.90}$$

$$\phi_2 = 8t_0m_\pi^2\,, \quad \phi_4 = 8t_0(m_K^2 + \frac{1}{2}m_\pi^2)\,, \tag{2.91}$$

where $f_{\pi/K}$ is the decay constant of the (charged) pion/kaon and $m_{\pi/K}$ is the pion/kaon mass of an ensemble. Their determinations on the lattice with open boundary condition are based on the two-point functions:

$$f_P^{pq}(x_0,y_0) = -\frac{a^6}{L^3}\sum_{\vec{x},\vec{y}}\langle P^{(pq)}(x_0,\vec{x})P^{(pq)}(y_0,\vec{y})\rangle\,, \tag{2.92}$$

$$f_A^{pq}(x_0, y_0) = -\frac{a^6}{L^3} \sum_{\vec{x},\vec{y}} \langle A_0^{(pq)}(x_0, \vec{x}) P^{(pq)}(y_0, \vec{y}) \rangle \,, \tag{2.93}$$

where $(p, q) = (u, d)$ for the pion and $(p, q) = (u, s)$ for the kaon. By inserting a complete set of intermediate states between two operators in each of these and using the spatial periodicity, it can be shown that these two-point functions are sums of a tower of exponentials. The pseudo-scalar meson masses m_{PS} are defined via fitting

$$\ln\left(\frac{f_P(x_0)}{f_P(x_0 + a)}\right) = a m_{\mathrm{PS}} (1 + c_1 e^{-E_1 x_0} + c_2 e^{-E_2 (T - x_0)} + \cdots) \,, \tag{2.94}$$

and the decay constants f_{PS} are extracted from

$$f_{\mathrm{PS}} = Z_A(\tilde{g}_0)[1 + \tilde{b}_A a \mathrm{Tr} M_{\mathrm{q}} + \tilde{b}_A a m_{pq}] \sqrt{\frac{2}{m_{\mathrm{PS}}}} R_{\mathrm{PS}} \,, \tag{2.95}$$

where M_{q} is the quark-mass matrix, m_{pq} is some linear combination of the bare-quark masses and R_{PS} is obtained from fitting

$$\sqrt{\frac{f_A(x_0, y_0) f_A(x_0, T - y_0)}{f_P(T - y_0, y_0)}} = R_{\mathrm{PS}} \Big(1 + c_1(y_0) \cosh[-E_1(T/2 - x_0)]\Big) \,. \tag{2.96}$$

Note that, if one neglects the excited states represented by the exponential correction terms on the right-hand side, Eq. (2.94) defines the *effective mass* of the pseudoscalar meson.

In most of the CLS $N_f = 2 + 1$ simulations, the ensembles with the same inverse coupling β are generated with the averaged quark mass kept constant. In order to match to a physical scale, one should tune the lattice parameters according to a *line of constant physics* to have a better control over discretization effects. Two strategies are proposed for setting the scale in Ref. [BKS17]. We will present the one that follows lines of constant $\phi_4 = \tilde{\phi}_4$ while moving toward the physical point. It leads to a better determination in Ref. [BKS17].

With this strategy, one starts by assuming a certain physical value of $t_0 = \tilde{t}_0$ and the target point $(\tilde{\phi}_2, \tilde{\phi}_4)$ where the physical information is read off. Note that the mistuning of the quark masses has to be corrected to shift ϕ_4 to the target value $\tilde{\phi}_4$. At the desired accuracy of Ref. [BKS17], this can be done with a Taylor expansion. It appears that the dimensionless quantity $\sqrt{t_0} f_{\pi K}$ is well described by the continuum extrapolation ansatz[7]

$$\sqrt{t_0} f_{\pi K} = F_{T/\chi}^{\mathrm{cont}}(\phi_2) + c_{T/\chi} \frac{a^2}{t_0^{\mathrm{sym}}} \,, \tag{2.97}$$

where t_0^{sym} is t_0 at the quark-mass-symmetric point, $m_u = m_d = m_s$. F_T^{cont} and F_χ^{cont} are two possible function forms supported by different motivations [Bie+11; BG14] which lead to consistent results for t_0 within error at the end and give an estimate of the systematic error of the fit. Once extrapolated to the physical point, we can then obtain the physical value of t_0 for our starting value $\tilde{t}_0$ because the physical value of $f_{\pi K}$ is known from experiment. One has to fine tune the initial target $\tilde{t}_0$ so that it coincides with the value obtained after the continuum extrapolation. This then gives

[7] An alternative to Eq. (2.97) proposed in the same paper is to fit $\sqrt{t_0^{\mathrm{sym}}} f_{\pi K}$ instead. Once the form of $\sqrt{t_0^{\mathrm{sym}}}$ is known, one can read off the lattice spacing a directly at the flavor-symmetric point without having to do chiral extrapolation.

us the true physical value of $t_0 = (t_0)^{\text{phys}}$. Finally, to get the lattice spacing a, one can, for instance, chirally extrapolate t_0/a^2 for a given β along the line of $\phi_4 = \tilde{\phi}_4$ and read off the lattice spacing there, knowing $(t_0)^{\text{phys}}$.

Chapter 3

Position-space method and the QED-kernel

To compute a_μ^{hlbl}, a position-space method is proposed and used for our project. In this approach, the QED part of the contribution is computed semi-analytically in the continuum and infinite-volume before being convoluted with the QCD correlation function computed on the lattice. The purpose of this chapter is to illustrate the techniques used for the position-space QED-kernel. We will explain the formalism in Sect. 3.1 and give the construction of the QED-kernel. A key element in the computation of the QED-kernel is the use of the Gegenbauer polynomial expansion. Technical details of the implementation of the QED-kernel will not be given. In Sect. 3.2, we will show how the Gegenbauer polynomial expansion can be used by computing the scalar-meson exchange contribution to a_μ^{hlbl} with a VMD form factor.

3.1 a_μ^{hlbl} and the QED-kernel

For a non-perturbative computation, one could put QED on the lattice and do Monte-Carlo simulations with a QED+QCD setup. However, the massless photon present in QED leads to power law corrections in the volume on a_μ^{hlbl} [Blu+20]. This makes it hard to have a good control over the volume effect. On top of that, the contribution of light intermediate hadronic states produced via $\gamma^*\gamma^* \to$ hadrons is expected to decay slowly, which is another difficulty for a calculation on the lattice because the signal from the Monte-Carlo simulation becomes worse at large separations. This thus motivates our position-space approach to a_μ^{hlbl} on the lattice [Asm+16; Asm+18; Asm+19]. One obvious advantage is that, when the arguments of the 4-point function are far apart, the 4-point function is exponentially suppressed in this setup. As we will see later, thanks to gauge-invariance, the QED-kernel admits different equivalent representations. Some of them turn out to be particularly good for a lattice calculation due to their behavior at short- or large-distances.

The position approach consists in separating the QED part from the QCD part and treat it in the continuum and infinite volume. To better illustrate this, let us first derive the master formula for our formalism following Ref. [Asm+16]. We work in Euclidean space-time throughout this section.

The second Pauli form factor at zero momentum can be expressed as

$$F_2(0) = -\frac{i}{48m}\text{Tr}\{[\gamma_\rho, \gamma_\sigma](-i\not{p} + m)\Gamma_{\rho\sigma}(p,p)(-i\not{p} + m)\}\,, \tag{3.1}$$

where p is the on-shell muon momentum and $\Gamma_{\rho\sigma}$ is a tensor depending on the diagram considered. In the case of the Hadronic Light-by-Light scattering process, we

have

$$\Gamma_{\rho\sigma}(p',p) = -e^6 \int_{q_1,q_2} \frac{d^4q_1}{(2\pi)^4}\frac{d^4q_2}{(2\pi)^4}\frac{1}{q_1^2 q_2^2 (q_1+q_2-k)^2}\frac{1}{(p'-q_1)^2+m^2}\frac{1}{(p'-q_1-q_2)^2+m^2} \times \Big(\gamma_\mu(i\not{p}' - i\not{q}_1 - m)\gamma_\nu(i\not{p}' - i\not{q}_1 - i\not{q}_2 - m)\gamma_\lambda\Big)\frac{\partial}{\partial k_\rho}\Pi_{\mu\nu\lambda\sigma}(q_1,q_2,k-q_1-q_2)\,, \tag{3.2}$$

with the 4-point function of electromagnetic currents evaluated in the QCD background

$$\Pi_{\mu\nu\lambda\sigma}(q_1,q_2,q_3) = \int_{x_1,x_2,x_3} e^{-i(q_1x_1+q_2x_2+q_3x_3)}\big\langle j_\mu(x_1)j_\nu(x_2)j_\lambda(x_3)j_\sigma(0)\big\rangle_{\text{QCD}}\,. \tag{3.3}$$

The subscript QCD will be dropped for simplicity.

Parametrizing the on-shell momentum by a unit vector $\hat{e}$ as

$$p = im\hat{e}\,, \tag{3.4}$$

we can then write the expression of $\Gamma_{\rho\sigma}$ in position-space:

$$\Gamma_{\rho\sigma}(p,p) = -e^6\int_{x,y}\hat{\Pi}_{\rho;\mu\nu\lambda}(x,y,p)K_{\mu\nu\lambda}(x,y,p)\,, \tag{3.5}$$

$$K_{\mu\nu\lambda}(x,y,p) = \gamma_\mu(i\not{p}+\not{\partial}^{(x)}-m)\gamma_\nu(i\not{p}+\not{\partial}^{(x)}+\not{\partial}^{(y)}-m)\gamma_\lambda\mathcal{J}(\hat{e},x,y)\,, \tag{3.6}$$

$$\mathcal{J}(\hat{e},x,y) = \int_{u,\text{IR-reg.}} G_0(u-y)J(\hat{e},u)J(\hat{e},x-u)\,, \tag{3.7}$$

$$J(\hat{e},y) = \int_x G_0(x+y)e^{-m\hat{e}x}G_m(x)\,, \tag{3.8}$$

$$\hat{\Pi}_{\rho;\mu\nu\lambda\sigma}(x,y) = \int_z iz_\rho\big\langle j_\mu(x)j_\nu(y)j_\sigma(z)j_\lambda(0)\big\rangle\,. \tag{3.9}$$

where

$$G_0(x) \equiv \int_q \frac{d^4q}{(2\pi)^4}\frac{e^{iqx}}{q^2} = \frac{1}{4\pi^2x^2}\,, \tag{3.10}$$

is the massless scalar propagator and

$$G_m(x) \equiv \int_q \frac{d^4q}{(2\pi)^4}\frac{e^{iqx}}{q^2+m^2} = \frac{m}{4\pi^2|x|}K_1(m|x|)\,, \tag{3.11}$$

where K_1 is a modified Bessel function of the second kind, is the massive scalar propagator with mass m. The positions of the vertices x, y, z and the origin 0 appearing in Eq. (3.9) are illustrated in Fig 3.1. Note that, in this representation, Eq. (3.7) needs to be regularized because of the logarithmic divergence in the soft region.

Inserting back the position-space expression of $\Gamma_{\rho\sigma}$ to Eq. (3.1) and evaluate the trace over the γ-matrices, we then get the expression for a_μ^{hlbl}:

$$a_\mu^{\text{hlbl}} = \frac{me^6}{3}\int_{x,y}\mathcal{L}_{[\rho,\sigma];\mu\nu\lambda}(\hat{e},x,y)i\hat{\Pi}_{\rho;\mu\nu\lambda\sigma}(x,y)\,. \tag{3.12}$$

Due to the derivatives appearing in Eq. (3.6), the divergence originates from Eq. (3.7) is absent in the resulting kernel $\mathcal{L}_{[\rho,\sigma];\mu\nu\lambda}$; it is hence a finite quantity. In fact, a_μ^{hlbl} is

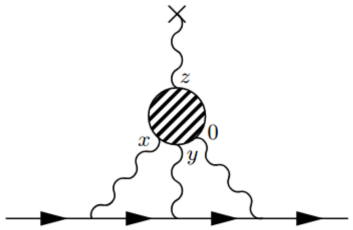

FIGURE 3.1: Diagrammatic representation of the hadronic light-by-light contribution to a_μ. Figure taken from Ref. [Asm+18].

independent of the on-shell muon momentum and we can take the angular average of $\hat{e}$ over the solid angle:

$$\bar{\mathcal{L}}_{[\rho,\sigma];\mu\nu\lambda}(x,y) = \frac{1}{2\pi^2}\int d\Omega_\epsilon \mathcal{L}_{[\rho,\sigma];\mu\nu\lambda}(\hat{e},x,y) \equiv \left\langle \mathcal{L}_{[\rho,\sigma];\mu\nu\lambda}(\hat{e},x,y)\right\rangle_{\hat{e}}\,. \tag{3.13}$$

With this, we arrive at our master formula for the position-space approach to a_μ^{hlbl}:

$$a_\mu^{\text{hlbl}} = \frac{me^6}{3}\int_{x,y} \bar{\mathcal{L}}_{[\rho,\sigma];\mu\nu\lambda}(x,y) i\hat{\Pi}_{\rho;\mu\nu\lambda\sigma}(x,y)\,. \tag{3.14}$$

Due to the Lorentz structure, we find it convenient to calculate a_μ^{hlbl} numerically via the representation

$$a_\mu^{\text{hlbl}} = \int_{|y|} d|y| f(|y|)\,, \tag{3.15}$$

with the x- and z-integrals performed inside the integrand $f(|y|)$.

As can be seen from the master formula Eq. (3.14), now the QED information is encoded in the kernel $\bar{\mathcal{L}}$, which is computed in the continuum and infinite volume semi-analytically. On the other hand, the hadronic quantity $\hat{\Pi}$ defined via QCD correlation function will be calculated non-perturbatively on the lattice. Note that the 4-point function Eq. (3.3) usually contains different terms computed with a diagrammatic approach. These terms are linearly combined in the master equation Eq. (3.14). In most of the computations presented in this thesis, we might prefer to re-arrange these terms using a change of variables in the integrals and exploiting translational-invariance of the 4-point function Eq. (3.3). Especially, as will be discussed in Chap. 6, we can optimize our lattice computation by doing so.

For the re-arrangement, we will often use the reflection symmetry of the kernel, which comes from its tensorial structure

$$\bar{\mathcal{L}}_{[\rho,\sigma];\mu\nu\lambda}(-x,-y) = -\bar{\mathcal{L}}_{[\rho,\sigma];\mu\nu\lambda}(x,y)\,. \tag{3.16}$$

Numerical aspects of the kernel

The numerical implementation of the averaged tensor $\langle K_{\mu\nu\lambda}(x,y,p)\rangle_{\hat{e}}$, the key element of the kernel, is done with a series of chain rules, once the derivatives of $\langle \mathcal{J}(\hat{e},x,y)\rangle_{\hat{e}}$ are known. As for $\mathcal{J}(\hat{e},x,y)$, it is a scalar function under an O(4)-transformation. Therefore, one can decompose it into different tensorial components with scalar functional coefficients which can be constructed with the remaining 4-vectors after the angular average, e.g. $|x|$, $|y|$ and $x\cdot y$. It turns out that the 4-dimensional integral Eq. (3.7) can be conveniently written in a series expansion

using Gegenbauer polynomials. Such a technique has been employed widely for the evaluation of Feynman integrals (e.g.Refs. [CKT80; KN02]). The method is a multipole expansion. It consists in putting the angular dependence in the basis polynomials of the expansion and the length dependence will be contained in the expansion coefficients. In Sect. 3.2, we will see how this works by computing the scalar-meson contribution to a_μ^{hlbl}.

In practice, the coefficients for the tensorial decomposition of the QED-kernel are pre-computed on a 2-dimensional grid covering the space of the variables $|x|$ and $|y|$ and the construction of the kernel is done via interpolation or Taylor expansion on-the-fly, depending on the arguments passed to it.

Gauge-invariance and the subtracted kernel

It has been pointed out in Ref. [Blu+17] that gauge-invariance can be exploited to modify the QED-kernel. This amounts to adding a boundary term which vanishes in the infinite-volume limit. It can be shown that, as a consequence of current conservation, a direct integration of the 4-point function $i\hat{\Pi}(x,y)$ over one of its arguments without any weight factor depending on it vanishes. This means that we can subtract from the QED-kernel any function which depends only on one of the variables x or y without changing the final result. In Ref. [Asm+19], a one-parameter family of kernel is defined

$$\begin{aligned}\bar{\mathcal{L}}^{(\Lambda)}_{[\rho,\sigma];\mu\nu\lambda}(x,y) =& \bar{\mathcal{L}}_{[\rho,\sigma];\mu\nu\lambda}(x,y) \\ &- \partial_\mu^{(x)}\left(x_\alpha e^{-\Lambda m_\mu^2 x^2/2}\right)\bar{\mathcal{L}}_{[\rho,\sigma];\alpha\nu\lambda}(0,y) - \partial_\nu^{(y)}\left(y_\alpha e^{-\Lambda m_\mu^2 y^2/2}\right)\bar{\mathcal{L}}_{[\rho,\sigma];\mu\alpha\lambda}(x,0)\,,\end{aligned} \tag{3.17}$$

with Λ a dimensionless tunable real parameter. The benefit of such a subtracted kernel is that one can smoothly transition from a more long-ranged kernel

$$\mathcal{L}^{(2)}_{[\rho,\sigma];\mu\nu\lambda}(x,y) = \bar{\mathcal{L}}_{[\rho,\sigma];\mu\nu\lambda}(x,y) - \bar{\mathcal{L}}_{[\rho,\sigma];\mu\nu\lambda}(0,y) - \bar{\mathcal{L}}_{[\rho,\sigma];\mu\nu\lambda}(x,0)\,, \tag{3.18}$$

at $\Lambda = 0$ to the original kernel at $\Lambda \to \infty$ [Cha+20]. Fig. 3.2 shows how the choice of the parameter Λ affects the shape of the $|y|$-integrand f [Eq. (3.15)] of the lepton loop contribution to a_μ^{hlbl}, where the mass of the lepton is set to that of the muon. Some details of this computation can be found in Sect. 4.1, where the finite-volume version of the same contribution is studied.

3.2 Scalar-meson-exchange contribution to a_μ^{HLbL}

As an example of the position-space method, we perform a semi-analytic study on the contribution of the scalar-meson exchange to a_μ^{hlbl} in the continuum and infinite-volume. This is done by substituting the hadronic four point function $i\hat{\Pi}_{\rho;\mu\nu\lambda\sigma}$ in Eq. (3.14) with scalar-meson-exchange diagrams (see Fig. 3.3).

As scalar mesons are resonances of QCD, we will study it in the framework of effective field theory and some approximations such as the Narrow-Width Approximation are needed for this computation. We will adopt the same formalism as in Ref. [Kne+18], where the scalar-meson-to-two-photons ($S\gamma\gamma$) transition is parametrized by a VMD-type form factor. Within VMD, the external photons are directly coupled to the vector meson resonance, such as the ρ-meson. Two vector mesons are then

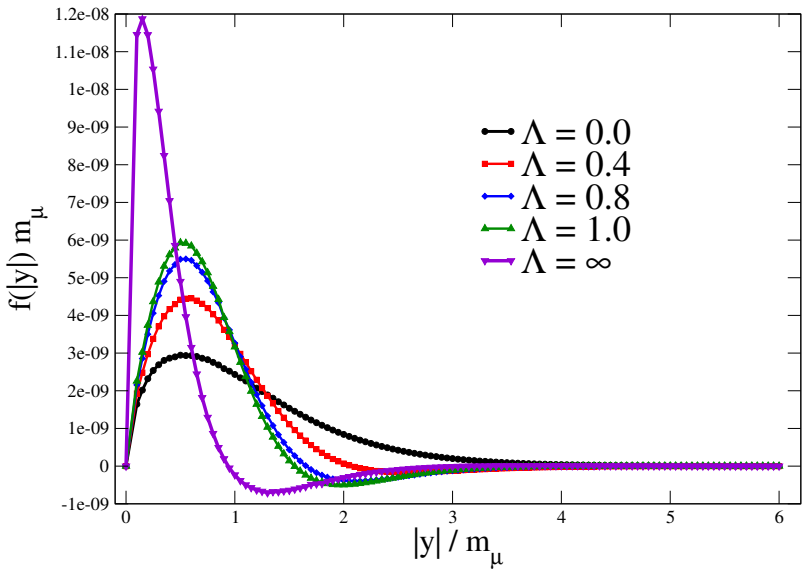

FIGURE 3.2: Dependence on the Λ-parameter in the kernel Eq. (3.17) of the lepton loop contribution to a_μ^{hlbl}. Plot taken from Ref. [Cha+20].

coupled to the scalar resonance when they reach the same point in space-time after the propagation.

From the tensor structure, the $S\gamma\gamma$ transition vertex in Euclidean space-time is parametrized by[1] [Kne+18]

$$\begin{aligned} -\int d^4x e^{-iq_1x}\langle 0|T\{j_\mu(x)j_\nu(0)\}|S(p_S)\rangle \\ = \mathcal{P}(q_1^2,q_2^2)P_{\mu\nu}(q_1,q_2) + \mathcal{Q}(q_1^2,q_2^2)Q_{\mu\nu}(q_1,q_2)\,, \end{aligned} \tag{3.19}$$

where

$$p_S = q_1 + q_2\,, \tag{3.20}$$

$$P_{\mu\nu}(q_1,q_2) = q_{1,\nu}q_{2,\mu} - \delta_{\mu\nu}q_1\cdot q_2\,, \tag{3.21}$$

$$Q_{\mu\nu}(q_1,q_2) = q_2^2 q_{1,\mu}q_{1,\nu} + q_1^2 q_{2,\mu}q_{2,\nu} - (q_1\cdot q_2)q_{1,\mu}q_{2,\nu} - q_1^2q_2^2\delta_{\mu\nu}\,. \tag{3.22}$$

Note that $P_{\mu\nu}$ and $Q_{\mu\nu}$ are transverse :

$$q_{i,\mu}P_{\mu\nu}(q_1,q_2) = q_{i,\nu}P_{\mu\nu}(q_1,q_2) = q_{i,\mu}Q_{\mu\nu}(q_1,q_2) = q_{i,\nu}Q_{\mu\nu}(q_1,q_2) = 0\,, \tag{3.23}$$

for $i = 1,2$.

Under VMD, the form factors are parametrized with two constants A and B by:

$$\mathcal{P}^{\text{VMD}}(q_1,q_2) = -\frac{1}{2}\frac{-B(q_1^2+q_2^2) + (2A + m_S^2B)}{(q_1^2+m_V^2)(q_2^2+m_V^2)}\,, \tag{3.24}$$

$$\mathcal{Q}^{\text{VMD}}(q_1,q_2) = -\frac{B}{(q_1^2+m_V^2)(q_2^2+m_V^2)}\,, \tag{3.25}$$

[1] The expressions are given in Minkowskian space-time in Ref. [Kne+18]. What we quote here has been adapted to Euclidean space-time formulation.

where m_S and m_V are the masses of the scalar meson and the vector meson used in VMD.

As in Ref. [Kne+18], we will use the Narrow-Width Approximation for the scalar resonance. Under this approximation, the scalar meson propagator with mass m_S in momentum-space is simply

$$\tilde{G}_{m_S}(p) = \frac{1}{p^2 + m_S^2}\,. \tag{3.26}$$

Replacing the electromagnetic current 4-point function appearing in Eq. (3.9) by the scalar-meson-exchange diagrams, we have

$$\begin{aligned}
i\hat{\Pi}_{\rho;\mu\nu\lambda\sigma}(x,y) &= i\hat{\Pi}^{\mathrm{I}}_{\rho;\mu\nu\lambda\sigma}(x,y) + i\hat{\Pi}^{\mathrm{II}}_{\rho;\mu\nu\lambda\sigma}(x,y) + i\hat{\Pi}^{\mathrm{III}}_{\rho;\mu\nu\lambda\sigma}(x,y)\,,\\
i\hat{\Pi}^{\mathrm{I}}_{\rho;\mu\nu\lambda\sigma}(x,y) &\equiv -\int_z z_\rho \Psi_{\mu\nu\lambda\sigma}(x,y;0,z)\,,\\
i\hat{\Pi}^{\mathrm{II}}_{\rho;\mu\nu\lambda\sigma}(x,y) &\equiv -\int_z z_\rho \Psi_{\mu\sigma\nu\lambda}(x,z;y,0)\,,\\
i\hat{\Pi}^{\mathrm{III}}_{\rho;\mu\nu\lambda\sigma}(x,y) &\equiv -\int_z z_\rho \Psi_{\mu\lambda\nu\sigma}(x,0;y,z)\,,
\end{aligned} \tag{3.27}$$

where $\Psi_{\alpha\beta\gamma\delta}(a,b;c,d)$ is the Feynman diagram where the points a and b are connected to the same $S\gamma\gamma$ blob and the points c and d are connected to another one. With this notation, the 3 terms on the right-hand side above represents the diagram (b), (a) and (c) of Fig. 3.3 respectively. As will be shown later, the z-integral of $i\hat{\Pi}$ can be computed analytically. To get a_μ^{hlbl}, we choose to rewrite the master formula Eq. (3.14) as

$$\begin{aligned}
a_\mu^{\mathrm{hlbl,scalar}} = \frac{me^6}{3}\int_{x,y}\Big(&\big(\bar{\mathcal{L}}_{[\rho,\sigma];\mu\nu\lambda}(x,y) + \bar{\mathcal{L}}_{[\rho,\sigma];\nu\mu\lambda}(y,x)\big)\big)i\hat{\Pi}^{\mathrm{III}}_{\rho;\mu\nu\lambda\sigma}(x,y)\\
&+ \bar{\mathcal{L}}_{[\rho,\sigma];\mu\nu\lambda}(x,y)i\hat{\Pi}^{\mathrm{I}}_{\rho;\mu\nu\lambda\sigma}(x,y)\Big)\,.
\end{aligned} \tag{3.28}$$

The implementation strategy consists in doing the x-integral numerically for a given set of y to reduce it to Eq. (3.15), and then compute the $|y|$-integral using trapezoidal rule. Note that, due to O(4)-symmetry and the tensorial structure, the x-integral can be reduced to a 2-dimensional one for a fixed y. We can exploit translational invariance of the 4-point function to transform the integrand of Eq. (3.28) such that only $i\hat{\Pi}^{\mathrm{I}}$ has to be computed. This is achieved by swapping the rôles of x and 0 in the expression of the integrand, with special care taken for the weight factor of the z-integral. More precisely, we first note that, due to the translational invariance of the 4-point function,

$$\begin{aligned}
i\hat{\Pi}^{\mathrm{III}}_{\rho;\mu\nu\lambda\sigma}(x,y) &= i\hat{\Pi}^{\mathrm{I}}_{\rho;\mu\lambda\nu\sigma}(x-y,-y) + i\check{\Pi}_{\rho;\mu\nu\lambda\sigma}(x,y)\,,\\
i\check{\Pi}_{\rho;\mu\nu\lambda\sigma}(x,y) &\equiv -\int_z y_\rho \Psi_{\mu\lambda\nu\sigma}(x-y,-y;0,z)\,.
\end{aligned} \tag{3.29}$$

In fact, as we will see later, $i\check{\Pi}_{\rho;\mu\nu\lambda\sigma}(x,y)$ vanishes with the VMD parametrization of the transition form factor. That is to say, upon performing the following change of variables

$$x \to x - y\,, \quad y \to -y\,, \tag{3.30}$$

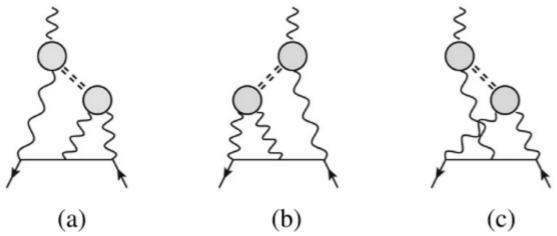

FIGURE 3.3: Different channels for the scalar-meson exchange in the light-by-light scattering process. The blobs represent the transition vertex $S\gamma\gamma$ and the double dash lines represent the scalar meson propagation. The external vertices are associated with the position variables in the same way as in Fig. 3.1, i.e. x, y and 0 from the left to the right on the muon line and z at the external on-shell photon. Figure taken from Ref. [Kne+18].

we have

$$a_\mu^{\text{hlbl,scalar}} = \frac{me^6}{3}\int_{x,y}\Big(\bar{\mathcal{L}}_{[\rho,\sigma];\mu\nu\lambda}(x,y) - \bar{\mathcal{L}}_{[\rho,\sigma];\mu\lambda\nu}(y-x,y) - \bar{\mathcal{L}}_{[\rho,\sigma];\lambda\mu\nu}(y,y-x)\Big) i\hat{\Pi}^{\text{I}}_{\rho;\mu\nu\lambda\sigma}(x,y)\,, \tag{3.31}$$

where the reflection symmetry of the QED-kernel is used.

3.2.1 Analytic calculation of the hadronic function for the scalar-meson exchange

It is simpler to start with the momentum Feynman rules and translate to position-space at the end. Let us call q_1, q_2 and q_3 the momenta entering by x, y and z respectively. Also we define

$$p_S = q_1 + q_2\,. \tag{3.32}$$

The weight factor z_ρ in the z-integral in Eq. (3.27) becomes a partial derivative $-i\frac{\partial}{\partial q_{3,\rho}}$ and the z-integral simply projects the integrand to vanishing q_3, which corresponds to the external on-shell photon momentum. With the VMD parametrization of the transition form factor Eq. (3.24) and Eq. (3.25), it is then clear that, due to the tensor structure of the polarization tensors, a simple z-integration of the 4-point amplitude without any z-depending weight factor also vanishes. We have used this fact to conclude that $i\check{\Pi}$ defined in Eq. (3.29) vanishes. As a result, we will only need the following 3 types of integral in position-space for the calculation of a_μ^{hlbl}: $I^{\text{PP}}_{1,\mu\nu\sigma\lambda;\rho}(x,y;C)$, $\bar{I}^{\text{PP}}_{1,\mu\nu\sigma\lambda;\rho}(x,y)$ and $I^{\text{QP}}_{1,\mu\nu\sigma\lambda;\rho}(x,y;C)$, defined in the subsequent sub-sections.

$\boxed{I^{\mathbf{PP}}_{1,\mu\nu\sigma\lambda;\rho}(x,y;C)}$

This type of integral is defined by its momentum-space expression:

$$\begin{aligned}
&\tilde{I}^{\mathrm{PP}}_{1,\mu\nu\sigma\lambda;\rho}(q_1,q_2;C)\\
=&-\frac{\partial}{\partial q_{3,\rho}}\Big\{\frac{(q_1^2+q_2^2+C)[q_{1,\nu}q_{2,\mu}-\delta_{\mu\nu}(q_1\cdot q_2)][q_3^2+(q_1+q_2+q_3)^2+C]}{(q_1^2+m_V^2)(q_2^2+m_V^2)(p_S^2+m_S^2)}\\
&\qquad\times\frac{[q_{3,\lambda}(q_1+q_2+q_3)_\sigma-\delta_{\lambda\sigma}q_3\cdot(q_1+q_2+q_3)]}{(q_3^2+m_V^2)[(q_1+q_2+q_3)^2+m_V^2]}\Big\}\Big|_{q_3=0}\\
=&-\frac{(q_1^2+q_2^2+C)[q_{1,\nu}q_{2,\mu}-\delta_{\mu\nu}(q_1\cdot q_2)][(q_1+q_2)^2+C][\delta_{\lambda\rho}(q_1+q_2)_\sigma-\delta_{\lambda\sigma}(q_1+q_2)_\rho]}{m_V^2(q_1^2+m_V^2)(q_2^2+m_V^2)(p_S^2+m_S^2)(p_S^2+m_V^2)}\\
=&-\frac{[q_{1,\nu}q_{2,\mu}-\delta_{\mu\nu}(q_1\cdot q_2)](q_1^2+q_2^2+C)[\delta_{\lambda\rho}(q_1+q_2)_\sigma-\delta_{\lambda\sigma}(q_1+q_2)_\rho]}{m_V^2(p_S^2+m_V^2)(q_1^2+m_V^2)(q_2^2+m_V^2)}\\
&+\frac{(m_S^2-C)[q_{1,\nu}q_{2,\mu}-\delta_{\mu\nu}(q_1\cdot q_2)](q_1^2+q_2^2+C)[\delta_{\lambda\rho}(q_1+q_2)_\sigma-\delta_{\lambda\sigma}(q_1+q_2)_\rho]}{m_V^2(p_S^2+m_S^2)(p_S^2+m_V^2)(q_1^2+m_V^2)(q_2^2+m_V^2)}\,.
\end{aligned}\tag{3.33}$$

The position-space expression is obtained after Fourier transforming back with regard to the momenta q_1 and q_2. With the definition of the massive scalar propagator Eq. (3.11), we get

$$I^{\mathrm{PP}}_{1,\mu\nu\sigma\lambda;\rho}(x,y)=-\frac{i}{m_V^2}\mathcal{O}^{\mathrm{PP}}_{1,\mu\nu\sigma\lambda;\rho}\Big(F(x,y)+\frac{C-m_S^2}{(m_V^2-m_S^2)}K_S(x,y)\Big)\,.\tag{3.34}$$

where

$$\mathcal{O}^{\mathrm{PP}}_{1,\mu\nu\sigma\lambda;\rho}=(\partial^{(x)}_\nu\partial^{(y)}_\mu-\delta_{\mu\nu}\partial^{(x)}\cdot\partial^{(y)})(\Box^{(x)}+\Box^{(y)}-C)[\delta_{\lambda\rho}(\partial^{(x)}_\sigma+\partial^{(y)}_\sigma)-\delta_{\lambda\sigma}(\partial^{(x)}_\rho+\partial^{(y)}_\rho)]\,,\tag{3.35}$$

$$F(x,y)\equiv\int_u G_{m_V}(u)G_{m_V}(x-u)G_{m_V}(y-u)\,,\tag{3.36}$$

$$K_S(x,y)\equiv\int_u[G_{m_S}(u)-G_{m_V}(u)]G_{m_V}(x-u)G_{m_V}(y-u)\,.\tag{3.37}$$

Note that in the above, a position-space derivative induces one power in the conjugate momentum. However, one should be careful with this operation, because the position-space propagator Eq. (3.11) is defined in the sense of distribution, as it comes from the Green function for solving the equation of motion. We shall come back to this detail later.

$\boxed{\bar{I}^{\mathbf{PP}}_{1,\mu\nu\sigma\lambda;\rho}(x,y)}$

This integral is defined as

$$\bar{I}^{\mathrm{PP}}_{1,\mu\nu\sigma\lambda;\rho}(x,y)=\frac{i}{m_V^2(m_V^2-m_S^2)}\bar{\mathcal{O}}^{PP}_{1,\mu\nu\sigma\lambda;\rho}K_S(x,y)\,,\tag{3.38}$$

where

$$\bar{\mathcal{O}}^{\mathrm{PP}}_{1,\mu\nu\sigma\lambda;\rho}=[\partial^{(x)}_\nu\partial^{(y)}_\mu-\delta_{\mu\nu}\partial^{(x)}\cdot\partial^{(y)}][\delta_{\lambda\rho}(\partial^{(x)}_\sigma+\partial^{(y)}_\sigma)-\delta_{\lambda\sigma}(\partial^{(x)}_\rho+\partial^{(y)}_\rho)]\,,\tag{3.39}$$

and $K_S(x,y)$ is defined in Eq. (3.37)

$\boxed{I^{\mathbf{QP}}_{1,\mu\nu\sigma\lambda;\rho}(x,y)}$

The momentum-space expression for this type of integral is

$$\begin{aligned}\tilde{I}^{\mathrm{QP}}_{1,\mu\nu\sigma\lambda;\rho} =& -\frac{\partial}{\partial q_{3,\rho}}\Big\{\frac{[q_2^2 q_{1,\mu}q_{1,\nu}+q_1^2 q_{2,\mu}q_{2,\nu}-(q_1\cdot q_2)q_{1,\mu}q_{2,\nu}-q_1^2q_2^2\delta_{\mu\nu}]}{(q_1^2+m_V^2)(q_2^2+m_V^2)(p_S^2+m_S^2)(q_3^2+m_V^2)[(q_1+q_2+q_3)^2+m_V^2]}\\ &\times[q_3^2+(q_1+q_2+q_3)^2+C][q_{3,\lambda}(q_1+q_2+q_3)_\sigma-\delta_{\lambda\sigma}q_3\cdot(q_1+q_2+q_3)]\Big\}\Big|_{q_3=0}.\end{aligned} \tag{3.40}$$

Consequently, the position-space expression is

$$I^{\mathrm{QP}}_{1,\mu\nu\sigma\lambda;\rho} = -\frac{i}{m_V^2}\mathcal{O}^{\mathrm{QP}}_{1,\mu\nu\sigma\lambda;\rho}\Big(F(x,y)+\frac{C-m_S^2}{(m_V^2-m_S^2)}K_S(x,y)\Big)\,, \tag{3.41}$$

where

$$\begin{aligned}\mathcal{O}^{\mathrm{QP}}_{1,\mu\nu\sigma\lambda;\rho} =& \Big(\Box^{(y)}\partial_\mu^{(x)}\partial_\nu^{(x)}+\Box^{(x)}\partial_\mu^{(y)}\partial_\nu^{(y)}-(\partial^{(x)}\cdot\partial^{(y)})\partial_\mu^{(x)}\partial_\nu^{(y)}-\Box^{(x)}\Box^{(y)}\delta_{\mu\nu}\Big)\\ &\times\Big(\delta_{\lambda\rho}(\partial_\sigma^{(x)}+\partial_\sigma^{(y)})-\delta_{\lambda\sigma}(\partial_\rho^{(x)}+\partial_\rho^{(y)})\Big)\,.\end{aligned} \tag{3.42}$$

Equation of motion and the distributional nature of the scalar propagator

Although the massive scalar propagator $G_m(x)$ is known analytically from Eq. (3.11), it should be noted that it is singular at $x=0$. As it is the Green function of the equation of motion (EOM) of a scalar particle of mass m,

$$(-\Box+m^2)G_m(x)=\delta(x)\,, \tag{3.43}$$

it should be considered as a distribution instead of just a simple function. In the case where δ-functions appear in the integrand, one should first perform the integral with δ-functions analytically before numerically integrating the expression. Not taking into account properly the contribution of these quantities will lead to inconsistent result, which implies for instance the violation of the electromagnetic current Ward identity.

By power counting, a δ-function only appears when one takes two derivatives of the scalar propagator with regard to the components of a 4-dimensional position variable x_μ, in which case the EOM Eq. (3.43) has to be applied. Using the Laplace operator $\Box$ in 4-dimensions, the EOM Eq. (3.43) becomes

$$\frac{d^2}{dr^2}G_m(x) = -\delta(x)-\frac{3}{|x|}\frac{d}{dr}G_m(x)+m^2G_m(x)\,, \tag{3.44}$$

where $r\equiv|x|$.

As a result, when we take two derivatives with regard to the 4-vector x_μ,

$$\begin{aligned}\partial_\mu^{(x)}\partial_\nu^{(x)}G_m(x) =& \delta_{\mu\nu}\frac{1}{|x|}G_m'(x)-\frac{x_\mu x_\nu}{|x|^3}G_m'(x)+\frac{x_\mu x_\nu}{|x|^2}G_m''(x)\\ =& \Big(\delta_{\mu\nu}\frac{1}{|x|}-\frac{4x_\mu x_\nu}{|x|^3}\Big)G_m'(x)+\frac{m^2x_\mu x_\nu}{|x|^2}G_m(x)-\frac{x_\mu x_\nu}{|x|^2}\delta(x)\,,\end{aligned} \tag{3.45}$$

where a prime in the superscript means taking derivative with regard to $|x|$.

The weight factor of the last term containing a δ-function in the last line of the equation above is not well-defined at $x = 0$. To understand this last term, one should consider the whole as a distribution. Consider a smooth test function $\phi(x) \equiv \psi(|x|)$. The action of the distribution reads

$$\int_x \delta(x) \frac{x_\mu x_\nu}{|x|^2} \phi(x) = \int_x \delta(x) \frac{x_\mu x_\nu}{|x|^2} \Big(\phi(0) + |x| \phi'(0) + \dots \Big) . \tag{3.46}$$

Apart from the constant term, all other terms in the Taylor expansion on the right-hand side vanish due to the projection to 0 of the δ-function. The contribution of the constant term vanishes in the case where $\mu \neq \nu$ due to the reflection symmetry of the 4-dimensional integral. Thus, the rank-2 tensor that $\delta(x) \frac{x_\mu x_\nu}{|x|^2}$ represents is proportional to the Kronecker $\delta_{\mu\nu}$. It is then easy to check by considering the trace of the tensor that

$$\frac{x_\mu x_\nu}{|x|^2} \delta(x) = \frac{1}{4} \delta_{\mu\nu} \delta(x) . \tag{3.47}$$

From this and Eq. (3.44), we deduce that

$$\partial_\mu^{(x)} \partial_\nu^{(x)} G(x) = \partial_\mu^{(x)} \partial_\nu^{(x)} G^{\text{reg.}}(x) - \frac{1}{4} \delta_{\mu\nu} \delta(x) , \tag{3.48}$$

where $\partial_\mu^{(x)} \partial_\nu^{(x)} G^{\text{reg.}}(x)$ is the usual derivative of the scalar propagator given in Eq. (3.11) by considering it as a smooth function away from the origin.

Using the EOM, we can simplify I^{PP} and I^{QP} by writing down explicitly the action of the Laplacian on the scalar functions $F(x, y)$ and $K_S(x, y)$. Further details are given in Appendix C.1.

Expression for $i\hat{\Pi}^{\text{I}}$

Finally, with all the quantities defined above, we are able to write down the analytical expression for $i\hat{\Pi}^{\text{I}}$ after performing the z-integration

$$\begin{aligned} & i\hat{\Pi}^{\text{I}}_{\rho;\mu\nu\lambda\sigma}(x, y) \\ & = \begin{cases} A^2 \bar{I}^{\text{PP}}_{1,\mu\nu\sigma\lambda;\rho}(x, y) , & \text{if } B = 0; \\ B^2 \Big(\frac{1}{4} I^{\text{PP}}_{1,\mu\nu\sigma\lambda;\rho}(x, y; -\frac{2A}{B} - m_S^2) + \frac{1}{2} I^{\text{QP}}_{1,\mu\nu\sigma\lambda;\rho}(x, y; -\frac{2A}{B} - m_S^2) \Big) , & \text{otherwise.} \end{cases} \end{aligned} \tag{3.49}$$

3.2.2 Gegenbauer polynomial technique and implementation of the scalar integrals

According to the previous section, $i\Pi^{\text{I}}$ depends on two scalar integrals F and K_S defined in Eq. (3.36) and Eq. (3.37) and their derivatives. It is hard to know if one can relate them to some well-known analytical functions. As they are 4-dimensional integrals, it would be computationally demanding if one computed them on the fly, in addition to the multi-dimensional integral needed for a_μ^{hlbl}. Fortunately, it is possible exploit their Gegenbauer polynomial (GP) expansions such that the 3-dimensional integral over the solid angle can be performed easily. Once the angular quantities are integrated over, the scalar integrals F and K_S depend only on two radial quantities, due to the tensor structure. Depending on the exact desired quantity, one can then

pre-compute F and K_S on several points and interpolate between them. This technique is similar to the one used for our position-space QED-kernel, but we would need to calculate the Gegenbauer polynomial expansion of the massive scalar propagator. We will see how this technique is applied.

The goal is to compute the quantity

$$\mathcal{K}(x,y;m_i) \equiv \int_u G_{m_i}(u) G_{m_V}(x-u) G_{m_V}(y-u)\,, \tag{3.50}$$

as F and K_S [Eqs. (3.36, 3.37)] can be expressed with it

$$F(x,y) = \mathcal{K}(x,y;m_V)\,, \quad K_S(x,y) = \mathcal{K}(x,y;m_S) - \mathcal{K}(x,y;m_V)\,. \tag{3.51}$$

In the following, we will omit the mass m_i in the argument of $\mathcal{K}$ and simply replace it by m_S in the subsequent expressions, but one should keep in mind that this parameter remains arbitrary. We will first compute $\mathcal{K}$ from its defining expression Eq. (3.50). This will be referred to as type I. Later on, we will derive two other variants that we call type II and type III, which describe the same quantity but are obtained from different integral representations. The motivation of these two variants is to obtain a better convergence for the GP expansion, which we trade our 3-dimensional angular integral for.

Type I

Using Graf's and Gegenbauer's addition theorem (c.f. p. 365 of Ref. [Wat44]), one obtains the following useful relation for the GP expansion, relevant for the massive scalar propagator:

$$\frac{K_\nu(w)}{w^\nu} = 2^\nu \Gamma(\nu) \sum_{m=0}^{\infty} (\nu+m) \frac{K_{\nu+m}(Z)}{Z^\nu} \frac{I_{\nu+m}(z)}{z^\nu} C_m^\nu(\cos\phi)\,, \tag{3.52}$$

where the variables Z, z and w form geometrically a triangle

$$Z > z, \quad Z^2 + z^2 - 2Zz\cos\phi = w^2\,, \tag{3.53}$$

and C_m^ν is the Gegenbauer polynomial defined by the generating function [CKT80]:

$$\frac{1}{|x_1 - x_2|^{2\nu}} = \frac{1}{|x_1|^{2\nu}} \sum_{n=0}^{\infty} C_m^\nu(\hat{x}_1 \cdot \hat{x}_2) \left(\frac{|x_2|}{|x_1|}\right)^n, \quad \text{with } |x_1| > |x_2|\,, \tag{3.54}$$

where $\hat{x}_i$ is the unit vector collinear to the vector x_i in a Euclidean space in arbitrary dimension. It is useful to note the orthogonality condition [CKT80]:

$$\int_{\hat{\Omega}} d\hat{x}_2 C_n^\lambda(\hat{x}_1 \cdot \hat{x}_2) C_m^\lambda(\hat{x}_2 \cdot \hat{x}_3) = \frac{\lambda}{n+\lambda} \delta_{n,m} C_n^\lambda(\hat{x}_1 \cdot \hat{x}_2)\,, \tag{3.55}$$

where the integration is performed on the unit sphere and normalized such that $\int_{\hat{\Omega}} d\hat{x} = 1$.

Now we restrict ourselves to 4 space-time dimensions. From Eq. (3.52), the GP expansion of the massive scalar propagator $G_m(x-u)$ reads:

$$G_m(x-u) = \sum_{n=0}^{\infty} \gamma_n(|x|,|u|;m) U_n(\hat{x}\cdot\hat{u})\,, \tag{3.56}$$

where $U_n \equiv C_n^1$ is the Chebyshev polynomial of the second kind and

$$\gamma_n(|x|,|u|;m) = \frac{1}{2\pi^2|x||u|}(n+1)\Big(K_{1+n}(m|x|)I_{1+n}(m|u|)\theta(|x|-|u|) + K_{1+n}(m|u|)I_{1+n}(m|x|)\theta(|u|-|x|)\Big)\,, \tag{3.57}$$

where θ is the Heaviside function.

The Chebyshev polynomials of the second kind satisfy another orthogonality condition [KN02]

$$\int_{\hat{\Omega}} d\hat{e}\, U_n(\hat{e}\cdot\hat{x})U_m(\hat{e}\cdot\hat{x}) = \delta_{nm}\,. \tag{3.58}$$

Then the 4-dimensional integral Eq. (3.50) can be reduced to a series of 1-dimensional integrals

$$\begin{aligned}&\int_u G_{m_S}(u)G_{m_V}(x-u)G_{m_V}(y-u)\\ &=\int_{|u|=0}^{\infty}|u|^3\sum_{n=0}^{\infty}\frac{1}{n+1}G_{m_S}(u)U_n(\hat{x}\cdot\hat{y})\gamma_n(|x|,|u|;m_V)\gamma_n(|y|,|u|;m_V)\,.\end{aligned} \tag{3.59}$$

Without loss of generality, let us assume $|x| \le |y|$ and focus on the non-vanishing Heaviside function in Eq. (3.57). Then, we obtain the type I Gegenbauer polynomial expansion of $\mathcal{K}$:

$$\begin{aligned}\mathcal{K}(x,y) =&\mathcal{K}^{\mathrm{I}}(x,y)\\ \equiv&\frac{m_S}{8\pi^4|x||y|}\sum_{n=0}^{\infty}(n+1)\Big[\mathcal{G}_n^{\mathrm{I}}(|x|)K_{1+n}(m_V|x|)K_{1+n}(m_V|y|)\\ &+\Big(\mathcal{G}_n^{\mathrm{II}}(|x|)-\mathcal{G}_n^{\mathrm{II}}(|y|)\Big)I_{1+n}(m_V|x|)K_{1+n}(m_V|y|)\\ &+\mathcal{G}_n^{\mathrm{III}}(|y|)I_{1+n}(m_V|x|)I_{1+n}(m_V|y|)\Big]U_n(\hat{x}\cdot\hat{y})\,,\end{aligned} \tag{3.60}$$

where

$$\begin{aligned}\mathcal{G}_n^{\mathrm{I}}(|x|) &= \int_{|u|=0}^{|x|}K_1(m_S|u|)I_{1+n}(m_V|u|)I_{1+n}(m_V|u|)\,,\\ \mathcal{G}_n^{\mathrm{II}}(|x|) &= \int_{|u|=|x|}^{\infty}K_1(m_S|u|)K_{1+n}(m_V|u|)I_{1+n}(m_V|u|)\,,\\ \mathcal{G}_n^{\mathrm{III}}(|x|) &= \int_{|u|=|x|}^{\infty}K_1(m_S|u|)K_{1+n}(m_V|u|)K_{1+n}(m_V|u|)\,.\end{aligned} \tag{3.61}$$

Accounting for the cancellation between the modified Bessel functions K_n and I_n in the small argument and asymptotic regions, we pre-compute and store the "regularized" functions instead

$$\begin{aligned}\mathcal{H}_n^{\mathrm{I}}(|x|) &= K_{1+n}^2(m_V|x|)\int_{|u|=0}^{|x|}K_1(m_S|u|)I_{1+n}(m_V|u|)I_{1+n}(m_V|u|)\,,\\ \mathcal{H}_n^{\mathrm{II}}(|x|) &= K_{1+n}(m_V|x|)I_{1+n}(m_V|x|)\int_{|u|=|x|}^{\infty}K_1(m_S|u|)K_{1+n}(m_V|u|)I_{1+n}(m_V|u|)\,,\\ \mathcal{H}_n^{\mathrm{III}}(|x|) &= I_{1+n}^2(m_V|x|)\int_{|u|=|x|}^{\infty}K_1(m_S|u|)K_{1+n}(m_V|u|)K_{1+n}(m_V|u|)\,.\end{aligned} \tag{3.62}$$

Then, Eq. (3.60) becomes

$$\begin{aligned}\mathcal{K}^{\mathrm{I}}(x,y) =& \frac{m_S}{8\pi^4|x||y|}\sum_{n=0}^{\infty}(n+1)\Big[\mathcal{H}_n^{\mathrm{I}}(|x|)\frac{K_{1+n}(m_V|y|)}{K_{1+n}(m_V|x|)} \\ &+\Big(\mathcal{H}_n^{\mathrm{II}}(|x|)\frac{K_{1+n}(m_V|y|)}{K_{1+n}(m_V|x|)}-\mathcal{H}_n^{\mathrm{II}}(|y|)\frac{I_{1+n}(m_V|x|)}{I_{1+n}(m_V|y|)}\Big) \\ &+\mathcal{H}_n^{\mathrm{III}}(|y|)\frac{I_{1+n}(m_V|x|)}{I_{1+n}(m_V|y|)}\Big]U_n(\hat{x}\cdot\hat{y})\,,\end{aligned} \tag{3.63}$$

which is what is numerically implemented for the type I representation of $\mathcal{K}$.

In practice, as the $\mathcal{H}^i$'s are uni-variate, one can pre-compute them on a given set of points and linearly interpolate to the point where we want to evaluate $\mathcal{K}$ as a function of $(|x|,\hat{x}\cdot\hat{y},|y|)$. Nonetheless, as the integrand of $\mathcal{K}$ becomes non-integrable in the vicinity of $x=y=0$, we expect that the $\mathcal{H}^i$'s to be badly approximated by linear interpolations in that region. Also, one might be concerned with the number of Gegenbauer polynomials needed in the expansion $\mathcal{K}^{\mathrm{I}}$ in order to reach a good convergence.

To study these problems, let us first recall the behavior of the modified Bessel functions near the origin

$$\begin{aligned}K_n(z) &\underset{z\to 0}{\sim} \begin{cases}-\ln(z/2)-\gamma & \text{if } n=0\,,\\ \frac{\Gamma(n)}{2}\left(\frac{2}{z}\right)^n & \text{else}\,.\end{cases}\\ I_n(z) &\underset{z\to 0}{\sim} \frac{1}{\Gamma(n+1)}\left(\frac{z}{2}\right)^n.\end{aligned} \tag{3.64}$$

It follows that the behaviors around the origin of the $\mathcal{H}^i$'s are given by

$$\begin{aligned}\mathcal{H}_n^{\mathrm{I}}(|x|) &\underset{|x|\to 0}{\sim} \frac{1}{8(1+n)^3 m_S}\,,\\ \mathcal{H}_n^{\mathrm{II}}(|x|) &\underset{|x|\to 0}{\sim} \frac{1}{4(1+n)^2 m_S}\ln|x|\,,\\ \mathcal{H}_n^{\mathrm{III}}(|x|) &\underset{|x|\to 0}{\sim} \frac{1}{8(1+n)^3 m_S}\,.\end{aligned} \tag{3.65}$$

As a result, the coefficient of the n-th order term in the GP expansion Eq. (3.63) with the pre-factor outside of the sum omitted can be written as

$$l_n(|x|,|y|) \equiv \frac{1}{4(1+n)^2 m_S}\left(\frac{|x|}{|y|}\right)^{1+n}\left[1-(1+n)\ln\left(\frac{|x|}{|y|}\right)+p(|x|,|y|)\right]+\mathcal{O}(|x|,|y|)\,, \tag{3.66}$$

where p is a smooth function in $|x|$ and $|y|$ coming from the sub-leading terms of $\mathcal{H}^{\mathrm{II}}$, negligible compared to $\ln|x|$ and $\ln|y|$. This implies that the Gegenbauer polynomial expansion would behave like a geometric series with ratio $\frac{|x|}{|y|}$ in the worst case in the vicinity of $x=y=0$. If $\frac{|x|}{|y|}$ is close to unity, the GP expansion would converge slowly. The strategy that we adopt at this geometric region is to factorize

out the singular behavior from Eq. (3.66). The function

$$g_n(|x|,|y|) \equiv \frac{|x||y|l_n(x,y)}{\left(\frac{|x|}{|y|}\right)^{1+n}\left[1+(1+n)\ln\left(\frac{|y|}{|x|}\right)\right]}, \tag{3.67}$$

is expected to be smooth enough for small $|x|$ and $|y|$ so that we can approximate it with a polynomial with low order. We can do a bi-cubic interpolation of g_n on a 2-dimensional grid (see e.g. Sect. 3.6.3 of Ref. [Pre+07]) and then transform it back to the original coefficient of the GP expansion. By writing the above as $g_n(|x|,|y|) = h_n(|x|,|y|)l_n(|x|,|y|)$, we have

$$\begin{pmatrix} g \\ \partial_x g \\ \partial_y g \\ \partial^2_{xy} g \end{pmatrix} = \begin{pmatrix} h & 0 & 0 & 0 \\ \partial_x h & h & 0 & 0 \\ \partial_y h & 0 & h & 0 \\ \partial^2_{xy} h & \partial_y h & \partial_x h & h \end{pmatrix} \begin{pmatrix} l \\ \partial_x l \\ \partial_y l \\ \partial^2_{xy} l \end{pmatrix}. \tag{3.68}$$

where the order index n and the norm symbol of the variable x and y are omitted. As $h(x,y) > 0$ in its domain of definition, the matrix on the right-hand side is definite positive. Thus, we have a one-to-one correspondence between the function g_n and h_n and their derivatives relevant for the bi-cubic interpolation.

For x and y away from the origin, we expect to be able to approximate the $\mathcal{H}^i$'s reasonably well with linear interpolation. However, the concern on the convergence rate of the GP expansion still persists. At large orders, the modified Bessel functions have very similar behavior as given in Eq. (3.64). This means that the coefficients of the GP expansion of $\mathcal{K}$ behave like Eq. (3.66) at large orders. The bad convergence rate is still expected while the ratio $\frac{|x|}{|y|}$ is close to unity. To avoid this case, we will introduce the type II and type III integral representations of $\mathcal{K}$.

Type II

It is noticed that in some regions where $|x| \approx |y|$, the Gegenbauer polynomial expansion does not converge well. We propose a type II representation of $\mathcal{K}$ based on rewriting the integrand using a change of variables:

$$\mathcal{K}(x,y) = \mathcal{K}^{\mathrm{II}}(x,y) \equiv \bar{\mathcal{K}}(x,x-y) \equiv \int_u G_{m_S}(x-u)G_{m_V}(x-y-u)G_{m_V}(u). \tag{3.69}$$

As in the Type I case, we introduce the regularized quantities

$$\begin{aligned}
\bar{\mathcal{H}}^{\mathrm{I}}_n(|x|) &= K_{1+n}(m_S|x|)K_{1+n}(m_V|x|)\int_{|u|=0}^{|x|} K_1(m_V|u|)I_{1+n}(m_S|u|)I_{1+n}(m_V|u|), \\
\bar{\mathcal{H}}^{\mathrm{II}}_n(|x|) &= K_{1+n}(m_V|x|)I_{1+n}(m_S|x|)\int_{|u|=|x|}^{\infty} K_1(m_V|u|)K_{1+n}(m_S|u|)I_{1+n}(m_V|u|), \\
\bar{\mathcal{H}}^{\mathrm{III}}_n(|x|) &= I_{1+n}(m_S|x|)I_{1+n}(m_V|x|)\int_{|u|=|x|}^{\infty} K_1(m_V|u|)K_{1+n}(m_S|u|)K_{1+n}(m_V|u|).
\end{aligned} \tag{3.70}$$

For $|x| \leq |x-y|$, the type II GP expansion of $\mathcal{K}$ is

$$\begin{aligned}\mathcal{K}^{\mathrm{II}}(x,y) =& \frac{m_V}{8\pi^4|x||x-y|}\sum_{n=0}^{\infty}(n+1)\Big[\bar{\mathcal{H}}_n^{\mathrm{I}}(|x|)\frac{K_{1+n}(m_V|x-y|)}{K_{1+n}(m_V|x|)} \\ &+\Big(\bar{\mathcal{H}}_n^{\mathrm{II}}(|x|)\frac{K_{1+n}(m_V|x-y|)}{K_{1+n}(m_V|x|)} - \bar{\mathcal{H}}_n^{\mathrm{II}}(|x-y|)\frac{I_{1+n}(m_S|x|)}{I_{1+n}(m_S|x-y|)}\Big) \\ &+\bar{\mathcal{H}}_n^{\mathrm{III}}(|x-y|)\frac{I_{1+n}(m_S|x|)}{I_{1+n}(m_S|x-y|)}\Big]U_n\big(\hat{x}\cdot\widehat{(x-y)}\big)\,.\end{aligned} \tag{3.71}$$

Otherwise, the rôles of $|x|$ and $|x-y|$ are swapped. Again in this case, the functions to be pre-computed, the $\bar{\mathcal{H}}^i$'s, are uni-variate.

A straightforward analysis as done in the end of the sub-section where the Type I representation is introduced, when $|x|$ is different enough from $|x-y|$, the GP series should converge quickly. We can thus find out the two most different between $|x|$, $|y|$ and $|x-y|$. If this pair is $|x|$ and $|y|$, then we can use $\mathcal{K}^{\mathrm{I}}$, otherwise we shall use $\mathcal{K}^{\mathrm{II}}$.

Type III

There is still a bad geometric configuration where type I and type II representations both have bad convergence rate: the case where $|x|$, $|y|$ and $|x-y|$ all have similar lengths. To handle this situation, we can use a different representation for the integrand which requires more Bessel functions but with more widely separated arguments. We expect that this will help the convergence of the series expansion.

By applying a change of variables, the scalar integral can be written as

$$\begin{aligned}\mathcal{K}(x,y) =& \tilde{\mathcal{K}}(x,y;v) \\ \equiv& \int_u G_{m_S}(u+v)G_{m_V}(x-v-u)G_{m_V}(y-v-u) \\ =& \int_u \sum_{i,j,k=0}^{\infty}\gamma_i(|u|,|v|;m_S)\gamma_j(|x-v|,|u|;m_V)\gamma_k(|y-v|,|u|;m_V) \\ &\times U_i(-\hat{u}\cdot\hat{v})U_j\big(\widehat{(x-v)}\cdot\hat{u}\big)U_k\big(\widehat{(y-v)}\cdot\hat{u}\big)\,.\end{aligned} \tag{3.72}$$

In the above, one can choose the shifting vector v to be $-y$. The advantages of this choice are the following. First, the Bessel functions resulting from the Gegenbauer coefficients γ take $|y|$, $|x+y|$ and $|2y|$ as arguments (assuming $|x| \leq |y|$). In the worse case, for $\cos\beta \equiv \hat{x}\cdot\hat{y} \approx 0.5$ and $|x| \approx |y|$, the smallest difference between the norms is of the order of $0.3\times|y|$. Second, the only non-trivial argument in the Gegenbauer polynomials for this choice is $\cos(\beta/2)$. In this special case, the computation becomes relatively simple. We make use of some results from Refs. [Nic78; Edm55]. Let us briefly review them in the following paragraph.

The 4-dimensional Cartesian coordinates (x,y,z,w) can be parametrized with four variables r, α, β and γ as

$$\begin{aligned}x &= r\sin\frac{\beta}{2}\sin\frac{\alpha-\gamma}{2}\,, \quad y = r\sin\frac{\beta}{2}\cos\frac{\alpha-\gamma}{2}\,, \\ z &= r\cos\frac{\beta}{2}\sin\frac{\alpha+\gamma}{2}\,, \quad w = r\cos\frac{\beta}{2}\cos\frac{\alpha+\gamma}{2}\,.\end{aligned} \tag{3.73}$$

The mapping between the solid angle Ω in 4 dimensions and the three angular variables $\alpha \in [0, 2\pi]$, $\beta \in [0, \pi]$ and $\gamma \in [0, 4\pi]$ is a diffeomorphism. We introduce the rotation matrices

$$D^{(j)}_{m'm}(\Omega) = e^{im'\gamma} d^{(j)}_{m'm}(\beta) e^{im\alpha} \,. \tag{3.74}$$

They verify the product formula

$$D^{(j_1)}_{m'_1 m_1}(\Omega) D^{(j_2)}_{m'_2 m_2}(\Omega) = \sum_j (2j+1) \begin{pmatrix} j_1 & j_2 & j \\ m'_1 & m'_2 & m' \end{pmatrix} \begin{pmatrix} j_1 & j_2 & j \\ m_1 & m_2 & m \end{pmatrix} D^{*(j)}_{m'm}(\Omega) \,. \tag{3.75}$$

where Wigner 3-j symbols are used.

It can be shown that the Chebyshev polynomials of the second kind are related to the previously introduced quantities

$$U_l(\cos\theta_{12}) = \sum_{mm'} D^{(l/2)}_{m'm}(\Omega_1) D^{*(l/2)}_{m'm}(\Omega_2) \,, \tag{3.76}$$

where θ_{12} is the angle between the two unit vectors Ω_1 and Ω_2.

The complex conjugate can be written as

$$D^{*(j)}_{m'm}(\Omega) = (-1)^{m'-m} D^{(j)}_{-m',-m}(\Omega) \,. \tag{3.77}$$

In the angular coordinate system (α, β, γ), the reflection can be realized by $\gamma \to \gamma + 2\pi$. Since $j - m' \in \mathbb{Z}$, we conclude that

$$D^{(j)}_{m'm}(-\hat{u}) = (-1)^{2j} D^{(j)}_{m'm}(\hat{u}) \,. \tag{3.78}$$

The 3-j symbol satisfies the orthogonality condition

$$\sum_{m1,m2} (2j_3+1) \begin{pmatrix} j_1 & j_2 & j_3 \\ m_1 & m_2 & m_3 \end{pmatrix} \begin{pmatrix} j_1 & j_2 & j_3 \\ m'_1 & m'_2 & m'_3 \end{pmatrix} = \delta_{j_3 j'_3} \delta_{m_3 m'_3} \delta(j_1 j_2 j_3) \,, \tag{3.79}$$

where the triangle condition is encoded in the last term of the right-hand side

$$\delta(j_1 j_2 j_3) = \begin{cases} 1, & \text{if } |j_1 - j_2| \le j_3 \le j_1 + j_2 \,, \\ 0, & \text{else} \,. \end{cases} \tag{3.80}$$

Using all the properties mentioned so far, we have, for

$$i + j + k \in 2\mathbb{Z} \,, \tag{3.81}$$

$$
\begin{aligned}
&\int_{\hat{\Omega}} d\hat{u} U_i(\hat{u}\cdot\hat{y}) U_j(\widehat{(x+y)}\cdot\hat{u}) U_k(\hat{y}\cdot\hat{u}) \\
=&\int_{\hat{\Omega}} d\hat{u} \sum_{\substack{m_1,m_2,m3\\ m_1',m_2',m_3'}} D^{(i/2)}_{m_1'm_1}(\hat{u}) D^{*(i/2)}_{m_1'm_1}(\hat{y}) D^{(j/2)}_{m_2'm_2}(\hat{u}) D^{*(j/2)}_{m_2'm_2}(\widehat{(x+y)}) D^{(k/2)}_{m_3'm_3}(\hat{u}) D^{*(k/2)}_{m_3'm_3}(\hat{y}) \\
=&2\pi^2 \sum_{m_l,m_l'} \begin{pmatrix} i/2 & j/2 & k/2 \\ m_1' & m_2' & m_3' \end{pmatrix} \begin{pmatrix} i/2 & j/2 & k/2 \\ m_1 & m_2 & m_3 \end{pmatrix} D^{*(j/2)}_{m_2'm_2}(\widehat{(x+y)}) \\
&\times \sum_n (2n+1) \begin{pmatrix} i/2 & k/2 & n \\ m_1 & m_3 & m_2 \end{pmatrix} \begin{pmatrix} i/2 & k/2 & n \\ m_1' & m_3' & m_2' \end{pmatrix} D^{(n)}_{m_2'm_2}(\hat{y}) \\
=&2\pi^2 \frac{1}{j+1} U_j(\widehat{(x+y)}\cdot\hat{y}) \delta(ijk)\,,
\end{aligned}
\tag{3.82}
$$

where the result of the angular integration has been derived in Ref. [Nic78]. The condition Eq. (3.81) is required by the selection rules of the 3-j symbol. Hence, assuming $|y| \le |x+y| \le 2|y|$, which is valid for the geometrical region that we are interested in, we can reduce Eq. (3.72) to a sum of one dimensional integrals, which defines the type III representation of the scalar integral $\mathcal{K}$

$$
\begin{aligned}
\mathcal{K}^{\mathrm{III}}(x,y) \equiv& \tilde{\mathcal{K}}(x,y;-y) \\
=&\frac{1}{8\pi^4|y|^2|x+y|} \sum_{ijk} (i+1)(k+1)\delta(ijk) U_j(\widehat{(x+y)}\cdot\hat{y}) \\
&\times \Big[\tilde{\mathcal{G}}_{1,ijk}(|y|) K_{1+i}(m_S|y|) K_{1+j}(m|x+y|) K_{1+k}(2m|y|) \\
&+ \tilde{\mathcal{G}}_{2,ijk}(|y|,|x+y|) I_{1+i}(m_S|y|) K_{1+j}(m|x+y|) K_{1+k}(2m|y|) \\
&+ \tilde{\mathcal{G}}_{3,ijk}(|y|,|x+y|) I_{1+i}(m_S|y|) I_{1+j}(m|x+y|) K_{1+k}(2m|y|) \\
&+ \tilde{\mathcal{G}}_{4,ijk}(|y|) I_{1+i}(m_S|y|) I_{1+j}(m|x+y|) I_{1+k}(2m|y|) \Big]\,,
\end{aligned}
\tag{3.83}
$$

where

$$
\begin{aligned}
\tilde{\mathcal{G}}_{1,ijk}(|y|) &= \int_{|u|=0}^{|y|} I_{1+i}(m_S|u|) I_{1+j}(m|u|) I_{1+k}(m|u|)\,, \\
\tilde{\mathcal{G}}_{2,ijk}(|y|,|d|) &= \int_{|u|=|y|}^{|d|} K_{1+i}(m_S|u|) I_{1+j}(m|u|) I_{1+k}(m|u|)\,, \\
\tilde{\mathcal{G}}_{3,ijk}(|y|,|d|) &= \int_{|u|=|d|}^{2|y|} K_{1+i}(m_S|u|) K_{1+j}(m|u|) I_{1+k}(m|u|)\,, \\
\tilde{\mathcal{G}}_{4,ijk}(|y|) &= \int_{|u|=2|y|}^{\infty} K_{1+i}(m_S|u|) K_{1+j}(m|u|) K_{1+k}(m|u|)\,.
\end{aligned}
\tag{3.84}
$$

In practice, we store the Chebyshev coefficients of $U_j(\widehat{(x+y)}\cdot\hat{y}) = U_j(\cos(\beta/2))$ as well as their partial derivatives $\partial_{|y|}$, $\partial_{|x+y|}$ and $\partial^2_{|x+y|,|y|}$ for given $|x+y|$ and $|y|$. Also, as done previously, we introduce the "regularized" quantities

$$
\begin{aligned}
\tilde{\mathcal{H}}^{\mathrm{I}}_{ijk}(|y|) =& K_{1+i}(m_S|y|) K_{1+j}(m|y|) K_{1+k}(2m|y|) \\
&\times \int_{|u|=0}^{|y|} I_{1+i}(m_S|u|) I_{1+j}(m|u|) I_{1+k}(m|u|)\,,
\end{aligned}
\tag{3.85}
$$

$$\begin{aligned}\tilde{\mathcal{H}}^{\mathrm{II}}_{ijk}(|y|,|d|) =& I_{1+i}(m_S|y|)K_{1+j}(m|d|)K_{1+k}(2m|y|)\\ &\times\int_{|u|=|y|}^{|d|} K_{1+i}(m_S|u|)I_{1+j}(m|u|)I_{1+k}(m|u|)\,,\end{aligned} \tag{3.86}$$

$$\begin{aligned}\tilde{\mathcal{H}}^{\mathrm{III}}_{ijk}(|y|,|d|) =& I_{1+i}(m_S|y|)I_{1+j}(m|d|)K_{1+k}(2m|y|)\\ &\times\int_{|u|=|d|}^{2|y|} K_{1+i}(m_S|u|)K_{1+j}(m|u|)I_{1+k}(m|u|)\,,\end{aligned} \tag{3.87}$$

$$\begin{aligned}\tilde{\mathcal{H}}^{\mathrm{IV}}_{ijk}(|y|) =& I_{1+i}(m_S|y|)I_{1+j}(2m|y|)I_{1+k}(2m|y|)\\ &\times\int_{|u|=2|y|}^{\infty} K_{1+i}(m_S|u|)K_{1+j}(m|u|)K_{1+k}(m|u|)\,,\end{aligned} \tag{3.88}$$

such that Eq. (3.72) can be written as

$$\begin{aligned}\mathcal{K}^{\mathrm{III}}(x,y) =& \frac{1}{8\pi^4|y|^2|x+y|}\sum_{j=0}^{\infty} U_j\big((x+\hat{y})\cdot\hat{y}\big)\sum_{ik}(i+1)(k+1)\delta(ijk)\\ &\times\Big[\tilde{\mathcal{H}}^{\mathrm{I}}_{ijk}(|y|)\frac{K_{1+j}(m|x+y|)}{K_{1+j}(m|y|)}+\tilde{\mathcal{H}}^{\mathrm{II}}_{ijk}(|y|,|x+y|)\\ &+\tilde{\mathcal{H}}^{\mathrm{III}}(|y|,|x+y|)+\tilde{\mathcal{H}}^{\mathrm{IV}}(|y|)\frac{I_{1+j}(m|x+y|)}{I_{1+j}(2m|y|)}\Big]\,.\end{aligned} \tag{3.89}$$

3.2.3 Details of the numerical implementation

Now, we give a summary of our implementation of the scalar integrals and their derivatives. As argued previously, the convergence rate of the GP expansion of the scalar integral $\mathcal{K}$ [Eq. (3.50)] depends on the geometric configuration of its arguments. We use three different representation of the integral, $\mathcal{K}^{\mathrm{I}}$ [Eq. (3.63)], $\mathcal{K}^{\mathrm{II}}$ [Eq. (3.71)] and $\mathcal{K}^{\mathrm{III}}$ [Eq. (3.89)]. In order to compute a_μ^{hlbl}, we also need various derivatives of these quantities with regard to scalar variables, so that we can obtain the derivatives of $\mathcal{K}$ with regard to variables in 4-dimensions after applying chain rules. To get the series sum involving Gegenbauer polynomials (which are just Chebyshev polynomials of the second kind in our case), it is numerically advantageous to use the Clenshaw algorithm (see e.g. Sect.5.4 of Ref. [Pre+07]). With the recursive method, the higher order derivatives with regard to angular variables can be easily computed (c.f. Appendix C.2.2). As the result is analytically known, the angular dependence can be computed at any point on the fly. As for the higher order derivatives with regard to radial variables, one has to pre-compute the form factors $\mathcal{H}^i_n$'s, $\bar{\mathcal{H}}^i_n$'s or $\tilde{\mathcal{H}}^i_n$'s and their derivatives on a line (for the first two) or a 2-dimensional grid (for the last one) according to the expression used. One can make use of the EOM Eq. (3.43) to reduce the number of radial derivatives that is actually required. In the latter computation, it is helpful to make use of the recurrence relations for the modified Bessel functions given in Appendix C.2.1. This helps to efficiently compute the desired GP expansions and derivatives to all order. Having the derivatives also allows for smoother interpolation from the pre-computed sites to the point that we want to evaluate $\mathcal{K}$. As we have to do a two dimensional interpolation because of the dependence on the norms of the two vectors in the argument of the GP expansion coefficients of $\mathcal{K}$, we decide to use a bi-cubic interpolation scheme. However, as mentioned, the non-linearity of $\mathcal{K}$ and its derivatives increases significantly at small argument region. A smoothened interpolation scheme is proposed according to Eq. (3.68). Finally, to check for the correctness and the precision

of the implementation, we check our result for the derivatives against numerical differentiation and also if the expected EOMs established between different orders of derivative are satisfied. The former task checks for the smoothness of the function, which is favored by the bi-cubic interpolation that we decide to use; while the latter checks for the convergence of the GP expansions and the truncation error. For instance, in the perfect arithmetic limit, the following identities should hold

$$\begin{aligned}\Box^{(x)}\mathcal{K}(x,y) &= m_V^2\mathcal{K}(x,y) - G_{m_S}(x)G_{m_V}(x-y)\,,\\ \Box^{(y)}\mathcal{K}(x,y) &= m_V^2\mathcal{K}(x,y) - G_{m_S}(y)G_{m_V}(x-y)\,,\\ \Box^{(x+y)}\mathcal{K}(x,y) &= m_S^2\mathcal{K}(x,y) - G_{m_V}(x)G_{m_V}(y)\,,\end{aligned} \tag{3.90}$$

under numerical differentiation with reasonably small step-size.

Introduce now a tunable parameter $r_{\min}$. We establish a scheme selecting procedure for computing $\mathcal{K}$ as follows. For given x and y, we define the ratio

$$r \equiv \frac{\min(|x|,|y|,|x-y|)}{\max(|x|,|y|,|x-y|)}\,. \tag{3.91}$$

Because of the asymptotic behavior of the modified Bessel functions at large order, the series expansions for $\mathcal{K}^{\mathrm{I}}$ and $\mathcal{K}^{\mathrm{II}}$ described above behave like geometric ones in the ratio of the involved vector lengths ($|x|$, $|y|$ or $|x-y|$) up to some extra dependence on the order. We expect that as the ratio r is far enough from unity, the series expansion $\mathcal{K}^{\mathrm{I}}$ or $\mathcal{K}^{\mathrm{II}}$ should converge fairly quickly. For $r \leq r_{\min}$, we will then use the series expansion $\mathcal{K}^{\mathrm{I}}$ if the largest and the smallest vector lengths are in $\{|x|,|y|\}$, and use $\mathcal{K}^{\mathrm{II}}$ otherwise. For $r > r_{\min}$, we will switch to $\mathcal{K}^{\mathrm{III}}$ and also truncate the GP expansion at much higher order. From the simple geometrical relation $|x+y|^2 = 2|x|^2 + 2|y|^2 - |x-y|^2$, we deduce that, for fixed $|y|$, we will need $\tilde{\mathcal{K}}^{\mathrm{III}}$ for the range

$$r_{\min}\sqrt{4r_{\min}^2-1}|y| \leq |x+y| \leq \sqrt{4-r_{\min}^2}|y|\,. \tag{3.92}$$

Note that typically $r_{\min}$ is chosen as close to unity as possible to reduce the necessity of computing too many values of $\tilde{K}$ on a 2-dimensional grid. At $r_{\min} \approx 0.8$, the lower bound of Eq. (3.92) is roughly equal to $|y|$. Recall that the expression for $\mathcal{K}^{\mathrm{III}}$ given in Eq. (3.83) is valid under the assumption $|y| \leq |x+y| \leq 2|y|$. For the validity of the expression, $r_{\min}$ should be slightly above 0.8. For each pre-computation, we fine-tune $r_{\min}$ until the result shows good consistency.

3.2.4 Result for the integrand for large $|y|$

Having now all the ingredients, we are about to study the $|y|$-integrand of the scalar-meson-exchange contribution to a_μ^{hlbl} with a VMD transition form factor. Note that the form factors can also be conveniently parametrized by the effective coupling between the scalar meson and two photons [Kne+18]

$$\tilde{g}_{S\gamma\gamma} \equiv \mathcal{P}^{\mathrm{VMD}}(0,0)\,, \tag{3.93}$$

and a free parameter

$$\kappa_S \equiv -\frac{2Bm_S^2}{Bm_S^2+2A} = -\frac{m_S^2\mathcal{Q}^{\mathrm{VMD}}(0,0)}{\mathcal{P}^{\mathrm{VMD}}(0,0)}\,. \tag{3.94}$$

We work with fixed effective coupling $\tilde{g}_{S\gamma\gamma} = 0.24\ \text{GeV}^{-1}$. This value is derived from the decay width of $\sigma/f_0(500)$ to two photons [Kne+18].

Due to the power divergence of $i\hat{\Pi}$ in the small-argument region, a cut-off regulator is used. A test for numerical stability of the implementation by varying the cut-off is performed for a scalar meson mass $M_S = 404$ MeV, a VMD vector meson mass of $M_V = 794$ MeV and $\kappa_S = 1$ (Fig. 3.4). In the displayed region, i.e. $|y|/\text{fm} \in [0.5, 2.0]$, the numerical stability of our implementation is acceptable. As the study of the scalar-meson-exchange integrand becomes relevant to the lattice calculation only at large separations, we deem it sufficient to guarantee the consistency of our implementation in this particular window of $|y|$. The numerical x-integration is done with the `hcubature` package. [2]

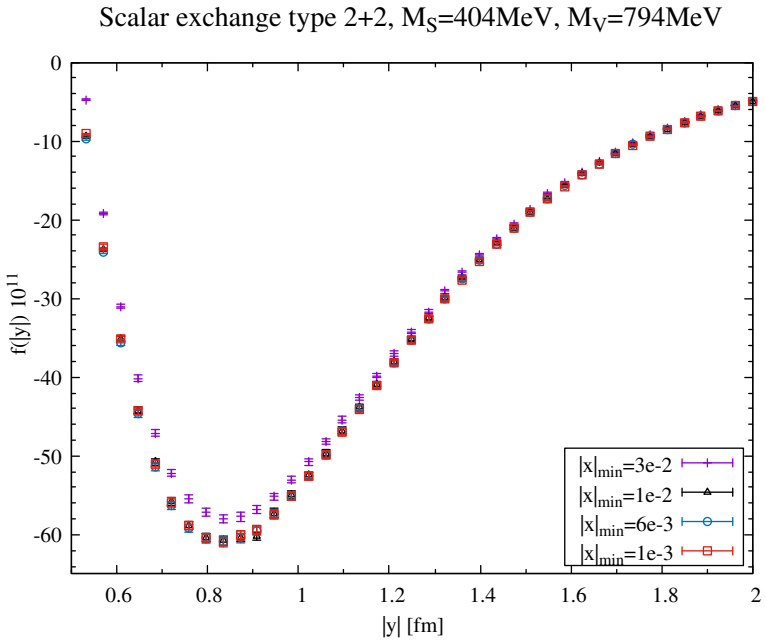

FIGURE 3.4: Test of numerical stability for our implementation of the $|y|$-integrand of the scalar-meson-exchange contribution to a_μ^{hlbl}. $|x|_{\text{min}}$ indicates the cut-off regulator used, in unit of fm.

Fig. 3.5 shows the $|y|$-integrand for a scalar meson mass of $M_S = 482$ MeV and a VMD vector-meson mass of $M_V = 740$ MeV, with 4 different values of κ_S. The mass parameters chosen here are supposed to mimic the lattice ensemble "C101" used in our lattice simulation. This ensemble a pion mass of about 220 MeV. M_S is obtained as the pole mass from a parametrization of the pion mass dependence of the scalar resonance [HPR14] of the *inverse amplitude method* [HPR08], whereas M_V is taken as the VMD mass from a dedicated lattice study of the pion transition form factor with a VMD parametrization [GMN19]. From Fig. 3.5, one can see that the free parameter κ_S can change the magnitude of the integrand quite drastically. Due to the fact that a clear hint on plausible values for κ_S is not really available from the literature to our best knowledge, we are not able to give a reliable estimate of the contribution of the scalar-meson exchange. However, it might be possible to constrain κ_S from comparing the integrand to the lattice result, if one can isolate the scalar meson contribution in the latter properly from the rest. This might be an interesting research direction in the future.

[2] `http://ab-initio.mit.edu/wiki/index.php/Cubature_(Multi-dimensional_integration)`

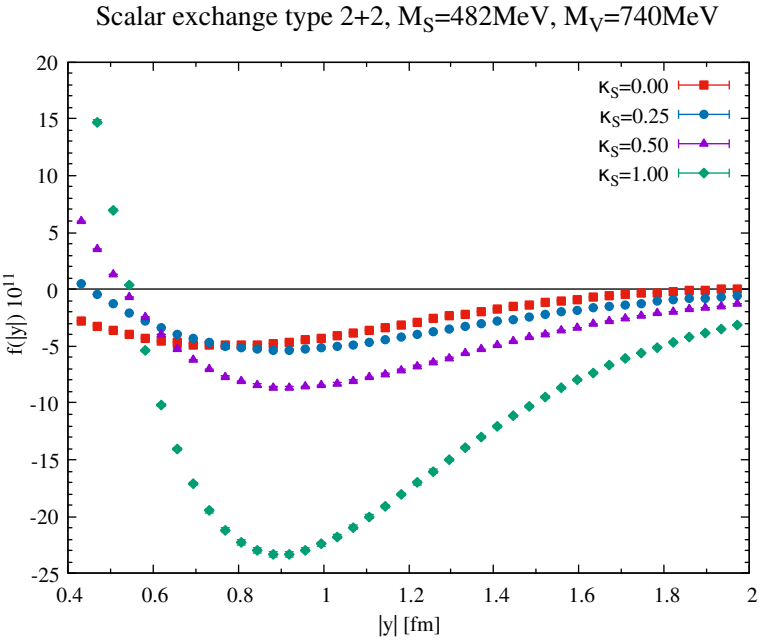

FIGURE 3.5: $|y|$-integrand of the scalar-meson-exchange contribution to a_μ^{hlbl} with $M_S = 482$ MeV and $M_V = 740$ MeV with different values of κ_S.

Chapter 4

Techniques for finite-size-effect correction

Although the position-space method provides a suitable framework for handling the long-ranged QED effects when studying a_μ^{hlbl} on the lattice, the 4-point hadronic correlation function evaluated on the lattice still suffers from finite-size effects (FSEs) coming especially from light mesons. In fact, as we will see in the detailed computations later, the periodic boundary condition in the spatial directions leads to wrap-around effects, i.e. hadronic bound states can go around the lattice and thus introduce other unwanted long-ranged effects to our observable a_μ^{hlbl}. Other than that, the bad signal-to-noise behavior of correlation functions calculated on the lattice at large-distances also makes it difficult to obtain lattice data of good quality in this region. In the study of the leading order contribution of a_μ, coming from the Hadronic Vacuum Polarization (HVP), various groups have shown that FSEs can be significant. In the case of a_μ^{hlbl}, it is believed from Chiral Perturbation theory (ChPT) that the contributions at long distances come principally from the neutral-pseudoscalar-meson exchange (π^0, η, η') and the charged-pseudoscalar-meson loop.[1] In particular, the former, allowed by chiral anomaly, is expected to be the major source of finite-volume effects, because it is the lightest propagating one-particle intermediate state.

In the case of (anti-)periodic spatial boundary condition[2], the FSEs can be easily estimated from finite-volume QFT. In this chapter, we will introduce the necessary mathematical tools for this purpose. We will apply these techniques to two examples: the first being the contribution to a_μ^{hlbl} of a lepton loop, and the second being that of a charged-meson loop. Note that these examples are only meant to illustrate how such a calculation can be done. For our lattice study [Cha+20] presented in Sect. 6.3 where we apply a FSE correction scheme, only the π^0-exchange model with a VMD TFF is used, due to the fact that it is the numerically dominant one at the considered pion mass and that we have a reasonable parametrization for the form factor. Nonetheless, it is not difficult to apply the techniques introduced in this chapter to the case of the π^0-exchange.

Like previously, the expressions are given in Euclidean space-time, if not specified. The calculations performed in this chapter are done in the continuum. Analogous to the previous chapter, we use the tensor structure to represent a_μ^{hlbl} as a 1-dimensional integral in $|y|$.[3] The semi-analytical approach that we are going to present consists in computing the z-integral analytically and treating the x-integral

[1] c.f. Sect. 1.2.

[2] By this, we refer to the situation where the spatial directions are periodic and the temporal direction is periodic/anti-periodic to account for the Bose/Fermi symmetry of the matter field.

[3] c.f. Eq. (3.15).

numerically to get the integrand for a given y-vector. The numerical x-integrations are done with the `hcubature` package, as is the case in Sect. 3.2.4.

When it comes to an x-integral, the 4-dimensional integration region is restricted to the finite box

$$\mathbb{B} = \left[-\frac{L_0}{2}, \frac{L_0}{2}\right] \times \left[-\frac{L_1}{2}, \frac{L_1}{2}\right] \times \left[-\frac{L_2}{2}, \frac{L_2}{2}\right] \times \left[-\frac{L_3}{2}, \frac{L_3}{2}\right], \tag{4.1}$$

with equal sides $L_0 = L_1 = L_2 = L_3 = L$ for simplicity.

Define the torus $\mathbb{T}$ as

$$\mathbb{T} = [0, L_0] \times [0, L_1] \times [0, L_2] \times [0, L_3]. \tag{4.2}$$

By assuming periodic boundary condition, we identify $\mathbb{T}$ to the equivalence class of the (continuum) lattice $(\mathbb{R}/L_0\mathbb{Z}) \times (\mathbb{R}/L_1\mathbb{Z}) \times (\mathbb{R}/L_2\mathbb{Z}) \times (\mathbb{R}/L_3\mathbb{Z})$.

Finally, we use the following mapping between lattice coordinates P and the real-world coordinates p

$$[p_\rho] = \begin{cases} P_\rho, & \text{if } P_\rho < L_\rho/2, \\ P_\rho - L_\rho, & \text{else.} \end{cases} \tag{4.3}$$

4.1 Finite-size effects from a lepton loop

Due to the similarity between the lepton loop and the charged-pion-loop 4-point function in their structures, it is instructive to start with the lepton loop case because it can be computed on the lattice by turning off the gauge field (up to discretization effects).

The fermion propagator with fermion mass m in position-space is given by

$$\begin{aligned} S(x,y) \equiv& \int \frac{d^4p}{(2\pi)^4} e^{ip(x-y)} \frac{-i\not{p} + m}{p^2 + m^2} \\ =& \frac{m^2}{4\pi^2|x|}\left[\gamma_\mu (x-y)_\mu \frac{K_2(m|x-y|)}{|x-y|} + K_1(m|x-y|)\right]. \end{aligned} \tag{4.4}$$

And the complete 4-point current correlation function is given by, up to one-loop,

$$\begin{aligned} &\langle j_\mu(x) j_\nu(y) j_\sigma(z) j_\lambda(0)\rangle \\ =& -2\Re\Big(I^{(1)}_{\mu\nu\sigma\lambda}(x,y,z,0) + I^{(2)}_{\mu\nu\sigma\lambda}(x,y,z,0) + I^{(3)}_{\mu\nu\sigma\lambda}(x,y,z,0)\Big), \end{aligned} \tag{4.5}$$

where

$$\begin{aligned} I^{(1)}_{\mu\nu\sigma\lambda}(x,y,z,w) &= \mathrm{Tr}[\gamma_\mu S(x,y)\gamma_\nu S(y,z)\gamma_\sigma S(z,w)\gamma_\lambda S(w,x)], \\ I^{(2)}_{\mu\nu\sigma\lambda}(x,y,z,w) &= I^{(1)}_{\mu\nu\lambda\sigma}(x,y,w,z), \\ I^{(3)}_{\mu\nu\sigma\lambda}(x,y,z,w) &= I^{(1)}_{\lambda\nu\sigma\mu}(w,y,z,x). \end{aligned} \tag{4.6}$$

The coordinate w will be set to 0 at the end. For the interest of our computation, we will keep it as a free variable and set it to 0 only at the very end.

For the purpose of this study, we will consider the following representation for a_μ^{hlbl}, which can be obtained after a re-parametrization of the integrand in infinite-volume using translational invariance of the current 4-point functions Eq. (4.6) and

a change of variables,[4]

$$a_\mu^{\text{hlbl,lep.-loop}} = \int_{|y|} f^{\text{hlbl,lep.-loop}}(|y|)\,, \tag{4.7}$$

where

$$\begin{aligned} &f^{\text{hlbl,lep.-loop}}(|y|) \\ &\equiv \frac{me^6}{3} 2\pi^2 |y|^3 \int_x \left[\int_z \mathcal{L}'_{[\rho,\sigma]\mu\nu\lambda} z_\rho I^{(1)}_{\mu\nu\sigma\lambda}(x,y,z,0) + \int_z x_\rho \mathcal{L}_{[\rho,\sigma]\lambda\nu\mu}(x,x-y) I^{(1)}_{\mu\nu\sigma\lambda}(x,y,z,0) \right], \end{aligned} \tag{4.8}$$

$$\mathcal{L}'_{[\rho,\sigma]\mu\nu\lambda}(x,y) \equiv \mathcal{L}_{[\rho,\sigma]\mu\nu\lambda}(x,y) + \mathcal{L}_{[\rho,\sigma]\nu\mu\lambda}(y,x) - \mathcal{L}_{[\rho,\sigma]\lambda\nu\mu}(x,x-y)\,. \tag{4.9}$$

To evaluate the finite-size effects from a lepton loop, we have to not only replace the infinite-volume position-space propagator S by their expression in finite-volume S^{L}, but also truncate the x, y and z-integrals according to the size of the lattice. It should be noted that the way that a_μ^{hlbl} is represented actually matters in this case. As we will see latter in our lattice calculation setup in Sect. 6.2, this choice here corresponds to the "Method 2" representation Eq. (6.24) that we adopt for the fully-connected Wick-contraction topology of the QCD 4-point function, which has a big computational advantage over evaluating the complete 4-point function Eq. (4.5) and contracting with the QED-kernel directly.[5]

Position-space propagator on a torus

In finite-volume with periodic boundary condition, the allowed momenta are quantized. To get the position-space expression, one starts from the propagator in momentum-space and perform an inverse discrete Fourier transform on the spectrum of allowed momenta. From the Poisson summation formula in 1-dimension

$$\sum_{n\in\mathbb{Z}} f(x+nL) = \sum_{k\in\frac{2\pi}{L}\mathbb{Z}} \frac{1}{L} \tilde{f}(k) e^{ikx}\,, \tag{4.10}$$

where $\tilde{f}$ is the infinite-volume Fourier transform of f, we deduce that the expression of the propagator on the torus $\mathbb{T}$ Eq. (4.2) is given by

$$S^{\mathrm{L}}(x,y) = \sum_{n\in\mathbb{Z}^4} S(x^{[n]},y)\,, \quad x^{[n]} \equiv x + \mathrm{diag}(n_0,n_1,n_2,n_3)\mathbf{L}\,, \quad \mathbf{L} \equiv (L_0,L_1,L_2,L_3)^\intercal\,. \tag{4.11}$$

One can understand this result as wrapping the propagator around the world. We will refer the term $S(x^{[n]},y)$ in the summand on the right-hand side as the *winding* of winding number n. Note that this result can be generalized to any anisotropic torus by changing L to the length of the side of the torus in which a winding is introduced. If one is to impose anti-periodic in one or several directions, similar expressions will be obtained. This aspect is discussed in Appendix D.4. In the following, we will assume periodic boundary condition in all directions and work with an isotropic torus with $\mathbf{L} = (L,L,L,L)$ for simplicity. Of course, one has to modify the expressions that we give in the end to their anti-periodic counterpart because of the spin-statistics of the lepton.

[4] c.f. the operations introduced in the beginning of Sect. 3.2 to get Eq. (3.31).

[5] Which corresponds to the "Method 1" representation Eq. (6.19) for the fully-connected topology in our lattice calculation discussed in Sect. 6.2.

Treatment of the weight factor z_ρ

The coordinate fixing procedure Eq. (4.3) is motivated by the fact that the matching of $(0,0,0,0)$ to the point (L_0, L_1, L_2, L_3) on the torus $\mathbb{T}$ allows us to treat the z_ρ-weighted function as a periodic function in z on the torus. This is convenient because we can then use discrete Fourier transform to compute the first term of Eq. (4.8) on the torus $\mathbb{T}$ instead of on $\mathbb{B}$. However, as we will see, the jump that we introduce for the coordinate-fixing requires further care. On the other hand, the z-integrand of the second term of Eq. (4.8) is already periodic in its arguments. The second term will be discussed in the end of this section after a long discussion on the first term.

4.1.1 The first term in the brackets of Eq. (4.8)

Define

$$F_{\rho\sigma}(y,w) = \int d^4z [z_\rho] S^{\mathrm{L}}(y,z)\gamma_\sigma S^{\mathrm{L}}(z,w)\,. \tag{4.12}$$

On the torus, the first term in the brackets of Eq. (4.8) can then be written as

$$\int_z d^4z z_\rho I^{(1)}_{\mu\nu\sigma\lambda}(x,y,z,0) = \mathrm{Tr}\Big[\gamma_\mu S^{\mathrm{L}}(x,y)\gamma_\nu F_{\rho\sigma}(y,0)\gamma_\lambda S^{\mathrm{L}}(0,x)\Big]\,. \tag{4.13}$$

Using the Poisson summation formula, we express F with the Fourier transform of the propagator in infinite-volume, $\tilde{S}$:

$$F_{\rho\sigma}(y,w) = \frac{1}{L^8}\sum_{p,q\in\left(\frac{2\pi}{L}\mathbb{Z}\right)^4} \int d^4z [z_\rho]\tilde{S}(q)\gamma_\sigma\tilde{S}(p)e^{i(p-q)z+iqy-ipw}\,. \tag{4.14}$$

After some algebras, one can show that, in 1-dimension,

$$\int_{u=0}^{L}[u]f(u) = -i\sum_{q\in\frac{2\pi}{L}\mathbb{Z}^*}\frac{\hat{f}(q)}{q}\cos(\frac{qL}{2})\,, \tag{4.15}$$

where $\hat{f}$ is the discrete (finite-volume) Fourier transform of a L-periodic function $f:[0,L]\to\mathbb{R}$:

$$\hat{f}(q) = \frac{1}{L}\int_{u=0}^{L} e^{-iqu}f(u)\,. \tag{4.16}$$

This leads to

$$\begin{aligned}\int_z [z_\rho]e^{i(p-q)z} &= -i\int d^3z_\perp [z_\rho]e^{i(p-q)_\perp z_\perp}\frac{L_\rho}{(p-q)_\rho}\cos\left(\frac{(p-q)_\rho L_\rho}{2}\right)\\ &= -iL^3\delta_{(p-q)_\perp,\vec{0}}\frac{L_\rho}{(p-q)_\rho}\cos\left(\frac{(p-q)_\rho L_\rho}{2}\right)\,,\end{aligned} \tag{4.17}$$

where $\perp$ is used to indicate all directions other than ρ. Note that the case where $(p-q)_\rho = 0$ is excluded above and there is no summation over ρ. Eq. (4.14) can thus be simplified to

$$F_{\rho\sigma}(y,w) = -\frac{i}{L^4}\sum_{\substack{p_\rho\in\frac{2\pi}{L}\mathbb{Z}^*\\ q\in(\frac{2\pi}{L}\mathbb{Z})^4}}\frac{1}{p_\rho}\cos(\frac{p_\rho L_\rho}{2})\tilde{S}(q)\gamma_\sigma\tilde{S}(p_\rho\hat{\rho}+q)e^{iq(y-w)-ip_\rho w_\rho}\,, \tag{4.18}$$

where $\hat{\rho}$ is the unit vector in the ρ-direction.

Plugging in the expression of the propagator in momentum-space, we have the relation

$$\begin{aligned}
&\tilde{S}(q)\gamma_\sigma\tilde{S}(p_\rho\hat{\rho}+q)\\
=&-\Big\{\frac{q_\alpha(p_\rho+q_\rho)}{(q^2+m^2)[(p_\rho+q_\rho)^2+q_\perp^2+m^2]}\gamma_\alpha\gamma_\sigma\gamma_\rho\\
&+\frac{q_\alpha q_\beta}{(q^2+m^2)[(p_\rho+q_\rho)^2+q_\perp^2+m^2]}\gamma_\alpha\gamma_\sigma\gamma_\beta\\
&+\frac{iq_\alpha m}{(q^2+m^2)[(p_\rho+q_\rho)^2+q_\perp^2+m^2]}\gamma_\alpha\gamma_\sigma\\
&+\frac{i(p+q_\rho)m}{(q^2+m^2)[(p_\rho+q_\rho)^2+q_\perp^2+m^2]}\gamma_\sigma\gamma_\rho\\
&+\frac{iq_\beta m}{(q^2+m^2)[(p_\rho+q_\rho)^2+q_\perp^2+m^2]}\gamma_\sigma\gamma_\beta\\
&-\frac{m^2}{(q^2+m^2)[(p_\rho+q_\rho)^2+q_\perp^2+m^2]}\gamma_\sigma\Big\}\,.
\end{aligned}\tag{4.19}$$

where the Einstein summation is applied to

$$\alpha\in\{0,1,2,3\}\,,\quad \beta\in E_\rho\equiv\{0,1,2,3\}\setminus\{\rho\}\,,\tag{4.20}$$

and

$$q_\perp^2\equiv\sum_{\lambda\in E_\rho}q_\lambda^2\,.\tag{4.21}$$

To compute Eq. (4.18), we note that, for a function $f:\mathbb{R}\to\mathbb{R}$ differentiable at 0,

$$\sum_{p\in\frac{2\pi}{L}\mathbb{Z}^*}\frac{f(p)}{p}\cos\frac{pL}{2}=\sum_{p\in\frac{2\pi}{L}\mathbb{Z}}g(p)e^{\frac{ipL}{2}}-f'(0)\,,\quad g(p)\equiv\begin{cases}\frac{f(p)-f(-p)}{2p} & \text{if } p\neq 0\,,\\ f'(0) & \text{if } p=0\,.\end{cases}\tag{4.22}$$

Applying this equation and the Poisson summation formula Eq. (4.10), we get the following relation which is useful for Eq. (4.18)

$$\begin{aligned}
H(y,w;\rho)\equiv&-\frac{1}{L^4}\sum_{\substack{p_\rho\in\frac{2\pi}{L}\mathbb{Z}^*\\ q\in(\frac{2\pi}{L}\mathbb{Z})^4}}\frac{1}{p_\rho}s_m(q,p_\rho\hat{\rho}+q)\cos\frac{p_\rho L_\rho}{2}e^{iq(y-w)-ip_\rho w_\rho}\\
=&-\frac{L_\rho}{2}\sum_{\substack{n\in\mathbb{Z}^4\\ l\in\mathbb{Z}}}\Big[\int_{\substack{q\in\mathbb{R}^4\\ p_\rho\in\mathbb{R}}}\frac{d^4q}{(2\pi)^4}\frac{dp_\rho}{2\pi}\frac{e^{iq(y-w)^{[n]}}}{p_\rho}\\
&\times\Big(s_m(q,p_\rho\hat{\rho}+q)e^{-ip_\rho(w_\rho^{[l]}-\frac{L_\rho}{2})}-s_m(q,-p_\rho\hat{\rho}+q)e^{ip_\rho(w_\rho^{[l]}-\frac{L_\rho}{2})}\Big)\Big]\\
&+\sum_{n\in\mathbb{Z}^4}\int_q\frac{d^4q}{(2\pi)^4}e^{iq(y-w)^{[n]}}\left[\frac{d}{dp_\rho}\Big(s_m(q,p_\rho\hat{\rho}+q)e^{-ip_\rho w_\rho}\Big)\right]_{p_\rho=0}\,,
\end{aligned}\tag{4.23}$$

where

$$s_m(u,v)\equiv\frac{1}{(u^2+m^2)(v^2+m^2)}\,,\tag{4.24}$$

and a re-parametrization of the winding number l is implicitly used.

The p_ρ-integral of the first term in the summand of Eq. (4.23) can be computed

via Cauchy's residue theorem. One has to choose carefully the integration contour in the complex plane in order to have a well-defined integral. Let us illustrate this with the first term in the first bracket on the right-hand side of Eq. (4.23) by writing it as $\frac{f(p_\rho)}{p_\rho}$. For the case where $\frac{L_\rho}{2} - w_\rho^{[l]} > 0$, we can consider the contour $\mathcal{C}_+$ depicted in Fig. 4.1. Then, in the limit $R \to \infty$, the integrand will converge to zero along the outer arc due to the exponential fall-off and we have

$$2\pi i \mathrm{Res}_{\mathrm{poles}} \frac{f(p_\rho)}{p_\rho} = \left(\int_{-\infty}^{-\epsilon} + \int_{\epsilon}^{\infty} \right) \frac{f(p_\rho)}{p_\rho} + \int_{\theta=\pi}^{2\pi} f(\epsilon e^{i\theta}) i d\theta \,. \tag{4.25}$$

For the case where $\frac{L_\rho}{2} - w_\rho^{[l]} < 0$, the calculation is similar but we have to flip the contour $\mathcal{C}_+$ and the orientation to obtain a well-defined integral. We call this flipped contour $\mathcal{C}_-$. To accomplish the calculation, we will have to take the $\epsilon \to 0$ limit in Eq. (4.25). It is clear that the first term on the right-hand side will become the integral that we want to compute. Obviously, if we are in the case where the contour $\mathcal{C}_+$ is considered for the first quantity in the first bracket, then $\mathcal{C}_-$ has to be used for the second one, and vice versa.

On the other hand, the last line on the right-hand side of Eq. (4.23) can be expressed in a rather straightforward way in terms of derivatives of a massive scalar propagator on the torus

$$G_m^{\mathrm{L}}(x) = \sum_{n \in \mathbb{Z}^4} \int_{q \in \mathbb{R}^4} \frac{d^4q}{(2\pi)^4} \frac{e^{iqx^{[n]}}}{q^2 + m^2} \,, \tag{4.26}$$

with regard to the mass-squared, which leads Eq. (4.23) to

$$\begin{aligned} H(y,w;\rho) =& - i w_\rho \partial_{m^2} G_m^{\mathrm{L}}(y-w) - i \partial_{y_\rho} \partial_{m^2}^2 G_m^{\mathrm{L}}(y-w) + I(y,w) \\ =& i \sum_{n \in \mathbb{Z}^4} \frac{y_\rho^{[n]} + w_\rho}{16\pi^2} K_0(m|(y-w)^{[n]}|) + I(y,w;\rho) \,, \end{aligned} \tag{4.27}$$

where

$$I(y,w;\rho) \equiv \frac{L_\rho}{2} \sum_{\substack{n \in \mathbb{Z}^4 \\ l \in \mathbb{Z}}} \int_{q \in \mathbb{R}^4} \frac{d^4q}{(2\pi)^4} \frac{e^{iq(y-w)^{[n]} + iq_\rho (w_\rho^{[l]} - \frac{L_\rho}{2}) - \sqrt{q_\perp^2 + m^2} |w_\rho^{[l]} - \frac{L_\rho}{2}|}}{(q^2 + m^2)\sqrt{q_\perp^2 + m^2}[q_\rho + i \mathrm{sgn}(w_\rho^{[l]} - \frac{L_\rho}{2})\sqrt{q_\perp^2 + m^2}]} \,. \tag{4.28}$$

Simplification of Eq. (4.28)

Let $n \in \mathbb{Z}^4$ and $l \in \mathbb{Z}$.

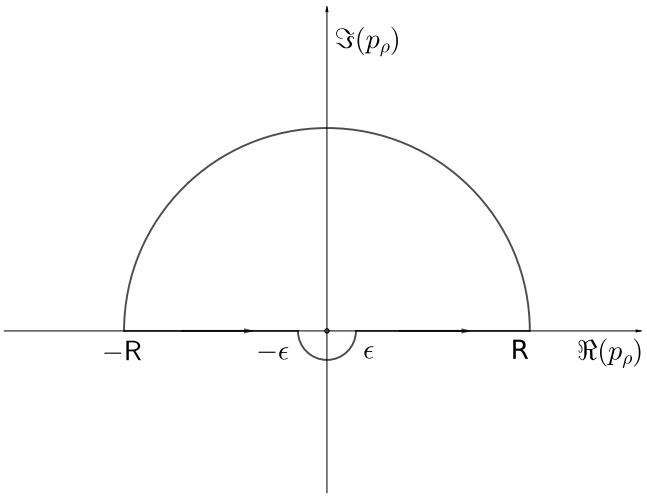

FIGURE 4.1: The p_ρ-integration contour $\mathcal{C}_+$.

Note that

$$\begin{aligned}
&\int \frac{dq_\rho}{2\pi} \frac{\exp\left[iq(y-w)^{[n]} + iq_\rho(w_\rho^{[l]} - \frac{L_\rho}{2}) - \sqrt{q_\perp^2+m^2}|w_\rho^{[l]} - \frac{L_\rho}{2}|\right]}{(q^2+m^2)\sqrt{q_\perp^2+m^2}\left[q_\rho + i\mathrm{sgn}(w_\rho^{[l]} - \frac{L_\rho}{2})\sqrt{q_\perp^2+m^2}\right]} \\
&= \int \frac{dq_\rho}{2\pi} \frac{\exp\left[iq_\perp(y-w)_\perp^{[n]} + iq_\rho(y_\rho^{[n_\rho+l]} - \frac{L_\rho}{2}) - \sqrt{q_\perp^2+m^2}|w_\rho^{[l]} - \frac{L_\rho}{2}|\right]}{(q^2+m^2)\sqrt{q_\perp^2+m^2}\left[q_\rho + i\mathrm{sgn}(w_\rho^{[l]} - \frac{L_\rho}{2})\sqrt{q_\perp^2+m^2}\right]} \\
&= \begin{cases} -i\mathfrak{s}\frac{\exp\left[iq_\perp(y-w)_\perp^{[n]} - \sqrt{q_\perp^2+m^2}\left(|y_\rho^{[n_\rho+l]} - \frac{L_\rho}{2}| + |w_\rho^{[l]} - \frac{L_\rho}{2}|\right)\right]}{4(q_\perp^2+m^2)^{\frac{3}{2}}}, & \text{if } \mathfrak{s} = \mathrm{sgn}(w_\rho^{[l]} - \frac{L_\rho}{2}), \\ i\mathfrak{s}\frac{\left(2|y_\rho - \frac{L_\rho}{2}|^{[n_\rho+l]}\sqrt{q_\perp^2+m^2}+1\right)\exp\left[iq_\perp(y-w)_\perp^{[n]} - \sqrt{q_\perp^2+m^2}\left(|y_\rho^{[n_\rho+l]} - \frac{L_\rho}{2}| + |w_\rho^{[l]} - \frac{L_\rho}{2}|\right)\right]}{4(q_\perp^2+m^2)^{\frac{3}{2}}}, & \text{else}, \end{cases}
\end{aligned} \tag{4.29}$$

where $\perp$ indicates the projection of a vector to the hyper-surface normal to ρ and

$$\mathfrak{s} \equiv \mathrm{sgn}\Big((y_\rho - \frac{L_\rho}{2})^{[n_\rho+l]}\Big). \tag{4.30}$$

This allows us to write $I(y,w,\rho)$ in the following form:

$$\begin{aligned}
I(y,w;\rho) =& \frac{L_\rho}{2}\sum_j K_j \int \frac{d^3q_\perp}{(2\pi)^3} \frac{e^{iq_\perp\cdot(y-w)_\perp^{[n]}} \exp\left(-\sqrt{q_\perp^2+m^2}[|y_\rho^{[n_\rho+l]} - \frac{L_\rho}{2}| + |w_\rho^{[l]} - \frac{L_\rho}{2}|]\right)}{(q_\perp^2+m^2)^{\alpha_j}} \\
=& -\frac{L_\rho}{2}\sum_j K_j \int_0^\infty \frac{du}{2\pi^2} \frac{u\sin\left[u|(y-w)_\perp|\right]}{|(y-w)_\perp^{[n]}|(u^2+q_\rho^2+m^2)^{\alpha_j}} \\
&\times \exp\Big[-\sqrt{u^2+m^2}\Big(|y_\rho^{[n_\rho+l]} - \frac{L_\rho}{2}| + |w_\rho^{[l]} - \frac{L_\rho}{2}|\Big)\Big],
\end{aligned} \tag{4.31}$$

where the coefficient K_j and the exponent α_j depend on y_ρ and w_ρ as given above.

We define

$$\begin{aligned}
J_\alpha(a,b) &= \int_0^\infty dq \frac{q\sin(aq)}{(q^2+m^2)^{\alpha+\frac{1}{2}}} \exp\big(-b\sqrt{q^2+m^2}\big) \\
&\underbrace{=}_{y=\frac{1}{\sqrt{q^2+m^2}}} \Im\Big\{\int_0^{\frac{1}{m}} dy y^{2(\alpha-1)} \exp\big(ia\sqrt{y^{-2}-m^2}-by\big)\Big\} \\
&\underbrace{=}_{u=\frac{1}{y}} \Im\Big\{\int_m^\infty du u^{-2\alpha} \exp\big(ia\sqrt{u^2-m^2}-bu\big)\Big\} \\
&\underbrace{=}_{u=m\cosh t} \Im\Big\{\int_0^\infty m^{-2\alpha+1}\sinh t(\cosh t)^{-2\alpha}\exp\big(-m\sqrt{a^2+b^2}\cosh(t+i\beta)\big)\Big\},
\end{aligned} \tag{4.32}$$

where

$$\beta \equiv \arctan\frac{a}{b}. \tag{4.33}$$

Let us start with $\alpha = 0$. We have

$$\begin{aligned}
&J_0(a,b) \\
=&\Im\Big\{m\int_0^\infty dt \sinh t \exp\big(-k\cosh(t+i\beta)\big)\Big\} \\
=&\Im\Big\{m\int_{i\beta}^{+\infty+i\beta} dt \sinh(t-i\beta)\exp(-k\cosh t)\Big\} \\
=&\Im\Big\{m\Big(\int_0^\infty dt\sinh t\cos\beta\exp(-k\cosh t) + i\int_0^\infty dt\sin\beta\cosh t\exp(-k\cosh t) \\
&-\int_0^\beta dt\cos\beta\sin t\exp(-k\cos t) + \int_0^\beta dt\sin\beta\cos t\exp(-k\cos t)\Big)\Big\},
\end{aligned} \tag{4.34}$$

where

$$k = m\sqrt{a^2+b^2}. \tag{4.35}$$

Recall the following relations for the modified Bessel function [Nis, Eq. (10.32.8) and Eq. (10.32.9)]

$$K_\nu(z) = \frac{\pi^{\frac{1}{2}}(\frac{1}{2}z)^\nu}{\Gamma(\nu+\frac{1}{2})}\int_0^\infty dt e^{-z\cosh t}(\sinh t)^{2\nu}, \tag{4.36}$$

$$K_\nu(z) = \int_0^\infty dt e^{-z\cosh t}\cosh(\nu t). \tag{4.37}$$

We get thus

$$J_0 = m\sin\beta K_1(k). \tag{4.38}$$

From the first line of Eq. (4.32), we have the following recurrence relations

$$\frac{\partial}{\partial b}J_{\alpha+\frac{1}{2}} = -J_\alpha, \tag{4.39}$$

$$\frac{\partial}{\partial m^2}J_\alpha = -(\alpha+\frac{1}{2})J_{\alpha+1} - \frac{1}{2}bJ_{\alpha+\frac{1}{2}}, \tag{4.40}$$

$$\partial_a^2 J_\alpha = -J_{\alpha-1} + m^2 J_\alpha. \tag{4.41}$$

Hence

$$J_{\frac{1}{2}}(a,b) = \int_{t_0}^{\infty} dt ma K_1(ma\cosh t)\,, \tag{4.42}$$

where t_0 is such that

$$b = a\sinh t_0\,. \tag{4.43}$$

Then, using [Nis, Eq. (10.32.17)]

$$K_\mu(z)K_\nu(z) = 2\int_0^{\infty} dt K_{\mu\pm\nu}(2z\cosh t)\cosh((\mu\mp\nu)t)\,, \tag{4.44}$$

we have

$$J_{\frac{1}{2}} = \frac{1}{2}maK_{\frac{1}{2}}^2(\frac{ma}{2}) - ma\int_0^{t_0} dt K_1(ma\cosh t)\,, \tag{4.45}$$

$$J_1 = -bJ_{\frac{1}{2}} - 2\frac{\partial J_0}{\partial m^2} = -bJ_{\frac{1}{2}} + aK_0(k)\,. \tag{4.46}$$

Combining everything together, we get the following analytic expression for I defined in Eq. (4.28)

$$\begin{aligned} &I(y,w;\rho) \\ &= \begin{cases} -i\mathfrak{s}\frac{L_\rho}{16\pi^2 a}J_1(a,b)\Big|_{a=|(y-w)_\perp^{[n]}|,b=|(y+w-L)_\rho^{[n_\rho+2l]}|}\,, & \text{if } \mathfrak{s} = \operatorname{sgn}(w_\rho^{[l]} - \frac{L_\rho}{2})\,, \\ i\mathfrak{s}\frac{L_\rho}{16\pi^2 a}\Big(2|(y_\rho - \frac{L_\rho}{2})^{[n_\rho+l]}|J_{\frac{1}{2}}(a,b) + J_1(a,b)\Big)\Big|_{a=|(y-w)_\perp^{[n]}|,b=|(y-w)_\rho^{[n_\rho]}|}\,, & \text{else}\,. \end{cases} \end{aligned} \tag{4.47}$$

A list of relevant derivatives of the functions J_α is given in Appendix D.1 and the numerical implementation for the expensive part of the computation is described in Appendix D.2.

The final expression

Finally, after treating the spinor decomposition Eq. (4.19) properly, we arrive at the following expression for Eq. (4.13)

$$
\begin{aligned}
&\int_z d^4z z_\rho I^{(1)}_{\mu\nu\sigma\lambda}(x,y,z,0)\\
=&\sum_{r,s\in\mathbb{Z}^4}\Big(\frac{m^2}{4\pi^2}\Big)^2\frac{1}{|(x-y)^{[r]}|}\frac{1}{|(-x)^{[s]}|}\\
&\mathrm{Tr}\Big\{\gamma_\mu\Big[\frac{K_2(m|(x-y)^{[r]}|)}{|(x-y)^{[r]}|}(x-y)^{[r]}_\beta\gamma_\beta+K_1(m|(x-y)^{[r]}|)\Big]\gamma_\nu F_{\rho\sigma}(y,0)\gamma_\lambda\\
&\times\Big[\frac{K_2(m|(-x)^{[s]}|)}{|(-x)^{[s]}|}(-x)^{[s]}_\gamma\gamma_\gamma+K_1(m|(-x)^{[s]}|)\Big]\Big\}\\
=&i\sum_{r,s}\Big(\frac{m^2}{4\pi^2}\Big)^2\frac{1}{|(x-y)^{[r]}|}\frac{1}{|(-x)^{[s]}|}\Big\{\frac{K_2(m|(x-y)^{[r]}|)K_2(m|(-x)^{[s]}|)}{|(x-y)^{[r]}||(-x)^{[s]}|}(x-y)^{[r]}_\beta(-x)^{[s]}_\gamma\\
&\times\Big(C^{1;\rho}_\alpha\mathrm{Tr}[\gamma_\mu\gamma_\beta\gamma_\nu\gamma_\alpha\gamma_\sigma\gamma_\rho\gamma_\lambda\gamma_\gamma]+C^{2;\rho}_{\alpha\delta}\mathrm{Tr}[\gamma_\mu\gamma_\beta\gamma_\nu\gamma_\alpha\gamma_\sigma\gamma_\delta\gamma_\lambda\gamma_\gamma]+C^{6;\rho}\mathrm{Tr}[\gamma_\mu\gamma_\beta\gamma_\nu\gamma_\sigma\gamma_\lambda\gamma_\gamma]\Big)\\
&+\frac{K_2(m|(x-y)^{[r]}|)K_1(m|(-x)^{[s]}|)}{|(x-y)^{[r]}|}(x-y)^{[r]}_\beta\\
&\times\Big(C^{3;\rho}_\alpha\mathrm{Tr}[\gamma_\mu\gamma_\beta\gamma_\nu\gamma_\alpha\gamma_\sigma\gamma_\lambda]+C^{4;\rho}\mathrm{Tr}[\gamma_\mu\gamma_\beta\gamma_\nu\gamma_\sigma\gamma_\rho\gamma_\lambda]+C^{5;\rho}_\delta\mathrm{Tr}[\gamma_\mu\gamma_\beta\gamma_\nu\gamma_\sigma\gamma_\delta\gamma_\lambda]\Big)\\
&+\frac{K_1(m|(x-y)^{[r]}|)K_2(m|(-x)^{(s)}|)}{|(-x)^{(s)}|}(-x)^{[s]}_\gamma\\
&\times\Big(C^{3;\rho}_\alpha\mathrm{Tr}[\gamma_\mu\gamma_\nu\gamma_\alpha\gamma_\sigma\gamma_\lambda\gamma_\gamma]+C^{4;\rho}\mathrm{Tr}[\gamma_\mu\gamma_\nu\gamma_\sigma\gamma_\rho\gamma_\lambda\gamma_\gamma]+C^{5;\rho}_\delta\mathrm{Tr}[\gamma_\mu\gamma_\nu\gamma_\sigma\gamma_\delta\gamma_\lambda\gamma_\gamma]\Big)\\
&+K_1(m|(x-y)^{[r]}|)K_1(m|(-x)^{[s]}|)\\
&\times\Big(C^{1;\rho}_\alpha\mathrm{Tr}[\gamma_\mu\gamma_\nu\gamma_\alpha\gamma_\sigma\gamma_\rho\gamma_\lambda]+C^{2;\rho}_{\alpha\delta}\mathrm{Tr}[\gamma_\mu\gamma_\nu\gamma_\alpha\gamma_\sigma\gamma_\delta\gamma_\lambda]+C^{6;\rho}_\alpha\mathrm{Tr}[\gamma_\mu\gamma_\nu\gamma_\sigma\gamma_\lambda]\Big)\Big\}\,,
\end{aligned}
\tag{4.48}
$$

where the Einstein summation is applied to $\alpha,\beta,\gamma\in\{0,1,2,3\}$ and $\delta\in E_\rho$ and the y-dependent coefficients are defined by

$$
\begin{aligned}
C^{1;\rho}_\alpha&=\partial_{y_\alpha}\partial_{w_\rho}H(y,w=0;\rho)\,,\\
C^{2;\rho}_{\alpha\beta}&=-\partial_{y_\alpha}\partial_{y_\beta}H(y,w=0;\rho)\,,\\
C^{3;\rho}_\alpha&=m\partial_{y_\alpha}H(y,w=0;\rho)\,,\\
C^{4;\rho}&=-m\partial_{w_\rho}H(y,w=0;\rho)\,,\\
C^{5;\rho}_\beta&=m\partial_{y_\beta}H(y,w=0;\rho)\,,\\
C^{6;\rho}&=-m^2H(y,w=0;\rho)\,.
\end{aligned}
\tag{4.49}
$$

The expressions for the C_i's are given in Appendix D.3. Note that from the expression of H given in Eq. (4.27), one can separate the finite-size effects into two categories: the first, corresponding to the first term in the last line of Eq. (4.27), coming from the addition of the "windings" of the infinite-volume result, and the second coming from the jump introduced for the weight factor z_ρ. We call the first category "usual" and the second "additional". It can be shown easily that the additional part vanishes in the infinite-volume limit. In practice, due to the typical size of the boxes

and the rapid exponential decay of the modified Bessel functions of the second kind, we only include the windings which stay in the hypercube $\mathbb{B}$.

4.1.2 The second term in the brackets of Eq. (4.8)

The z-integral that we want to compute is

$$N_{\mu\nu\sigma\lambda}(x,y) \equiv \int d^4z I^{(1)}_{\mu\nu\sigma\lambda}(x,y,z,0) = \mathrm{Tr}\Big[\gamma_\mu S^L(x,y)\gamma_\nu M_\sigma(y)\gamma_\lambda S^L(0,x)\Big]\,, \tag{4.50}$$

where

$$M_\sigma(y) \equiv \int d^4z S^L(y,z)\gamma_\sigma S^L(z,0) = \frac{1}{L^8}\sum_{p,q\in(\frac{2\pi}{L}\mathbb{Z})^4}\int d^4z\tilde{S}(q)\gamma_\sigma\tilde{S}(p)e^{i(p-q)z+iqy}\,. \tag{4.51}$$

With a similar calculation using the Poisson summation formula, we end up with

$$M_\sigma = -\sum_{n\in\mathbb{Z}^4}\mathfrak{D}_\sigma\partial_{m^2}G_m(y^{[n]})\,, \tag{4.52}$$

where the operator $\mathfrak{D}$ is defined as

$$\mathfrak{D}_\sigma = (-\not{\partial}+m)\gamma_\sigma(-\not{\partial}+m) = \gamma_\sigma(-\Delta_y+m^2)+2(\not{\partial}-m)\partial_{y_\sigma}\,. \tag{4.53}$$

With some simple algebras, we get

$$M_\sigma = \sum_{n\in\mathbb{Z}^4}(\gamma_\alpha D^{1;\sigma}_\alpha + D^{2;\sigma})\,, \tag{4.54}$$

where

$$D^{1;\sigma}_\sigma = \frac{1}{4\pi^2}\Big(m^2\big(\frac{y^{[n]}_\sigma}{|y^{[n]}|}\big)^2K_0(m|y^{[n]}|)+2m\frac{(y^{[n]}_\sigma)^2}{|y^{[n]}|^3}K_1(m|y^{[n]}|)\Big)\,, \tag{4.55}$$

$$D^{1;\sigma}_\alpha = \frac{1}{4\pi^2}\Big(m^2\frac{y^{[n]}_\sigma y^{[n]}_\alpha}{|y^{[n]}|^2}K_0(m|y^{[n]}|)+\frac{2my^{[n]}_\sigma y^{[n]}_\alpha}{|y^{[n]}|^3}K_1(m|y^{[n]}|)\Big)\,,\quad \text{for } \alpha\neq\sigma\,, \tag{4.56}$$

$$D^{2;\sigma} = \frac{m}{4\pi^2}\frac{y^{[n]}_\sigma}{|y^{[n]}|}K_1(m|y^{[n]}|)\,. \tag{4.57}$$

Finally,

$$
\begin{aligned}
&N_{\mu\nu\sigma\lambda}(x,y) \\
&= \sum_{r,s\in\mathbb{Z}^4} \left(\frac{m^2}{4\pi^2}\right)^2 \frac{1}{|(x-y)^{[r]}|}\frac{1}{|(w-x)^{[s]}|}\Big\{ \\
&\frac{K_2(m|(x-y)^{[r]}|)K_2(m|(w-x)^{[s]}|)}{|(x-y)^{[r]}||(w-x)^{[s]}|}(x-y)^{[r]}_\beta (w-x)^{[s]}_\gamma D^{1;\sigma}_\alpha \mathrm{Tr}[\gamma_\mu\gamma_\beta\gamma_\nu\gamma_\alpha\gamma_\lambda\gamma_\gamma] \\
&+ \frac{K_2(m|(x-y)^{[r]}|)K_1(m|(w-x)^{[s]}|)}{|(x-y)^{[r]}|}(x-y)^{[r]}_\beta D^{2;\sigma}\mathrm{Tr}[\gamma_\mu\gamma_\beta\gamma_\nu\gamma_\lambda] \\
&+ \frac{K_1(m|(x-y)^{[r]}|)K_2(m|(w-x)^{[s]}|)}{|(w-x)^{[s]}|}(w-x)^{[s]}_\gamma D^{2;\sigma}\mathrm{Tr}[\gamma_\mu\gamma_\nu\gamma_\lambda\gamma_\gamma] \\
&+ K_1(m|(x-y)^{[r]}|)K_1(m|(w-x)^{[s]}|)D^{1;\sigma}_\alpha \mathrm{Tr}[\gamma_\mu\gamma_\nu\gamma_\alpha\gamma_\lambda]\Big\}\,,
\end{aligned}
\tag{4.58}
$$

where the Einstein summation is applied to $\alpha \in \{0,1,2,3\}$.

4.1.3 Implication of the distributional nature of the scalar propagator

As discussed in Sect. 3.2.1, one should keep in mind the distributional nature of the scalar propagator. One might be worried if any δ-function is needed for the derivatives of the C^i's and $\partial_m^2 G_m$. Fortunately, this is not the case. This can be easily checked by a power-counting in the momenta of these expressions in momentum-space.

4.1.4 Comparison with free theory on the lattice

We check our calculation qualitatively against a free theory calculation on the lattice with Wilson fermion with the mass of the lepton $m_{\text{lep.}}$ set to the mass of the muon. The latter can be calculated exactly on the lattice by setting all the gauge links to unit matrix.[6] The result is shown in Fig. 4.2. For both the analytic and lattice computations, various hypercubic boxes with equal sides are used. We impose periodic boundary condition for the spatial boundaries and anti-periodic boundary condition for the temporal one. The latter requires a phase of -1 while adding odd number of windings in the formulae given in the previous section (c.f. Appendix D.4). We plot the $|y|$-integrand Eq. (4.8) with y following the diagonal of the box, i.e. the $(1,1,1,1)$ direction. The area under each curve gives the corresponding value for a_μ. In our semi-analytical computation, we only include up to one non-vanishing winding in each direction because of the smallness of the propagators when the argument gets larger. Note that the quantitative difference between the semi-analytic result and the lattice result is expected: the lattice spacing for both boxes used in the lattice computations is around 0.1 fm ($am_{\text{lep.}} = 0.05625$), which results in non-negligible cut-off effects. Nonetheless, from the comparison between calculations at different $m_{\text{lep.}}L$, we see that the volume dependence is very well captured by our semi-analytic approach. This study shows how significant finite-volume QED effects due to a light lepton can be. One can notice that the finite-volume effects become severe as $|y|$ gets bigger, which is a general feature that one encounters in other models as well.

[6] The lattice data are generated and communicated privately by Antoine Gérardin.

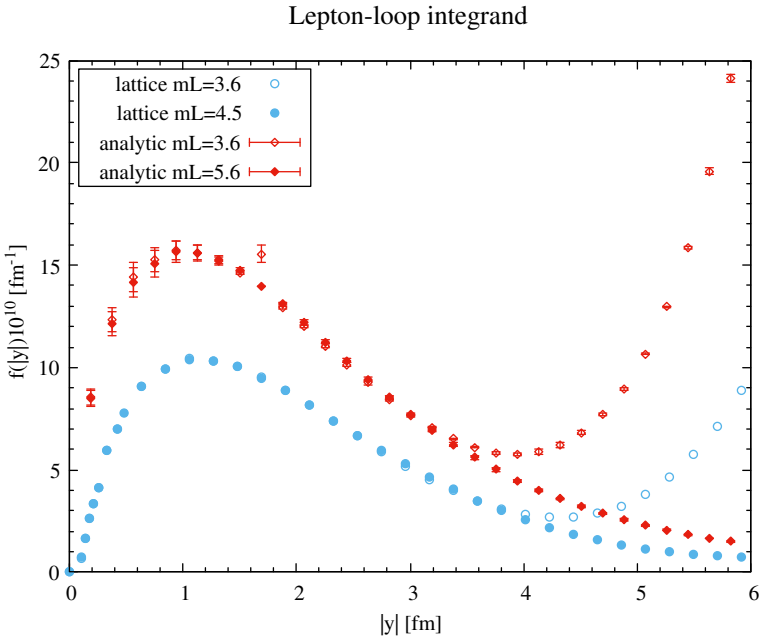

FIGURE 4.2: Semi-analytical results v.s. lattice results with different values of $m_{\text{lep.}}L$. The kernel $\mathcal{L}^{(2)}$ [Eq. (3.18)] is used. The circle points correspond to the lattice results and the diamond points are the semi-analytic ones. The filled points have bigger values of $m_{\text{lep.}}L$ and can be consider as close to the infinite-volume results. For the calculations on the lattice, we use a 64^4 box for $m_{\text{rep.}}L = 3.6$ and an 80^4 box for $m_{\text{rep.}}L = 4.5$. The error bars for the semi-analytic calculations are due to the tolerance used for the 4-dimensional x-integration. Typically, a relative error of 1-5% is picked for numerical integration.

4.2 Finite-size effects from scalar QED

Now that we have worked out the lepton-loop contribution to a_μ^{hlbl} (spinor QED), we can extend the study to the contribution of the charged-pseudoscalar-meson loop to a_μ^{hlbl} thanks to the similarity of the mathematical structure between them. The latter is equivalent to a scalar-QED calculation at one-loop according to Chiral Perturbation Theory (ChPT) up to O(p^4).[7] This contribution is considered to be important at large distances due to the lightness of the pion. Nevertheless, it should be noted that the point-like pseudoscalar-meson interaction described by ChPT up to O(p^4) alone does not capture the physical process very well due to the internal quark structure of the mesons and the existence of resonances. As far as a_μ^{hlbl} is concerned, it is shown that estimating the charged-pseudoscalar-meson loop contribution using a simple scalar QED gives a much bigger answer than estimating with a form factor for the photon-to-two-pseudoscalar-meson vertices from models [HKS95; KNO85; BPP95]. Clearly, this uncertainty affects principally the short-distance behavior. As we are concerned with the finite-size effects of the charged-pseudoscalar-meson loop here, we carry out a study simply in scalar QED as a first step to get some qualitative insight.

Most of the calculations reported in this section are very similar to the ones encountered in the previous section. We might skip some technical details. After introducing the notations and the analytic expressions for some building blocks, we will

[7] See Chap. 5 for details.

exhibit results for different integral representation of $a_\mu^{\rm hlbl}$ for particular choices of pseudoscalar-meson mass, which correspond to the pion masses measured on some lattice ensembles used for our simulation. The expressions are given in Euclidean space-time.

4.2.1 Notations and analytic expressions

We recall the scalar-QED Lagrangian

$$\mathcal{L}^{\rm sQED} = (D_\mu\phi)^* D^\mu\phi + m^2\phi\phi^* + \frac{1}{4}F_{\mu\nu}F^{\mu\nu}\,, \tag{4.59}$$

where

$$D_\mu = \partial_\mu - ieA_\mu\,, \tag{4.60}$$

is the covariant derivative associated to the U(1)-gauge group, ϕ is a complex scalar field, F is the field strength of the photon field A and m is the mass of the scalar particle.

It is clear that the propagator of the scalar particle is the usual scalar propagator

$$\langle\phi(x)\phi^*(0)\rangle_0 = \int \frac{d^4p}{(2\pi)^4}\frac{e^{ipx}}{p^2+m^2} = G_m(x)\,, \quad G_m(x) \equiv \frac{m}{4\pi^2|x|}K_1(m|x|)\,, \tag{4.61}$$

where the subscript 0 indicates that the expectation value is taken in the free theory.

We can infer from the Lagrangian that two scalar particles of opposite charge couple to external photons at point x in two ways. The first one is achieved via

$$-i\phi^*\partial_\alpha\phi(x) + \text{c.c.}\,, \tag{4.62}$$

The second one is a coupling to two external photons described by a contact term

$$-\phi^*\phi A_\mu(x)A_\nu(y)\delta(x-y)\delta_{\mu\nu}\,. \tag{4.63}$$

In the following, we will denote the coupling Eq. (4.62) by J and the coupling Eq. (4.63) by K. The Lagrangian of interaction can then be written as

$$\mathcal{L}_{\rm int} = J_\mu A_\mu + K_{\mu\nu}A_\mu A_\nu\,. \tag{4.64}$$

Because of the contact term $K_{\mu\nu}$, the electromagnetic current 4-point function $\langle A_\mu(x)A_\nu(y)A_\sigma(z)A_\rho(w)\rangle$ required for the hadronic 4-point function $i\hat{\Pi}$ involves three classes of Feynman diagram at one-loop: the box, the triangle and the bubble (Fig. 4.3). In the rest of the section, we will use sub/super-script "4" for the quantities belonging to the "box" class, "3" for those belonging to the "triangle" class and "2" for those coming from the "bubble" class.

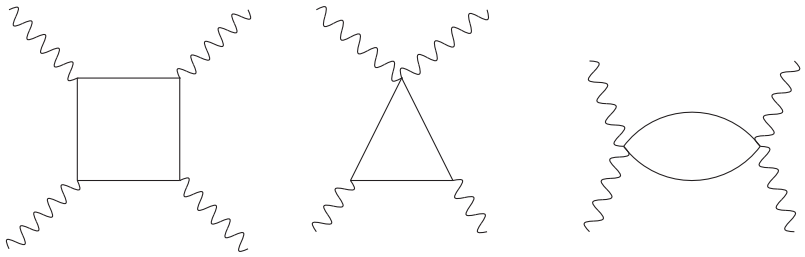

FIGURE 4.3: Three different diagrammatic classes appearing while computing a_μ^{hlbl} at leading order in scalar QED due to the interaction vertices Eq. (4.62) and Eq. (4.63). From left to right are the box, the triangle and the bubble classes. The plain lines are scalar particles and the wavy lines are photons. Each class contains all possible permutations of the vertices, so if we pair up those with particle flow in opposite orientation, we have 3 diagrams for the box class, 6 for the triangle class and 3 for the bubble class.

At the level of the electromagnetic current 4-point function, these diagrams represent the following functions

$$\begin{aligned}
I^{4,1}_{\mu\nu\sigma\lambda}(x,y,z,w) &= 2\hat{I}^4_{\mu\nu\sigma\lambda}(x,y,z,w)\,,\\
I^{4,2}_{\mu\nu\sigma\lambda}(x,y,z,w) &= 2\hat{I}^4_{\nu\mu\sigma\lambda}(y,x,z,w)\,,\\
I^{4,3}_{\mu\nu\sigma\lambda}(x,y,z,w) &= 2\hat{I}^4_{\lambda\nu\sigma\mu}(w,y,z,x)\,,\\
I^{3,1}_{\mu\nu\sigma\lambda}(x,y,z,w) &= 4\hat{I}^3_{\mu\nu}(x,y,w)\delta_{\sigma\lambda}\delta(z-w)\,,\\
I^{3,2}_{\mu\nu\sigma\lambda}(x,y,z,w) &= 4\hat{I}^3_{\nu\lambda}(y,w,x)\delta_{\mu\sigma}\delta(z-x)\,,\\
I^{3,3}_{\mu\nu\sigma\lambda}(x,y,z,w) &= 4\hat{I}^3_{\mu\lambda}(x,w,y)\delta_{\nu\sigma}\delta(z-y)\,,\\
I^{3,4}_{\mu\nu\sigma\lambda}(x,y,z,w) &= 4\hat{I}^3_{\sigma\lambda}(z,w,y)\delta_{\mu\nu}\delta(x-y)\,,\\
I^{3,5}_{\mu\nu\sigma\lambda}(x,y,z,w) &= 4\hat{I}^3_{\sigma\nu}(z,y,w)\delta_{\mu\lambda}\delta(x-w)\,,\\
I^{3,6}_{\mu\nu\sigma\lambda}(x,y,z,w) &= 4\hat{I}^3_{\sigma\mu}(z,x,w)\delta_{\nu\lambda}\delta(y-w)\,,\\
I^{2,1}_{\mu\nu\sigma\lambda}(x,y,z,w) &= 4\hat{I}^2(x,z)\delta_{\mu\nu}\delta_{\sigma\lambda}\delta(x-y)\delta(z-w)\,,\\
I^{2,2}_{\mu\nu\sigma\lambda}(x,y,z,w) &= 4\hat{I}^2(x,w)\delta_{\mu\sigma}\delta_{\nu\lambda}\delta(x-z)\delta(y-w)\,,\\
I^{2,3}_{\mu\nu\sigma\lambda}(x,y,z,w) &= 4\hat{I}^2(x,y)\delta_{\mu\lambda}\delta_{\nu\sigma}\delta(x-w)\delta(y-z)\,,
\end{aligned} \tag{4.65}$$

where

$$\begin{aligned}
\hat{I}^4_{\mu\nu\sigma\lambda}(x,y,z,w) = \quad & \tilde{I}^{++++}_{4,\mu\nu\sigma\lambda}(x,y,z,w) + \tilde{I}^{----}_{4,\mu\nu\sigma\lambda}(x,y,z,w) + \tilde{I}^{+++-}_{4,\mu\nu\sigma\lambda}(x,y,z,w)\\
&+ \tilde{I}^{++-+}_{4,\mu\nu\sigma\lambda}(x,y,z,w) + \tilde{I}^{+-++}_{4,\mu\nu\sigma\lambda}(x,y,z,w) + \tilde{I}^{-+++}_{4,\mu\nu\sigma\lambda}(x,y,z,w)\\
&+ \tilde{I}^{---+}_{4,\mu\nu\sigma\lambda}(x,y,z,w) + \tilde{I}^{--+-}_{4,\mu\nu\sigma\lambda}(x,y,z,w) + \tilde{I}^{-+--}_{4,\mu\nu\sigma\lambda}(x,y,z,w)\\
&+ \tilde{I}^{+---}_{4,\mu\nu\sigma\lambda}(x,y,z,w) + \tilde{I}^{++--}_{4,\mu\nu\sigma\lambda}(x,y,z,w) + \tilde{I}^{+--+}_{4,\mu\nu\sigma\lambda}(x,y,z,w)\\
&+ \tilde{I}^{--++}_{4,\mu\nu\sigma\lambda}(x,y,z,w) + \tilde{I}^{-++-}_{4,\mu\nu\sigma\lambda}(x,y,z,w) + \tilde{I}^{+-+-}_{4,\mu\nu\sigma\lambda}(x,y,z,w)\\
&+ \tilde{I}^{-+-+}_{4,\mu\nu\sigma\lambda}(x,y,z,w)\,,
\end{aligned} \tag{4.66}$$

$$\hat{I}^3_{\mu\nu}(x,y,w) = \tilde{I}^{++}_{3,\mu\nu}(x,y,w) + \tilde{I}^{--}_{3,\mu\nu}(x,y,w) + \tilde{I}^{-+}_{3,\mu\nu}(x,y,w) + \tilde{I}^{+-}_{3,\mu\nu}(x,y,w)\,, \tag{4.67}$$

$$\hat{I}^2(x,w) = [G_m(x-w)]^2\,. \tag{4.68}$$

The sixteen $\tilde{I}_4$'s and four $\tilde{I}_3$'s are given in Appendices E.1.1 and E.2.1 to avoid clutter.

As in the previous section, we will consider several modified versions of integral representation of a_μ^{hlbl}, obtained by applying a change of variables and exploiting translational invariance. The analytic calculation of the z-integral requires the following two classes of functions

$$N^{i,j}_{\mu\nu\sigma\lambda}(x,y) \equiv -\int_z I^{i,j}_{\mu\nu\sigma\lambda}(x,y,z,0)\,, \tag{4.69}$$

$$i\hat{\Pi}^{i,j}_{[\rho,\sigma];\mu\nu\lambda}(x,y) \equiv -\int_z z_{[\rho|} I^{i,j}_{\mu\nu|\sigma]\lambda}(x,y,z,0)\,, \tag{4.70}$$

where the anti-symmetrization with regard to ρ and σ is introduced in order to match the symmetry of the QED kernel. The anti-symmetrization of the hadronic moment $i\Pi$ helps simplify the expression. The exact expressions of N and $i\hat{\Pi}$ can be found in Appendices E.1.2, E.1.3 and E.2.2.

Treatment of the distributional nature of the scalar propagator

Some expressions listed in Appendix E contain a second order derivative of the scalar propagator. These terms lead to δ-functions in x or y in addition to the existing ones due to the contact term. This has been discussed in Sect. 3.2 in detail. In particular we have to use Eq. (3.48) for the second derivative of the propagator. Fortunately, gauge invariance tells us that there should be some specific pattern that one can use to simplify the calculation. With some care, one finds out that the effect of these extra δ-functions amounts to modifying the contributions from the triangle and the bubble class containing the same δ-functions by a factor of $\frac{3}{4}$.

4.2.2 Charged-pion-loop contribution to a_μ^{hlbl} with different mass and in different integral representation in finite-volume

As we have all the necessary tools for our lattice computation of the charged-pion-loop contribution to a_μ^{hlbl}, it is instructive to compute the quantity with parameters corresponding to the lattices on which we run our simulations. We chose to do this for the ensembles C101 ($m_\pi \approx 220$ MeV, $m_\pi L = 4.64$) and D200 ($m_\pi \approx 200$ MeV, $m_\pi L = 4.15$) of the CLS consortium. These ensembles have a $L^3 \times T$ type geometry, with the temporal extent $T = 3L$, and are of open boundary condition. Due to the large values of $m_\pi T$, the temporal direction can almost be treated as infinite. For this reason, we do not wrap around the time direction, i.e. the windings are only applied to the spatial ones.

We carry out the FSE study by computing two modified integral representations of the charged-pion-loop contribution to a_μ^{hlbl}, with charge factors put by hand to match different Wick-contraction topologies calculated on the lattice.[8] The $|y|$-integrands for these two quantities are defined as

- **Type 4**

$$\begin{aligned} f^4(|y|) =& \frac{34}{81}\frac{me^6}{3}2\pi^2|y|^3 \\ &\times \Big(\int_x \mathcal{L}'_{[\rho,\sigma]\mu\nu\lambda}(x,y) i\hat{\Pi}^{\mathrm{M2}}_{[\rho,\sigma]\mu\nu\lambda}(x,y) + \int_x x_\rho \mathcal{L}_{[\rho,\sigma]\lambda\nu\mu}(x,x-y) N^{\mathrm{M2}}_{\mu\nu\sigma\lambda}(x,y)\Big)\,, \end{aligned} \tag{4.71}$$

[8] c.f. Sect. 5.3 and Sect. 6.2.

where

$$i\hat{\Pi}^{\mathrm{M2}}_{[\rho,\sigma]\mu\nu\lambda} \equiv i\hat{\Pi}^{4,1}_{[\rho,\sigma]\mu\nu\lambda} + \frac{1}{2}i\hat{\Pi}^{3,1}_{[\rho,\sigma]\mu\nu\lambda} + \frac{1}{2}i\hat{\Pi}^{3,3}_{[\rho,\sigma]\mu\nu\lambda} + \frac{1}{2}i\hat{\Pi}^{3,4}_{[\rho,\sigma]\mu\nu\lambda} + \frac{1}{2}i\hat{\Pi}^{3,5}_{[\rho,\sigma]\mu\nu\lambda} + \frac{1}{2}i\hat{\Pi}^{2,1}_{[\rho,\sigma]\mu\nu\lambda} + \frac{1}{2}i\hat{\Pi}^{2,3}_{[\rho,\sigma]\mu\nu\lambda}\,, \tag{4.72}$$

$$N^{\mathrm{M2}}_{\mu\nu\sigma\lambda} \equiv N^{4,1}_{\mu\nu\sigma\lambda} + \frac{1}{2}N^{3,1}_{\mu\nu\sigma\lambda} + \frac{1}{2}N^{3,3}_{\mu\nu\sigma\lambda} + \frac{1}{2}N^{3,4}_{\mu\nu\sigma\lambda} + \frac{1}{2}N^{3,5}_{\mu\nu\sigma\lambda} + \frac{1}{2}N^{2,1}_{\mu\nu\sigma\lambda} + \frac{1}{2}N^{2,3}_{\mu\nu\sigma\lambda}\,. \tag{4.73}$$

and $\mathcal{L}'$ is defined in Eq. (4.9).

- **Type 2+2**

$$f^{2+2}(|y|) = \frac{25}{81}\frac{m_\mu e^6}{3}2\pi^2|y|^3 \times \int_x \Big(2\mathcal{L}_{[\rho,\sigma];\mu\nu\lambda}(x,y) + \mathcal{L}_{[\rho,\sigma];\nu\mu\lambda}(y,x)\Big) i\hat{\Pi}^{\mathrm{M1}}_{[\rho,\sigma]\mu\nu\lambda}(x,y)\,, \tag{4.74}$$

where

$$\begin{aligned} i\hat{\Pi}^{\mathrm{M1}}_{[\rho,\sigma]\mu\nu\lambda} \equiv &+ i\hat{\Pi}^{4,1}_{[\rho,\sigma]\mu\nu\lambda} + i\hat{\Pi}^{4,2}_{[\rho,\sigma]\mu\nu\lambda} + i\hat{\Pi}^{4,3}_{[\rho,\sigma]\mu\nu\lambda} \\ &+ i\hat{\Pi}^{3,1}_{[\rho,\sigma]\mu\nu\lambda} + i\hat{\Pi}^{3,2}_{[\rho,\sigma]\mu\nu\lambda} + i\hat{\Pi}^{3,3}_{[\rho,\sigma]\mu\nu\lambda} \\ &+ i\hat{\Pi}^{3,4}_{[\rho,\sigma]\mu\nu\lambda} + i\hat{\Pi}^{3,5}_{[\rho,\sigma]\mu\nu\lambda} + i\hat{\Pi}^{3,6}_{[\rho,\sigma]\mu\nu\lambda} \\ &+ i\hat{\Pi}^{2,1}_{[\rho,\sigma]\mu\nu\lambda} + i\hat{\Pi}^{2,2}_{[\rho,\sigma]\mu\nu\lambda} + i\hat{\Pi}^{2,3}_{[\rho,\sigma]\mu\nu\lambda}\,, \end{aligned} \tag{4.75}$$

However, as it is written, some terms in Eq. (4.75) contain $\delta(y)$, which makes it tricky to plot the $|y|$-integrand because the contribution of these terms will be missing. To remove this ambiguity, we deliberately swap the rôles of x and y for these quantities. Of course, this will change the shape of the $|y|$-integrand, but we expect that this does not change much the long-distance behavior. After all, a more realistic pion electromagnetic form factor will be needed if one really intends to make a more quantitative statement on the finite-size effects from the charged-pion loop.

The two integrand representations introduced above are in fact motivated by the charged-pion-loop contribution to the "fully-connected" and "2+2" QCD Wick-contraction topologies, with the appropriate weight factors defined in Sect. 6.2. The infinite- and finite-volume $|y|$-integrands for both Type 4 and Type 2+2 are plotted in Fig. 4.4. Qualitatively, we have a very similar divergent behavior for the finite-volume integrand as for the lepton loop case. Presumably, this similarity is due to the one-loop structure present in both cases. Apparently, with a value of $m_\pi L \approx 4$, one already picks up sizeable finite-size effects at around $|y| = 1.5$ fm. Although it is known that the charged-pion loop has a strong chiral enhancement [PRV09], what one sees from different resulting FSE passing from C101 to D200, with a very little change in the pion mass and $m_\pi L$, is kind of intimidating. Nonetheless, in our lattice calculation, we seldom go beyond 1.5 fm for our light ensembles with our lattice data due to the loss of the signal. In this worrying region, only an infinite-volume tail

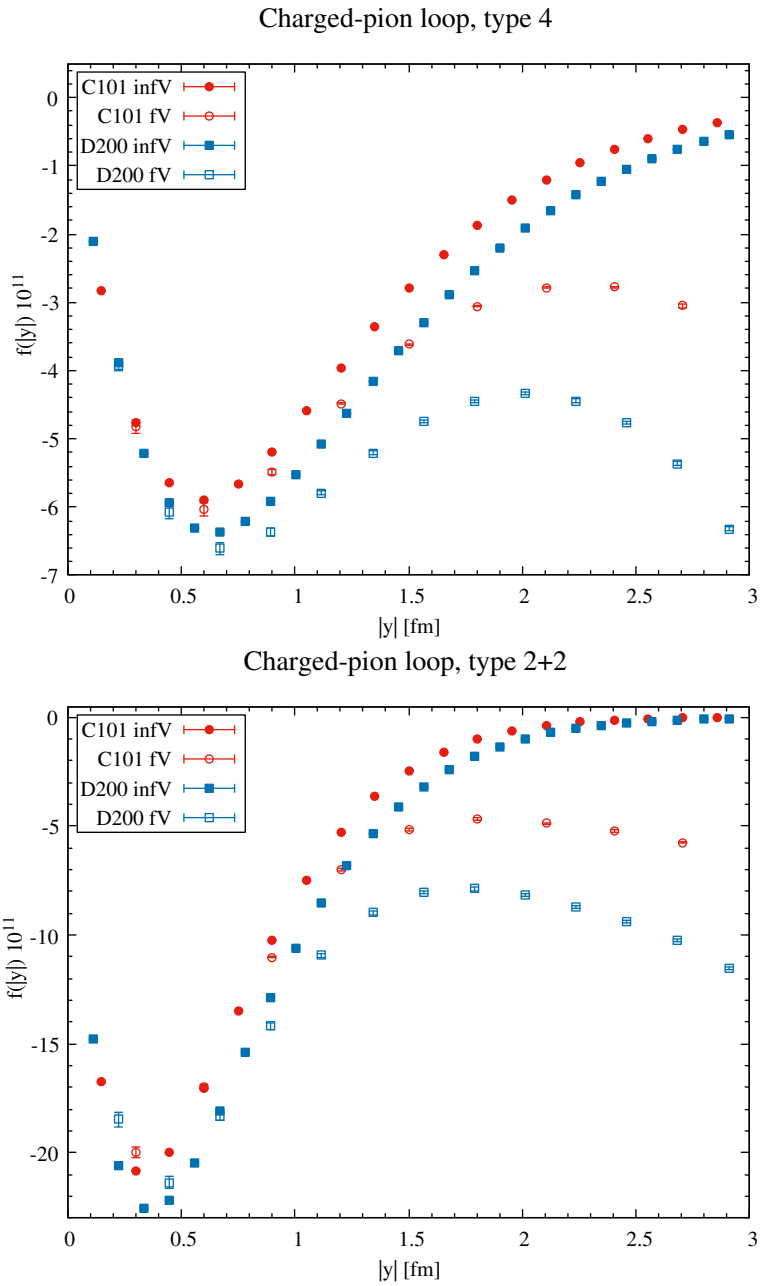

FIGURE 4.4: Comparison between the finite-size effects computed with with different lattice parameters and in different representations. The kernel $\bar{\mathcal{L}}^{(\Lambda)}$ [Eq. (3.17)] with $\Lambda = 0.4$ is used for all the displayed results.

reconstruction is applied.[9] Finally, as has already been stressed, the charged-pion-loop contribution depends heavily on the form factor because of the short distance behavior, and therefore this study should not be used as a precise estimate for the FSE. Instead, in our study of the integrand for lattice data, the neutral-pseudoscalar-meson exchange alone gives a reasonable estimate of the FSE and can be used as a guideline for treating the long-distance tail at the same time.

[9] c.f. Sect. 6.4.

Chapter 5

Partially-Quenched Chiral Perturbation Theory and applications

Even though Lattice QCD provides a way of computing hadronic observables non-perturbatively from first-principles, the signal degrades gradually as the separations between the operators in the correlation function that we want to compute become larger. Commonly, these regimes are treated with the knowledge from effective field theories (EFTs) of QCD at low energies. By doing so, one trades the statistical error for a systematic error due to the use of effective models. Chiral Perturbation Theory (ChPT) is a widely used effective field theory for estimating observables at low energies. The theory is built upon the breaking of chiral symmetry in QCD.

In the explicit examples given in Chap. 3 and Chap. 4, we have seen that, with the position-space approach, one can re-arrange the terms appearing in the expression so that one does not have to evaluate the complete set of Feynman diagrams but only a subset of them to obtain the final targeted observable a_μ^{hlbl}. In our actual lattice computation of a_μ^{hlbl}, which will be discussed in great detail in Chap. 6, this re-parametrization freedom allows us to reduce the computational cost considerably by avoiding the calculation of costly QCD Wick-contractions in Lattice QCD. However, as one can treat each of the Wick-contraction topologies differently[1], one needs to find a way to match each individual contraction to the corresponding Feynman diagrams in an EFT in order to mimic the physics faithfully. In the context of Chiral perturbation theory, this can be done with Partially-Quenched Chiral Perturbation Theory (PQChPT). The technique has been used, for instance, to isolate the connected and the disconnected contributions in the computation of the Hadronic Vacuum Polarization contribution to a_μ [DMJ10].

The purpose of this chapter is to explain how to apply PQChPT to match a QCD Wick-contraction to the relevant Feynman diagrams in ChPT. Ultimately, we would like to understand how the two major contributions to a_μ^{hlbl} at long distances, the neutral-pseudoscalar-meson exchange and the charged-pseudoscalar-meson loop[2], affect each individual QCD Wick-contraction at leading order (tree-level for the former and one-loop for the latter). This chapter is organized as follows. We will briefly discuss some generalities including a brief review of the basic notions in ChPT and the diagram matching principle using PQChPT. Then, we will give a general method for obtaining the propagator in a PQChPT with up to two different quark masses in the underlying theory (QCD). We shall also discuss the inclusion of the flavor-singlet pseudoscalar meson (η'), which might introduce a non-negligible contribution due

[1] See Chap. 6 for more details.
[2] c.f. Sect. 1.2.

to its mixing with the η-meson. Finally, we will give the Feynman rules for the relevant interaction vertices for the neutral-pseudoscalar-meson exchange and the charged-pseudoscalar-meson loop.

Conventions we will keep the expressions in Minkowski space-time if they are taken from the literature. However, all the Feynman rules that we give at the end are in Euclidean space-time as that is what is relevant to our position-space computation. The main nuance is at the level of the Lagrangian. To distinguish these, we will use a superscript "E" to indicate that a Lagrangian is given in Euclidean space-time, otherwise it is in Mikowski space-time. All the discussions are restricted to the sector of up-, down-, and strange-quarks of QCD, with the up- and down-quarks being mass-degenerate.

5.1 Brief review on Chiral Perturbation Theory

Let us briefly review some basic aspects of Chiral Perturbation Theory following the line of Ref. [Sch03]. We will use the term *chiral limit* for the limit of vanishing u- and d-quark masses in QCD throughout the section. This terminology is different from the one in the lattice QCD language, which refers to the point in the parameter space with physical pion mass.

Due to the running of the strong coupling, low-energy properties of QCD can not be obtained from direct perturbative calculations. Besides treating QCD on the lattice using a Euclidean space-time formulation, a common approach for studying hadronic physics consists in building an effective field theory with inputs from experiment in the low-energy regime. ChPT is an example which incorporates the QCD current algebra and symmetries into a theory based on the Goldstone bosons as a result of chiral-symmetry breaking. We limit ourselves to the case where the charm-, bottom- and top-quarks are integrated out because of their heaviness.

As is well known, in the exact massless limit, QCD admits a global $\mathrm{U}(3)_L \times \mathrm{U}(3)_R$ symmetry at classic level, under which the left-handed and the right-handed components of a quark field transform independently under $\mathrm{U}(3)$ group acting on the flavor space comprising the up-, down- and strange-quarks. Conventionally, one uses the isomorphism between the groups

$$\mathrm{U}(3)_L \times \mathrm{U}(3)_R \simeq \mathrm{SU}(3)_L \times \mathrm{SU}(3)_R \times \mathrm{U}(1)_V \times \mathrm{U}(1)_A\,, \tag{5.1}$$

to single out the flavor-singlet vector and axial symmetries responsible for different Noether currents. At quantum level, the axial symmetry is broken due to the Adler-Bell-Jackiw (ABJ) anomaly [Adl69; BJ69] and thus the symmetry group is actually $\mathrm{SU}(3)_L \times \mathrm{SU}(3)_R \times \mathrm{U}(1)_V$. The group $\mathrm{SU}(3)_L \times \mathrm{SU}(3)_R$ embedded in the symmetry group is called the *chiral group*. Often it is convenient to rewrite the symmetry transformations generated by the chiral group to take into account the chirality. The chiral group can thus be written as a Cartesian product of an $\mathrm{SU}(3)_V$ corresponding to the vector sector and an $\mathrm{SU}(3)_A$ corresponding to the axial sector. In the Hamiltonian picture, the conserved charge due to the $\mathrm{U}(1)_V$ symmetry gives rise to the baryon number [Sch03]. In the following discussion, we will stay in the mesonic sector, i.e. with zero baryon number.

In the real world, the lightest part of the observed hadronic spectrum: the pions (π), the kaons (K) and the η-meson, forms a pseudoscalar octet. A way for this to be realized is via spontaneous symmetry breaking of the chiral group down to

$\mathrm{SU}(3)_V$, with $\mathrm{SU}(3)_A$ spontaneously broken and leading to the 8 Goldstone bosons which form this light-meson octet. Note that $\mathrm{SU}(3)_A$ will be explicitly broken if the quarks have non-vanishing masses. As the three quarks in our theory have small but non-zero masses, the spontaneous symmetry breaking results in massive but light pseudo-Goldstone bosons, instead them being massless. A sufficient condition for chiral symmetry breaking to happen in QCD in the chiral limit is the existence of non-vanishing quark condensate, i.e. $\langle \bar{q}q \rangle \neq 0$ with q a quark field and $\bar{q}$ the corresponding anti-quark field .[3] These light pseudo-Goldstone bosons constitute the degrees of freedom of Chiral Perturbation Theory. The construction of ChPT is based on the power-counting scheme of Ref. [Wei79] in the following way. As we stay in the "soft" regime, i.e. lower energies, we construct our EFT order by order in the characteristic momentum squared (p^2). At each order, we should include all possible terms that we can build from the pseudoscalar meson fields. A legitimate term should be invariant under the symmetry transformation of the pseudoscalar meson fields, which they inherit from the underlying theory, i.e. QCD. To determine the coefficients associated to each term in the effective Lagrangian, one then takes inputs from experiment and matches computable matrix elements from the effective theory.

5.1.1 $\mathbf{SU}(3)$ Chiral Perturbation Theory

We start with the chiral QCD Lagrangian [GL84]

$$\mathcal{L}^0_{\mathrm{QCD}} = -\frac{1}{2g^2}\mathrm{Tr}_c[G_{\mu\nu}G^{\mu\nu}] + \bar{q}\gamma_\mu(\partial_\mu - iA_\mu)q\,, \quad q = (u,d,s)^{\mathrm{T}}\,, \tag{5.2}$$

where $G_{\mu\nu}$ is the field strength of the gluon field A_μ, and we require the Lagrangian in the presence of external fields to be

$$\mathcal{L} = \mathcal{L}^0_{\mathrm{QCD}} + \bar{q}\gamma_\mu(v^\mu + \gamma_5 a^\mu)q - \bar{q}(s - i\gamma_5 p)q - \frac{1}{16\pi^2}\theta\mathrm{Tr}_c[G_{\mu\nu}\tilde{G}^{\mu\nu}]\,, \tag{5.3}$$

where the external fields are: a flavor-octet vector current v^μ, a flavor-octet axial vector current a^μ, a scalar field s, a pseudoscalar field p and a pseudoscalar field θ coupled to the winding number density, which is generated due to the ABJ-anomaly. Here, $\tilde{G}^{\mu\nu}$ denotes the Hodge dual of the field strength $G^{\mu\nu}$. Note that, written in this way, we can make the quark mass term appear by considering a scalar perturbation s around the target mass matrix.

Given the ABJ-anomaly breaking of the $\mathrm{U}(1)_A$ symmetry, the remaining $\mathrm{SU}(3)_L \times \mathrm{SU}(3)_R$ symmetry of the chiral QCD Lagrangian comes from the fact that Eq. (5.2) is invariant under the local quark-field transformation

$$q(x) \to V_R(x)\frac{1}{2}(1+\gamma_5)q(x) + V_L(x)\frac{1}{2}(1-\gamma_5)q(x)\,, \tag{5.4}$$

where V_L and V_R are two elements of $\mathrm{SU}(3)$ acting on the flavor space. To preserve the symmetry, a gauge transformation of the external fields is required [GL84]:

$$\begin{aligned} v'_\mu + a'_\mu &= V_R(v_\mu + a_\mu)V_R^\dagger + iV_R\partial_\mu V_R^\dagger\,, \\ v'_\mu - a'_\mu &= V_L(v_\mu - a_\mu)V_L^\dagger + iV_L\partial_\mu V_L^\dagger\,, \\ s' + ip' &= V_R(s+ip)V_L^\dagger\,. \end{aligned} \tag{5.5}$$

[3] See Ref. [Sch03] for a proof.

ChPT up to O(p^2)

Now, let us write down the ChPT Lagrangian at leading order in p^2 with the flavor-octet pseudoscalar mesons corresponding to the Lagrangian Eq. (5.3). The spontaneous breaking of the symmetry group from $\mathrm{SU}(3)_L\times\mathrm{SU}(3)_R$ to $\mathrm{SU}(3)_V$ leads to 8 Goldstone bosons. For them to form an SU(3) octet and transform according to the same global symmetry group $\mathrm{SU}(3)_L\times\mathrm{SU}(3)_R$ as in chiral QCD, one can make use of a non-linear realization of the group.[4] This is done by grouping the 8 pseudoscalar mesons into a single SU(3) field U such that

$$U(x) = \exp\left(i\frac{\phi(x)}{F_0}\right), \tag{5.6}$$

where F_0 is a dimension-1 parameter related to the decay constant and

$$\phi(x) = \sum_{a=1}^{8}\lambda_a\phi_a(x) \equiv \begin{pmatrix} \pi^0+\frac{1}{\sqrt{3}}\eta & \sqrt{2}\pi^+ & \sqrt{2}K^+ \\ \sqrt{2}\pi^- & -\pi^0+\frac{1}{\sqrt{3}}\eta & \sqrt{2}K^0 \\ \sqrt{2}K^- & \sqrt{2}\bar{K}^0 & -\frac{2}{\sqrt{3}}\eta \end{pmatrix}, \tag{5.7}$$

with λ_a being the Gell-Mann matrices. We require the field U to transform under local $\mathrm{SU}(3)_L\times\mathrm{SU}(3)_R$ as

$$U(x) \to U'(x) = V_R(x)U(x)V_L^\dagger(x)\,. \tag{5.8}$$

Concerning the coupling to the external fields in Eq. (5.3), the gauge invariance permits v_μ and a_μ to enter only via covariant derivative, which is defined as [GL85]

$$D_\mu U = \partial_\mu U - i(v_\mu+a_\mu)U + iU(v_\mu-a_\mu)\,. \tag{5.9}$$

At $\mathrm{O}(p^2)$, the effective Lagrangian with only the terms involving meson fields kept thus takes the form [GL85]

$$\mathcal{L}^{(2)} = \frac{1}{4}F_0^2\mathrm{Tr}[D_\mu U^\dagger D^\mu U] + 2B_0\mathrm{Tr}[(s-ip)U] + 2B_0^*\mathrm{Tr}[(s+ip)U^\dagger]\,, \tag{5.10}$$

where $B_0\in\mathbb{C}$ is another coefficient to be determined, which is related to the meson masses. In fact, if one assumes that the ground-state of QCD is an eigenstate of parity, one will arrive at the constraint $B_0\in\mathbb{R}$ [GL85], which will be admitted throughout the rest of this chapter. One can easily check that Eq. (5.10) is indeed invariant under a global $\mathrm{SU}(3)_L\times\mathrm{SU}(3)_R$ transformation.

For higher order terms in p^2, one just has to systematically include all possible operators built from the field U and its higher order covariant derivatives which are invariant under $\mathrm{SU}_L(3)\times\mathrm{SU}_R(3)$. The coefficients for these terms are called *low-energy constants*. The number of allowed operators increases considerably as we go to higher order in p^2. Even though most of them are correction terms, some physically important processes first appear in ChPT only when we go to higher order. For instance, if one wants to study the ρ-meson resonance contribution to a_μ^{hvp}, one should go to $\mathrm{O}(p^6)$[BR16a]. For our purpose, it suffices to stop with the terms that we found at $\mathrm{O}(p^2)$.

[4] A pedagogical review can be found in Ref. [Sch03].

The Wess-Zumino-Witten term

A ChPT Lagrangian preserving only $SU(3)_L \times SU(3)_R$ can not reproduce physical processes which are possible due to the ABJ-anomaly, such as $\pi^0 \to \gamma\gamma$. A term introduced by Wess and Zumino [WZ71] and Witten [Wit83] fills up the gap. Here, we review briefly the construction of the Wess-Zumino-Witten (WZW) term as given in Ref. [GL85].

The external field θ in Eq. (5.3) breaks the $U(1)_A$ symmetry. Consider a local $U(3)_L \times U(3)_R$ infinitesimal chiral transformation of the quark field,

$$\begin{aligned} V_R(x) &= 1 + i\alpha(x) + i\beta(x) + \dots , \\ V_L(x) &= 1 + i\alpha(x) - i\beta(x) + \dots . \end{aligned} \tag{5.11}$$

In order to account for the anomaly, we require θ to undergo an infinitesimal transformation [GL84]

$$\delta\theta(x) = -2\mathrm{Tr}_f\beta . \tag{5.12}$$

Note that here α and β are two Hermitian-matrix-valued fields. Obviously, if we had stayed with $SU(3)_L \times SU(3)_R$ transformations, α and β would have been traceless and $\delta\theta$ would have been identically zero.

Now, we require the field U to transform according to Eq. (5.8), with V_R and V_L taking the infinitesimal form Eq. (5.11) with $\alpha(x) = 0$. In this case, everything is parametrized by the angle $\beta(x)$. The anomaly is reproduced by introducing an extra generating functional Z_A which transforms properly under this infinitesimal transformation to our effective theory. One can write down explicitly the change that this infinitesimal transformation induces to the generating functional of the underlying theory (QCD) and require Z_A to transform infinitesimally in the same way. This amounts to solving a differential equation in Z_A, which is itself a functional in the external fields and the field U. As the transformation of the field U under the symmetry group is known, one can impose a boundary condition at $U = \mathbb{I}$ and then the problem is well-posed. At leading order in $1/F_0$, the solution for Z_A is

$$Z_A[v, a, U] = \frac{N_c}{16\pi^2} \int dx \mathrm{Tr}[\beta(x)\epsilon^{\alpha\beta\mu\nu} v_{\alpha\beta}(x) v_{\mu\nu}(x)] + \dots , \tag{5.13}$$

where $v_{\mu\nu}$ is the field strength of the external field v_μ and N_c is the number of colors. This leading order term corresponds to the $\pi^0 \to \gamma\gamma$ vertex.

5.1.2 U(3) Chiral Perturbation Theory

In nature, it is observed that the η-meson mixes with the flavor-singlet pseudoscalar meson η'. Even though the latter has a much higher mass — a puzzle known as the $U(1)_A$ problem — the η/η'-mixing makes it important to account for the dynamics of η' for physics at long-distances. A possible scenario that one can use to include η' in the established $SU(3)$ ChPT is to extend the Goldstone fields to $U(3)$-valued ones [GL85]. The outcome of this scheme is that the flavor-eigenstates (η, η') are rotated by a *mixing angle* to the eigenstates of the mass matrix due to the non-degeneracy of quark masses. Although many other possible schemes for the η/η'-mixing inspired by phenomenology do exist, for instance one can introduce two mixing angles instead of one [FKS98], we will focus on the construction with $U(3)$-nonet pseudoscalar mesons proposed in Ref. [GL85]. For simplicity we assume the mass-degeneracy for the light-quarks, i.e. $m_u = m_d$. In order to keep the notational coherence compared to Ref. [GL85], the expressions in this sub-section are given in

Minkowski space-time. Also, the field definition being taken from the reference, a scaling by the decay constant would be required to go back to the usual definition that we introduced previously. These subtleties should not be confusing as we go back to the original convention that we started with after this subsection.

Analogously to the previous case, we regroup the 8 flavor-octet and 1 flavor-singlet pseudoscalar mesons into

$$U(x) = \tilde{U}(x) \exp\left(\frac{1}{3} i\phi_0(x)\mathbb{I}\right), \tag{5.14}$$

where $\tilde{U}(x) = \exp\left(i\phi(x)\right)$ contains the usual octet mesons with unitary determinant and ϕ_0 is a flavor-singlet real field. These flavor-nonet fields are Goldstone bosons of the spontaneous breaking of the symmetry group $\mathrm{U}(3)_L \times \mathrm{U}(3)_R$ to $\mathrm{U}(3)_V$. A noticeable difference here compared to the previous SU(3) case is the interplay between the ABJ-anomaly and the flavor-singlet field via the external field θ. Due to the relaxation of the unit determinant condition on $U(x)$, the construction of Ref. [GL85] demands θ to enter as

$$\det U(x) = e^{-i\theta(x)}, \tag{5.15}$$

and be related to the external axial current via the covariant derivative

$$D_\mu \theta = \partial_\mu \theta + 2\mathrm{Tr} a_\mu . \tag{5.16}$$

Eq. (5.15) implies that $\phi_0 + \theta$ is invariant under $\mathrm{U}(3)_L \times \mathrm{U}(3)_R$ chiral transformations. Therefore, at order p^2, the most general chiral Lagrangian can be parametrized as

$$\begin{aligned} \mathcal{L}_1 = &- V_0 + V_1 \mathrm{Tr}[D_\mu U^\dagger D^\mu U] + V_2 \mathrm{Tr}[(s - ip)U] + V_2^* \mathrm{Tr}[(s + ip)U^\dagger] \\ &+ V_3 D_\mu \phi_0 D^\mu \theta + V_4 D_\mu \theta D^\mu \theta + V_5 D_\mu \phi_0 D^\mu \phi_0 , \end{aligned} \tag{5.17}$$

where

$$D_\mu \phi_0 = \partial_\mu \phi_0 - 2\mathrm{Tr} a_\mu = -i\mathrm{Tr}[U^\dagger D_\mu U] , \tag{5.18}$$

$$V_i = V_i(\phi_0 + \theta) . \tag{5.19}$$

Note that V_5 can be eliminated by re-parametrizing the fields and apart from V_2, the V_i's are real functions. All of the V_i's satisfy

$$V_i(\alpha) = V_i^*(-\alpha) , \tag{5.20}$$

as required by symmetry under parity.

Large-N_c limit

Similar arguments can be applied to infer the behaviors of the V_i's at large-N_c limit. Using the same notations and conventions as in Ref. [GL85], define

$$G_{QW} = \langle 0 | T\{j_1(x_1) \cdots j_Q(x_Q) \omega(y_1) \cdots \omega(y_W)\} | 0 \rangle_c , \tag{5.21}$$

where

$$j_i = \bar{q} \Gamma_i q , \quad \omega = \frac{1}{16\pi^2} \mathrm{Tr}(G\tilde{G}) , \tag{5.22}$$

and the Γ's are matrices acting on the spinor space.

An N_c-counting gives[5]

$$G_{QW} = \begin{cases} \mathrm{O}(N_c^{2-W}) & \text{if } Q = 0\,, \\ \mathrm{O}(N_c^{1-W}) & \text{if } Q \neq 0\,. \end{cases} \tag{5.23}$$

For $\alpha = \phi_0 + \theta$, we have

$$\begin{gathered} V_0(\alpha) = N_c^2 v_0\left(\frac{\alpha}{N_c}\right)\,, \quad V_1(\alpha) = N_c v_1\left(\frac{\alpha}{N_c}\right)\,, \quad V_2(\alpha) = N_c v_2\left(\frac{\alpha}{N_c}\right)\,, \\ V_3(\alpha) = v_3\left(\frac{\alpha}{N_c}\right)\,, \quad V_4(\alpha) = v_4\left(\frac{\alpha}{N_c}\right)\,, \end{gathered} \tag{5.24}$$

where the functions $v_i(x)$'s are analytical in the argument and of order $\mathrm{O}(1)$ at large-N_c. In the case of $U(3)$, it is then easy to get the N_c-dependence of the η/η' mixing angle and their mass eigenvalues. In particular, with the assumption that η' is heavier than η, in the vanishing-quark-mass limit, the η' mass squared $M_{\eta'}^2$ is of $\mathrm{O}\left(N_c^{-1}\right)$. On the other hand, at $N_c \to \infty$ with non-vanishing quark masses, η is degenerate with the pion and the ratio $M_{\eta'}^2/M_\eta^2$ equals that of the strange-quark to the light-quark .

5.2 Partially-Quenched Chiral Perturbation Theory

In Lattice QCD, different contraction topologies are often treated separately due to the computational cost (propagator solves, color- and spin-contractions etc). Although the use of an EFT allows to estimate hadronic correlation functions with all Feynman diagrams included, sometimes it is more interesting to study a particular Wick-contraction class rather than the entire correlation function. As a quark field can only be contracted with another anti-quark field with the same flavor, if enough quark species are present in the theory, one can construct correlation functions which involve only certain contraction diagrams that we are interested in. One can then interpret the same correlation function in the desired EFT and give an estimate of it. For example, in $N_f = 2+1$ QCD with mass-degenerate up- and down-quarks, the 2-point correlation function

$$\langle \bar{u}\Gamma_i d(x)\bar{d}\Gamma_j u(y)\rangle\,, \tag{5.25}$$

only receives a contribution from the light-quark-connected diagram. However, this separation is not always possible. For instance, one can not write down a 4-point with only quark-connected diagrams in an $N_f = 2+1$ QCD. A way to enlarge the number of quark species without changing the underlying theory is to introduce pairs of mass-degenerate quark and ghost to the theory. Formally, this amounts to applying the following modification to the Euclidean QCD path integral measure

$$\begin{aligned} &\mathcal{D}[U]\prod_f\left(\mathcal{D}[\bar{\psi}_f]\mathcal{D}[\psi_f]\right)e^{-S_G-\int_x\sum_f\bar{\psi}_f D_f\psi_f} \\ &\longrightarrow \mathcal{D}[U]\prod_f\left(\mathcal{D}[\bar{\psi}_f]\mathcal{D}[\psi_f]\right)\prod_h\left(\mathcal{D}[\bar{q}_h]\mathcal{D}[q_h]\mathcal{D}[\tilde{q}_h^\dagger]\mathcal{D}[\tilde{q}_h]\right)e^{-S_G-\int_x\left[\sum_f\bar{\psi}_f D_f\psi_f+\sum_h\left(\bar{q}_h D_h q_h+\tilde{q}_h^\dagger D_h\tilde{q}\right)\right]}\,, \end{aligned} \tag{5.26}$$

[5]Note that the convention used in Ref. [GL85] for the coupling constant differs from some other popular choices, e.g. the one in Ref. [Wit79], in terms of the N_c-scaling.

where U is the gauge field, S_G is the pure gauge action, ψ_f and $\bar{\psi}_f$ are the original sea quark/anti-quark fields with flavor f, the $(q_h, \tilde{q}_h$'s are the pairs of introduced quark and ghost fields with flavor h and the D_i's are the Dirac operators for the flavor i with the mass term contained. Note that the ghost fields $\tilde{q}_h$'s take values as commuting number, unlike the quark fields. The extra quarks from these pairs are called *quenched* because their contribution in the sea gets cancelled by the one coming from their ghost partners.[6] Nevertheless, they can still be used as valence quarks and one can build correlation functions with them. A theory built in this way with a non-zero number of dynamical quarks in the underlying theory is called *partially-quenched*. For instance, if we introduce two quark/ghost pairs $(p, \tilde{p})$ and $(q, \tilde{q})$ with the same mass as the light-quarks to our $N_f = 2+1$ QCD, the 4-point correlation function

$$\langle \bar{u}\Gamma_i d(x)\bar{d}\Gamma_j p(y)\bar{p}\Gamma_k q(z)\bar{q}\Gamma_l u(w)\rangle\,, \tag{5.27}$$

will contain only the light-quark-connected contribution.

Using Partially-Quenched QCD (PQQCD) to determine the contribution of a particular contraction diagram in an EFT has been broadly applied in LQCD studies (e.g. Refs. [BG92; SS00; DTWL06; GL09; DMJ10]). For the purpose of studying $a_\mu^{\rm hlbl}$ on the lattice with $N_f = 2+1$ QCD, we will find the following theories useful:

(i) A PQQCD with dynamical up-, down- and strange-quark supplemented with 2 quenched quarks and their ghost partners at the mass of the light-quark mass.

(ii) A PQQCD with dynamical up-, down- and strange-quark supplemented with 3 quenched quarks and their ghost partners at the mass of the strange-quark mass.

We will refer them as PQQCD (i) and PQQCD (ii). As the two major known contributions to $a_\mu^{\rm hlbl}$ at long-distances are the neutral-pseudoscalar-meson exchange and the charged-pseudoscalar-meson loop, we want to gain some insight by figuring out how they contribute to each individual Wick-contraction up to leading order in ChPT. To do so, we will explain how one gets the relevant Feynman rules in the two Partially-Quenched Chiral Perturbation Theories (PQChPTs) corresponding to the aforementioned PQQCD respectively, with or without taking into account the η/η'-mixing. The construction is based on graded Lie groups, which encodes properly the required symmetry of the flavor space.

5.2.1 Graded Lie groups

The ghost partner of a quenched quark has to satisfy the Bose-statistics to cancel the sea effect of the quenched quark. At the chiral limit, a fundamental difference compared to N_f-flavor QCD is that the flavor symmetry group can not be only the special unitary Lie group $\mathrm{SU}(N_f)$: it has to be promoted to a *graded Lie group* [BG92]. More precisely, for a PQQCD theory with $N-M$ dynamical quarks and M quenched quarks and their ghost partners, we require the quark/ghost flavor symmetry group

[6] The pairs of quark and ghost are introduced in the same bilinear form. Due to their different spin-statistics, the resulting determinants after the quenched quark and ghost fields integrated out cancel each other, so the underlying theory remains the same. This is similar to the pseudo-fermion technique explained in Sect. 2.2.2.

to be the graded Lie group SU$(N|M)$ (or U$(N|M)$ to include the flavor singlet pseudoscalar meson).[7] We will recall some useful definitions and properties for the group SU$(N|M)$ following Ref. [FSS96], relevant for our construction of the corresponding PQChPT.

Let $\mathcal{A}$ be an algebra over a field $\mathbb{K} = \mathbb{R}$ or $\mathbb{C}$. $\mathcal{A}$ is a ($\mathbb{Z}_2$-)*graded algebra*, or *superalgebra*, if $\mathcal{A}$ can be written as a direct sum of two spaces $\mathcal{A} = \mathcal{A}_0 \oplus \mathcal{A}_1$, such that the multiplication of the algebra acts on the two subspaces as [FSS96]

$$\mathcal{A}_0 \cdot \mathcal{A}_0 \subset \mathcal{A}_0\,, \quad \mathcal{A}_0 \cdot \mathcal{A}_1 \subset \mathcal{A}_1\,, \quad \mathcal{A}_1 \cdot \mathcal{A}_1 \subset \mathcal{A}_0\,. \tag{5.28}$$

We say that an element $X \in \mathcal{A}$ is of degree $\deg X = 0$ if $X \in \mathcal{A}_0$ and $\deg X = 1$ if $X \in \mathcal{A}_1$.

We define the *super-commutator* of two elements $X, Y \in \mathcal{A}$ as

$$[X, Y] = XY - (-1)^{\deg X \times \deg Y} YX\,. \tag{5.29}$$

Consider a real or complex Grassmann algebra $\Gamma(n)$ generated by $\{1, \theta_1, \ldots, \theta_n\}$, where the θ_i's are Grassmann numbers. We use the decomposition $\Gamma(n) = \Gamma_{\bar{0}}(n) \oplus \Gamma_{\bar{1}}(n)$, where $\Gamma_{\bar{0}}(n)$ is generated by monomials of an even number of θ_i's and $\Gamma_{\bar{1}}(n)$ is generated by monomials of an odd number of θ_i's. In other words, $\Gamma_{\bar{0}}$ is the commuting sector and $\Gamma_{\bar{1}}$ is the anti-commuting one. We define the *Grassmann envelope* of $\mathcal{A}$ over $\Gamma(n)$ the linear combination $\sum_i \eta_i a_i$ where $\{a_i\}$ is a basis of $\mathcal{A}$ and $\eta_i \in \Gamma(n)$. We will omit the number of Grassmann generators n in the following.

Finally, a graded Lie group, or *Lie supergroup*, is built via the exponential mapping of the Grassmann envelope of $\mathcal{A}$. Under this framework, in analogy to the usual SU(3)-ChPT case discussed previously, the "meson" fields, entering as the coefficients taking values in Γ accompanying the group generators in a given basis, can be either commuting or anti-commuting numbers, which is desired because of the different spin-statistics between quarks and ghosts.

Supermatrices

Let $N, M \in \mathbb{N}$ and $K \in \mathbb{M}_{(N+M)\times(N+M)}(\Gamma)$ such that

$$K = \begin{pmatrix} A & B \\ C & D \end{pmatrix}\,, \tag{5.30}$$

where

$$A \in \mathbb{M}_{N\times N}(\Gamma)\,, \quad B \in \mathbb{M}_{N\times M}(\Gamma)\,, \quad C \in \mathbb{M}_{M\times N}(\Gamma)\,, \quad D \in \mathbb{M}_{M\times M}(\Gamma)\,. \tag{5.31}$$

We say that K is of degree $\deg K = 0$ if A and D take entries in Γ_0 and B and C take entries in Γ_1, and of degree $\deg K = 1$ if A and D take entries in Γ_1 and B and C take entries in Γ_0. We call such a matrix *supermatrix*.

The multiplication of supermatrices is exactly the same as the usual matrix product. The transpose and the adjoint of a supermatrix are also defined in the same

[7] In fact, it has been pointed out in Ref. [SS01] that this choice for the symmetry group alone does not lead to a well-defined field theory and additional constraints need to be supplemented in order to remedy the problem with a well-behaved path-integral measure. However, it is also argued in the same reference that the use of this "fake" symmetry group should not be problematic, if only perturbative properties within the resulting effective field theory are to be studied.

usual ways. We say that a supermatrix K is invertible if there exists supermatrix K' such that $KK' = K'K = \mathbb{I}$.

We define the *supertrace* of K, $\mathrm{str}(K)$, as

$$\mathrm{str}(K) \equiv \mathrm{Tr}(A) - (-1)^{\deg K}\mathrm{Tr}(D)\,, \tag{5.32}$$

and the *superdeterminant* of an invertible supermatrix K, $\mathrm{sdet}(K)$ as

$$\mathrm{sdet}(K) \equiv \frac{\det(A - BD^{-1}C)}{\det(D)}\,. \tag{5.33}$$

Finally, the following relation holds

$$\mathrm{sdet}\big(\exp(K)\big) = \exp\big(\mathrm{str}(K)\big)\,. \tag{5.34}$$

For our construction of PQChPTs, we will only work with supermatrices of degree 0 and $\mathbb{K} = \mathbb{C}$ Grassmann algebras for the rest of the chapter. The vector space of supermatrices allows us to define a graded Lie algebra. With the notations used earlier, we have for the decomposition of the vector space $\mathcal{A} = \mathcal{A}_0 \oplus \mathcal{A}_1$,

$$\mathcal{A}_0 = \left\{ \begin{pmatrix} A & 0 \\ 0 & D \end{pmatrix} \Big| A \in \mathbb{M}_{N\times N}(\Gamma)\,, \quad D \in \mathbb{M}_{M\times M}(\Gamma) \right\}\,, \tag{5.35}$$

$$\mathcal{A}_1 = \left\{ \begin{pmatrix} 0 & B \\ C & 0 \end{pmatrix} \Big| B \in \mathbb{M}_{N\times M}(\Gamma)\,, \quad C \in \mathbb{M}_{M\times N}(\Gamma) \right\}\,. \tag{5.36}$$

Unitary and special unitary graded Lie groups and their Lie algebras

We define the *unitary graded Lie group* $\mathrm{U}(N|M)$ and the *special unitary graded Lie group* $\mathrm{SU}(N|M)$:

$$\mathrm{U}(N|M) \equiv \{K \in \mathbb{M}_{(N+M)\times(N+M)}(\Gamma) \,|\, KK^\dagger = K^\dagger K = \mathbb{I}\}\,, \tag{5.37}$$

$$\mathrm{SU}(N|M) \equiv \{K \in \mathrm{U}(N|M) \,|\, \mathrm{sdet}(K) = 1\}\,. \tag{5.38}$$

They are generated by Hermitian matrices and super-traceless Hermitian matrices respectively.

For $\mathrm{SU}(N|M)$, we will find it convenient to work with the generator basis $I \cup J \cup W$, where

$$\begin{aligned} I &= \left\{ C^{ij} \,|\, 1 \le i < j \le N+M, \quad (C^{ij})_{ab} = \frac{1}{2}(\delta_{ai}\delta_{bj} + \delta_{aj}\delta_{bi}) \right\}, \\ J &= \left\{ D^{ij} \,|\, 1 \le i < j \le N+M, \quad (D^{ij})_{ab} = \frac{i}{2}(\delta_{ai}\delta_{bj} - \delta_{aj}\delta_{bi}) \right\}. \end{aligned} \tag{5.39}$$

$$W = \left\{ \frac{1}{\sqrt{2|\mathrm{str}[(B^j)^2]|}} B^j \Big| 1 \le j \le N+M-1,\, B^j = \mathrm{diag}(\underbrace{1,\cdots,1}_{j}, a_j, \underbrace{0,\cdots,0}_{N+M-1-j}) \right\}, \tag{5.40}$$

with

$$a_j = \begin{cases} -j & \text{if } j \le N-1, \\ 2N - j & \text{otherwise.} \end{cases} \tag{5.41}$$

Analogous to the pseudoscalar meson content in SU(3)-theory, we will call the set of off-diagonal elements $I \cup J$ the "charged" sector and W the "neutral" sector. Also, we will call the element of W generated by B^1 "π^0".

This choice of generator basis satisfies the normalization condition similar to the one used for the Gell-Mann matrices in SU(3). Upon appropriate enumeration, for any two generators T^a and T^b belonging to the basis described above,

$$\mathrm{str}(T^a T^b) = \frac{1}{2} g_{ab}, \tag{5.42}$$

where

$$g = \begin{pmatrix} \mathbb{I}_{(N^2-1)\times(N^2-1)} & 0 & 0 \\ 0 & \mathbb{I}_{MN\times MN} \otimes (-\sigma_2) & 0 \\ 0 & 0 & -\mathbb{I}_{M^2\times M^2} \end{pmatrix}, \quad \sigma_2 = \begin{pmatrix} 0 & -i \\ i & 0 \end{pmatrix}. \tag{5.43}$$

Having a basis of generators for SU$(N|M)$, we can extend it to a basis of generators of U$(N|M)$ easily by adding an element with non-vanishing trace:

$$T^0 = \frac{1}{\sqrt{2(N-M)}} \mathbb{I}. \tag{5.44}$$

With this choice, the normalization Eq. (5.42) can remain valid upon substituting the metric g in Eq. (5.43) by

$$\bar{g} = \begin{pmatrix} 1 & \mathbf{0} \\ \mathbf{0} & g \end{pmatrix}. \tag{5.45}$$

In the following, if not specified, we will use T^i to denote generators of the considered graded Lie group in the so-far constructed basis. In particular, the index 0 will be used to indicate the flavor-singlet sector.

5.2.2 The kinetic part of the chiral SU$(N|M)$ Lagrangian

We will state in this section how to construct a PQChPT theory and especially we will give a general computational strategy that we employ to get the propagators. Consider now a PQQCD theory with $N - M$ dynamical quarks, $r_1, \ldots r_{N-M}$, and M pairs of quenched quark and ghost, $(t_1, \tilde{t}_1), \ldots (t_M, \tilde{t}_M)$. We group all of them together into one quark field

$$q' = (r_1, \ldots, r_{N-M}, t_1, \ldots, t_M, \tilde{t}_1, \ldots, \tilde{t}_{N-M})^\intercal. \tag{5.46}$$

Then, the PQQCD Lagrangian in the chiral limit, Eq. (5.2) with q replaced by q', is invariant under global U$(N|M)_L \times$U$(N|M)_R$ transformations at classic level. The same rationale used for SU(3)-ChPT can thus be applied straightforwardly to construct a PQChPT. We put all the (pseudo-)Goldstone bosons/fermions into one field which they generate in the same way as Eq. (5.6) and require it to transform under local SU$(N|M)_L \times$SU$(N|M)_R$ as Eq. (5.8). To arrive at a Lagrangian which is invariant under global SU$(N|M)_L \times$SU$(N|M)_R$, one simply has to replace the traces appearing in Eq. (5.10) by super-traces to guarantee the invariance of the Lagrangian.

For simplicity, we will assume that there are only two possible values for the quark masses for the quark species appearing in our PQQCD: either the light-quark mass m_l or the strange-quark mass m_s. If one considers a perturbation around the

external fields $s = \mathrm{diag}(m_l, m_l, m_s, \ldots)$ and $p = 0$[8], the kinetic part of the PQChPT Lagrangian in Euclidean space-time can then be arranged as

$$\mathcal{L}^{\mathrm{E}}_{\mathrm{kin}} = \frac{1}{2} g_{ab} \left(\partial_\mu \phi^a \partial_\mu \phi^b + M_\pi^2 \phi^a \phi^b \right) + \frac{1}{2} \Delta M^2 K_{ab} \phi^a \phi^b , \tag{5.47}$$

where, motivated by the physical meson mass eigenstates,

$$M_\pi^2 \equiv 2B_0 m_l \,, \quad M_K^2 \equiv B_0 (m_l + m_s) \,, \tag{5.48}$$

and

$$\Delta M^2 = M_K^2 - M_\pi^2 \,, \quad K_{ab} = 4\,\mathrm{str}[\mathcal{S} T^a T^b]. \tag{5.49}$$

The repeated indices a and b are implicitly summed over the whole generator basis. Here $\mathcal{S}$ is an $(N+M) \times (N+M)$ diagonal matrix which is related to the quark species of the underlying PQQCD, where the quark fields live in the fundamental representation of $\mathrm{SU}(N|M)$. For our purpose, we require the underlying PQQCD to be an extension of $N_f = 2+1$ QCD by setting $\mathcal{S} = \mathrm{diag}(0, 0, 1, \cdots)$. Under this convention, the first two positions in the fundamental representation correspond to the u- and d-quark, the third to the s-quark and the remaining are quenched quarks and their ghost counterparts. The remaining elements of $\mathcal{S}$ are set in the following way: $\mathcal{S}_{ii} = 0$ if the i-th quark in the underlying PQQCD is of mass m_l and $\mathcal{S}_{ii} = 1$ if it is of mass m_s.

To determine whether a field ϕ^a is bosonic or fermionic, one can infer from the generator T^a to which the field is associated: it is a boson if $T^a \in \mathcal{A}_0$ and fermion if $T^a \in \mathcal{A}_1$.[9] This can also be understood from the quark content of a meson. By construction, if a meson contains a pair of quark/anti-quark (quenched or not) or ghost/anti-ghost, it is a boson; if it contains one (anti-)quark and one (anti-)ghost, then it is a fermion. As a remark, the self-consistency of the Lagrangian is guaranteed by the following lemmas:

- **Lemma 1**: $\forall a, b$ and field ϕ (bosonic or fermionic), $\mathrm{str}(T^a T^b)\phi^a \phi^b = \mathrm{str}(T^b T^a)\phi^b \phi^a$.
- **Lemma 2**: $\forall a, b$ and field ϕ (bosonic or fermionic), $[T^a, T^b]\phi^a \phi^b = -[T^b, T^a]\phi^b \phi^a$. Here, $[\cdot, \cdot]$ is the super-commutator.

The propagator

The propagators can be inferred from the kinetic part of the PQChPT Lagrangian Eq. (5.47). We will give here the recipe that we use to get the propagators for the two theories PQChPT(i) and PQChPT(ii) corresponding respectively to PQQCD(i) and PQQCD(ii) introduced in the beginning of this section. It turns out that the propagators in both theories take the form [GL09]

$$S_{ab}(x) = g_{ab} G_1(x, M_{ab}) - \Delta M^2 \tilde{H}_{ab} G_2(x, M_{ab}, \tilde{M}_{ab}) \,, \tag{5.50}$$

where

$$G_1(x, m) = \int d^4 p \, \frac{e^{ipx}}{p^2 + m^2}, \quad G_2(x, m_1, m_2) = \int d^4 p \, \frac{e^{ipx}}{(p^2 + m_1^2)(p^2 + m_2^2)}. \tag{5.51}$$

[8] c.f. Eq. (5.10) for notations.
[9] c.f. Eq. (5.35) and Eq. (5.36).

The mass parameters, M_{ab} and $\tilde{M}_{ab}$, and the matrix $\tilde{H}$ depend on the PQChPT but only the neutral sector with strange-quark content is affected by the propagator mixing induced by the second term on the right-hand side of Eq. (5.50), due to flavour-symmetry breaking.

The rationale of the ansatz Eq. (5.50) goes as follows. If we can find a diagonal matrix D such that

$$\exists \lambda \in \mathbb{R}, \quad (\tilde{K}g)^2 = \lambda \tilde{K}g\,, \quad \tilde{K} \equiv K - D\,, \tag{5.52}$$

a solution for $\tilde{H}$ is

$$\tilde{H}_{ab} = (g\tilde{K}g)_{ab}\,, \tag{5.53}$$

and the matrix D defines the mass parameters

$$M_{ab}^2 = M_\pi^2 + (gD)^{ab}\Delta M^2\,, \tag{5.54}$$

$$\tilde{M}_{ab}^2 = M_{ab}^2 + \lambda \Delta M^2\,. \tag{5.55}$$

We are able to use this strategy to get the propagators for the partially quenched theory that we are interested in. In the charged meson sector, for both PQChPT(i) and PQChPT(ii), we have $H_{ab} = 0$ and

$$M_{ab}^2 = \begin{cases} M_\pi^2 & \text{if the underlying PQQCD content is light-light,} \\ M_K^2 & \text{if the underlying PQQCD content is light-strange,} \\ M_{\bar{s}s}^2 \equiv M_\pi^2 + 2\Delta M^2 & \text{if the underlying PQQCD content is strange-strange.} \end{cases} \tag{5.56}$$

For the neutral sector, the results for PQChPT(i) and PQChPT(ii) are as follows:

(i)

$$M_{ab}^2 = M_\pi^2\,, \quad \tilde{M}_{ab}^2 = M_\pi^2 + \frac{4}{3}\Delta M^2\,, \quad \tilde{H}_{ab} = (gKg)_{ab}, \tag{5.57}$$

(ii)

$$\begin{aligned} M_{ab}^2 &= \begin{cases} M_\pi^2 & \text{for } a = b = \pi^0, \\ M_{\bar{s}s}^2 & \text{else,} \end{cases} \\ \tilde{K}_{ab} &= \begin{cases} K_{ab} & \text{for } a = b = \pi^0, \\ K_{ab} - 2g_{ab} & \text{else,} \end{cases} \\ \tilde{M}_{ab}^2 &= M_{ab}^2 - \frac{2}{3}\Delta M^2\,, \quad \tilde{H}_{ab} = (g\tilde{K}g)_{ab}. \end{aligned} \tag{5.58}$$

5.2.3 The kinetic part of the chiral U($N|M$) Lagrangian

Now let us work out the kinetic part of the U($N|M$) Lagrangian and the propagators. The flavor-singlet meson, which we will call η' for convenience, will mix with other flavor-octet ones in the neutral sector with quark/ghost constituents with a mass of m_s. Moreover, one also has to introduce another mass scale for the mass-splitting between η and η' in the underlying U(3) ChPT, which leads to higher technical complexity. Although this can be done much more easily in a different choice of generator basis [BG94], we will present our recipe for getting the propagators for PQChPT(i) and PQChPT(ii) starting from the generator basis given at the beginning of the section, due to the fact that it is more closely related to the physical states.

To construct the chiral Lagrangian, we shall again figure out operators invariant under flavor symmetry transformation. Analog to the SU$(N|M)$ case, the operators involving traces become invariant under global U$(N|M)_L\times$U$(N|M)_R$ transformations if one replaces the traces in the operators with supertraces. The coupling to the anomaly, however, involves the determinant of the unitary field U [Eq. (5.15)]. This is rendered U$(N|M)_L\times$U$(N|M)_R$-invariant if we replace the determinant by the superdeterminant. Upon these modifications, we get the kinetic term of the U$(N|M)$ chiral Lagrangian from Eq. (5.17)[10]

$$\begin{aligned}\mathcal{L}^{(2)}_{\text{kin}} =& -\frac{4}{2F_0^2}V_0''(0)\phi_0^2+\frac{4V_1(0)}{F_0^2}\partial_\mu\phi^a\partial^\mu\phi^b\text{str}[T^aT^b]\\ &+\frac{4}{F_0^2}V_2''(0)\phi_0^2\text{str}[\mathcal{M}]+\frac{8i}{F_0^2}\phi_a\phi_0V_2'(0)\text{str}[\mathcal{M}T^a]-\frac{4}{F_0^2}V_2(0)\phi_a\phi_b\text{str}[\mathcal{M}T^aT^b]\\ =&\frac{4V_1(0)}{F_0^2}\Big(\frac{1}{2}\partial_\mu\phi^a\partial^\mu\phi^b\bar{g}_{ab}-\frac{1}{2}M_\pi^2\phi_a\phi_bg^{ab}\\ &-\frac{1}{2}\Delta M^2K_{ab}\phi^a\phi^b-\frac{1}{2}\Delta\mathring{M}^2_{\eta'}\phi_0^2-\frac{1}{2}\Delta\bar{M}^2\mathring{K}_{ab}\phi^a\phi^b\Big)\,,\end{aligned} \tag{5.59}$$

where

$$M_\pi^2\equiv\frac{V_2(0)}{V_1(0)}m_l\,,\quad M_K^2\equiv\frac{m_s+m_l}{2m_l}M_\pi^2\,,\quad \Delta M^2\equiv M_K^2-M_\pi^2\,,\quad K_{ab}\equiv 4\text{str}[\mathcal{S}T^aT^b]\,, \tag{5.60}$$

$$\Delta\mathring{M}^2_{\eta'}\equiv\frac{V_0''(0)}{V_1(0)}-\Big(\frac{2V_2''(0)}{V_1(0)}+\frac{1}{\sqrt{2(N-M)}}\frac{4iV_2'(0)}{V_1(0)}\Big)\text{str}[\mathcal{M}]\,, \tag{5.61}$$

$$\Delta\bar{M}^2\equiv-\frac{4iV_2'(0)}{\sqrt{2(N-M)}V_1(0)}\Delta M^2\,, \tag{5.62}$$

$$\mathring{K}_{ab}\equiv\begin{cases}\Big(\text{str}[\mathcal{S}T^a]\delta_{b0}+\text{str}[\mathcal{S}T^b]\delta_{a0}\Big)\,, & \text{if } (a,b)\neq(0,0)\,,\\ 0\,, & \text{else.}\end{cases} \tag{5.63}$$

Note that the expressions for the meson masses-squared are different from the SU$(N|M)$ case. However, by matching the U$(N|M)$-PQChPT to the SU$(N|M)$ one at the limit where η' is integrated out (heavy and non-dynamical), we should be able to identify the parameters in both theories.

Derivation of the propagators

It might seem more complicated to get the propagators with the extra mixing term K_{ab}, but in fact a rescaling in the field ϕ_0 will bring the situation back to the known case. Define

$$\begin{aligned}&\tilde{\phi}_0=\Lambda\phi_0\,,\quad \Lambda\equiv 1-\frac{iV_2'(0)}{V_1(0)}\,,\\ &\tilde{\phi}_a=\phi_a\,,\quad \text{if } a\neq 0\,.\end{aligned} \tag{5.64}$$

[10] Note that here we use the definition of the meson field Eq. (5.6), which contains a rescaling by the decay constant.

Then, the term giving rise to the mixing between the flavor-multiplet and flavor-singlet sectors in Eq. (5.59) can be written as, for $b \neq 0$

$$\phi_0\Big(K_{0b}\Delta M^2 + \mathring{K}_{0b}\Delta\bar{M}^2\Big)\phi_b = \Delta M^2\Big(1 - \frac{iV_2'(0)}{V_1(0)}\Big)\phi_0 K_{0b}\phi_b = \Delta M^2\tilde{\phi}_0 K_{0b}\tilde{\phi}_b\,. \quad (5.65)$$

The rescaling Eq. (5.64) allows us to normalize the non-diagonal part of the mixing matrix. Nonetheless, the rescaling also affects the splitting mass of η' and would thus require a redefinition of the $\mathrm{U}(N|M)$ group metric $\bar{g}$ [Eq. (5.45)]. We introduce

$$\tilde{g} = \begin{pmatrix} \Lambda^{-2} & \mathbf{0} \\ \mathbf{0} & g_{SU(N|M)} \end{pmatrix}, \quad (5.66)$$

and

$$\Delta M_{\eta'}^2 = \Lambda^{-2}\Delta\mathring{M}_{\eta'}^2 + (\Lambda^{-2} - 1)K_{00}\Delta M^2\,. \quad (5.67)$$

Then, the Euclidean space-time version of Eq. (5.59) can then be written in a simpler form

$$\mathcal{L}_{\mathrm{kin}}^{\mathrm{E}} = \frac{1}{2}\tilde{g}_{ab}\Big(\partial_\mu\tilde{\phi}_a\partial_\mu\tilde{\phi}_b + M_\pi^2\tilde{\phi}_a\tilde{\phi}_b\Big) + \frac{1}{2}\Delta M^2 K_{ab}\tilde{\phi}_a\tilde{\phi}_b + \frac{1}{2}\Delta M_{\eta'}^2(\tilde{\phi}_0)^2\,. \quad (5.68)$$

Due to the splitting η'-splitting mass, our previous strategy for propagator solving for $\mathrm{SU}(N|M)$-theories can not be directly applied. Nonetheless, we can borrow a technique used in Ref. [Gol09].

Rewrite Eq. (5.68) equivalently as[11]

$$\mathcal{L}_{\mathrm{kin}}^{E} = \frac{1}{2}\tilde{\phi}_a\Gamma_{ab}\tilde{\phi}_b + \frac{1}{2}\Delta M_{\eta'}^2(\tilde{\phi}_0)^2\,, \quad (5.69)$$

where

$$\Gamma_{ab} = \tilde{g}_{ab}(-\Box + M_\pi^2) + \Delta M^2 K_{ab}\,. \quad (5.70)$$

Let us first state our way of getting the propagators and then justify its validity.

1. Find a matrix $D \propto \bar{g}$ and a real number λ such that

$$\big(\tilde{K}\tilde{g}^{-1}\big)^2 = \lambda\tilde{K}\tilde{g}^{-1}\,, \quad \tilde{K} = K - D\,. \quad (5.71)$$

2. Rewrite the Lagrangian in Euclidean space-time as

$$\mathcal{L}_{\mathrm{kin}}^{E} = \frac{1}{2}\tilde{\phi}_a\bar{\Gamma}_{ab}\tilde{\phi}_b + \frac{1}{2}\Delta\bar{M}_{\eta'}^2\tilde{\phi}_0^2\,, \quad (5.72)$$

where

$$\Delta\bar{M}_{\eta'}^2 = \Delta M_{\eta'}^2 + (1 - \Lambda^{-2})D_{00}\Delta M^2\,. \quad (5.73)$$

For the theories PQChPT(i) and PQChPT(ii) that we are interested in, $\bar{\Gamma}$ can be parametrized as

$$\bar{\Gamma}_{ab}^{-1}(x) = (\tilde{g}^{-1})_{ab}G_1(x, M_{ab}^2) - \Delta M^2 H_{ab}G_2(x, M_{ab}^2, \tilde{M}_{ab}^2)\,, \quad (5.74)$$

where

$$H = \tilde{g}^{-1}\tilde{K}\tilde{g}^{-1}\,, \quad M_{ab}^2 = M_\pi^2 + (\bar{g}^{-1}D)_{ab}\Delta M^2\,, \quad \tilde{M}_{ab}^2 = M_{ab}^2 + \lambda\Delta M^2\,. \quad (5.75)$$

[11] Up to a boundary term in the action.

The relevant matrices for each theory will be given later.

3. Finally, the U$(N|M)$ propagators can be solved by the ansatz

$$\begin{aligned} S_{ab}(x) = \quad & (\tilde{g}^{-1})_{ab} G_1(x, M_{ab}) \\ & - \Delta M^2 H_{ab} G_2(x, M_{ab}, \tilde{M}_{ab}) \\ & - \Delta \bar{M}^2_{\eta'} \Sigma_{ab} G_2(x, M_{ab}, \tilde{M}_{ab}) \\ & - \Delta M^2 \Delta \bar{M}^2_{\eta'} (\Theta_{ab} + \lambda \Sigma_{ab}) G_3(x, M_{ab}, M_\eta, M_{\eta'}) \\ & - \Delta \bar{M}^2_{\eta'} (\Delta M^2)^2 \Xi_{ab} G_4(x, M_{ab}, \tilde{M}_{ab}, M_\eta, M_{\eta'}) \,, \end{aligned} \tag{5.76}$$

where

$$\Sigma_{ab} \equiv (\tilde{g}^{-1})_{a0} (\tilde{g}^{-1})_{0b} \,, \quad \Theta_{ab} \equiv -\Big((\tilde{g}^{-1})_{a0} H_{0b} + H_{a0} (\tilde{g}^{-1})_{0b} \Big) \,, \quad \Xi_{ab} \equiv H_{a0} H_{0b} , \tag{5.77}$$

$$G_3(x, a, b, c) \equiv \int_p \frac{e^{ipx}}{(p^2 + a^2)(p^2 + b^2)(p^2 + c^2)} \,, \tag{5.78}$$

$$G_4(x, a, b, c, d) \equiv \int_p \frac{e^{ipx}}{(p^2 + a^2)(p^2 + b^2)(p^2 + c^2)(p^2 + d^2)} \,. \tag{5.79}$$

Proof of Eq. (5.76)

Define the matrix E^{00} with element

$$\left(E^{00}\right)_{ab} = \delta_{0a} \delta_{0b} \,. \tag{5.80}$$

Solving the propagator of the rescaled Lagrangian amounts to computing

$$\left(\bar{\Gamma} + \Delta \bar{M}^2_{\eta'} E^{00} \right)^{-1} = \Big(\mathbb{I} + \sum_{k=1} (-\Delta \bar{M}^2_{\eta'})^k (\bar{\Gamma}^{-1} E^{00})^k \Big) \bar{\Gamma}^{-1} \,. \tag{5.81}$$

Following the line of Ref. [Gol09], we note that

$$(E^{00} \bar{\Gamma}^{-1} E^{00})_{ad} = \delta_{a0} \delta_{b0} (\bar{\Gamma}^{-1})_{bc} \delta_{c0} \delta_{d0} = (\bar{\Gamma}^{-1})_{00} \left(E^{00}\right)_{ad} \,. \tag{5.82}$$

As a result, Eq. (5.81) can be written as

$$\Big(\mathbb{I} - \Delta \bar{M}^2_{\eta'} \sum_{k=1} [-\Delta \bar{M}^2_{\eta'} (\bar{\Gamma}^{-1})_{00}]^{k-1} (\bar{\Gamma}^{-1} E^{00}) \Big) \bar{\Gamma}^{-1} = \Big(\mathbb{I} - \frac{\Delta \bar{M}^2_{\eta'}}{1 + \Delta \bar{M}^2_{\eta'} (\bar{\Gamma}^{-1})_{00}} \bar{\Gamma}^{-1} E^{00} \Big) \bar{\Gamma}^{-1} \,. \tag{5.83}$$

To get the explicit expression, it is more convenient to work in momentum-space first. In each sector, the momentum-space representation of the propagator can be parametrically written as

$$(\bar{\Gamma}^{-1})_{ab} = \frac{1}{p^2 + m^2} (\tilde{g}^{-1})_{ab} - \Delta M^2 \frac{1}{(p^2 + m^2)(p^2 + \tilde{m}^2)} H_{ab} \,. \tag{5.84}$$

Then, we have

$$\begin{aligned}\left(\bar{\Gamma}^{-1}E^{00}\bar{\Gamma}^{-1}\right)_{ab} =& \frac{1}{(p^2+m^2)^2}\Sigma_{ab} + \Delta M^2 \frac{1}{(p^2+m^2)^2(p^2+\tilde{m}^2)}\Theta_{ab} \\ &+ (\Delta M^2)^2 \frac{1}{(p^2+m^2)^2(p^2+\tilde{m}^2)^2}\Xi_{ab}\,,\end{aligned} \tag{5.85}$$

and

$$\begin{aligned}1+\Delta\bar{M}^2_{\eta'}(\bar{\Gamma}^{-1})_{00} =& \frac{1}{(p^2+m^2)(p^2+\tilde{m}^2)} \\ &\times \left(p^4 + (m^2+\tilde{m}^2+\Delta\bar{M}^2_{\eta'}\Lambda^2)p^2 + m^2\tilde{m}^2 + \Lambda^2\Delta\bar{M}^2_{\eta'}\tilde{m}^2 - H_{00}\Delta M^2\Delta\bar{M}^2_{\eta'}\right) \\ \equiv& \frac{(p^2+\bar{m}_1^2)(p^2+\bar{m}_2^2)}{(p^2+m^2)(p^2+\tilde{m}^2)}\end{aligned} \tag{5.86}$$

Therefore, in position-space, we have

$$\begin{aligned}\left(\bar{\Gamma}+\Delta\bar{M}^2_{\eta'}E^{00}\right)^{-1}(x) =& \tilde{g}^{-1}G_1(x,m^2) \\ &- \Delta M^2 H G_2(x,m,\tilde{m}) \\ &- \Delta\bar{M}^2_{\eta'}\Sigma G_2(x,\bar{m}_1,\bar{m}_2) \\ &- \Delta M^2\Delta\bar{M}^2_{\eta'}(\Theta+\lambda\Sigma)G_3(x,m,\bar{m}_1,\bar{m}_2) \\ &- \Delta\bar{M}^2_{\eta'}(\Delta M^2)^2\Xi G_4(x,m,\tilde{m},\bar{m}_1,\bar{m}_2)\end{aligned} \tag{5.87}$$

As we will see, $\bar{m}_1$ and $\bar{m}_2$ are two non-degenerate masses which appear as poles in the neutral-pseudoscalar-meson exchange. They can thus be identified with the masses of η and η'.

Parameters for Eq. (5.76) for PQChPT(i) and PQChPT(ii)

Finally, we give the parameters appearing in the expressions above for Eq. (5.76) for PQChPT(i) and PQChPT(ii):

(i)

$$\begin{aligned}&M^2_{ab} = M^2_\pi\,, \quad \tilde{M}^2_{ab} = M^2_\pi + \lambda\Delta M^2\,, \quad \lambda = \frac{2}{3}(2+\Lambda^2)\,, \\ &D_{00} = 0\,, \quad H_{ab} = (\tilde{g}^{-1}K\tilde{g}^{-1})_{ab}\,.\end{aligned} \tag{5.88}$$

(ii)

$$M^2_{ab} = \begin{cases} M^2_\pi & \text{for } a=b=\pi^0, \\ M^2_{\bar{s}s} & \text{else,}\end{cases}$$

$$\tilde{K}_{ab} = \begin{cases} K_{ab}-2\delta_{ab} & (a\neq\pi^0 \text{ and has no ghost constituent}) \text{ or } (a=\eta'), \\ K_{ab}+2\delta_{ab} & a\neq\pi^0,\eta' \text{ and has ghost contituents}, \\ K_{ab} & \text{else,}\end{cases}$$

$$\tilde{M}^2_{ab} = M^2_{ab} + \lambda\Delta M^2\,, \quad \lambda = -\frac{2}{3}(1+2\Lambda^2)\,, \quad D_{00} = 2\,, \quad H_{ab} = (\tilde{g}^{-1}\tilde{K}\tilde{g}^{-1})_{ab}\,. \tag{5.89}$$

For both PQChPT(i) and PQChPT(ii), we obtain the same η and η' masses

$$M_\eta^2 \equiv M_\pi^2 + \Delta M^2 + \frac{1}{2}\Delta\mathring{M}_{\eta'}^2 - \frac{1}{2}\delta\bar{m}^2\,, \quad M_{\eta'}^2 \equiv M_\eta^2 + \delta\bar{m}^2\,, \tag{5.90}$$

where

$$\delta\bar{m}^2 = \frac{1}{3}\sqrt{(2\Delta M^2 - 3\Delta\mathring{M}_{\eta'}^2)^2 + 32\Delta M^4\Lambda^2}\,. \tag{5.91}$$

The meanings of the parameters $\Delta\mathring{M}_{\eta'}^2$ and $\delta\bar{m}^2$ become clear at this stage

$$\begin{aligned} \delta\bar{m}^2 &= M_{\eta'}^2 - M_\eta^2\,, \\ \Delta\mathring{M}_{\eta'}^2 &= M_\eta^2 + M_{\eta'}^2 - 2M_K^2\,. \end{aligned} \tag{5.92}$$

Also, from the η/η'-mixing angle δ in the case of $U(3)$ [GL85]

$$\sin^2\delta = \frac{1}{3}\frac{(4M_K^2 - M_\pi^2 - 3M_\eta^2)}{M_{\eta'}^2 - M_\eta^2}\,, \tag{5.93}$$

we deduce the physical meaning of Λ:

$$\Lambda = \frac{\frac{3}{2}\Delta\mathring{M}_{\eta'}^2 - \Delta M^2}{2\sqrt{2}\Delta M^2}\tan(2\delta)\,. \tag{5.94}$$

We conclude this section with a remark. It has been known that in a certain way of treating a PQChPT, one will encounter double-poles in the propagator, which makes the theory pathological [BG94]. With our approach, the two PQChPT theories that we are interested in happen to be free of double-poles.

5.2.4 Interaction vertices in Partially-Quenched Chiral Perturbation Theory

Now let us turn to the interaction vertices for the charged-pseudoscalar-meson loop and the neutral-pseudoscalar exchange contribution to a_μ^{hlbl} at leading order. As illustrated before, we can single out a particular Wick-contraction diagram by computing the 4-point function of isovector-vector currents v_μ. We will thus focus on the coupling between pseudoscalar mesons and isovector-vector currents. The relevant couplings for the charged-pseudoscalar-meson loop arise from the covariant derivatives of the leading order Lagrangian, whereas the WZW vertex in a PQChPT is needed to describe the neutral-pseudoscalar-meson exchange. Contrary to the propagators, the expressions for these vertices are rather simple and can be applied to generic (S)U$(N|M)$-theories.

Expansion of the kinetic term up to O(p^4)

Expanding the kinetic term proportional to $\mathrm{str}(D_\mu^\dagger\phi D_\mu\phi)$ up to O(p^4) yields

$$\mathcal{L}^{(2),\mathrm{E}} \supset -\sum_k C_k^{bc} g^{ak}\partial_\mu\phi^a v_\mu^b\phi^c + \frac{1}{2}\sum_{k,l} C_k^{ab}C_l^{cd}g^{kl}v_\mu^a\phi^b\phi^c v_\mu^d\,, \tag{5.95}$$

where

$$C_a^{bc} = -2i\sum_k \mathrm{str}\{[T^b,T^c]T^k\}g^{ka}\,. \tag{5.96}$$

Again here $[\cdot,\cdot]$ is the super-commutator. The summed indices run over the whole basis of generators. The 3-point and 4-point vertices in Euclidean space-time are then given by

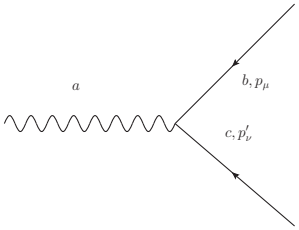

$$\begin{aligned} V_{3;\mu}^{cb;a} &= -\left(\tilde{C}_c^{ab} p'_\mu + \tilde{C}_b^{ac} p_\mu\right), \\ \tilde{C}_a^{bc} &\equiv 2\mathrm{str}([T^b, T^c]T^a) = iC_i^{bc} g^{ai}, \end{aligned} \tag{5.97}$$

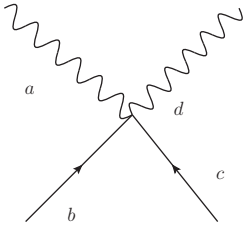

$$\begin{aligned} V_{4;\mu\nu}^{ad;bc} =& -\delta_{\mu\nu} g^{mn} (C_m^{ab} C_n^{cd} + C_m^{ac} C_n^{bd}) \\ =& 2\delta_{\mu\nu}\Big(\mathrm{str}([T^a, T^b][T^c, T^d]) + \mathrm{str}([T^a, T^c][T^b, T^d])\Big). \end{aligned} \tag{5.98}$$

It should be clear at this point that the flavor-singlet pseudoscalar meson can not couple to an external isovector-vector current via these vertices, because of the super-commutator. One should be careful with the extra factor of -1 due to the ghost loops.

Wess-Zumino-Witten term at leading order

Let us first consider an $\mathrm{SU}(N|M)$-theory. It can be shown that, in terms of the meson multiplet field U, the $\mathrm{SU}(N)$ WZW vertex in Minkowski space-time Eq. (5.13) can be written as [Sch03]

$$S_{\mathrm{WZW}}^{\mathrm{ext}} = -\frac{i}{48}\int d^4x \epsilon^{\mu\nu\rho\sigma} \mathrm{Tr}(Z_{\mu\nu\rho\sigma}), \tag{5.99}$$

where the relevant terms to the two-photons-to-pseudoscalar-meson interaction at leading order contained in $Z_{\mu\nu\rho\sigma}$ are

$$\begin{aligned} Z_{\mu\nu\rho\sigma} \supset\ & \mathcal{U}_\mu^L U^\dagger \partial_\nu r_\rho U l_\sigma - \mathcal{U}_\mu^R U \partial_\nu l_\rho U^\dagger r_\sigma \\ & - \mathcal{U}_\mu^L \mathcal{U}_\nu^L U^\dagger r_\rho U l_\sigma + \mathcal{U}_\mu^R \mathcal{U}_\nu^R U l_\rho U^\dagger r_\sigma \\ & + \mathcal{U}_\mu^L l_\nu \partial_\rho l_\sigma - \mathcal{U}_\mu^R r_\nu \partial_\rho r_\sigma \\ & + \mathcal{U}_\mu^L \partial_\nu l_\rho l_\sigma - \mathcal{U}_\mu^R \partial_\nu r_\rho r_\sigma \end{aligned} \tag{5.100}$$

with

$$\mathcal{U}_\mu^L \equiv U^\dagger \partial_\mu U, \quad \mathcal{U}_\mu^R \equiv U \partial_\mu U^\dagger. \tag{5.101}$$

To pass to $\mathrm{SU}(N|M)$, one should take into account all possible combinations of supertraces of product of operators while constructing the effective Lagrangian in PQChPT [DTWL06]. For our purpose, we are only interested in the coupling to external isovector-vector currents, i.e. for the external $\mathrm{SU}(N|M)_L \times \mathrm{SU}(N|M)_R$ field with

$$l_\mu = r_\mu = v_\mu^a T^a. \tag{5.102}$$

Intuitively, one might think of replacing the trace by a supertrace in the WZW vertex Eq. (5.100) to convert it to its PQChPT version. From a pure EFT point of view, one should also consider other possible terms which are $\mathrm{SU}(M|N)$-invariant and can lead to a $\pi^0\gamma\gamma$-type interaction [DTWL06]. However, due to the tracelessness of the

generators of the theory and the isovector nature of v_μ, the terms involving only one supertrace vanish. Therefore, it suffices to replace the traces appearing in the SU(N)-WZW vertex by supertraces to get the WZW vertex in SU$(N|M)$. As a result, the relevant term for the $\pi^0\gamma\gamma$ process in the effective WZW action in PQChPT is proportional to

$$\mathrm{str}(T^a T^b T^c) \int d^4x \phi^c \epsilon^{\mu\nu\rho\sigma} F^a_{\mu\nu} F^b_{\rho\sigma}\,, \tag{5.103}$$

where

$$F^{ab}_{\mu\nu} \equiv \partial_\mu v^a_\nu - \partial_\nu v^a_\mu\,. \tag{5.104}$$

In practice, we would use a more realistic transition form factor (such as the one from Vector-Meson Dominance) instead of just considering the interaction as point-like. As what really matters for our diagram matching study is the flavor structure, we give the Feynman rule with the kinematic-dependent factor left out:

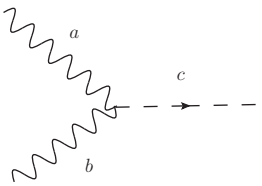

$$V^{ab;c}_{\rm WZW} \propto \mathrm{str}[\{T^a, T^b\}T^c]\,. \tag{5.105}$$

On the other hand, if one is to consider the η/η'-mixing with U$(N|M)$-PQChPT, there might be some additional terms because of the supertrace of the flavor-singlet meson is not vanishing. A consequence of this is that one will have to include terms that violate the Okubo-Zweig-Iizuka (OZI) rule or come from the mass-non-degeneracy between the light- and strange-quarks [KL00]. In the analysis that we present in the next section, we will simply neglect these higher-order effects.

5.3 Wick-contraction topologies in LQCD and the leading pseudoscalar meson contributions to $a_\mu^{\rm hlbl}$

Based on the Feynman rules given previously, we list the result of the matching between different QCD Wick-contraction topologies and the diagrams from the charged-pseudoscalar-meson loop and the neutral-pseudoscalar-meson exchange contributions to $a_\mu^{\rm hlbl}$.

5.3.1 Charged-pseudoscalar-meson loop

We define the functions Ω and Ω_c in Fig. 5.1 as collections of Feynman diagrams appearing in a scalar-QED computation, with the coefficients given in Tab. 5.1. The matchings between different Wick-contractions to the charged-pseudoscalar-meson loop contribution are summarized in Fig. 5.2 and Tab. 5.2, where vanishing contributions are not listed. Note that Ω and Ω_c are themselves gauge-invariant objects, in that the vector-current Ward identity holds for both cases. This is consistent with the fact that each individual Wick-contraction diagram on the left-hand side of Fig. 5.2 also satisfies the vector-current Ward identity.

	a_1	a_2	a_3	b_1	b_2	b_3	b_4	b_5	b_6	c_1	c_2	c_3
Ω	1	1	1	1	1	1	1	1	1	1	1	1
Ω^c	1	0	0	$\frac{1}{2}$	$\frac{1}{2}$	$\frac{1}{2}$	$\frac{1}{2}$	0	0	$\frac{1}{2}$	$\frac{1}{2}$	0

TABLE 5.1: Coefficients defined in Fig. 5.1.

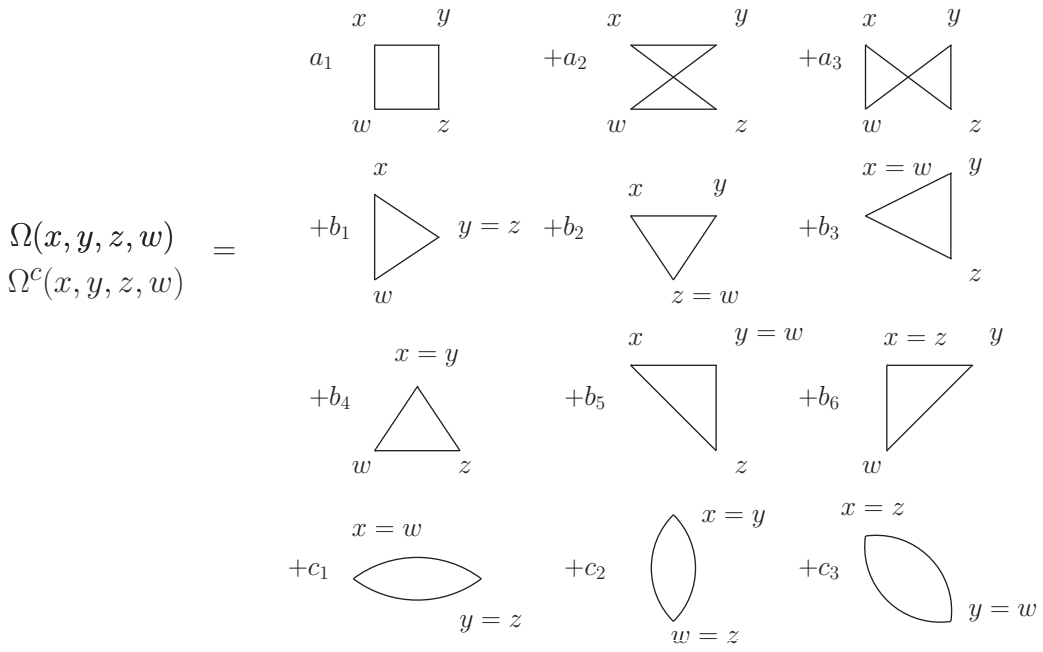

FIGURE 5.1: Diagrammatic definition of Ω and Ω^c

i	(4)-l	(4)-s	(2+2)-ll	(2+2)-ls	(2+2)-ss	(3+1)-l	(3+1)-s
π	2	0	1	0	0	-1	0
K	1	2	0	2	0	1	-1
$\bar{s}s$	0	1	0	0	1	0	1

TABLE 5.2: Coefficients d_i (for fully-connected, (4)), e_i (for (3+1)) and f_i (for (2+2)) for the contribution of different charged pseudoscalar mesons defined in Fig. 5.2. We use the same convention for our lattice calculation as defined in Sect. 6.2. In particular, "(4),l/s" refers to the fully-connected light/strange contribution, "(2+2)-ls" refers to the sum of the 2+2 diagrams with one light and one strange-quark, and "(3+1)-l/s" refers to the light/strange-quark triangle correlated with light-minus-strange disconnected loop.

5.3.2 Neutral-pseudoscalar-meson exchange

Without the flavor-singlet meson

We first study the matching without the flavor-singlet meson using an SU$(N|M)$ theory, which gives rather simple results tabulated in Tab. 5.3. Note that for the reason we explained before, we omit the absolute normalization and the normalization convention that we choose here is to make c_π for the (4)-l equal to 1.

With the flavor-singlet meson

The inclusion of the flavor-singlet meson does not change the matching for the fully-connected diagrams. However, for the $(2+2)$-disconnected, we have:

- **(2+2), light-light**

$$c_{\pi^0} = -1, \tag{5.106}$$

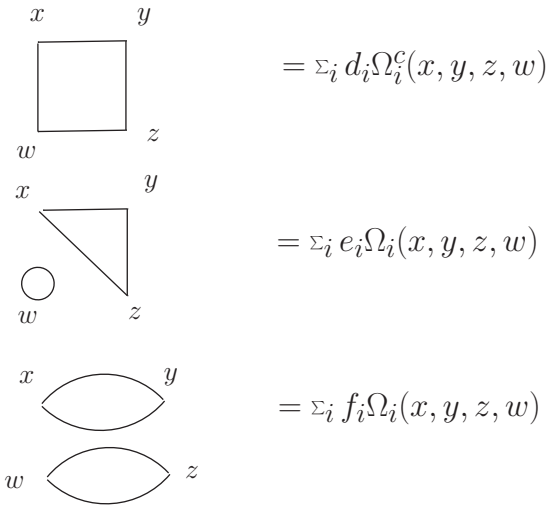

FIGURE 5.2: Matching of different QCD Wick-contraction to charged pseudoscalar loop contributions.

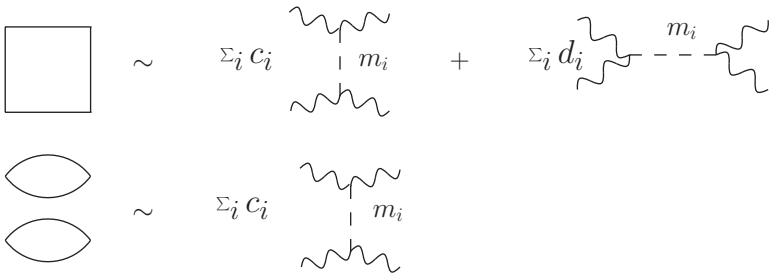

FIGURE 5.3: Matching pattern between QCD Wick-contractions and pseudoscalar pole exchange channels.

	(4)-*l*	(4)-*s*	(2+2)-*ll*	(2+2)-*ls*	(2+2)-*ss*
c_π	1	0	-1	0	0
c_η	0	0	$\frac{1}{3}$	$-\frac{4}{3}$	$\frac{4}{3}$
$c_{\bar{s}s}$	0	1	0	0	-2
d_π	1	0			
$d_{\bar{s}s}$	0	1			

TABLE 5.3: Relative weights for different exchange channels for each contributing QCD Wick-contraction according to the definition of Fig. 5.3. Again here "(4)" refers to the fully-connected topology.

$$
\begin{aligned}
c_\eta =& \frac{2}{27}\frac{1}{\delta\bar{m}^2(-2\Delta M^2 - \Delta\mathring{M}^2_{\eta'} + \delta\bar{m}^2)} \\
&\times \Big(-6\Delta M^2 \Delta\mathring{M}^2_{\eta'}(1+2\Lambda^2) + 4\Delta M^4(1-\Lambda^2)(1-4\Lambda^2) \\
&+ 6\Delta M^2(-1+\Lambda^2)\delta\bar{m}^2 + 9\Delta\mathring{M}^2_{\eta'}\Lambda^2(\Delta\mathring{M}^2_{\eta'} - \delta\bar{m}^2)\Big),
\end{aligned}
\tag{5.107}
$$

$$
\begin{aligned}
c_{\eta'} =& \frac{2}{27}\frac{1}{\delta\bar{m}^2(2\Delta M^2+\Delta\mathring{M}^2_{\eta'}+\delta\bar{m}^2)} \\
&\times\Big(-6\Delta M^2\Delta\mathring{M}^2_{\eta'}(1+2\Lambda^2)+4\Delta M^4(1-\Lambda^2)(1-4\Lambda^2) \\
&-6\Delta M^2(-1+\Lambda^2)\delta\bar{m}^2+9\Delta\mathring{M}^2_{\eta'}\Lambda^2(\Delta\mathring{M}^2_{\eta'}+\delta\bar{m}^2)\Big).
\end{aligned}
\tag{5.108}
$$

- **(2+2), light-strange**

$$
c_\eta = \frac{2}{9\delta\bar{m}^2}\Big(-2\Delta M^2(-1+\Lambda^2)-3\Delta\mathring{M}^2_{\eta'}(1+\Lambda^2)+3(-1+\Lambda^2)\delta\bar{m}^2\Big), \tag{5.109}
$$

$$
c_{\eta'} = \frac{2}{9\delta\bar{m}^2}\Big(2\Delta M^2(-1+\Lambda^2)+3\Delta\mathring{M}^2_{\eta'}(1+\Lambda^2)+3(-1+\Lambda^2)\delta\bar{m}^2\Big). \tag{5.110}
$$

- **(2+2), strange-strange**

$$
c_{\bar{s}s} = -2, \tag{5.111}
$$

$$
\begin{aligned}
c_\eta =& -\frac{4}{27}\frac{\Lambda^2[3\Delta\mathring{M}^2_{\eta'}+4\Delta M^2(-1+\Lambda^2)]}{\delta\bar{m}^2(2\Delta M^2-\Delta\mathring{M}^2_{\eta'}+\delta\bar{m}^2)[-3\Delta\mathring{M}^2_{\eta'}+2\Delta M^2(1-4\Lambda^2)+3\delta\bar{m}^2]} \\
&\times\Big(4\Delta M^4(5+4\Lambda^2)-9\Delta\mathring{M}^2_{\eta'}(-\Delta\mathring{M}^2_{\eta'}+\delta\bar{m}^2)-6\Delta M^2(-2\Delta\mathring{M}^2_{\eta'}+3\delta\bar{m}^2)\Big),
\end{aligned}
\tag{5.112}
$$

$$
\begin{aligned}
c_{\eta'} =& \frac{4}{27}\frac{\Lambda^2[3\Delta\mathring{M}^2_{\eta'}+4\Delta M^2(-1+\Lambda^2)]}{\delta\bar{m}^2(-2\Delta M^2+\Delta\mathring{M}^2_{\eta'}+\delta\bar{m}^2)[3\Delta\mathring{M}^2_{\eta'}-2\Delta M^2(1-4\Lambda^2)+3\delta\bar{m}^2]} \\
&\times\Big(4\Delta M^4(5+4\Lambda^2)+9\Delta\mathring{M}^2_{\eta'}(\Delta\mathring{M}^2_{\eta'}+\delta\bar{m}^2)+6\Delta M^2(2\Delta\mathring{M}^2_{\eta'}+3\delta\bar{m}^2)\Big).
\end{aligned}
\tag{5.113}
$$

A consistency check: the total contribution

As a check for the correctness of the procedure, one can compute the full neutral-pseudoscalar-meson contribution to a_μ in the two different partially-quenched theories mentioned previously and check if one gets the same result for both of them. Especially, one should expect that, in the final physical result, only three pole-masses will appear, which correspond to the masses of π^0, η and η'. This is actually the case and we have the following relations for the ratios between the contribution of the π^0-exchange to the light-by-light scattering amplitude Π^{LbL,π^0} and that of the η ($\Pi^{\text{LbL},\eta}$) and η' ($\Pi^{\text{LbL},\eta'}$):

$$
\frac{\Pi^{\text{LbL},\eta}}{\Pi^{\text{LbL},\pi^0}} = \frac{(A+B)\Pi^{\text{PS-pole},\eta}}{72\Pi^{\text{PS-pole},\pi^0}}\,, \quad \frac{\Pi^{\text{LbL},\eta'}}{\Pi^{\text{LbL},\pi^0}} = \frac{(A-B)\Pi^{\text{PS-pole},\eta'}}{72\Pi^{\text{PS-pole},\pi^0}}\,, \tag{5.114}
$$

where

$$
\begin{aligned}
A &= 12(1+8\Lambda^2)\,, \\
B &= \frac{4}{\delta\bar{m}^2}\Big((-2+48\Lambda^2)\Delta M^2+3(1-8\Lambda^2)\Delta\mathring{M}^2_{\eta'}\Big)\,,
\end{aligned}
\tag{5.115}
$$

and $\Pi^{\text{PS-pole},i}$ is a kinematic function parametrized by the mass of the particle i that takes into account the exchange of the particle i in the s-, t- and u-channels combined.

As an easy first check, one can see that in the limit $\Delta\mathring{M}^2_{\eta'} \to \infty$, η' is indeed decoupled and we obtain the expected ratio between the contribution from η and the one from π^0, which is independent of Λ.

Remark on the rôle of Λ

In the limit $\Delta\mathring{M}^2_{\eta'} \to \infty$, we have

$$\frac{\Pi^{\mathrm{LbL},\eta'}}{\Pi^{\mathrm{LbL},\pi^0}} \approx \frac{8\Lambda^2}{3}\frac{\Pi^{\mathrm{PS\text{-}pole},\eta'}}{\Pi^{\mathrm{PS\text{-}pole},\pi^0}} \tag{5.116}$$

As discussed in Ref. [G+18], in the case where one neglects the higher order effect in $1/N_c$ coming from the single quark loop, one can compute the same ratio from the charge factors and would expect it to be $8/3$. This is also consistent with our result here because $\Lambda = 1 + \mathcal{O}(1/N_c)$ at the large-N_c limit.

Chapter 6

Lattice results on a_μ^{hlbl}

In this chapter, we will report the main findings of our series of two papers on the lattice determination of a_μ^{hlbl} with comments on some specific technical details. In the first paper [Cha+20], we carry out studies on the CLS $N_f = 2+1$ lattice ensembles at the $\mathrm{SU}(3)_f$-symmetry point, i.e. at the limit of degenerate light- and strange-quark masses. The pion masses of these ensembles are around 420 MeV. At this point in the flavor phase space, only two of the five Wick-contraction topologies contribute, rendering the calculation easier to handle. Together with their smaller volumes, the computation becomes more manageable and thus we are able to achieve a good statistical accuracy. A specific finite-size-effect correction and tail-reconstruction procedure is proposed in this first study, where we attribute the long-distance effects to the neutral-pion (π^0)-exchange contribution. Subsequently, to determine the value of a_μ^{hlbl} at the flavor-symmetric point, only a continuum extrapolation is needed. In the second paper [Cha+21], we extend our analysis to include ensembles with lighter pion mass down to about 200 MeV. Due to the loss of statistical precision and the higher computational cost for the calculation of the propagators, a more data-driven approach is adopted for the dominant contraction topologies. A simultaneous chiral, infinite-volume and continuum extrapolation is performed at the end to determine the leading contribution to a_μ^{hlbl}. Also, the second paper is an exhaustive study of all the sub-dominant contraction topologies, which are not present in at the $\mathrm{SU}(3)_f$-symmetric point.

This chapter is organized as follows. First, we will discuss some issues with the definition of the electromagnetic current, our main operator, on the lattice. A brief discussion about the renormalization of the local vector current on the lattice will be brought up. Then, we will recall the formalism and give the expressions for the integral representation that we use for each contraction topology. Finally, we will go through the analysis of the data in Ref. [Cha+20] and Ref. [Cha+21] in two dedicated sections, with some comments on the specific LQCD techniques implied in each of the papers. Some details such as the data used for the plots might not be given exhaustively as they can be found in the published work.

6.1 Vector current on the lattice and its renormalization

In the continuum, the vector current is a conserved quantity coming from Noether's theorem under quark field phase rotation in QCD. Upon discretization, the Ward-identity of this symmetry is modified due to lattice artifacts. On the lattice, one can define the vector current in two ways: either by keeping its definition in the continuum, or by implementing the exactly conserved version on the lattice obtained from the lattice version of the Ward-identity. The former is called *local vector current* and the latter is called *conserved vector current*. On the other hand, as discussed

previously for the case of the axial current in Sect. 2.1.3, there exists also an improvement program for the vector current. Analogously to the determination of c_{SW}, the improvement of the operators also relies on the restoration of some Ward-identities and is achieved by including extra possible higher dimensional operators which respect the same discrete symmetries as the vector current. It is also important to take into account the $\mathrm{SU}(3)_f$-symmetry-breaking while working in the $N_f = 2+1$ framework.

Due to lattice artifacts, the local vector current is improved and renormalized in a different way than the conserved one. We will review these points based on Ref. [GHM19], where the improvement coefficients used for our work are determined. For other quantities beyond the vector current, an exhaustive list of improved quark-bilinear operators and the Ward identities that one can consider for operator improvement can be found in Ref. [Bha+06].

Consider a generic N_f-flavor QCD. Recall the definition of the vector current in the continuum

$$V_\mu^{l,(ij)} \equiv \bar{\psi}_i(x)\gamma_\mu\psi_j(x)\,, \tag{6.1}$$

which comes from the quark-field rotation in flavor space

$$\psi(y) \to \big(1+\lambda\alpha(y)\big)\psi(y)\,, \quad \bar{\psi}(y) \to \bar{\psi}(y)\big(1-\lambda\alpha(y)\big)\,, \tag{6.2}$$

where λ is a matrix acting on the flavor space. However, for Wilson-clover fermions, the vector Ward identity with a generic operator $\mathcal{O}$ becomes [Boc+85]

$$\left\langle \frac{\delta\mathcal{O}}{\delta\alpha(y)} \right\rangle = a^4\partial_\mu^* \left\langle \mathrm{Tr}\{\lambda^T V_\mu^c(y)\}\mathcal{O}\right\rangle + a^4\left\langle \bar{\psi}(y)[M_0,\lambda]\psi(y)\mathcal{O}\right\rangle, \tag{6.3}$$

where $M_0 \equiv \mathrm{diag}(\mathrm{m_{q,1}},\cdots,\mathrm{m_{q,N_f}})$ is the bare quark mass matrix and $V_\mu^{c,(ij)}(y)$ is defined as the *point-split (conserved)* vector current

$$V_\mu^{c,(ij)}(x) = \frac{1}{2}\Big(\bar{\psi}_i(x+a\hat{\mu})(1+\gamma_\mu)U_\mu^\dagger(x)\psi_j(x) - \bar{\psi}_i(x)(1-\gamma_\mu)U_\mu(x)\psi_j(x+a\hat{\mu})\Big)\,. \tag{6.4}$$

The point-split current is conserved on the lattice, because if we choose λ to be flavor-diagonal and $\mathcal{O}$ with support not containing the site y, we recover the discrete version of the current Ward-identity naïvely derived from the one in the continuum.

The $\mathrm{SU}(N_f)$ components of the vector current V_μ renormalize as [Bha+06]

$$\begin{aligned}\mathrm{Tr}(\lambda V_\mu)_{\mathrm{R}} =& Z_V(\tilde{g}_0^2)\Big[(1+N_f\bar{b}_V(g_0^2)am_{\mathrm{q}}^{\mathrm{av}})\mathrm{Tr}(\lambda V_\mu^{\mathrm{I}}) + \frac{1}{2}b_V(g_0^2)\mathrm{Tr}(\{\lambda, aM_{\mathrm{q}}V_\mu^{\mathrm{I}}\}) \\ &+ f_V(g_0^2)\mathrm{Tr}(\lambda aM_{\mathrm{q}})\mathrm{Tr}(V_\mu^{\mathrm{I}})\Big]\,,\end{aligned} \tag{6.5}$$

where $\lambda \in \mathrm{SU(N_f)}$, $Z_V(\tilde{g}_0^2)$ is a renormalization factor which depends on the modified bare coupling defined with a constant b_{g}

$$\tilde{g}_0^2 \equiv g_0^2(1+b_{\mathrm{g}}am_{\mathrm{q}}^{\mathrm{av}})\,, \tag{6.6}$$

$\bar{b}_V$, b_V and f_V are improvement coefficients depending only on the bare coupling g_0^2, $M_{\mathrm{q}} \equiv \mathrm{diag}(m_{\mathrm{q},1},\cdots,m_{\mathrm{q},N_f})$ is the subtracted quark-mass matrix with $m_{q,i} \equiv m_{0,i} - m_c$ with m_c the critical mass, $m_{\mathrm{q}}^{\mathrm{av}}$ is the average of the subtracted quark masses,

and finally the improved vector current $V^{\rm I}$ is matrix-valued with

$$(V^{\rm I})_\mu^{(ij)}(x) = V_\mu^{(ij)}(x) + ac_V(g_0^2)\tilde{\partial}_\nu \Sigma_{\mu\nu}^{(ij)}(x)\,, \tag{6.7}$$

where $V_\mu^{(ij)}$ is $V_\mu^{l,(ij)}$ or $V_\mu^{c,(ij)}$,

$$\Sigma_{\mu\nu}^{(ij)}(x) \equiv -\frac{1}{2}\bar{\psi}_i[\gamma_\mu,\gamma_\nu]\psi^j\,, \tag{6.8}$$

and $\tilde{\partial}_\nu$ is the symmetrized lattice derivative

$$\tilde{\partial}_\nu \phi(x) = \frac{\phi(x+a\hat{\nu}) - \phi(x-a\hat{\nu})}{2a}\,. \tag{6.9}$$

The coefficients Z_V, b_V and $\bar{b}_V$ are tuned such that the Ward-identity Eq. (6.3) is satisfied for the vector current in question. The strategy presented in Ref. [GHM19] consists in using a bi-local operator

$$\mathcal{O}(x,z) = P^{(ji)}(x)P^{(ij)}(z)\,, \quad P^{(ij)}(x) \equiv \bar{\psi}_i(x)\gamma_5\psi_j(x)\,, \tag{6.10}$$

with $i \neq j$ as a probe of the Ward-identity. This choice leads to the identity

$$\Big\langle P^{(ji)}(x)P^{(ij)}(z)\Big\rangle\big(\delta(y-z)-\delta(y-x)\big) = a^4\partial^*_{y,\mu}\Big\langle P^{(ji)}(x)V_\mu^{c,(ii)}(y)P^{(ij)}(z)\Big\rangle \tag{6.11}$$

The delta functions on the left-hand side imply that the 3-point function on the right-hand side is piecewisely constant, except at the point where y coincides with x or z. Upon summation over the spatial coordinates $\mathbf{y}$ and taking a volume average, one can show that the ratio

$$R(x_0-z_0,y_0-z_0) = \frac{\langle a^6\sum_{\mathbf{x},\mathbf{y}} P^{(ji)}(x)V_0^{c,(ii)}(y)P^{(ij)}(z)\rangle}{\langle a^3\sum_{\mathbf{x}} P^{(ji)}(x)P^{(ij)}(z)\rangle}\,, \tag{6.12}$$

is unity under spatial periodic boundary condition.

In an $N_f = 2+1$ theory, if we choose the matrix λ to be the Gell-Mann matrix proportional to $\mathrm{diag}(1,-1,0)$ in Eq. (6.5), we will pick up the iso-vector component $V_\mu^{\rm I,3} \equiv \frac{1}{2}\bar{\psi}\lambda^3\gamma_\mu\psi$ of $V^{\rm I}$, which is multiplicatively renormalized due to the fact that the second and the third terms on the right-hand side of Eq. (6.5) vanish. As P is also multiplicatively renormalized[1], we conclude that the renormalization factor for the point-split current, Z_V^c, is also unity and $\bar{b}_V^c = b_V^c = f_V^c = 0$. Knowing this, we can impose the renormalization condition for the local vector current to be such that the ratio

$$R_\pi(x_0-z_0,y_0-z_0) = \frac{\langle a^6\sum_{\mathbf{x},\mathbf{y}} P^{(21)}\frac{1}{2}\big((V_0)_{\rm R}^{l,(11)}(y) - (V_0)_{\rm R}^{l,(22)}(y)\big)P^{(12)}(z)\rangle}{\langle a^3\sum_{\mathbf{x}} P^{(21)}(x)P^{(12)}(z)\rangle}\,, \tag{6.13}$$

is unity[2]. If we replace the renormalized local currents in Eq. (6.13) by the unrenormalized ones, we get $R_\pi(t,t_1) \to 1/\hat{Z}_V$ in the asymptotic region $t_1, t-t_1 \to \infty$, where $\hat{Z}_V$ is proportional to Z_V up to lattice artifacts as expressed in Eq. (6.5). By performing a global fit with lattice data from different lattice-spacings and quark

[1] c.f. Sect. 2.1.3.

[2] An alternative using $P^{(13)}$ instead of $P^{(12)}$ (respectively, the ones with the super-script swapped) is also used in Ref. [GHM19], which provides a consistency check of the method

masses, the improvement coefficients appearing in the renormalization Eq. (6.5) and the renormalization factor can be obtained.

An efficient way of computing the 2-point and 3-point functions required for Eq. (6.13) which has been implemented for measuring $\hat{Z}_V$ for some ensembles used in this project is to use the stochastic *Z2PSWall* and *Z2SEMWall* sources for propagator solves as proposed in Ref. [Boy+08]. The method exploits the commonly used "one-end-trick" stochastic method [FM99] and the spinor structure of pseudoscalar interpolators to effectively reduce the computing cost. We refer to Sect. 6.3 for a discussion on the use of stochastic sources.

6.2 Calculating a_μ^{hlbl} on the lattice

As already discussed in detail in Sect. 3.1, our strategy for computing a_μ^{hlbl} consists in treating the QED part semi-analytically in the continuum and infinite-volume in order to mitigate the finite-size effects due to the massless photons. For a lattice calculation, the hadronic function $i\hat{\Pi}$ defined in the master equation Eq. (3.14) is computed as a gauge-field average over the gauge field ensembles. More precisely, we use the local formulation of the hadronic component of the electromagnetic current on the lattice

$$j_\mu(x) = \frac{2}{3}(\overline{u}\gamma_\mu u)(x) - \frac{1}{3}(\overline{d}\gamma_\mu d)(x) - \frac{1}{3}(\overline{s}\gamma_\mu s)(x)\,, \tag{6.14}$$

and compute in the QCD background

$$\begin{aligned} i\widehat{\Pi}_{\rho;\mu\nu\lambda\sigma}(x,y) &= -\int_z z_\rho\, \widetilde{\Pi}_{\mu\nu\sigma\lambda}(x,y,z), \\ \widetilde{\Pi}_{\mu\nu\sigma\lambda}(x,y,z) &\equiv \Big\langle\, j_\mu(x)\, j_\nu(y)\, j_\sigma(z)\, j_\lambda(0)\,\Big\rangle_{\text{QCD}}. \end{aligned} \tag{6.15}$$

As explained in Sect. 2.3, to compute the lattice expectation value of the current 4-point function $\widetilde{\Pi}$ in the QCD background, one has to take into account all the possible ways of doing Wick-contraction and compute each of them correspondingly. In our case, there are 5 diagrammatic classes (*topologies*): the fully-connected, the $(2+2)$, the $(3+1)$, the $(2+1+1)$ and the $(1+1+1+1)$. These are illustrated in Fig. 6.1.

As we work with $N_f = 2+1$ ensembles, the topologies containing self-contracted disconnected loops, i.e. the last three of the listed categories, are suppressed near the $\text{SU}(3)_f$-symmetric point due to the quark charge factors. Also, the last three of the listed categories require strictly more gluon insertions compared to the fully-connected and the (2+2) in the perturbative picture. We thus expect the first two listed topologies to contribute in a more major way to a_μ^{hlbl}. Therefore, we call the first two topologies the *leading topologies* and the rest the *sub-leading topologies*.

We adopt the same strategy to deal with the integrals as already stated in Chap. 3 by representing a_μ^{hlbl} as

$$a_\mu^{\text{hlbl}} = \sum_{\text{Topology}} \int_0^\infty d|y|\, f^{(\text{Topology})}(|y|), \tag{6.16}$$

and compute the *integrand* $f^{(\text{Topology})}$ for a set of $|y|$-value for each topology with the x- and z-integrals performed as discrete sums on the lattice. Subsequently, the $|y|$-integral is computed via the trapezoidal rule to get a_μ^{hlbl}. Note that one can compute

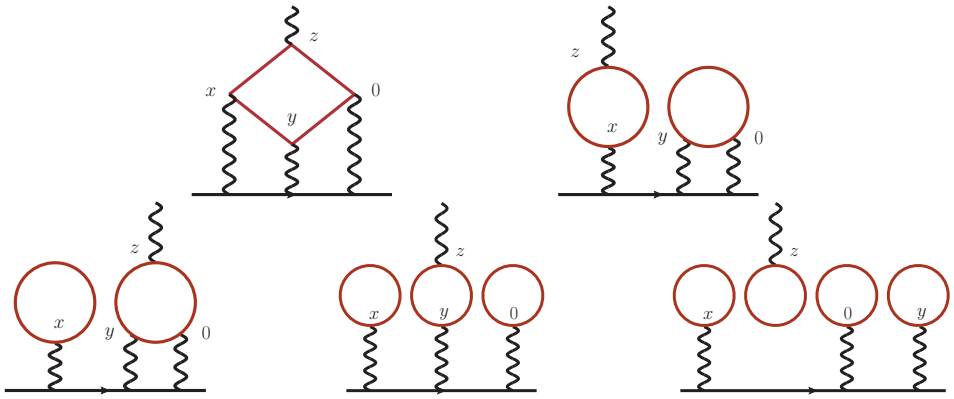

FIGURE 6.1: Different quark Wick-contraction classes appearing in the computation of the QCD four-point correlation function. The straight horizontal lines represent muon propagators, wavy lines represent photon propagators. The remaining lines are quark propagators in the QCD background. From left to right, top to bottom, they are the fully-connected, (2+2), (3+1), (2+1+1) and (1+1+1+1). Each class contains the diagrams obtained from all the possible permutations of the four points attached to photons. Figure taken from Ref. [Cha+20].

the integrand for each topology separately with different QED-kernels in principle because they are gauge-invariant objects.

From our experience with the π^0-exchange with a VMD TFF computation and the lepton loop computation, we find that the subtracted kernel $\bar{\mathcal{L}}^{(\Lambda)}$ defined in Eq. (3.17) helps a lot in reshaping the integral in a way that the extent of the integrand is neither too long-ranged, nor too peaked at short-distances [Cha+20]. This suggests that we should be able to truncate the lattice data when it becomes noisy at long-distances while not suffering too much from the cut-off effects from short-distances. The exact expressions for the integrand for each topology will be given explicitly later. Our preferred value for Λ is 0.4, which is the default setup for the results presented in this chapter.

Exploiting translational invariance of the 4-point correlation function $\widetilde{\Pi}$, one can achieve expressions for the integrands which are more computationally favorable [Cha+20]. We also find it useful to present the partially summed quantity

$$a_\mu(|y|_{\text{Max.}}) = \int_0^{|y|_{\text{Max.}}} d|y| f(|y|)\,, \tag{6.17}$$

We will again use a handy notation as already introduced in Sect. 4.1

$$\mathcal{L}'_{[\rho,\sigma];\mu\nu\lambda}(x,y) = \bar{\mathcal{L}}^{(\Lambda)}_{[\rho,\sigma];\mu\nu\lambda}(x,y) + \bar{\mathcal{L}}^{(\Lambda)}_{[\rho,\sigma];\nu\mu\lambda}(y,x) - \bar{\mathcal{L}}^{(\Lambda)}_{[\rho,\sigma];\lambda\nu\mu}(x,x-y). \tag{6.18}$$

In the following paragraphs, we will give the expressions that we used to compute the contribution of each topology on the lattice. Note that one has to include the renormalization constant properly as explained in the previous section[3].

[3]Note that we use neither the improved version of the electromagnetic current, nor its conserved formulation, due to the higher computational complexity. Therefore, an exact O(a)-improved scaling is not *a priori* expected. The inclusion of the renormalization is however important because it enters with the fourth power. We have checked that the difference between $\hat{Z}_V$ and Z_V due to lattice artifacts is numerically very minor, as far as our target precision is concerned.

6.2.1 The leading topologies

The fully-connected contribution

We have investigated two possible expressions for the integrand for the fully-connected contribution. We call them Method 1 and Method 2 respectively. Due to the higher computational cost of Method 1, most of our computations for the fully-connected are done with Method 2 only. If not otherwise specified, the presented results from Method 2.

- **Method 1** From the definition Eq. (6.15) and the original formulation of the position-space method Eq. (3.14), the fully-connected contribution to the integrand of a_μ^{hlbl} is written as

$$f^{(\text{Conn. M1})}(|y|) = -\sum_{j\in u,d,s} \hat{Z}_V^4 Q_j^4 \frac{m_\mu e^6}{3} 2\pi^2 |y|^3 \int_x \left(\bar{\mathcal{L}}^{(\Lambda)}_{[\rho,\sigma]\mu\nu\lambda}(x,y) \int_z z_\rho \widetilde{\Pi}^{\text{Conn.},j}_{\mu\nu\sigma\lambda}(x,y,z) \right), \tag{6.19}$$

where

$$\widetilde{\Pi}^{\text{Conn.},j}_{\mu\nu\sigma\lambda}(x,y,z) = \widetilde{\Pi}^{(1),j}_{\mu\nu\sigma\lambda}(x,y,z) + \widetilde{\Pi}^{(2),j}_{\mu\nu\sigma\lambda}(x,y,z) + \widetilde{\Pi}^{(3),j}_{\mu\nu\sigma\lambda}(x,y,z)\,, \tag{6.20}$$

$$\widetilde{\Pi}^{(1),j}_{\mu\nu\sigma\lambda}(x,y,z) = -2\text{Re}\left\langle \text{Tr}\left[S^j(0,x)\gamma_\mu S^j(x,y)\gamma_\nu S^j(y,z)\gamma_\sigma S^j(z,0)\gamma_\lambda \right] \right\rangle_U . \tag{6.21}$$

$$\widetilde{\Pi}^{(2),j}_{\mu\nu\sigma\lambda}(x,y,z) = -2\text{Re}\left\langle \text{Tr}\left[S^j(0,y)\gamma_\nu S^j(y,z)\gamma_\sigma S^j(z,x)\gamma_\mu S^j(x,0)\gamma_\lambda \right] \right\rangle_U . \tag{6.22}$$

$$\widetilde{\Pi}^{(3),j}_{\mu\nu\sigma\lambda}(x,y,z) = -2\text{Re}\left\langle \text{Tr}\left[S^j(0,y)\gamma_\nu S^j(y,x)\gamma_\mu S^j(x,z)\gamma_\sigma S^j(z,0)\gamma_\lambda \right] \right\rangle_U . \tag{6.23}$$

Here $S^j(x,y)$ is the flavour j-quark propagator from source y to sink x, Q_j is the charge factor ($Q_u = \frac{2}{3}$, $Q_d = -\frac{1}{3}$, $Q_s = -\frac{1}{3}$), and $\langle\cdot\rangle_U$ denotes the ensemble average. In the above, the γ_5-Hermiticity of the propagator is used.

A drawback of this representation is its higher computational cost on the propagator inversion due to the fact that one has to integrate over x and z on the whole lattice. As a result, one can not just compute the propagator $S^j(x,z)$ with a fixed point-source. The z-integral can be performed with the *sequential propagator* technique. Let us illustrate this technique with an example. To compute the object $\int_z z_\rho S(x,z)\gamma_\sigma S(z,0)$, one can first solve the propagator $S(z,0)$ with a point-source at the origin, and then the quantity to be computed is nothing but the solution of the Dirac equation with $z_\rho\gamma_\sigma S(z,0)$ as a source. Obviously, this introduces a computational overhead. Therefore, this integrand representation is only used for a consistency check for the integrand representation that we call Method 2 at the end.

- **Method 2** As is done in Sect. 3.2, we can use a change of variables in the integrals and exploit translational invariance of the hadronic 4-point function to

arrive at a different representation for the integrand of a_μ^{hlbl}[4]

$$f^{(\mathrm{Conn.})}(|y|) = -\sum_{j\in u,d,s} \hat{Z}_{\mathrm{V}}^4 Q_j^4 \frac{m_\mu e^6}{3} 2\pi^2 |y|^3 \times \int_x \left(\mathcal{L}'_{[\rho,\sigma]\mu\nu\lambda}(x,y) \int_z z_\rho \widetilde{\Pi}^{(1),j}_{\mu\nu\sigma\lambda}(x,y,z) + \bar{\mathcal{L}}^{(\Lambda)}_{[\rho,\sigma];\lambda\nu\mu}(x,x-y) x_\rho \int_z \widetilde{\Pi}^{(1),j}_{\mu\nu\sigma\lambda}(x,y,z) \right). \tag{6.24}$$

This quantity can be more easily computed on the lattice because only point-sources are needed for computing $\widetilde{\Pi}^{(1)}$. Eq. (6.24) is thus our master formula for the fully-connected contribution.

The $(2+2)$ contribution

One subtlety in the calculation of the quark-disconnected contribution is the subtraction of the vacuum expectation value (VEV). In the perturbative picture, the subtraction of a non-vanishing VEV is necessary to make sure that the diagram stays connected by gluon lines. Define

$$\Pi^j_{\mu\nu}(x,y) = -\mathrm{Re}\left(\mathrm{Tr}[S^j(y,x)\gamma_\mu S^j(x,y)\gamma_\nu]\right), \tag{6.25}$$

and its VEV-subtracted counterpart

$$\hat{\Pi}^j_{\mu\nu}(x,y) = \Pi^j_{\mu\nu}(x,y) - \langle \Pi^j_{\mu\nu}(x,y)\rangle_U. \tag{6.26}$$

Applying change of variables and exploiting translational invariance of the hadronic 4-point function as before, we arrive at the integral representation for $a_\mu^{(2+2)}$

$$f^{(2+2)}(|y|) = -\sum_{i,j\in u,d,s} Q_i^2 Q_j^2 \hat{Z}_{\mathrm{V}}^4 \frac{m_\mu e^6}{3} 2\pi^2 |y|^3 \times \left\langle \int_x \left((\bar{\mathcal{L}}^{(\Lambda)}_{[\rho,\sigma];\mu\nu\lambda}(x,y) + \bar{\mathcal{L}}^{(\Lambda)}_{[\rho,\sigma];\nu\mu\lambda}(y,x)) \hat{\Pi}^i_{\mu\lambda}(x,0) \int_z z_\rho \hat{\Pi}^j_{\sigma\nu}(z,y) + \bar{\mathcal{L}}^{(\Lambda)}_{[\rho,\sigma];\mu\nu\lambda}(x,y) \hat{\Pi}^i_{\mu\nu}(x,y) \int_z z_\rho \hat{\Pi}^j_{\sigma\lambda}(z,0) \right) \right\rangle_U. \tag{6.27}$$

In this representation, the factorisation of the x- and z-integrations makes the lattice computation easier. As an appealing feature in our Method 2, we only have to use point-source propagators for such a calculation.

We call *light-light* contribution the set of diagrams consisting exclusively of light-quarks. Likewise, the *strange-strange* contribution contains only strange-quark loops. Finally, the *light-strange* case covers all diagrams containing one light and one strange-quark loop. These sub-contributions can easily be constructed by combining different terms in Eq. (6.27). As the integral is constructed as a post-processing step, the light-quark and strange-quark loops can easily be combined.

[4] c.f. e.g. the operations used in Eq. (3.28) and Eq. (3.29).

6.2.2 The sub-leading topologies

As we work with $N_f = 2+1$ lattice ensembles, we assume the mass-degeneracy between the u- and d-quark from here on to simplify our expressions. From now on, l and s refer to light- and strange-quarks respectively. We define

$$T_\mu(x) = \text{Im}\Big(\text{Tr}[\gamma_\mu S^l(x,x)] - \text{Tr}[\gamma_\mu S^s(x,x)]\Big), \tag{6.28}$$

which represents the contribution from the self-contracted disconnected quark loop, or *disconnected loop* for short.

The $(3+1)$ contribution

Define the *triangle* with quark species i,

$$R^i_{\mu\nu\lambda}(x,y,z) = \text{Im}\Big(\text{Tr}[\gamma_\mu S^i(x,y)\gamma_\nu S^i(y,z)\gamma_\lambda S^i(z,x)]\Big). \tag{6.29}$$

Our expression for the integrand for the (3+1)-topology reads

$$\begin{aligned} f^{(3+1)}(|y|) = \frac{2m_\mu e^6}{9} \sum_{j\in u,d,s} \hat{Z}_V^4 Q_j^3 2\pi^2 |y|^3 \times \\ \Big\langle \int_x \mathcal{L}'_{[\rho,\sigma]\mu\nu\lambda}(x,y) T_\mu(x) \int_z z_\rho R^j_{\lambda\nu\sigma}(0,y,z) \\ + \int_x \bar{\mathcal{L}}^{(\Lambda)}_{[\rho,\sigma]\lambda\nu\mu}(x,x-y) x_\rho T_\mu(x) \int_z R^j_{\lambda\nu\sigma}(0,y,z) \\ + \int_x \bar{\mathcal{L}}^{(\Lambda)}_{[\rho,\sigma]\mu\nu\lambda}(x,y) R^j_{\mu\nu\lambda}(x,y,0) \int_z z_\rho T_\sigma(z) \Big\rangle_U. \end{aligned} \tag{6.30}$$

It is worth noting that unlike in the $(2+2)$ case, no VEV-subtraction is needed for the $(3+1)$ contribution, because the VEV of the three-point function and the one-point function vanish due to the charge conjugation symmetry of the QCD action. In later sections, we will call $(3+1)_{\text{light}}$ and $(3+1)_{\text{strange}}$ the sub-contribution with light- and strange-quark triangle respectively.

The $(2+1+1)$ contribution

We can derive a representation for $f^{(2+1+1)}$ from the expression for the $(3+1)$ topology; the idea is to split the triangles appearing in the expression of the $(3+1)$ integrand into a sum of products of two- and one-point functions, and then correct the diagram double-counting. In doing so, the terms involving the disconnected quark loop T in Eq. (6.30) can be reused for the $(3+1)$ calculation, as we perform more self-averages for this noisy, more-disconnected quantity (see Sect. 6.4.3). Moreover, we apply a change of variables to avoid the case where a disconnected loop is located at the origin to increase the number of available samples per $|y|$.

More explicitly, we define the two quantities

$$\begin{aligned} h^i_{\mu\nu\lambda}(x,y) &= \hat{\Pi}^i_{\mu\lambda}(x,0) T_\nu(y), \\ g^i_{\mu\nu\lambda}(x,y) &= h^i_{\mu\nu\lambda}(x,y) + 2h^i_{\nu\mu\lambda}(y,x), \end{aligned} \tag{6.31}$$

and we write

$$
\begin{aligned}
f^{(2+1+1)}(|y|) = \frac{m_\mu e^6}{54}\hat{Z}_{\mathrm{V}}^4 \sum_{i\in u,d,s} Q_i^2 2\pi^2 |y|^3 \times \\
\Big\langle -\int_x \mathcal{L}'_{[\rho,\sigma]\mu\nu\lambda}(y-x,y)T_\mu(x)\int_z (z_\rho - y_\rho) h^i_{\sigma\lambda\nu}(z,y) \\
+\int_x (x-y)_\rho \bar{\mathcal{L}}^{(\Lambda)}_{[\rho,\sigma]\lambda\nu\mu}(x-y,x)T_\mu(x)\int_z h^i_{\sigma\lambda\nu}(z,y) \\
+\int_x \mathcal{L}'_{[\rho,\sigma]\mu\nu\lambda}(x,y)T_\mu(x)\int_z z_\rho g^i_{\sigma\nu\lambda}(z,y) \\
+\int_x \bar{\mathcal{L}}^{(\Lambda)}_{[\rho,\sigma]\lambda\nu\mu}(x,x-y)x_\rho T_\mu(x)\int_z g^i_{\sigma\nu\lambda}(z,y)\Big\rangle_U .
\end{aligned}
\tag{6.32}
$$

The $(1+1+1+1)$ contribution

Here we finally give our parametrisation of the fully-disconnected $(1+1+1+1)$ contribution. This again takes advantage of the quantities computed in the previous cases. Here, one needs to carefully subtract the non-vanishing VEVs appearing in different pieces in this contribution. We define the following quantity:

$$
\begin{aligned}
\langle T_\mu(x)T_\nu(y)T_\sigma(z)T_\lambda(0)\rangle_U^c = &+\langle T_\mu(x)T_\nu(y)T_\sigma(z)T_\lambda(0)\rangle_U \\
&-\langle T_\mu(x)T_\nu(y)\rangle_U\langle T_\sigma(z)T_\lambda(0)\rangle_U \\
&-\langle T_\mu(x)T_\sigma(z)\rangle_U\langle T_\nu(y)T_\lambda(0)\rangle_U \\
&-\langle T_\mu(x)T_\lambda(0)\rangle_U\langle T_\nu(y)T_\sigma(z)\rangle_U .
\end{aligned}
\tag{6.33}
$$

With this definition in place, we can write down the expression we used for the integrand for this topology, after correcting the triple-counting of the diagrams,

$$
\begin{aligned}
f^{(1+1+1+1)}(|y|) = -\frac{m_\mu e^6}{729}\hat{Z}_{\mathrm{V}}^4 2\pi^2 |y|^3 \times \\
\Big\langle \int_x \bar{\mathcal{L}}^{(\Lambda)}_{[\rho,\sigma]\lambda\nu\mu}(x,x-y)x_\rho T_\mu(x)\int_z T_\nu(y)T_\lambda(0)T_\sigma(z) \\
+\int_x \mathcal{L}'_{[\rho,\sigma]\mu\nu\lambda}(x,y)T_\mu(x)\int_z z_\rho T_\nu(y)T_\lambda(0)T_\sigma(z)\Big\rangle_U^c .
\end{aligned}
\tag{6.34}
$$

As a concluding remark for this sub-section, in some of the provided expressions, terms with a z-integral without a z-dependent weight factor appear. These could be reduced and in some cases vanish in the infinite-volume limit due to the Ward-identity associated with current conservation. Such a modification would in general change the shape of the integrand, as well as its statistical variance. For definiteness, our lattice calculations are done precisely with the expressions given in this section.

6.2.3 Numerical implementation

The number of configurations that we use for each ensemble is between $\mathrm{O}(250)$ and $\mathrm{O}(5000)$. As the integrand $f(|y|)$ depends only on the scalar quantity $|y|$, in the limit of infinite statistics, it depends on neither the choice for the origin, nor the y-vector, if the resulting $|y|$ is the same. Therefore, our general strategy for reducing the noise is to sample the integrand by averaging the measured result on many pairs of origin and y-vector. As we use point-source for our propagator solves, we put the sources according to some specific geometry such that we can efficiently construct many equivalent $|y|$, as the origin and y-vector will be one of these source positions.

To be more specific, in the case of the fully-connected, our choice is to make these points aligned on several lines in space-time; while for the (2+2), the sources are spread on a 2-dimensional grid where the same $|y|$ can be obtained from at least two non-collinear directions, e.g. $y = (1,1,1,3)$ and $y = (2,2,2,0)$ give the same $|y|$. The reason for choosing different geometry here is that the (2+2) has a much worse signal-to-noise behavior compared to the fully-connected and more sampling is required to improve the quality of the signal. One should be careful with the choice of the source points while dealing with ensembles with open boundary condition. Unwanted boundary effects might be introduced if they are too closed to the temporal boundaries.

As propagator solve is one of the expensive operations in our calculation, we have decided to merge the triangle part [Eq. (6.29)] of the (3+1) calculation to the same program which computes the fully-connected, due to the similarity in their structure. For instance, both of them require a quantity of type $S(a,b)\gamma_\alpha S(b,c)$. Therefore, combining them in the same program will save some computing time. Another avoidable source of overhead is the waste in memory for objects that will be spin/color-traced at the end. For instance, because the gamma matrices are color-blind, one can identify the color-dependent part of a quantity that we want to compute and trace out the color indices first before multiplying it with a gamma matrix prior to taking the final trace.

As already mentioned, the expressions for the disconnected contributions, Eqs. (6.27, 6.30, 6.32, 6.34), all contain a factorized pattern for the x- and z-integrals. It suffices to first compute the x- and z-integral separately with the spin- and color-indices contracted for each expression and combine these objects in post-processing. Some details of the numerical aspect of the disconnected loop will be given in Sect. 6.4.1. As one might also notice, both the (2+2) and the (2+1+1) require the 2-point object $\hat{\Pi}_{\mu\nu}$ but with different weight functions in both the x- and z-integrals. We pre-computed $\hat{\Pi}_{\mu\nu}$ on a limited number of ensembles and stored them as lattice objects for each given reference point that we use as the origin in order to have even more samples for the self-averaging of the (2+1+1) integrand. However, we did not apply this strategy to the (2+2) because the requirement of data storage will be very demanding in order to have a good error reduction. Contrary to the (2+1+1), the resolution of the (2+2) is crucial as it leads to big cancellations with the fully-connected in the final a_μ^{hlbl}. So despite their similar structures, the (2+2) and the (2+1+1) are nonetheless treated separately.

Some information of the ensembles that are involved in our study is given in Tab. 6.1 for convenience. The ensembles are generated along trajectories with the trace of the quark-mass matrix kept constant. We refer the reader to Refs. [Cha+20; Cha+21] for more details, such as the statistics and how the source positions are selected for the propagator solves.

6.3 Analysis of the $\mathrm{SU}(3)_f$ study

Now let us turn to the analysis of our $\mathrm{SU}(3)_f$ study [Cha+20]. A particular feature of this study is the quantification of the finite-size effects (FSEs) from effective models. Under SU(3)-flavor symmetry, the contraction topologies which contain a self-contracted disconnected loop, namely the (3+1), the (2+1+1) and the (1+1+1+1) classes, vanish due to the electric charge factors, which makes the study simpler. In the rest of this section, we will refer to the (2+2)-contribution as the disconnected one. In addition, the quark mass-degeneracy also implies that of the pions, the kaons

β	Ensemble	$T \times L^3$	a^2 [GeV]$^{-2}$	m_π^2 [GeV]^2	m_K^2 [GeV]^2	$m_\pi L$	$\hat{Z}_V$
3.34	A653	48×24^3	0.2532	0.171	0.171	5.31	0.70351
	A654	48×24^3		0.107	0.204	4.03	0.69789
3.40	**U103**	128×24^3	0.1915	0.172	0.172	4.35	0.71562
	H101	96×32^3		0.173	0.173	5.82	0.71562
	U102	128×24^3		0.127	0.194	3.74	0.71226
	H105	96×32^3		0.0782	0.213	3.92	0.70908
	C101	96×48^3		0.0488	0.237	4.64	0.70717
3.46	**B450**	64×32^3	0.1497	0.173	0.173	5.15	0.72647
	D450	128×64^3		0.0465	0.226	5.38	0.71921
3.55	**H200**	96×32^3	0.1061	0.175	0.175	4.36	0.74028
	N202	128×48^3		0.168	0.168	6.41	0.74028
	N203	128×48^3		0.120	0.194	5.40	0.73792
	N200	128×48^3		0.0798	0.214	4.42	0.73614
	D200	128×64^3		0.0397	0.230	4.15	0.73429
3.70	**N300**	128×48^3	0.06372	0.178	0.178	5.11	0.75909

TABLE 6.1: List of ensembles used for our study of a_μ^{hlbl} at the physical point in Ref. [Cha+21]. Here β is the inverse bare coupling. The underlined ensembles are of periodic boundary condition, while the rest are of open boundary condition. The ensembles in bold are also used in the SU(3)$_f$-symmetric study Ref. [Cha+20].

and the η, which reduces the input parameters for the study of the integrand using effective models.[5] While the pion masses of the ensembles are all roughly around 420 MeV, there are four different lattice spacings among the six ensembles that we used. The lattice spacings a and the spatial extents L of the ensembles used in the study are given in Tab. 6.1.

6.3.1 Modelling the integrand

An attempt at modeling the $|y|$-integrand of the fully-connected contribution computed on the lattice ensemble N202 is shown in Fig. 6.2 with $\Lambda = 0.16$ for the QED-kernel. Note that the "Method 1" representation of the integrand is used. In the plot, three contributions estimated from models are shown: the constituent quark loop, the neutral-pseudoscalar-meson exchange and the charged-pseudoscalar-meson loop. Except for the π^0 and η contributions, the other integrands computed from models are in infinite-volume. The meson masses are the ones measured on the lattice. The $\pi^0 \to \gamma\gamma$ transition form factors are parametrized with a VMD ansatz, where the vector meson masses for each considered ensemble are obtained in a dedicated lattice study [GMN19]. As for the charged-pseudoscalar-meson loops, we simply assume point-like interaction (scalar QED) between the charged mesons and the photon. The mass of the constituent quark falls in the common range that is used in the literature[6] and such that the peak of the total integrand computed from the models matches the one from the lattice data. The model computation in Fig. 6.2 describes the integrand computed on the lattice to a satisfactory degree. As one can directly notice, the only long-ranged contribution beyond $|y| = 1$ fm is the pseudoscalar-meson exchange. Note that the large value of $m_\pi L$ of N202 makes it almost an

[5] Under SU(3)$_f$-symmetry, there is no η/η'-mixing effect.

[6] c.f. Sect. 1.2 and references therein.

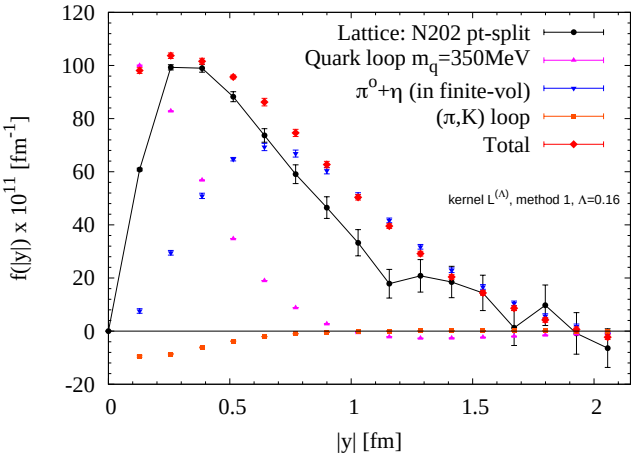

FIGURE 6.2: Modelling of the integrand and the comparison with the lattice data.

infinite-volume environment for other heavier hadronic bound states. However, the pseudoscalar-meson exchange still somehow overshoots the lattice data in the large $|y|$-region. One might thus wonder if there would still be any missing important contribution from other heavier meson states.

Distillation method and lattice spectroscopy

A dedicated lattice spectroscopy study is carried out for the ensemble H101 to probe other possible mesonic contributing states. In this study the *distillation* method [Pea+09] and its stochastic formulation [Mor+11] are used. In the determination of the hadron spectrum on the lattice, one has to construct interpolators which have the same quantum numbers as the hadrons that one wants to study in order to overlap with the hadronic states. Then, the spectrum can be read off from for instance the large-time behavior of the correlation functions in Euclidean space-time. Studies show that the overlap with the states and the statistical fluctuation can be improved by using *smearing* methods, which can be considered as a smoothening procedure of the fields. Under such an operation, the high-frequency part of the fields is suppressed and thus it would be sufficient to work only on the vector space spanned by the low-modes. Using the notations of Ref. [Pea+09], denoting $V(t)$ a matrix comprised of a certain number of low-modes of the smearing operator at time slice t up to the truncation, an essential quantity for extracting the mesonic spectrum is the connected 2-point correlation function at time t and t'

$$C_M^{(2)}(t',t) = \mathrm{Tr}[\Phi^B(t')\tau(t',t)\Phi^A(t)\tau(t,t')]\,, \tag{6.35}$$

where

$$\Phi_{\alpha\beta}(t) = V^\dagger(t)[\Gamma^A(t)]_{\alpha\beta}V(t)\,, \tag{6.36}$$

contains the spinorial information and

$$\tau_{\alpha\beta}(t',t) = V^\dagger(t')M^{-1}_{\alpha\beta}(t',t)V(t)\,, \tag{6.37}$$

is called *perambulator* with M the lattice representation of the Dirac operator. The upside of the distillation method is that the perambulator τ also appears in various

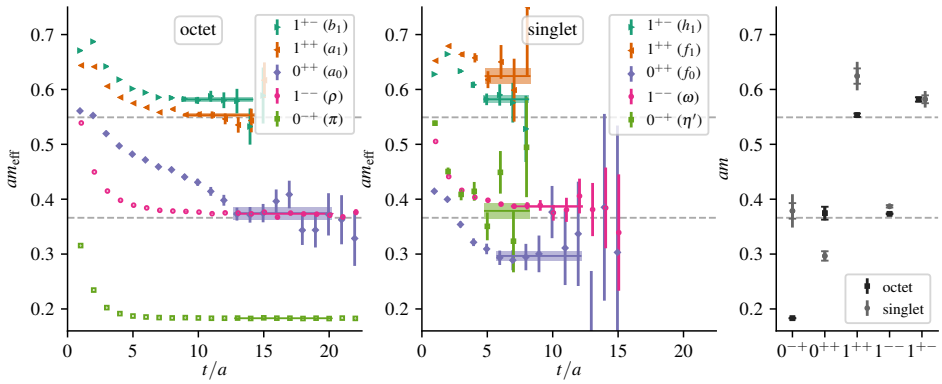

FIGURE 6.3: Dedicated study of the mesonic spectrum of H101. The plateaued value from the two plots from the left are the estimated value of the effective mass in lattice unit. The legends indicate the quantum numbers J^{PC} of the lowest meson states that we are interested in. The plot on the right summarizes the findings of the other two. The grey dashed lines on each plots correspond to two- and three-pion thresholds. Figure taken from Ref. [Cha+20].

different correlators. As it is a rather small object, it can be stored once computed and then be reused for various purposes.

The stochastic version of distillation proposed in Ref. [Mor+11] goes a step further by noting that a precise determination of the quantities defined above is not really necessary as one is limited by the statistical fluctuation of the gauge field ultimately. It is suggested that, while solving the Dirac equation, one can take the source vector in Eq. (2.73) from a set of random noise vectors η satisfying

$$\mathbb{E}(\eta_i) = 0\,, \quad \mathbb{E}(\eta_i \eta_j^*) = \delta_{ij}\,, \tag{6.38}$$

where $\mathbb{E}(\cdot)$ denotes the expectation value. It helps in reducing the variance of the estimate of a physical observable if one further projects the random noise vectors to a particular subspace [Wil99; Fol+05]. This technique is known as *dilution*. The implementation of this method requires minor modifications of the original formulation of the distillation framework by properly including the dilution projector.

The mesonic spectrum of H101 is shown in Fig. 6.3. The scalar meson f_0 turns out to be located well below the two-pion threshold. Note that this study uses merely the smeared quark bilinears and the lack of non-local multimeson-like interpolators makes the mass estimate less robust. However, the identified bound states below the two-pion threshold should provide a strong hint about the origin of the mismodelling of the $|y|$-integrand of a_μ^{hlbl}. The scalar meson is known to contribute negatively to the total a_μ^{hlbl} [Kne+18; DHS21]. A single-meson exchange of f_0 would supposedly contribute at long distances. This in part motivates the study of the scalar-meson-exchange contribution using a VMD parametrization for the transition form factor done in Sect. 3.2. Nonetheless, as pointed out in the conclusion of Sect. 3.2, the sensitivity to the free parameters of the integrand computed under this framework makes it difficult to draw any quantitative conclusion from the model.

6.3.2 Correction for the finite-size effects

On the lattice, one needs to correct two sorts of finite-size effects for a_μ^{hlbl}. The first one is due to the truncation of the integral at $|y| = |y|_{\mathrm{max}}$. Due to the finite physical

sizes of the boxes that we use, the information of the integrand at large $|y|$ can not be easily obtained. On top of that, the degradation of the signal at medium-large $|y|$ limits the range of effectiveness of the lattice data. The second source of FSE is the wrap-around effect of the intermediate states due to periodic boundary conditions. This type of effect can sometimes be significant as shown for two different models in Chap. 4.

As already discussed in the previous section, even though not exact, the pseudoscalar exchange contribution to a_μ^{hlbl} seems to provide a reasonable description of the lattice data at large-distances. Moreover, among the most substantial contributions to a_μ^{hlbl}, which we plot in Fig. 6.2, the neutral-pseudoscalar-meson exchange appears to dominate over the rest. It is thus legitimate to ask if one can use the neutral-pseudoscalar-meson exchange to model the long-distance contribution of the integrand. The expression of the neutral-pseudoscalar-meson-exchange contribution using a VMD TFF for all the three contributing channels is given in Ref. [Asm+18]. Note that one has to be careful with the diagram matching between the Wick-contractions and the pseudoscalar-meson-exchange channels when Method 2 is used for the connected topology. The matching is studied in the framework of Partially-Quenched Chiral Perturbation Theory in Chap. 5 with results given in Sect. 5.3.2. The result from Ref. [Asm+18] can be easily adapted to the situation that we consider. The technically difficult part of the numerical implementation of its infinite-volume version is very similar to the scalar-meson-exchange contribution using a VMD TFF that we discuss in Sect. 3.2 and the finite-volume version can be easily obtained following the procedure detailed in Chap. 4.

A comparison between the integrands of the connected contribution on two lattice ensembles, H200 and N202, which only differ in the box size, and the corresponding finite-volume pseudoscalar-meson-exchange contributions are shown in Fig. 6.4. One can see that the order of magnitude of the finite-size effects obtained from a direct comparison between the lattice data is very well captured by the finite-volume neutral-pseudoscalar-meson exchange. Of course, a comparable systematic error should be assigned for the FSEs estimated in this way due to the imperfection of its modelling by the neutral-pseudoscalar-meson exchange.

Due to the aforementioned considerations, we come up with the following FSE correction scheme, where the data is truncated at a cut-off value $|y|_{\text{cut}}$ determined *a posteriori*:

1. Write $a_\mu = a_\mu^{\text{data}} + a_\mu^{\text{tail}} + a_\mu^{\text{FSE}}$ where
   - a_μ^{data} is the integrated lattice data up to $|y|_{\text{cut}}$;
   - $a_\mu^{\text{FSE}} \equiv a_\mu^{\text{nPS,VMD,infV}} - a_\mu^{\text{nPS,VMD,fV}}$ is the finite-volume correction estimated from the difference between the neutral-pseudoscalar-meson exchange contribution with a VMD TFF in infinite- and finite-volume, integrated up to $|y|_{\text{cut}}$.
   - a_μ^{tail} is the integrand of the pseudoscalar-meson exchange computed with a VMD TFF integrated from $|y| = |y|_{\text{cut}}$ to $|y| = \infty$.
2. A systematic error of 25% of the size of the quantity estimated from the model, i.e. $a_\mu^{\text{FSE}} + a_\mu^{\text{tail}}$, is assigned and added in quadrature to the statistical error for the total error.
3. Find $|y|_{\text{cut}}$ for which the error estimate is minimized with some degree of stability while varying $|y|_{\text{cut}}$ within a range.

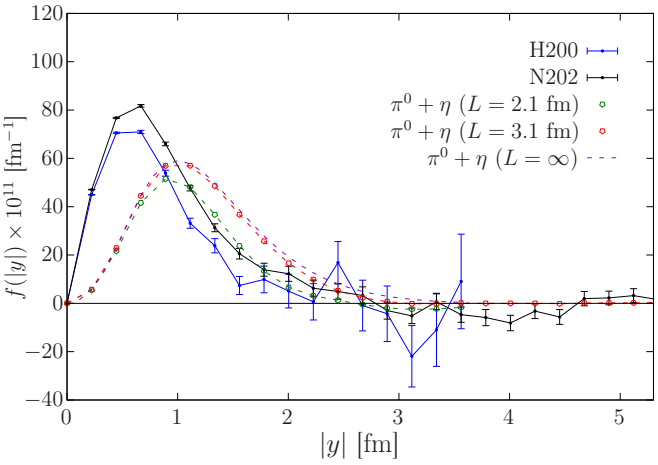

FIGURE 6.4: Direct FSE study from the lattice data and comparison to the model on the fully-connected integrand using Method 2. $\Lambda = 0.4$ is chosen for the QED-kernel. The ensembles H200 and N202 differ only in the physical volume (N202 is larger in physical unit). The corresponding finite-volume pseudoscalar-meson exchange ($\pi^0 + \eta$) is given for each ensemble. The infinite-volume pseudoscalar-meson-exchange contribution is also given for comparison. Plot taken from Ref. [Cha+20].

The main idea of this FSE correction scheme is to find the best compromise between the statistical error and the systematic error. Typically, we find the relation between the estimated a_μ^{hlbl} and the chosen value for $|y|_{\mathrm{cut}}$ as shown in Fig. 6.5. One can see from this plot that the error is minimized between 2.5 fm and 3 fm. Furthermore, the central value and the error stay quite stable in this range. Therefore, our $|y|_{\mathrm{cut}}$ is taken at the indicated value of the plot. Of course, for the (2+2)-disconnected data, the same procedure also applies. But it being statistically noisier forces $|y|_{\mathrm{cut}}$ to be chosen smaller in general.

The FSE corrected data for each individual ensemble are given in Appendix F.1 for completeness.

6.3.3 Continuum extrapolation

As the pion masses of the ensembles are almost identical, the finite-volume-effect-corrected data require only an extrapolation in the lattice spacing. There are at least two ways to analyze the data: the first one being a simultaneous extrapolation in both the connected and the disconnected data with a mutual constraint on the dependence on the lattice spacing a; while the second one consisting in summing up the connected and the disconnected data first and then performing a continuum extrapolation. These are motivated by the observation that the connected and the disconnected data are of different sign and tend to cancel each other. Given that we are particularly interested in the total a_μ^{hlbl}, both methods are expected to give us a better controlled continuum extrapolation. We observe that using the first method with a fit ansatz linear in a^2 in both the connected and disconnected data with the slope constrained to be identical for both quantities gives a result consistent to that obtained using the second strategy with a fit ansatz linear in a^2, with a slightly smaller error. This makes us quote the result from the first fitting strategy for our final estimate for a_μ^{hlbl} and to estimate the systematic error from varying the fit ansatz and constraint in the first fitting strategy.

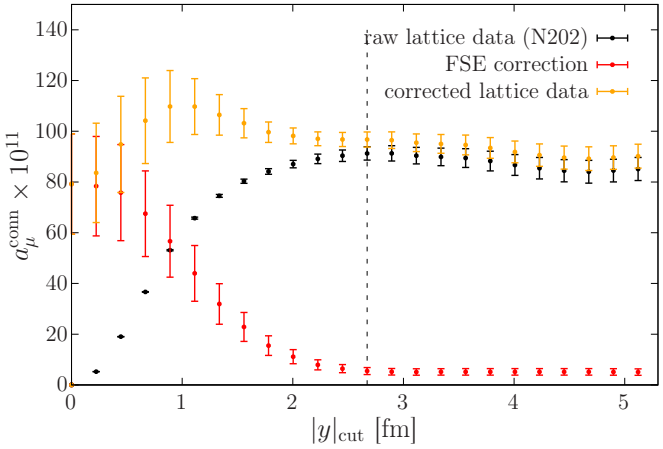

FIGURE 6.5: Stability test of the finite-size-effect-corrected connected contribution to $a_\mu^{\rm hlbl}$ calculated on N202 according to the procedure described in the text. The vertical dotted line indicates the chosen value for $|y|_{\rm rm}$, which is at about 2.6 fm. Plot taken from Ref. [Cha+20].

The fit forms that we consider are of type

$$a_\mu^{\rm conn}(a) = a_\mu^{\rm conn}(0) + Aa^n\,, \quad a_\mu^{\rm disc}(a) = a_\mu^{\rm disc}(0) + Ba^m\,. \tag{6.39}$$

The different fit Ansätze used for the estimation of the systematic error are listed in Table 6.2 and the results for each fit as well as the final estimate for the fitting-systematic error are shown on the left panel of Fig. 6.6. To see the sensitivity of our fits Ansätze to the data, we also included several fits with coarse lattices cut out. Based on the χ^2/d.o.f. of the fits, we quote the fit number 7 (χ^2/d.o.f. $= 2$) for the final result and the systematic error is determined by taking the band bounded between the highest lower end of the 68% confidence interval and the lowest upper end of the interval of all the fits listed in Table 6.2. The continuum extrapolation with fit number 7 is shown on the right panel of Fig. 6.6 for illustration. We arrive at the determination of $a_\mu^{\rm hlbl}$ for our $SU(3)_f$ ensembles:

$$a_\mu^{\rm hlbl} = 65.4(4.9)(6.6) \times 10^{-11}\,, \tag{6.40}$$

where the first error comes from the uncertainty of each individual gauge ensembles (the statistical error plus the systematic error from the FSE correction) and the second is the systematic error due to the continuum extrapolation.

Index	a-Cut [fm]	Constraint	n	m	Index	a-Cut [fm]	Constraint	n	m
1	None	None	1	1	6	None	None	2	2
2	None	$A = B$	1	1	7	None	$A = B$	2	2
3	None	$B = 0$	1	-	8	None	$B = 0$	2	-
4	< 0.0864	None	1	1	9	< 0.0864	None	2	2
5	< 0.0864	$A = B$	1	1	10	< 0.0864	$A = B$	2	2

TABLE 6.2: Different fit forms used to estimate the continuum extrapolation systematic. Table taken from Ref. [Cha+20].

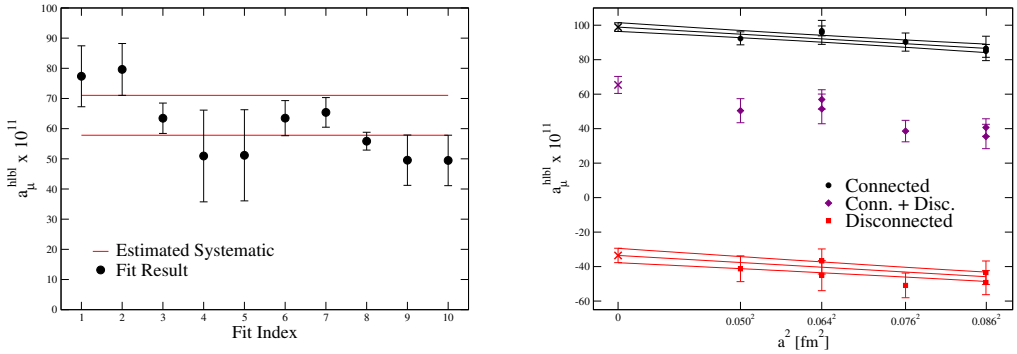

FIGURE 6.6: Left: an estimate for the fitting-systematic error to the total a_μ^{hlbl}. Right: illustration of the continuum extrapolation with the fit form 7 of Table 6.2. Figures taken from Ref. [Cha+20].

A naïve estimate at the physical point from the SU$(3)_f$ result

Although it is necessary to include lattice ensembles with lighter pion masses to really determine a_μ^{hlbl} at the physical point, one can still make a naïve estimate for a_μ^{hlbl} at the physical point from the SU$(3)_f$ result if one has an idea about the chiral dependence of a_μ^{hlbl} based on model predictions. A plausible scenario studied in Ref. [Cha+20] consists in assuming that the steepest pion mass dependence comes from the neutral-pseudoscalar-meson-exchange process. If this assumption holds, when one subtracts the latter from the a_μ^{hlbl} computed at SU$(3)_f$, the rest should remain almost constant while moving from SU$(3)_f$ to the physical point. By adding back the contribution of the neutral-pseudoscalar-meson exchange at the physical point, we obtain a naïve estimate of a_μ^{hlbl} at the physical point:

$$a_\mu^{\mathrm{hlbl,SU(3)}_f} - a_\mu^{\mathrm{hlbl},\pi^0,\mathrm{SU(3)}_f} + a_\mu^{\mathrm{hlbl},\pi^0,\mathrm{phys}} = (104.1 \pm 9.1) \times 10^{-11}\,. \tag{6.41}$$

Note that this is a very rough estimate and a systematic error at the 20-percent level should be assigned on top of the quoted error, which is purely statistical.

6.4 Analysis of the approach to the physical point

In this section, we will review the result of our lattice determination of a_μ^{hlbl} at the physical point published in Ref. [Cha+21]. There are two essential differences compared to the SU$(3)_f$ analysis presented previously. First, one should now consider all five classes of Wick-contractions because the quantity Eq. (6.28) is not identically zero anymore. The computation of the all-to-all propagator $S^f(x,x)$, henceforth referred to as *disconnected loop*, is numerically very expensive. Usually this quantity is estimated using stochastic methods in order to reduce the numerical cost. Within the Mainz Lattice QCD group, there exists a program of computing the disconnected loops for physically interesting ensembles in position-space. The data are stored on disk and shared among various projects. The second difference is that, as the data become noisier due to the enhancement of statistical fluctuations at low simulation quark masses, a particular tail-reconstruction prescription of the integrand is used. Under this prescription, the FSEs are taken care of by a combined chiral, infinite-volume and continuum extrapolation. This kind of extrapolation might be difficult due to the lack of clear theoretical guidance and the larger parameter space.

Nonetheless, it turns out that our data can be well described by some rather simple Ansätze.

The method for the disconnected loop data generation will be reported in the upcoming sub-section. After that, we will discuss our treatment for the dominant contributions, i.e. the connected and the (2+2)-disconnected and their extrapolation to the physical point. Finally, we will present our results on the SU(3)$_f$-suppressed (sub-leading) topologies, namely the (3+1), the (2+1+1) and the (1+1+1+1), for which a specific theoretical treatment of the noisy tail of the integrand is applied.

6.4.1 Calculation of the disconnected loops

A detailed description of the Mainz methodology for the calculation of the disconnected loops can be found in Ref. [C+]. For this purpose, a variant of the method proposed in Ref. [Giu+19b] is adopted. The starting point is the relation for Wilson fermion with a generic quark bilinear Γ

$$\mathrm{tr}\left[\Gamma(D_i^{-1} - D_{i+1}^{-1})\right] = (m_{i+1} - m_i)\mathrm{tr}\left[\Gamma D_i^{-1} D_{i+1}^{-1}\right] , \tag{6.42}$$

where $m_1 < m_2 < \ldots < m_N$ are N different quark masses and the D_i's are the corresponding Dirac operators. The right-hand side of Eq. (6.42) can be efficiently computed using the so-called *one-end-trick*, which is commonly applied while computing with twisted mass fermion [MM06; JMU08]. It consists in substituting the implicit identity matrix between the two Dirac operators in the trace on the right-hand side of Eq. (6.42) by its stochastic estimator $\eta\eta^\dagger$, where η is a normalized random variable. For observables with electromagnetic vector currents in $N_f = 2 + 1$ flavors, we only need the difference between the light and the strange disconnected loops; the estimation of Eq. (6.42) using the one-end-trick is thus sufficient.

6.4.2 The leading topologies at the physical point

In this sub-section, we will describe the way in which the analysis of the leading-order topology contribution is done. The results are given later in Tab. 6.5.

Purely light-quark contribution

As the difference between the light- and the strange-quark masses increases, it is very natural to expect that the purely light-quark contribution of the leading topologies dominates in the calculation of a_μ^{hlbl}. This corresponds to taking all the quark-flavor indices in Eq. (6.24) and Eq. (6.27) to be the light one. Empirically, the time cost for propagator solve scales as $\frac{V^n}{m_\pi^m}$, where V is the lattice volume and n and m are some positive numbers. Therefore, it will become computationally more demanding as we decrease the pion mass. While the numerical setup for the fully-connected remains the same as the SU(3)$_f$ case, to ameliorate the signal for the (2+2)-disconnected, which contributes the most to the total statistical error, a truncated solver technique [BCS10; BIS13] is employed. It consists in choosing a larger tolerance for the propagator solve ("sloppy") and then correcting the bias in the physical observable by estimating it from the difference between the sloppy and exact solves. In doing so, the gain in computing time implies that more measurements can be done for the same computational effort.

To handle the significant degradation of the signal in the non-flavor-symmetric ensembles as compared to the SU(3)$_f$-symmetric point, a data-driven tail-reconstruction

procedure is employed. Before the signal is completely lost, we observe that, for both of the leading topologies with light-quarks, the tail of lattice integrand with $\Lambda = 0.4$ for the QED-kernel can be well described by the ansatz

$$f(|y|) = |y|^3 A e^{-B|y|}\,, \tag{6.43}$$

where A and B are free parameters (see Fig. 6.7 and Fig. 6.8). We also find that this ansatz describes the π^0-exchange model very well. Of course, this procedure is QED-kernel-dependent because the shape of the integrand changes with the kernel and sometimes it dives under the horizontal axis. The results obtained for each individual ensemble are given in Appendix F.2.1 for completeness. By fitting the lattice data to this tail ansatz, the errors are much more reduced. This makes us adopt a different finite-size analysis compared to the previous $\mathrm{SU}(3)_f$ case: a global chiral, continuum and infinite-volume fit is performed to the tail-reconstructed lattice data for the leading contributions.

The experience with the $\mathrm{SU}(3)_f$-symmetric ensembles tells us that there will be substantial cancellations between the fully-connected and the (2+2)-disconnected. Indeed, if one assumes the dominance of the neutral-pseudoscalar-meson exchanges, the leading order analysis from Sect. 5.3 tells us that the π^0-exchange contributes with comparable sizes but opposite signs to the fully-connected and to the (2+2) (cf. Tab. 5.3). This expectation has also already been made in the literature based on the interpolation between the charge factor analyses in flavor-symmetric $N_f = 2$ and $N_f = 3$ cases [BR16b; G+18]. This motivates us to perform the global fit for the extrapolation to the physical point in two ways: either to fit the fully-connected and the (2+2)-disconnected separately and sum them up at the end, or to fit the combined data directly.

While treating the fully-connected and the (2+2)-disconnected separately, we can see from the tail-reconstructed data points in Fig. 6.7 and Fig. 6.8 that some curvature in m_π^2 appears. Therefore, for the first approach, we fit both the fully-connected and the (2+2)-disconnected data with different Ansätze of the form

$$a_\mu(m_\pi^2, m_\pi L, a^2) = A e^{-m_\pi L/2} + B a^2 + C\, S(m_\pi^2) + D + E m_\pi^2\,, \tag{6.44}$$

where the candidate function forms for $S(m_\pi^2)$ are inspired by the chiral behavior of the π^0-exchange and the $\pi^\pm$-loop [PRV09] and the volume dependence is inspired by the π^0-exchange alone. The fits with different choices of $S(m_\pi^2)$ that we made turn out to give consistent results with each other, with good $\chi^2/\mathrm{d.o.f}$ close to unity. This signifies that our data are probably not accurate enough to really distinguish the exact chiral behavior.

On the other hand, the combined data displayed in Fig. 6.9 exhibits a very smooth chiral dependence. For this approach, we find that the data are well described by the ansatz

$$a_\mu(m_\pi^2, m_\pi L, a^2) = a_\mu(0, \infty, 0)(1 + A m_\pi^2 + B e^{-m_\pi L/2} + C a^2)\,. \tag{6.45}$$

This encourages us to continue our study with the combined data and use the first approach for consistency checks. A comparison between the values obtained by performing a global fit directly on the combined data and by fitting the fully-connected and the (2+2)-disconnected individually using Eq. (6.44) and adding them up afterward is shown on the right panel of Fig. 6.10, where different considered curvature

terms $S(m_\pi^2)$ are

$$\text{Pole} \equiv \frac{1}{m_\pi^2}\,, \quad \text{Log} \equiv \log m_\pi^2\,, \quad \text{Log2} \equiv \log^2 m_\pi^2\,, \quad \text{m2Log} \equiv m_\pi^2 \log m_\pi^2\,. \tag{6.46}$$

From this plot, we are convinced that the approach with the combined data is consistent.

Nevertheless, just like the $\mathrm{SU}(3)_f$-symmetric case, there is an ambiguity in the approach to the continuum limit. We realize that changing the a^2 term in Eq. (6.45) to a leads to an equally good fit in terms of χ^2/d.o.f. Due to the slight tension between the fits linear in a and a^2, we decide to treat them on an equal footing. We quote our result from a constant fit to both of the results, linear in a or a^2, using all of our data.

The systematic error of the global fit is estimated by considering the fit results from different cut datasets, in the lattice spacing, the volume and in the pion mass respectively (see Fig. 6.10). This is also done with both of the fit forms, linear in a or in a^2. From this procedure, we quote the root-mean-squared deviation of the central values obtained from the cut datasets to the central value that we quote from our analysis with the complete dataset as the systematic error of the global fit. The reason to take the root-mean-squared deviation is that it is supposed to be quite sensitive to outliers. From the left panel of Fig. 6.10, this procedure seems to be conservative enough to cover all different fit results.

On the other hand, the fact that we do not have very precise data at light pion mass might be another point to worry about. As shown on the left panel of Fig. 6.10, the error grows significantly when we cut out the ensembles with $m_\pi^2 > 0.165\,\mathrm{GeV}^2$. This consequence is expected due to the fact that our most precise data points come from the $\mathrm{SU}(3)_f$-symmetric ensembles, where the pion masses are heavy. One could ask how reliable the absence of curvature in m_π^2 in the global fit of the combined data is, especially in our case where the lightest pion mass is about 200 MeV. We address this issue by performing another fit with the m_π^2 term in Eq. (6.45) replaced by a more divergent term $\log m_\pi^2$. This change is motivated by the fact that one can interpolate the combined contribution of the π^0-exchange and the $\pi^\pm$-loop in scalar QED with simplified parametrizations[7] in the range of $m_\pi \in [m_\pi^{\text{phys.}}, 420\,\text{MeV}]$ within small enough deviation. This is the most divergent among the curvature terms listed in Eq. (6.46) which can still capture the chiral dependence of the considered quantity to a good degree. We quote an additional systematic error for our chiral extrapolation by taking half the difference between the central values from this new fit and the one that we quote.

Contributions with strange-quark

The tail-reconstruction procedure described in the previous sub-section also applies to the rest of the leading topologies with strange-quark. The results obtained for each individual ensemble are given in Appendix F.2.2 for completeness. While for the fully-connected, the strange-quark contribution contains only the diagram with only strange-quark flowing in all quark lines; for the (2+2), one can have a purely strange contribution and a light-strange mixed contribution, i.e. when one quark-flavor index of Eq. (6.27) taken to be light and the other taken to be strange. From the analysis given in Sect. 5.3, we see that, at the considered leading orders, only mesonic states with strange-quark constituents contribute to these diagrams with strange-quarks. One would therefore expect that the strange-quark contributions

[7] See Ref. [Cha+21] for details.

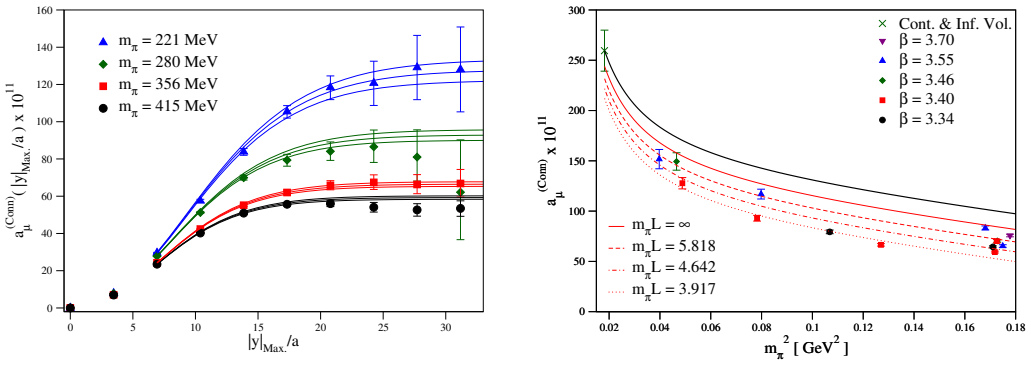

FIGURE 6.7: Left: Partially-integrated light-quark connected contribution to a_μ^{hlbl} for ensembles C101, H105, U102, and U103. The points are the numerically integrated lattice data and the curves result from switching the integrand to the fit of Eq. (6.43) above a certain value of $|y|$. Right: Chiral, continuum, and infinite-volume extrapolation of the light-quark connected contribution according to Eq. (6.44) with a curvature term $1/m_\pi^2$. The red curves are the extrapolated results at fixed lattice spacing with $\beta = 3.4$ but at different $m_\pi L$; whereas the black curve is final result in the continuum and infinite-volume limit.

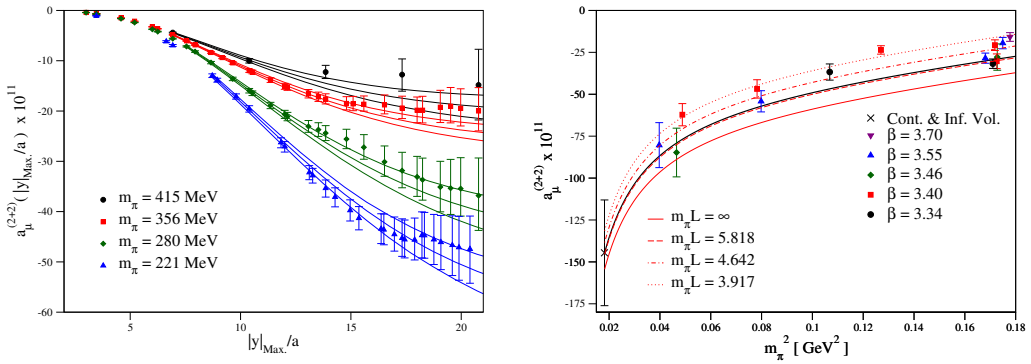

FIGURE 6.8: Light-quark (2+2)-disconnected contribution to a_μ^{hlbl}. See the caption of Fig. 6.7 for explanation.

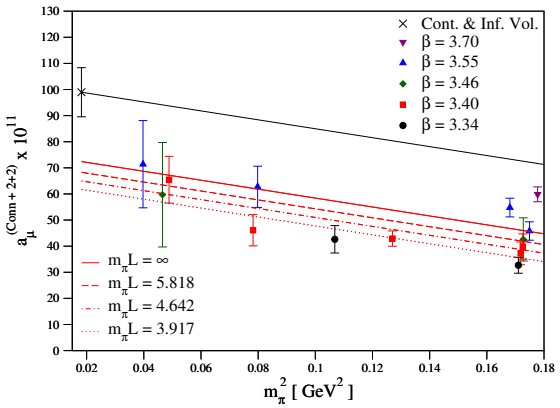

FIGURE 6.9: Global fit of the combined data. See the caption for the right panel of Fig. 6.7 for explanation.

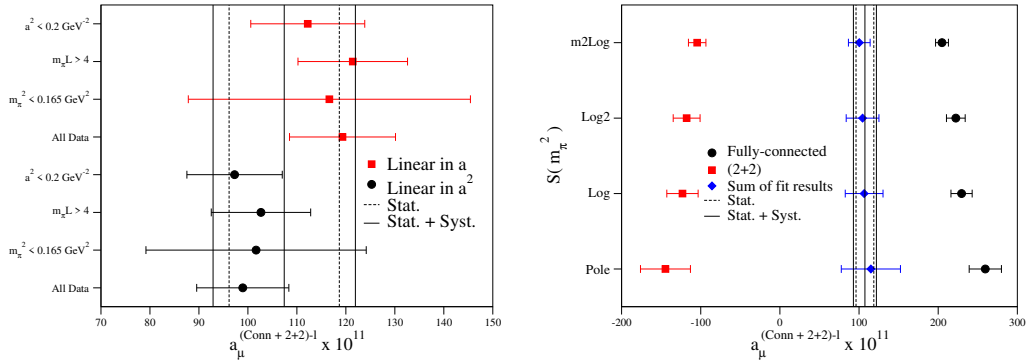

FIGURE 6.10: Study of fitting systematics. Left: fits to the combined purely light-quark fully-connected and (2+2)-disconnected data with different cut datasets. Right: fitting the light-quark fully-connected and the (2+2)-disconnected separately with different curvature terms.

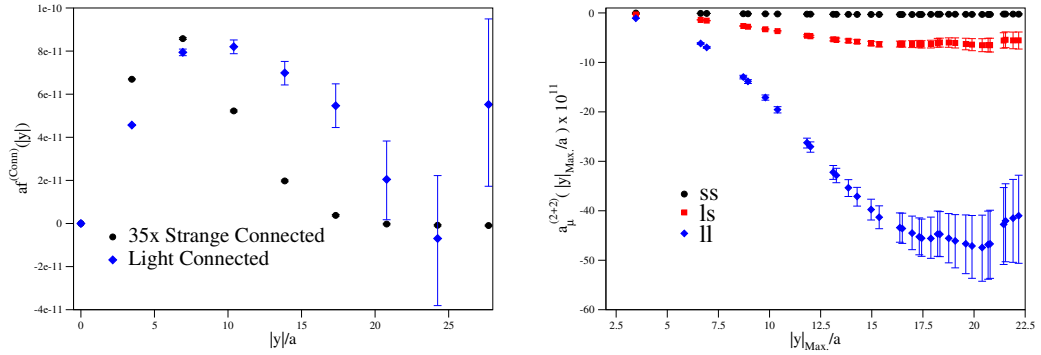

FIGURE 6.11: Strange contributions for ensemble C101. Left: Strange and light connected integrands, in lattice units. The strange integrand has been multiplied by 35 for visibility. Right: Partially integrated $(2+2)$ contributions with three different flavor combinations.

are much smaller at the physical point than the purely light-quark ones. Indeed, this can already be seen on each ensemble before the extrapolation to the physical point. We find that the all-combined tail-reconstructed data can be well described by the following ansatz

$$a_\mu(m_K^2, m_\pi L, a^2) = a_\mu(0,\infty,0)(1 + Am_K^2 + Be^{-m_\pi L} + Ca^2)\,. \tag{6.47}$$

The kaon mass is used here because it is the light mesonic state which could contribute and the exponent for the finite-volume correction is $-m_\pi L$ instead of $-m_\pi L/2$ due to the fact that we do not expect π^0 to contribute at long-distances.

6.4.3 The sub-leading topologies

In this section, we discuss the results for the sub-leading topologies. Note that due to the rapid degradation of the signal, we truncate the x-integral of the integral of the computed integrand when the norm of the x-dependent argument of the QED-kernel exceeds R_{max} given in Tab. 6.3 because of the expected exponential decay of the kernel. We have checked on several ensembles that varying R_{max} does not change the central value of the result much and the error grows as expected, which

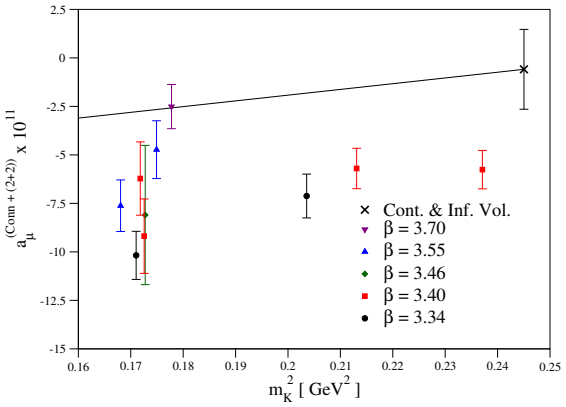

FIGURE 6.12: An extrapolation of the sum of the fully-connected strange and $(2+2)$ *ls* and *ss* contributions to a_μ^{hlbl}.

Id	$R_{\max}$	$R_{\max}/(L/2)$	Id	$R_{\max}$	$R_{\max}/(L/2)$
A654	8	2/3	D450	12	3/8
U102	9	3/4	N200	12	1/2
H105	8	1/2	N203	9	3/8
C101	9	3/8	D200	12	3/8

TABLE 6.3: $R_{\max}$ in lattice unit for the analyzed ensembles for the sub-leading topologies.

suggests that a larger $R_{\max}$ would just result in more noise. The same observation has also been made for the (2+2)-disconnected in Ref. [Cha+20].

The (3+1)-contribution

From the expression of the (3+1)-integrand Eq. (6.30), we can decompose the (3+1)-contribution into two parts: one with a light-quark triangle $R^l_{\mu\nu\lambda}$ and the other with a strange-quark triangle $R^s_{\mu\nu\lambda}$. We will call the former $(3+1)_{\mathrm{light}}$ and the latter $(3+1)_{\mathrm{strange}}$. Already from the heaviness of the strange-quark and the charge factors, one can expect that the $(3+1)_{\mathrm{strange}}$ is much suppressed than the $(3+1)_{\mathrm{light}}$. Therefore, we think that a detailed computation of the $(3+1)_{\mathrm{light}}$ contribution and a semi-quantitative comparison to the $(3+1)_{\mathrm{strange}}$ on several ensembles to see how different they are in order of magnitude should be sufficient to give an estimate of the contribution of this topology, at least up to the precision that we aim for for a_μ^{hlbl}.

The partially integrated $(3+1)_{\mathrm{light}}$ lattice data turn out to be entirely consistent with zero. To sensibly truncate the integral at a given $|y|$, we apply a scheme based on the conclusion from the PQChPT computation summarized in Tab. 5.2 that the only non-vanishing contributions from the lightest particles are due to charged-pseudoscalar-meson loops. We thus use this contribution as a guidance to estimate the missing contribution due to the truncation of the integral at $|y| = |y|_{\mathrm{cut}}$. To this end, we compute the relevant charged-pseudoscalar-meson loops in the framework of scalar QED and weigh them according to Tab. 5.2. Heuristically, the point-like interaction vertices from scalar QED will enhance the short-distance contributions and tend to lead to an over-estimate of the result. Therefore, we think that using this prediction as a guideline for the missing quantity should be already conservative enough.

Our integral truncation scheme goes as follows.

1. Take the central value from the partially integrated lattice data up to each $|y|$ where the data is available as the estimate for the partially integrated $a_\mu^{\rm hlbl}$ up to $|y|$.

2. Compute the residual of the partially integrated charged-pseudoscalar-meson-loop contribution to $(3{+}1)_{\rm light}$ in infinite-volume $\delta a_\mu^{\rm PS}$ according to the matching given in Tab. 5.2 for the same set of $|y|$'s.

3. Estimate the systematic error of the truncation as $w_{\rm sys.} \times \delta a_\mu^{\rm PS}$, where $w_{\rm sys.}$ is a weight factor which we leave variable, then add the systematic error in quadrature to the statistical error from the lattice data to get the total error.

4. Choose $|y| = |y|_{\rm cut}$ where the total error is minimized with a certain stability with respect to the truncation point and read off the contribution of $(3{+}1)_{\rm light}$ to $a_\mu^{\rm hlbl}$ at this point.

A typical outcome of the procedure is shown in Fig. 6.13 for the ensemble C101 ($m_\pi \approx 220$ MeV). One can see that the charged-pseudoscalar meson contribution decays quite rapidly at this pion mass and the minimum of the total error is quite often dominated by the statistical one rather than the systematic one that we assign for the tail-truncation. The results obtained with this tail-truncation procedure for each individual ensemble are given in Appendix F.2.3 for completeness.

For the extrapolation to the physical point, we assume that the volume dependence is blurred by the rather conservative systematic error from the truncation procedure. Since $(3{+}1)_{\rm light}$ contribution to $a_\mu^{\rm hlbl}$ vanishes at the SU(3)$_f$-symmetric limit, we can use it is as a constraint in our extrapolation to the physical point. Several different fit Ansätze have been tried out and listed in Appendix F.3. We notice that the data are still too noisy to show any clear dependence on the lattice spacing. Our attempts at fitting the a-dependence only lead to nuisance parameters that are zero with large errors. Without over-fitting the data, we find that the simplest fit ansatz

$$a_\mu^{(3+1),\rm l} = A(m_K^2 - m_\pi^2)\,, \tag{6.48}$$

describes our data well (see left panel of Fig. 6.14).

To have an idea about the stability of the tail-truncation procedure and the stability of the fit, we vary the weight parameter $w_{\rm sys.}$ in the range from 100% to 200% and perform fits on different cut data sets (see Tab. 6.4). The right panel of Fig. 6.14 shows very good consistency between different alternatives. We choose to quote the result from $w_{\rm sys.} = 120\%$ with the coarsest ensemble dropped ($a^2 < 0.2$ GeV^{-2}) for our final estimate of $a_\mu^{(3+1),\rm l}$.

$w_{\rm sys.}$	All data	$a^2 < 0.2$ GeV^{-2}	$m_\pi^2 < 0.1$ GeV^2
1.0	-0.36(0.35)	-0.15(0.56)	0.07(0.75)
1.2	-0.34(0.38)	0.00(0.61)	0.31(0.81)
1.5	-0.36(0.42)	0.12(0.66)	0.48(0.89)
2.0	-0.35(0.47)	0.18(0.73)	0.61(1.00)

TABLE 6.4: $a_\mu^{(3+1),\rm l}$ obtained with fit ansatz Eq. (6.48) with different $w_{\rm sys.}$ and cuts in the data.

Now let us come back to the $(3+1)_{\rm strange}$ contribution. We have computed it on several ensembles and they are all at least an order of magnitude smaller than $(3+1)_{\rm light}$ in the raw lattice data (see Fig. 6.15). As the $a_\mu^{(3+1),{\rm l}}$ result already achieves the required accuracy for the total $a_\mu^{\rm hlbl}$ and no strong pion dependence is observed in the comparison between C101 and H105 ($m_\pi \approx 280$ MeV) in Fig. 6.15, which is also predicted by our PQChPT computation in Sect. 5.3, we conclude that the precise determination of this quantity is irrelevant to the total $a_\mu^{\rm hlbl}$ for our purpose.

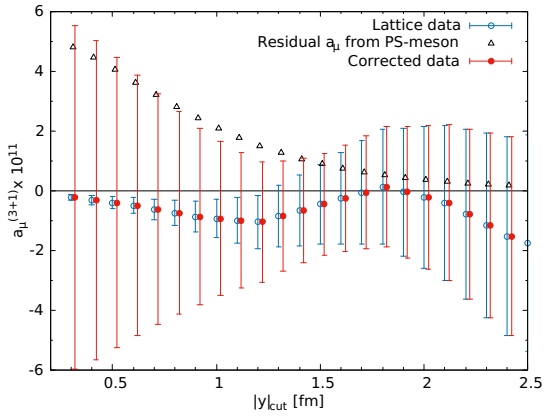

FIGURE 6.13: Determination of the $(3+1)_{\rm light}$ contribution to $a_\mu^{\rm hlbl}$ on ensemble C101 using the tail treatment procedure. Horizontal offsets are applied for visibility.

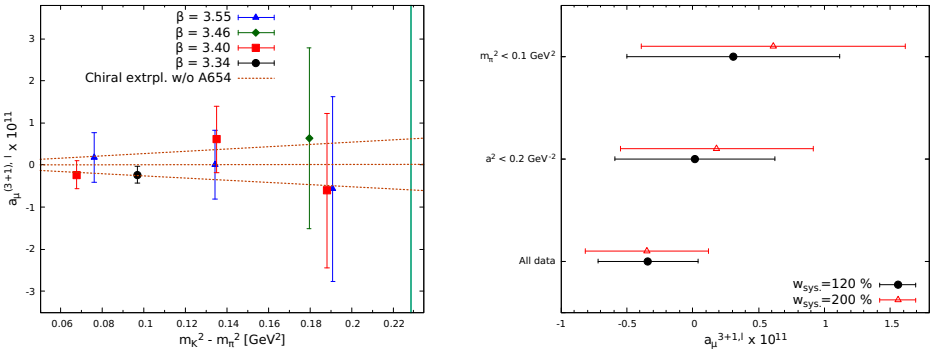

FIGURE 6.14: Left: Extrapolation of the $(3+1)_{\rm light}$ contribution to $a_\mu^{\rm hlbl}$, determined using $w_{\rm sys.} = 120\%$. The points show the results from each ensemble and the vertical green line indicates physical meson masses. The orange dashed lines show the extrapolation to the physical point with Eq. (6.48), excluding the coarsest ensemble A654. Right: Fit results of Eq. (6.48) after applying cuts to the data, with two choices of $w_{\rm sys.}$.

The (2+1+1)- and (1+1+1+1)-contributions

For both the (2+1+1)- and (1+1+1+1)-contributions, we carry out studies on at most two ensembles. Our intention here is again to provide evidence of the smallness of these quantities and their irrelevance to the precision that we aim at achieving for the total $a_\mu^{\rm hlbl}$. For the (2+1+1), we only compute the "light" contribution, i.e.,

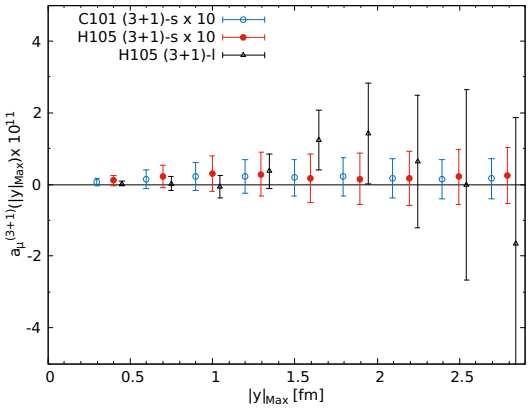

FIGURE 6.15: Partially-integrated $(3+1)_{\text{strange}}$ contribution to a_μ^{hlbl} for ensembles C101 ($m_\pi \approx 220$ MeV, $m_K \approx 470$ MeV) and H105 ($m_\pi \approx 280$ MeV, $m_K \approx 460$ MeV), compared to the $(3+1)_{\text{light}}$ for the ensemble H105. The $(3+1)_{\text{strange}}$ data are multiplied by 10 for visibility. As for the statistics for the $(3+1)_{\text{strange}}$, it is 50% compared to the $(3+1)_{\text{light}}$ for C101 and about 15% for H105.

when the "bubble" terms $g_{\mu\nu\lambda}$ and $h_{\mu\nu\lambda}$ appearing in Eq. (6.32) are computed with light-quarks because of the expectation that the strange contribution is much suppressed compared to it. As they are more "disconnected" than the (2+2)- and (3+1)-contributions, a noise-reduction method should be considered. To this end, we precompute the building block $\hat{\Pi}$ of the bubble terms (defined in Eq. (6.25)) and store it as a lattice object for various choices for the origin. Due to the latter and the disconnected loops stored as lattice-wide objects, we have access to more y-vectors having the same norm. This gives rise to much more statistics for the self-averaging over $|y|$ of the integrand and effectively reduces the noise. The available results are shown in Fig. 6.16. One can see these two contributions are consistent with zero and have way smaller uncertainties than the (3+1)-contribution. We decide to quote zero for both of their central values and estimate the errors from the upper bound of the ratios of their error bars to that of the (3+1).

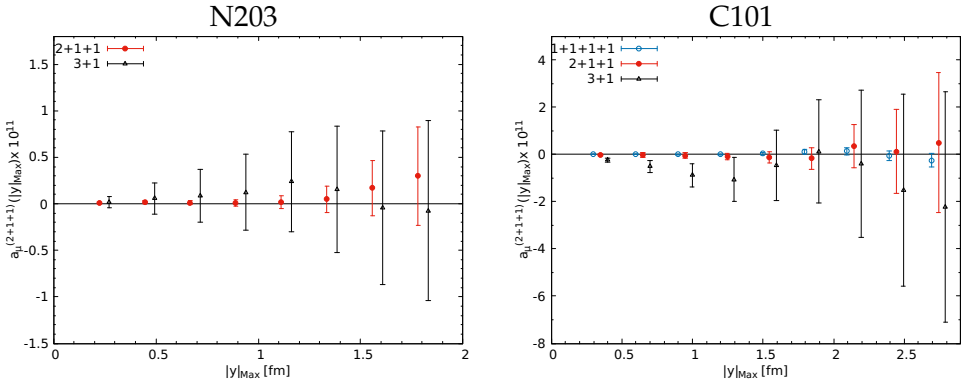

FIGURE 6.16: Partially-integrated higher-order contributions to a_μ^{hlbl}, in comparison with $(3+1)_{\text{light}}$. Left: Ensemble N203 ($m_\pi \approx 340$ MeV). Right: Ensemble C101 ($m_\pi \approx 220$ MeV).

6.4.4 The total a_μ^{hlbl}

Our determinations for the contribution to a_μ^{hlbl} of each Wick-contraction topology are given in Tab. 6.5. Note that for the light-quark fully-connected and (2+2), the errors are estimated from three different sources: the first one being statistical, the second one being the systematic error estimated with different cut datasets, and the last one coming from the extra systematic error assigned specifically to our chiral extrapolation (see the corresponding sub-section for details). With this determination, the overall error is at the level of 15%, which meets the precision requirement for a_μ^{hlbl} for understanding the discrepancy between theory and experiment on a_μ. For the total, all different errors are added in quadrature.

Contribution	Value$\times 10^{11}$
Light-quark fully-connected and $(2+2)$	$107.4(11.3)_{\text{stat.}}(9.2)_{\text{syst.}}(6.0)_{\text{chiral}}$
Strange-quark fully-connected and $(2+2)$	$-0.6(2.0)$
$(3+1)$	0.0(0.6)
$(2+1+1)$	0.0(0.3)
$(1+1+1+1)$	0.0(0.1)
Total	106.8(15.9)

TABLE 6.5: A breakdown of our result for a_μ^{hlbl}.

A comparison of our result and other determinations based on phenomenological or lattice calculations in the literature is given in Fig. 6.17. Our result is consistent with the existing ones. With the accuracy that we achieve, the resolution of the discrepancy between theory and experiment for the anomalous magnetic moment of the muon now mainly relies on better determinations of the HVP contribution.

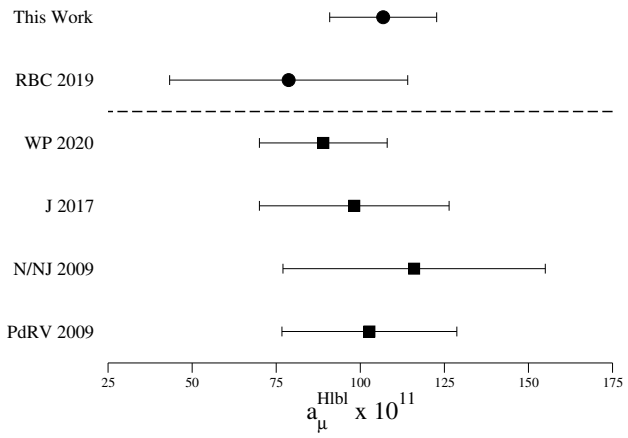

FIGURE 6.17: A comparison of our result for the u-, d-, and s-quark contribution to a_μ^{hlbl} with other estimates from the literature. The results in circles are the two available lattice determinations (this work and Ref. [Blu+20], above the horizontal dashed line). The results in squares are phenomenological predictions from Ref. [Aoy+20], Ref. [Jeg17], Ref. [Nyf09; JN09], and Ref. [PRV09].

Chapter 7

Summary and outlook

In this thesis, the essential notions and techniques involved in our lattice determination of a_μ^{hlbl} [Cha+20; Cha+21] are presented and our publications themselves are reviewed. As the experimental accuracy is being improved and new data will come out in the near future, a precise theory determination of a_μ from the Standard Model is required to confirm the tension between theory and experiment on a_μ. Although data-driven methods are quite well established for many important components of the hadronic contribution to a_μ^{hlbl}, determinations from LQCD are awaited because LQCD provides a way to calculate this quantity from first-principles in QCD.

The position-space method that we adopt requires to compute a QED-kernel function semi-analytically in the continuum and infinite-volume and a QCD correlation function on the lattice, which has the advantage of avoiding large finite-volume effects due to the massless photons compared to a lattice QED+QCD setup. Although the QED-kernel itself is a non-trivial multi-dimensional integral, its numerical implementation can be achieved using the Gegenbauer polynomial expansion of propagators in position-space. As a proof-of-principle, we show how the same approach can be used to calculate the scalar-meson contribution to a_μ^{hlbl} with a VMD TFF. In the latter, our numerical method handles different geometrical situations of the two 4-dimensional vectors appearing in the argument of these particular integrals carefully in order to optimize the convergence of the expansion. We also present the result for the integrand of the scalar-meson contribution to a_μ^{hlbl} in a region relevant to our study on the lattice, with the scalar-meson mass chosen to match one of our lightest pion-mass ensembles according to an EFT prediction and at fixed coupling to two photons. Due to the strong dependence on a free parameter of the TFF parametrization that we observe, we conclude that it would be hard to justify the choice for such a parameter and use this model to explain the lattice data. From an opposite viewpoint, one could consider using the lattice data to constrain the value of the free parameter. However, this will not be an easy task because one has to take into account other non-negligible contributing states properly as well. A remaining task is to find a good treatment for the very short distance region. The numerical implementation becomes very unstable due to the contact terms appearing under this parametrization of the TFF. We do not show the result in this region as it is not really relevant for the lattice study. To improve this, one might have to consider re-calculating some pre-computed data used by the QED-kernel to sample it even better in this region.

On the lattice, the finite-size effects might be an issue if an observable is sensitive to long-distance physics. This is expected to significantly affect a_μ^{hlbl} due to the π^0-exchange, which is a propagating light intermediate state. As a complement

to the finite-size-effect correction that we use in our first lattice study with $\mathrm{SU}(3)_f$-symmetric ensembles [Cha+20], we have shown with examples in spinor QED and in scalar QED how the finite-size effects can be estimated with a finite-volume QFT computation. In particular, the example with scalar QED might be physically interesting because it describes the interaction between two charged pseudoscalar mesons and a photon according to Chiral Perturbation Theory at leading order. However, a more realistic form factor has to be included if one wants to have a reliable estimate for the finite-size effects due to the charged-pseudoscalar-meson loop.

With Partially-Quenched Chiral Perturbation Theory, we establish a way to match a Wick-contraction diagram in LQCD to the contribution it receives from a certain process in ChPT. This allows us to make predictions for each individual Wick-contraction diagram from an EFT. The diagram matching is important because in our lattice calculation in position-space, we usually do not compute the whole set of Wick-contraction diagrams but only a subset of it and compensate by performing changes of coordinate-space integration variables. We establish the correspondence for the neutral-pseudoscalar-meson exchange and the charged-pseudoscalar-meson loop, which are considered to be the dominant long-distance contributions to a_μ^{hlbl}. In particular, we also study the diagram matching with the η/η'-mixing included. This is done with the simplest model where η' is just part of a nonet pseudoscalar-meson field and only one mixing angle is considered. It might be of interest to use a more realistic model to account for the mixing. As shown in our lattice study, the (2+2) topology with a light-quark loop and a strange-quark loop is small but can be quite precisely determined compared to the purely light-quark contribution of the same topology. According to our simplistic nonet-meson model, η and η' make important contributions to this topology. A good description of this topology would thus help understand how η and η' contribute to a_μ^{hlbl}.

Our lattice calculation at the $\mathrm{SU}(3)_f$-symmetric point [Cha+20] is a good playground for testing different ideas due to the fact that we have very precise data. We have tried to understand the finite-size effects by comparing the model prediction to a direct comparison between data generated with lattices of difference size. Also, due to the heaviness of other bound states, we find it possible to describe the integrand with hadronic models to a good degree. However, the modelling is not perfect and it might be useful to understand the missing ingredients in our modelling. A naïve extrapolation of our result at $\mathrm{SU}(3)_f$ to the physical point with the π^0-exchange agrees surprisingly well with the actual value that we obtain at the physical point with lighter pion ensembles [Cha+21]. Our lattice determination of a_μ^{hlbl} at the physical point [Cha+21] is the first lattice calculation to include all five different Wick-contractions. Most importantly, it meets the required precision for a_μ^{hlbl} to be aligned with the experimental accuracy on a_μ. Previously undetermined sub-leading topologies turn out to be small as expected. With the result that we show, any further improvement of the determination from the lattice should focus on the leading-topology contributions, namely, the fully-connected and the (2+2), with purely light-quarks. Despite the achieved accuracy, there are still some further investigations that can be done. The first one is about the FSE correction. As we adopted a more data-driven analysis, we did not continue with the FSE correction that we had established for our study at the $\mathrm{SU}(3)_f$-symmetric point [Cha+20]. We did observe that the predictions from the pseudoscalar exchange still gave the right ball-park while going to lighter pion masses. However, as we are limited by

the quality of our light pion-mass lattice data at large separations, it is hard to confirm the applicability of the same FSE correction procedure. Also, a further question would be if there are any other intermediate states that can have non-negligible finite-size effects as we approach the physical point. A better understanding of the hadronic composition of the HLbL amplitude will definitely help. Second, the pion mass dependence below 200 MeV has not been probed. Although we have assigned an extra systematic error estimation for this part, the pion-mass dependence is estimated by assuming certain models for the π^0-exchange and the $\pi^{\pm}$-loop. It is known that the absolute size of the cancellation between these two leading pionic contributions tends to increase as the pion mass decreases within the used models. Probably a much better understanding of the competition between these two contributions would shed light on the validity of our treatment to the concerned systematic error. Among the CLS $N_f = 2 + 1$ ensembles, there is one (E250) that is of pion mass slightly lower than physical. The inclusion of it would be helpful for understanding the chiral behavior of a_μ^{hlbl}. However, it will be a computationally-daunting task due to its large size.

Appendix A

Data analysis

A.1 Analysis of data from Monte Carlo simulations

In a Monte Carlo simulation, a physical quantity is estimated as the statistical average of a random variable over available Monte Carlo samples. In the limit of infinite statistics, the estimate is exact if the MC simulation samples the configuration space correctly. However, in practice, only a limited number of samples are available and thus one needs a procedure to quantify the error of the estimate. One can use *resampling* techniques to provide an estimate of the error due to finite statistics. This should be done with care because the MC samples might be correlated within themselves due to the fact that the samples are generated one after another from the same simulation run. We will discuss how to handle the auto-correlation between MC samples and how to give a reliable estimate of the error based on resampling in this section.

In the following, $\{X_i\}_{i\in[\![1,N]\!]}$ will refer to a set of a given physical observable computed on each Monte Carlo sample, indexed in the same order in which the Monte Carlo samples are generated. The X_i's should be understood as random variables.

A.1.1 Auto-correlation time

As this is a classic textbook subject, we follow Sect. 4.5 of Ref. [GL10]. Denote $\langle X\rangle$ the expectation value and σ_X^2 the variance of the observable in the infinite-statistics limit. The unbiased estimators for the expectation value and the variance of the observable X are given by

$$\hat{X} = \frac{1}{N}\sum_{i=1}^{N} X_i\,, \quad \hat{\sigma}_X^2 = \frac{1}{N-1}\sum_{i=1}^{N}\left(X_i - \hat{X}\right)^2\,. \tag{A.1}$$

Note that the unbiased estimator $\hat{X}$ itself is a random variable due to the fact that it depends on the set of N configurations that we use for our simulation. In the infinite-statistics limit $N\to\infty$, it should coincide with the true expectation value $\langle X\rangle$. As we will see, the convergence rate of $\hat{X}$ to $\langle X\rangle$ depends on the auto-correlation between the samples.

Define the *auto-correlation function* as

$$C_X(t) = \langle X_i X_{i+t}\rangle - \langle X_i\rangle\langle X_{i+t}\rangle\,, \tag{A.2}$$

which quantifies the correlation between the samples separated by a Monte Carlo time of t. Note that in the limit of infinite statistics, the index i on the left-hand side above is irrelevant.

At large separation times, the normalized auto-correlation function behaves asymptotically as

$$\Gamma_X(t) \equiv \frac{C_X(t)}{C_X(0)} \sim e^{-t/\tau_{X,\text{exp}}}\,, \tag{A.3}$$

where $\tau_{X,\text{exp}}$ is the *exponential auto-correlation time*. A proof of Eq. (A.3) for simulation algorithms with detailed balance can be found in Ref. [SSV11].

It can be shown that we have the following relation between the variance of the estimator $\hat{X}$ and the true variance of X

$$\sigma^2_{\hat{X}} \equiv \left\langle \left(\hat{X} - \langle X\rangle\right)^2 \right\rangle \approx \frac{2\tau_{X,\text{int}}}{N}\sigma^2_X\,, \tag{A.4}$$

where $\tau_{X,\text{int}}$ is the *integrated auto-correlation time*

$$\tau_{X,\text{int}} \equiv \frac{1}{2} + \sum_{t=1}^{N} \Gamma_X(t)\,. \tag{A.5}$$

If the samples are uncorrelated between themselves, $\tau_{X,\text{int}}$ will be $1/2$. From Eq. (A.4), it is clear that the error of our estimator $\hat{X}$ decreases with $1/\sqrt{N}$. The convergence rate is controlled by the auto-correlation time $\tau_{X,\text{int}}$ and it reduces the effective number of samples by a factor of $1/(2\tau_{X,\text{int}})$. Hence, the simulation becomes costly when the auto-correlation gets stronger because the error reduction decreases more slowly with the number of samples.

A popular way to check the auto-correlation in practice is to use *binning*. It consists in putting B consecutive samples in a batch and take the average of them. One then estimates the error of the estimator of the expectation value over the N/B binned samples and sees how it compares to the original error estimate. If the MC samples are uncorrelated, the error should stay stable when we increase B, as long as there are enough samples to make statistically sensible predictions.

Note that Eq. (A.4) remains a rough estimate. A more elaborate error analysis of Monte Carlo data and the binning method can be found in Ref. [Wol04].

A.1.2 Resampling methods

We will introduce two commonly used resampling methods for the error analysis of Monte Carlo data: *jackknife* resampling [Que49] and *bootstrap* resampling [Efr79]. A useful resource for these methods is Ref. [Efr82].

Jackknife resampling

From a set of N samples, we construct N jackknife samples X^{J}_i defined by the average over the subsets of data built from the original one with one element left out at each time

$$X^{\text{J}}_i = \frac{1}{N-1}\sum_{j=1,j\neq i}^{N} X_i\,. \tag{A.6}$$

We can write down an estimator for the expectation value of X using the jackknife samples

$$\hat{X}^{\text{J}} = \frac{1}{N}\sum_{i=1}^{N} X^{\text{J}}_i\,. \tag{A.7}$$

The variance of $\hat{X}^{\mathrm{J}}$ can be estimated with

$$\sigma^2_{\hat{X}^{\mathrm{J}}} = \frac{N-1}{N}\sum_{i=1}^{N}\left(X_i^{\mathrm{J}} - \hat{X}^{\mathrm{J}}\right)^2 . \tag{A.8}$$

Compared to the usual definition of variance estimator, there is a factor of $\mathrm{O}(N)$ in the jackknife error estimator, which accounts for the correlation between the jackknife samples.

Note that Eq. (A.7) contains in general a bias of order $\mathrm{O}(N^{-1})$. This bias can be easily removed with a refined definition of the estimator with a bias of order $\mathrm{O}(N^{-2})$. This is equivalent to the Aitken acceleration technique in numerical evaluation of series. We refer to Ref. [Efr82] for details.

Bootstrap resampling

The idea of bootstrap resampling is to draw N samples with repetition from the original dataset with N samples randomly with equal probability and then take the expectation value of the physical observable from this new set of data as a bootstrap sample. This procedure is repeated B times so that we will have B bootstrap samples at the end. This procedure can be seen as a MC simulation on the existing dataset.

The bootstrap estimator of the expectation value of X and its variance estimator are given by

$$\hat{X}^{\mathrm{B}} = \frac{1}{B}\sum_{i=1}^{B} X_i^{\mathrm{B}} , \quad \sigma^2_{\hat{X}^{\mathrm{B}}} = \frac{1}{B}\sum_{i=1}^{B}\left(X_i^{\mathrm{B}} - \hat{X}^{\mathrm{B}}\right)^2 , \tag{A.9}$$

where the X_i^{B}'s are the bootstrap samples.

Bootstrap resampling is numerically more expensive than jackknife resampling. However, it turns out to be very useful in the case of χ^2-fitting, which will be discussed next.

A.2 χ^2-fitting

Given a model f and data points $\mathbf{y} = (y_1, \ldots, y_M)$ at M different input values $t = t_1, \ldots, t_M$, we want to find a set of parameters $\{\theta\}$ such that $f(\cdot|\{\theta\})$ "describes the data well". Very often, and also in the analyses presented in this thesis, the best fit is defined by the maximum likelihood estimation based on the minimization of the χ^2-function

$$\chi^2 \equiv \mathbf{v}^{\mathsf{T}}\mathbf{C}^{-1}\mathbf{v} , \tag{A.10}$$

where

$$\mathbf{v} = (v_1, \ldots, v_M) , \quad v_i = y_i - f\left(t_i|\{\theta\}\right) , \tag{A.11}$$

and $\mathbf{C}$ is the covariance matrix between different data points. In some analyses, more than one observable have to be fitted in the same time. In this case, one also has to take into account the correlation between different observables properly.

The minimization of the χ^2-function admits an exact solution for fit Ansätze linear in the fit parameters. The errors of the best-fit parameters are precisely known in this case. As for non-linear fit Ansätze, no direct solution is known and typically one uses iterative algorithms starting with an initial guess of the fit parameters, such as the Levenberg-Marquardt algorithm, to numerically minimize χ^2. Then, to obtain reliable error estimates of the best-fit parameters, one needs to perform numerical

experiments such as Monte Carlo simulation to get the fluctuation of the best-fit parameters with regard to the input data (see e.g. Sect. 15.6 of Ref. [Pre+07]). A practical way is to perform χ^2-minimization on the resampled data. In repeating the same χ^2-minimization procedure over a pool of different resampled data, we will obtain a set of results for the best-fit parameters reflecting the underlying distribution of the data. Applying the same error estimation as in the chosen resampling method will then give us estimates for the errors of the best-fit parameters.

Obviously, jackknife resampling can only be used in the case where we have the same statistics for each data point. Suppose that we have data points obtained from different MC simulations, for instance different lattice ensembles, but for each of them, a different number of configurations is used. In this case, bootstrap resampling is preferred as it allows us to obtain the same number of samples respecting the underlying probability distribution for each data point.

Appendix B

Complements for Chap. 2

B.1 Convention for the γ-matrices

We use the same convention for the γ-matrices in Euclidean space-time as in the `openQCD` package. The Lorentz indices run from 0 to 3 with 0 referring to the temporal direction. A way to obtain a representation of the Euclidean γ-matrices is to start from the Clifford algebra satisfied by the Minkowski space-time γ-matrices, γ_μ^{M}, with a mostly-negative space-time signature $\eta_{\mu\nu} \equiv \mathrm{diag}(1,-1,-1,-1)$:

$$\{\gamma_\mu^{\mathrm{M}}, \gamma_\nu^{\mathrm{M}}\} = 2\eta_{\mu\nu}\mathbb{I}\,. \tag{B.1}$$

A set of generators for the Euclidean Clifford algebra, defined by

$$\{\gamma_\mu, \gamma_\nu\} = 2\delta_{\mu\nu}\mathbb{I}\,, \tag{B.2}$$

can be constructed by multiplying the spatial generators in Minkowski space-time γ_i^{M} by i and the temporal one by -1. Using the chiral representation of the Minkowskian space-time γ-matrices, we have

$$\gamma_\mu = \begin{pmatrix} 0 & e_\mu \\ e_\mu^\dagger & 0 \end{pmatrix}\,, \tag{B.3}$$

where

$$e_0 = -1\,, \quad e_k = -i\sigma_k\,, \quad k \in \{1,2,3\}\,, \tag{B.4}$$

with σ_k the usual Pauli matrices. The γ-matrices so-constructed are obviously hermitian.

As for $\gamma_5 = \gamma_0\gamma_1\gamma_2\gamma_3$, we have, in the chiral representation

$$\gamma_5 = \begin{pmatrix} 1 & 0 \\ 0 & -1 \end{pmatrix}\,. \tag{B.5}$$

B.2 Discrete symmetries on the lattice

The discrete symmetries C (charge-conjugation), P (parity) and T (Euclidean time reflection) are realized on the lattice by the following transformations (c.f. Chap. 5.4 of Ref. [GL10])

- **Charge conjugation**

$$\begin{aligned} \psi(n) &\to \psi^{\mathcal{C}}(n) = C^{-1}\bar{\psi}^{\intercal}(n)\,, \\ \bar{\psi}(n) &\to \bar{\psi}^{\mathcal{C}}(n) = -\psi^{\intercal}(n)C\,, \\ U_\mu(n) &\to U_\mu^{\mathcal{C}}(n) = U_\mu^*(n)\,, \end{aligned} \tag{B.6}$$

  where C is the charge conjugation matrix

$$C\gamma_\mu C^{-1} = -\gamma_\mu^{\intercal}\,. \tag{B.7}$$

- **Parity and Euclidean reflections**
  Define

$$\begin{aligned} \psi(n) &\to \psi^{\mathcal{P}_\mu}(n) = \gamma_\mu \psi\left(P_\mu(n)\right)\,, \\ \bar{\psi}(n) &\to \bar{\psi}^{\mathcal{P}_\mu}(n) = \bar{\psi}\left(P_\mu(n)\right)\gamma_\mu\,, \\ U_\nu(n) &\to U_\nu^{\mathcal{P}_\mu}(n) = U_\nu^{\dagger}\left(P_\mu(n) - \hat{v}\right)\,, \quad \nu \neq \mu\,, \\ U_\mu(n) &\to U_\mu^{\mathcal{P}_\mu}(n) = U_\mu\left(P_\mu(n)\right)\,, \end{aligned} \tag{B.8}$$

  where P_μ reverses the sign for all but the μ-th component of a 4-vector.

  The parity transformation on the lattice corresponds to $\mathcal{P}_4$ and the Euclidean time reversal corresponds to $\mathcal{P}_1\mathcal{P}_2\mathcal{P}_3$.

The discrete symmetries C, P and T should be respected by a lattice action if they are symmetries of its continuum version.

Appendix C

Complements for Sect. 3.2

C.1 Computational details of $i\hat{\Pi}^{\mathrm{I}}$

We give here some computational details for the operators $\mathcal{O}_1^{\mathrm{PP}}$ [Eq. (3.35)] and $\mathcal{O}_1^{\mathrm{QP}}$ [Eq. (3.42)] acting on $F(x,y)$ [Eq. (3.36)] and $K_S(x,y)$ [Eq. (3.37)]. As mentioned in the main text, one has to separate the δ-function contributions from the rest in order to account for the distributional nature of the scalar propagator. The Lorentz indices for the operators are implicit but should be understood as in the same order as in their definitions given in Sect. 3.2.

$\boxed{\mathcal{O}^{\mathbf{PP}}_{1,\mu\nu\sigma\lambda;\rho}}$

Let C be a generic constant and

$$D = \frac{C - m_S^2}{m_V^2 - m_S^2}\,. \tag{C.1}$$

Then,

$$\begin{aligned}
&(\Box^{(x)} + \Box^{(y)} - C)F(x,y)\\
=&\int_u G_{m_V}(u)\Big\{[m_V^2 G_{m_V}(x-u) - \delta(x-u)]G_{m_V}(y-u)\\
&+ [m_V^2 G_{m_V}(y-u) - \delta(y-u)]G_{m_V}(x-u) - C G_{m_V}(y-u)G_{m_V}(x-u)\Big\}\\
=&(2m_V^2 - C)F(x,y) - G_{m_V}(x)G_{m_V}(y-x) - G_{m_V}(y)G_{m_V}(x-y)\,.
\end{aligned} \tag{C.2}$$

Similarly,

$$\begin{aligned}
&(\Box^{(x)} + \Box^{(y)} - C)K_S(x,y)\\
=&(2m_V^2 - C)K_S(x,y) - [G_{m_S}(x) - G_{m_V}(x)]G_{m_V}(y-x)\\
&- [G_{m_S}(y) - G_{m_V}(y)]G_{m_V}(x-y)\,.
\end{aligned} \tag{C.3}$$

Hence,

$$\begin{aligned}
&\mathcal{O}_1^{PP}[F(x,y) + DK_S(x,y)]\\
=&[\partial_\nu^{(x)}\partial_\mu^{(y)} - \delta_{\mu\nu}(\partial^{(x)}\cdot\partial^{(y)})][\delta_{\lambda\rho}(\partial_\sigma^{(x)} + \partial_\sigma^{(y)}) - \delta_{\lambda\sigma}(\partial_\rho^{(x)} + \partial_\rho^{(y)})]\\
&\Big\{(2m_V^2 - C)[F(x,y) + DK_S(x,y)] + (D-1)[G_{m_V}(x) + G_{m_V}(y)]G_{m_V}(x-y)\\
&- D[G_{m_S}(x) + G_{m_S}(y)]G_{m_V}(x-y)\Big\}\,.
\end{aligned} \tag{C.4}$$

Using Eq. (3.43), we have

$$\begin{aligned}
&\partial_\alpha^{(x)}\partial_\beta^{(y)}(\partial_\gamma^{(x)}+\partial_\gamma^{(y)})[G_{m_1}(x)+G_{m_1}(y)]G_{m_2}(x-y)\\
=&+[\partial_\alpha^{(x)}\partial_\gamma^{(x)}G^{\mathrm{reg.}}_{m_1}(x)-\frac{1}{4}\delta_{\alpha\gamma}\delta(x)]\partial_\beta^{(y)}G_{m_2}(x-y)\\
&+[\partial_\beta^{(y)}\partial_\gamma^{(y)}G^{\mathrm{reg.}}_{m_1}(y)-\frac{1}{4}\delta_{\beta\gamma}\delta(y)]\partial_\alpha^{(x)}G_{m_2}(x-y)\\
&-\partial_\gamma^{(x)}G_{m_1}(x)[\partial_\alpha^{(x)}\partial_\beta^{(x)}G^{\mathrm{reg.}}_{m_2}(x-y)-\frac{1}{4}\delta_{\alpha\beta}\delta(x-y)]\\
&-\partial_\gamma^{(y)}G_{m_1}(y)[\partial_\alpha^{(x)}\partial_\beta^{(x)}G^{\mathrm{reg.}}_{m_2}(x-y)-\frac{1}{4}\delta_{\alpha\beta}\delta(x-y)]\,.
\end{aligned}\tag{C.5}$$

For convenience, we extract the terms with containing δ-functions in Eq. (C.4), which we denote as the "singular" part of the quantity:

$$\begin{aligned}
&\Big[\mathcal{O}^{PP}_{1,\mu\nu\sigma\lambda;\rho}\Big(F(x,y)+DK_S(x,y)\Big)\Big]^{\mathrm{sing.}}\\
=&\frac{1}{4}\delta_{\lambda\rho}\Big\{\delta_{\nu\sigma}\delta(x)\partial_\mu^{(y)}G_{m_V}(x-y)+\delta_{\mu\sigma}\delta(y)\partial_\nu^{(x)}G_{m_V}(x-y)\\
&-\delta_{\mu\nu}\Big(\delta(x)\partial_\sigma^{(y)}G_{m_V}(x-y)+\delta(y)\partial_\sigma^{(x)}G_{m_V}(x-y)\Big)\\
&+3\delta_{\mu\nu}\Big((1-D)[\partial_\sigma^{(x)}G_{m_V}(x)+\partial_\sigma^{(y)}G_{m_V}(y)]+D[\partial_\sigma^{(x)}G_{m_S}(x)+\partial_\sigma^{(y)}G_{m_S}(y)]\Big)\delta(x-y)\Big\}\\
&-(\sigma\leftrightarrow\rho)\,.
\end{aligned}\tag{C.6}$$

Alternatively, one could also use the equation of motion Eq. (3.43) and the Fourier representation of $\partial^{(x)}\cdot\partial^{(y)}$ applied to F and K_S (see next sub-section) to get:

$$\begin{aligned}
&[\partial^{(x)}\partial_\mu^{(y)}-\delta_{\mu\nu}\partial^{(x)}\cdot\partial^{(y)}][\delta_{\lambda\rho}(\partial_\sigma^{(x)}+\partial_\sigma^{(y)})-\delta_{\lambda\sigma}(\partial_\rho^{(x)}+\partial_\rho^{(y)})]\Big(F+DK_S\Big)\\
=&[\delta_{\lambda\rho}(\partial_\sigma^{(x)}+\partial_\sigma^{(y)})-\delta_{\lambda\sigma}(\partial_\rho^{(x)}+\partial_\rho^{(y)})]\Big(\mathcal{O}^{PP;F}_{\mu\nu}F+\mathcal{O}^{PP;K}_{\mu\nu}K_S+\frac{1}{2}\delta_{\mu\nu}H\Big)\,,
\end{aligned}\tag{C.7}$$

where

$$\mathcal{O}^{PP;F}_{\mu\nu}\equiv\partial_\nu^{(x)}\partial_\mu^{(y)}+\frac{1}{2}\delta_{\mu\nu}[(1+D)m_V^2-Dm_S^2]\,,\tag{C.8}$$

$$\mathcal{O}^{PP;K}_{\mu\nu}\equiv D[\partial_\nu^{(x)}\partial_\mu^{(y)}+\frac{1}{2}\delta_{\mu\nu}(2m_V^2-m_S^2)]\,,\tag{C.9}$$

$$\begin{aligned}
H\equiv&-\Big[D\Big(G_{m_S}(x)+G_{m_S}(y)\Big)+(1-D)\Big(G_{m_V}(x)+G_{m_V}(y)\Big)\Big]G_{m_V}(x-y)\\
&+G_{m_V}(x)G_{m_V}(y)\,.
\end{aligned}\tag{C.10}$$

$\boxed{\mathcal{O}^{\mathbf{QP}}_{1,\mu\nu\sigma\lambda;\rho}}$

Note that $F(x,y)$ and $K_S(x,y)$ are symmetric in their arguments by definition. Due to the equation of motion Eq. (3.43), we have:

$$\Box^{(y)}F(x,y)=m_V^2F(x,y)-G_{m_V}(y)G_{m_V}(x-y)\,,\tag{C.11}$$

$$\Box^{(y)}K_S(x,y)=m_V^2K_S(x,y)-[G_{m_S}(y)-G_{m_V}(y)]G_{m_V}(x-y)\,,\tag{C.12}$$

$$\begin{aligned}\Box^{(x)}\Box^{(y)}F(x,y) =& m_V^4 F(x,y) - m_V^2 G_{m_V}(x)G_{m_V}(x-y)\\ & - m_V^2 G_{m_V}(y)G_{m_V}(x-y) + \delta(x-y)G_{m_V}(y)\,,\end{aligned} \tag{C.13}$$

$$\begin{aligned}\Box^{(x)}\Box^{(y)}K_S(x,y) =& m_V^4 K_S(x,y) - m_V^2[G_{m_S}(x) - G_{m_V}(x)]G_{m_V}(x-y)\\ & - m_V^2[G_{m_S}(y) - G_{m_V}(y)]G_{m_V}(x-y)\\ & + \delta(x-y)[G_{m_S}(y) - G_{m_V}(y)]\,.\end{aligned} \tag{C.14}$$

Note that

$$q_1 \cdot q_2 = \frac{1}{2}\Big((q_1+q_2)^2 - q_1^2 - q_2^2\Big)\,, \tag{C.15}$$

we can write

$$\begin{aligned}& - (\partial^{(x)}\cdot\partial^{(y)})\partial_\mu^{(x)}\partial_\nu^{(y)}K(x)\\ =& \frac{1}{2}\partial_\mu^{(x)}\partial_\nu^{(y)}\Big[\Big(\Box^{(x)} + \Box^{(y)} - m_S^2\Big)K_S(x) + (m_V^2 - m_S^2)F(x)\Big]\\ =& + \frac{1}{2}(2m_V^2 - m_S^2)\partial_\mu^{(x)}\partial_\nu^{(y)}K_S(x,y)\\ & + \frac{1}{2}(m_V^2 - m_S^2)\partial_\mu^{(x)}\partial_\nu^{(y)}F(x,y)\\ & - \frac{1}{2}\partial_\mu^{(x)}[G_{m_S}(x) - G_{m_V}(x)]\partial_\nu^{(y)}G_{m_V}(y-x)\\ & - \frac{1}{2}\partial_\nu^{(y)}[G_{m_S}(y) - G_{m_V}(y)]\partial_\mu^{(x)}G_{m_V}(x-y)\\ & + \frac{1}{2}[G_{m_S}(x) + G_{m_S}(y) - G_{m_V}(x) - G_{m_V}(y)]\partial_\mu^{(x)}\partial_\nu^{(x)}G^{\text{reg.}}_{m_V}(x-y)\\ & - \frac{1}{4}\delta_{\mu\nu}[G_{m_S}(x) - G_{m_V}(x)]\delta(x-y)\,,\end{aligned} \tag{C.16}$$

$$\begin{aligned}& - (\partial^{(x)}\cdot\partial^{(y)})\partial_\mu^{(x)}\partial_\nu^{(y)}F(x,y)\\ =& \frac{1}{2}\partial_\mu^{(x)}\partial_\nu^{(y)}\Big[\Big(\Box^{(x)} + \Box^{(y)} - m_V^2\Big)F(x,y) + G_{m_V}(x)G_{m_V}(y)\Big]\\ =& \frac{1}{2}\partial_\mu^{(x)}\partial_\nu^{(y)}\Big[m_V^2 F(x,y) - G_{m_V}(x)G_{m_V}(y-x) - G_{m_V}(y)G_{m_V}(x-y) + G_{m_V}(x)G_{m_V}(y)\Big]\\ =& + \frac{1}{2}\partial_\mu^{(x)}\partial_\nu^{(y)}\Big[m_V^2 F(x,y) + G_{m_V}(x)G_{m_V}(y)\Big]\\ & - \frac{1}{2}\partial_\mu^{(x)}G_{m_V}(x-y)\partial_\nu^{(y)}G_{m_V}(y) - \frac{1}{2}\partial_\mu^{(x)}G_{m_V}(x)\partial_\nu^{(y)}G_{m_V}(x-y)\\ & + \frac{1}{2}[G_{m_V}(x) + G_{m_V}(y)]\partial_\mu^{(x)}\partial_\nu^{(x)}G^{\text{reg.}}_{m_V}(x-y) - \frac{1}{4}\delta_{\mu\nu}G_{m_V}(x)\delta(x-y)\,.\end{aligned} \tag{C.17}$$

All combined, one gets, after tedious computations

$$\begin{aligned}
&\mathcal{O}^{QP}_{1,\mu\nu\sigma\lambda;\rho}\Big(F(x,y)+DK(x,y)\Big)\\
=&[\delta_{\lambda\rho}(\partial^{(x)}_\sigma+\partial^{(y)}_\sigma)-\delta_{\lambda\sigma}(\partial^{(x)}_\rho+\partial^{(y)}_\rho)]\Big\{\mathcal{O}^{QP;F}_{\mu\nu}F(x,y)+\mathcal{O}^{QP;K}_{\mu\nu}K_S(x,y)\\
&-\frac{1}{2}\Big((1-D)[G_{m_V}(x)+G_{m_V}(y)]+D[G_{m_S}(x)+G_{m_S}(y)]\Big)\\
&\times\Big(\partial^{(x)}_\mu\partial^{(x)}_\nu G^{\text{reg.}}_{m_V}(x-y)-\frac{1}{4}\delta_{\mu\nu}\delta(x-y)\Big)\\
&+\frac{1}{2}\partial^{(x)}_\mu G_{m_V}(x)\partial^{(y)}_\nu G_{m_V}(y)\\
&-\frac{1}{2}\partial^{(x)}_\mu G_{m_V}(x-y)[(1-D)\partial^{(y)}_\nu G_{m_V}(y)+D\partial^{(y)}_\nu G_{m_S}(y)]\\
&-\frac{1}{2}\partial^{(y)}_\nu G_{m_V}(x-y)[(1-D)\partial^{(x)}_\mu G_{m_V}(x)+D\partial^{(x)}_\mu G_{m_S}(x)]\\
&+m_V^2\delta_{\mu\nu}\Big(D[G_{m_S}(x)+G_{m_S}(y)]G_{m_V}(x-y)\\
&+(1-D)[G_{m_V}(x)+G_{m_V}(y)]G_{m_V}(x-y)\Big)\\
&-\delta_{\mu\nu}\delta(x-y)\Big((1-D)G_{m_V}(y)+DG_{m_S}(y)\Big)\Big\}\,,
\end{aligned}\tag{C.18}$$

where

$$\mathcal{O}^{QP;F}_{\mu\nu}\equiv m_V^2(\partial^{(x)}_\mu\partial^{(x)}_\nu+\partial^{(y)}_\mu\partial^{(y)}_\nu)+\frac{1}{2}[m_V^2(1+D)-Dm_S^2]\partial^{(x)}_\mu\partial^{(y)}_\nu-\delta_{\mu\nu}m_V^4\,,\tag{C.19}$$

$$\mathcal{O}^{QP;K}_{\mu\nu}\equiv D\Big(m_V^2(\partial^{(x)}_\mu\partial^{(x)}_\nu+\partial^{(y)}_\mu\partial^{(y)}_\nu)+\frac{1}{2}[2m_V^2-m_S^2]\partial^{(x)}_\mu\partial^{(y)}_\nu-\delta_{\mu\nu}m_V^4\Big)\,.\tag{C.20}$$

Finally, for convenience, we give here the terms containing δ-functions in Eq. (C.18)

$$\begin{aligned}
&\Big[\mathcal{O}^{QP}_{1,\mu\nu\sigma\lambda;\rho}\Big(F(x,y)+DK(x,y)\Big)\Big]^{\text{sing.}}\\
=&\frac{1}{8}\Big\{-\delta_{\sigma\mu}\delta(x)\partial^{(y)}_\nu G_{m_V}(y)-\delta_{\sigma\nu}\delta(y)\partial^{(x)}_\mu G_{m_V}(x)\\
&+\partial^{(x)}_\mu G_{m_V}(x-y)\delta_{\nu\sigma}\delta(y)+\partial^{(y)}_\nu G_{m_V}(x-y)\delta_{\mu\sigma}\delta(x)\\
&-6\delta_{\mu\nu}\delta(x-y)\Big((1-D)\partial^{(x)}_\sigma G_{m_V}(x)+D\partial^{(x)}_\sigma G_{m_S}(x)\Big)\Big\}\delta_{\lambda\rho}-(\sigma\leftrightarrow\rho)\\
=&-\frac{3}{4}\delta_{\mu\nu}\delta(x-y)\Big((1-D)\partial^{(x)}_\sigma G_{m_V}(x)+D\partial^{(x)}_\sigma G_{m_S}(x)\Big)\Big\}\delta_{\lambda\rho}-(\sigma\leftrightarrow\rho)
\end{aligned}\tag{C.21}$$

C.2 Useful recurrence relations

C.2.1 Modified Bessel functions

There exists recurrence relations between modified Bessel functions of different orders:

$$K_{n-1}(x)-K_{n+1}(x)=-\frac{2n}{x}K_n(x)\,,\tag{C.22}$$

$$I_{n-1}(x)-I_{n+1}(x)=\frac{2n}{x}I_n(x)\,.\tag{C.23}$$

Derivatives of any order of modified Bessel functions can be built from the modified Bessel functions via (an arbitrary scaling constant $m > 0$ is put in here for convenience):

$$\begin{aligned} &\frac{d}{dx}K_0(mx) = -mK_1(mx)\,, \\ &\frac{d}{dx}K_{n+1}(mx) = -mK_n(mx) - \frac{n+1}{x}K_{n+1}(mx)\,, \quad \forall n \in \mathbb{N}\,. \end{aligned} \tag{C.24}$$

$$\begin{aligned} &\frac{d}{dx}I_0(mx) = mI_1(mx)\,, \\ &\frac{d}{dx}I_{n+1}(mx) = mI_n(mx) - \frac{n+1}{x}I_{n+1}(mx)\,, \quad \forall n \in \mathbb{N}\,. \end{aligned} \tag{C.25}$$

C.2.2 Chebyshev polynomial of the second kind

The Clenshaw algorithm requires the knowledge of a linear recurrence relation between three consecutive terms. We can establish such a relation for the derivatives of Chebyshev polynomials for any order. We give here an example of how one constructs such a recursion relation for the first derivative.

Noting that

$$\begin{aligned} &T_n(z) = \frac{1}{2}\Big(U_n(z)(1+\delta_{n0}) - U_{n-2}(z)\Big)\,, \\ &T_n'(z) = nU_{n-1}(z)\,, \end{aligned} \tag{C.26}$$

where T_n's are Chebyshev polynomials of the first kind, and recalling the defining recurrence relation satisfied by the U_n's:

$$U_0(z) = 1\,, \quad U_1(z) = 2z\,, \quad U_{n+1}(z) = 2zU_n(x) - U_{n-1}(z)\,, \quad \forall n \in \mathbb{N}^*\,, \tag{C.27}$$

we then have

$$U_0'(z) = 0\,, \quad U_1'(z) = 2\,, \quad U_{n+1}'(z) = \frac{2z}{n}U_n'(z) - \frac{n+2}{n}U_{n-1}'(z)\,, \quad \forall n \in \mathbb{N}^*\,. \tag{C.28}$$

Derivatives of higher order can be obtained similarly.

Appendix D

Complements for Sect. 4.1

D.1 Derivatives of the functions J_α's and related quantities

In this section, we give explicitly the expressions of the terms with the functions $J_\alpha(a,b)$'s [Eq. (4.45) and Eq. (4.46)] involved which are needed for the calculation of $I(y,w;\rho)$ [Eq. (4.47)]. Throughout the section, $\alpha,\beta,\gamma \neq \rho$ and $k \equiv m\sqrt{a^2+b^2}$.

The following relations will come in handy

$$\partial_a J_0 = \frac{m^4(b^2-a^2)}{k^3}K_1(k) - \frac{m^4a^2}{k^2}K_0(k)\,, \tag{D.1}$$

$$\partial_b J_0 = -\frac{m^4ab}{k^3}K_1(k) + \frac{m^4ab}{k^2}\big(-K_0(k) - \frac{1}{k}K_1(k)\big)\,, \tag{D.2}$$

$$\begin{aligned}\partial_a J_{\frac12} =& \frac{1}{2}mK_{\frac12}^2(\frac{ma}{2}) + \frac{am^2}{2}\big(-K_{\frac32}(\frac{ma}{2}) + \frac{1}{ma}K_{\frac12}(\frac{ma}{2})\big)K_{\frac12}(\frac{ma}{2})\\ &+ \frac{bm^2}{k}K_1(k) + m^2a\int_0^{t_0}dt\cosh t K_0(ma\cosh t)\,,\end{aligned} \tag{D.3}$$

$$\partial_a^2 J_{\frac12} = \partial_b J_0 + m^2 J_{\frac12}\,, \tag{D.4}$$

$$\partial_{ab}^2 J_0 = \Big(-\frac{2m^4b}{k^3} + \frac{8m^6a^2b}{k^5} + \frac{m^6a^2b}{k^3}\Big)K_1(k) + \Big(\frac{4m^6a^2b}{k^4} - \frac{m^4b}{k^2}\Big)K_0(k)\,, \tag{D.5}$$

$$\begin{aligned}\partial_{aa}^2 J_0 =& -\Big(\frac{3m^6(b^2-a^2)a}{k^5} + \frac{2m^4a}{k^3}\Big)K_1(k) - \frac{m^6(b^2-a^2)a}{k^4}\Big(K_0(k) + \frac{1}{k}K_1(k)\Big)\\ &- \Big(\frac{2m^4a}{k^2} - \frac{2m^6a^3}{k^4}\Big)K_0(k) + \frac{m^4a^2}{k^2}K_1(k)\,.\end{aligned} \tag{D.6}$$

Case $\mathbf{sgn}(y^{[n_\rho+l]} - \frac{L_\rho}{2}) = \mathbf{sgn}(w_\rho^{[l]} - \frac{L_\rho}{2})$

Recall that in this case, we have to set, according to Eq. (4.47)

$$a = |(y-w)_\perp^{[n]}|\,, \quad b = |(y+w-L)_\rho^{[n_\rho+2l]}|\,. \tag{D.7}$$

We define

$$v \equiv (y-w)_\perp^{[n]}\,, \quad s \equiv \mathrm{sgn}[(y+w-L)_\rho^{[n_\rho+2l]}]\,. \tag{D.8}$$

Then,

$$\partial_{w_\rho} J_1 = s\big(bJ_0 - J_{\frac{1}{2}} - \frac{abm^2}{k}K_1(k)\big)\,. \tag{D.9}$$

$$\partial_{y_\alpha}\partial_{w_\rho} J_1 = -\partial_a J_{\frac{1}{2}} s\frac{v_\alpha}{|v|}\,. \tag{D.10}$$

$$\partial_{y_\rho}\partial_{w_\rho} J_1 = 2m\sin\beta K_1(k) - \frac{m^2 a}{k}K_1(k)\,. \tag{D.11}$$

$$\partial_{y_\alpha} J_1 = \Big(-b\partial_a J_{\frac{1}{2}} + K_0(k) - \frac{a^2m^2}{k}K_1(k)\Big)\frac{v_\alpha}{|v|}\,. \tag{D.12}$$

$$\begin{aligned}\partial^2_{y_\beta y_\alpha} J_1 =& \Big[-b\partial_a^2 J_{\frac{1}{2}} - \frac{3m^2 a}{k}K_1(k) + \frac{a^3m^4}{k^2}\Big(K_0(k) + \frac{2}{k}K_1(k)\Big)\Big]\frac{v_\alpha v_\beta}{|v|^2}\\ &+\Big(-b\partial_a J_{\frac{1}{2}} + K_0(k) - \frac{a^2m^2}{k}K_1(k)\Big)\Big\{\Big(\frac{1}{|v|} - \frac{(v_\beta)^2}{|v|^3}\Big)\delta_{\alpha\beta} - (1-\delta_{\alpha\beta})\frac{v_\alpha v_\beta}{|v|^3}\Big\}\,.\end{aligned} \tag{D.13}$$

$$\partial_{y_\rho} J_1 = \partial_{w_\rho} J_1\,. \tag{D.14}$$

$$\partial^2_{y_\rho y_\alpha} J_1 = \partial^2_{y_\alpha w_\rho} J_1\,. \tag{D.15}$$

$$\partial^3_{y_\beta y_\alpha w_\rho} J_1 = -\partial_a^2 J_{\frac{1}{2}} s\frac{v_\alpha v_\beta}{|v|^2} - \partial_a J_{\frac{1}{2}} s\Big(\frac{1}{|v|}\delta_{\alpha\beta} - \frac{v_\alpha v_\beta}{|v|^3}\Big)\,. \tag{D.16}$$

$$\begin{aligned}\partial^3_{y_\gamma y_\beta y_\alpha} J_1 =& \frac{v_\alpha v_\beta v_\gamma}{|v|^3}\Big\{-b\partial_a^3 J_{\frac{1}{2}} - \frac{3m^2}{k}K_1(k) + \frac{3m^4a^2}{k^3}K_1(k) + \frac{3m^4a^2}{k^2}\Big(K_0(k) + \frac{1}{k}K_1(k)\Big)\\ &+\Big(3\frac{a^2m^4}{k^2} - \frac{2a^4m^6}{k^4}\Big)\Big(K_0(k) + \frac{2}{k}K_1(k)\Big) - \frac{a^4m^6}{k^3}\Big(K_1(k) + \frac{2}{k}K_0(k) + \frac{2}{k^2}K_1(k)\Big)\Big\}\\ &+\frac{v_\gamma}{|v_\perp|}\Big(-b\partial_a^2 J_{\frac{1}{2}} - \frac{3m^2a}{k}K_1(k) + \frac{m^4a^3}{k^3}K_1(k) + \frac{a^3m^4}{k^2}[K_0(k) + \frac{1}{k}K_1(k)]\Big)\\ &\times\Big\{\Big(\frac{1}{|v|} - \frac{(v_\beta)^2}{|v|^3}\Big)\delta_{\alpha\beta} - (1-\delta_{\alpha\beta})\frac{v_\alpha v_\beta}{|v|^3}\Big\}\\ &+\Big(-b\partial_a J_{\frac{1}{2}} + K_0(k) - \frac{a^2m^2}{k}K_1(k)\Big)\\ &\times\Big\{\Big(-\frac{v_\gamma}{|v|^3} - \frac{2v_\beta}{|v|^3}\delta_{\beta\gamma} + \frac{3(v_\beta)^2 v_\gamma}{|v|^5}\Big)\delta_{\alpha\beta}\\ &-(1-\delta_{\alpha\beta})\Big(\frac{v_\alpha}{|v|^3}\delta_{\beta\gamma} + \frac{v_\beta}{|v_\perp|^3}\delta_{\alpha\gamma} - \frac{3v_\alpha v_\beta v_\gamma}{|v|^5}\Big)\Big\}\,.\end{aligned} \tag{D.17}$$

$$\partial^3_{y_\rho y_\alpha w_\rho} J_1 = \partial_a J_0\frac{v_\alpha}{|v|}\,, \tag{D.18}$$

$$\partial^3_{y_\rho y_\alpha y_\beta} J_1 = \partial^3_{y_\beta y_\alpha w_\rho} J_1\,. \tag{D.19}$$

Case sgn$(y^{[n_\rho+l]} - \frac{L_\rho}{2}) \neq$ **sgn**$(w_\rho^{[l]} - \frac{L_\rho}{2})$

In this case, Eq. (4.47) requires to set

$$a = |(y-w)_\perp^{[n]}|\,, \quad b = |(y-w)_\perp^{[n_\rho]}|\,. \tag{D.20}$$

We have to compute derivatives for J_1 and

$$\tilde{J} \equiv (y_\rho - \frac{L_\rho}{2})^{[n_\rho+l]} J_{\frac{1}{2}}\,. \tag{D.21}$$

The former can be obtained by taking the previous results and replacing the a, b by the right values. We define, for this case

$$v \equiv (y-w)_\perp^{[n]}\,, \quad s \equiv \text{sgn}[(y-w)_\rho^{[n]}]\,, \quad t \equiv (y_\rho - \frac{L_\rho}{2})^{[n_\rho+l]}\,. \tag{D.22}$$

Then,

$$\partial_{w_\rho}\tilde{J} = stJ_0\,. \tag{D.23}$$

$$\partial^2_{y_\alpha w_\rho}\tilde{J} = st\frac{v_\alpha}{|v|}\Big(\frac{m^4(b^2-a^2)}{k^3}K_1(k) - \frac{m^4a^2}{k^2}K_0(k)\Big)\,. \tag{D.24}$$

$$\partial^2_{y_\rho w_\rho}\tilde{J} = sJ_0 - t\frac{m^4ab}{k^3}\Big(2K_1(k) + kK_0(k)\Big)\,. \tag{D.25}$$

$$\partial_{y_\rho}\tilde{J} = J_{\frac{1}{2}} - stJ_0\,. \tag{D.26}$$

$$\partial^2_{y_\rho y_\beta}\tilde{J} = \frac{v_\beta}{|v|}\partial_a J_{\frac{1}{2}} - st\frac{v_\beta}{|v|}\Big(\frac{m^4(b^2-a^2)}{k^3}K_1(k) - \frac{m^4a^2}{k^2}K_0(k)\Big)\,. \tag{D.27}$$

$$\partial_{y_\alpha}\tilde{J} = t\frac{v_\alpha}{|v|}\partial_a J_{\frac{1}{2}}\,. \tag{D.28}$$

$$\partial^2_{y_\alpha y_\beta}\tilde{J} = t\Big\{\Big(\frac{1}{|v|} - \frac{(v_\beta)^2}{(|v|)^3}\Big)\delta_{\alpha\beta} - (1-\delta_{\alpha\beta})\frac{v_\alpha v_\beta}{|v|^3}\Big\}\partial_a J_{\frac{1}{2}} + t\frac{v_\alpha v_\beta}{|v|^2}\partial^2_a J_{\frac{1}{2}}\,. \tag{D.29}$$

$$\begin{aligned}\partial^3_{y_\beta y_\alpha w_\rho}\tilde{J} =& st\Big(\frac{1}{|v|}\delta_{\alpha\beta} - \frac{v_\alpha v_\beta}{|v|^3}\Big)\Big(\frac{m^4(b^2-a^2)}{k^3}K_1(k) - \frac{m^4a^2}{k^2}K_0(k)\Big)\\ &+ st\frac{v_\alpha v_\beta}{|v|^2}\Big[-\frac{3m^6(b^2-a^2)a}{k^5}K_1(k) - \frac{2m^4a}{k^3}K_1(k)\\ &- \frac{m^6(b^2-a^2)a}{k^4}\Big(K_0(k) + \frac{1}{k}K_1(k)\Big) - \Big(\frac{2m^4a}{k^2} - \frac{2m^6a^3}{k^4}\Big)K_0(k) + \frac{m^6a^3}{k^3}K_1(k)\Big)\Big]\,.\end{aligned} \tag{D.30}$$

$$\begin{aligned}\partial^3_{y_\gamma y_\beta y_\alpha}\tilde{J} =& + t\partial_a^2 J_{\frac{1}{2}}\frac{v_\gamma}{|v|}\Big\{\Big(\frac{1}{|v|}-\frac{(v_\beta)^2}{|v|^3}\Big)\delta_{\alpha\beta}-(1-\delta_{\alpha\beta})\frac{v_\alpha v_\beta}{|v|^3}\Big\}\\ &+ t\partial_a J_{\frac{1}{2}}\Big\{\Big(-\frac{v_\gamma}{|v|^3}-\frac{2v_\beta}{|v|^3}\delta_{\beta\gamma}+\frac{3(v_\beta)^2 v_\gamma}{|v|^5}\Big)\delta_{\alpha\beta}\\ &-(1-\delta_{\alpha\beta})\Big[\frac{1}{|v|^3}\Big(v_\alpha\delta_{\beta\gamma}+v_\beta\delta_{\alpha\gamma}\Big)-\frac{3v_\alpha v_\beta v_\gamma}{|v|^5}\Big]\Big\}\\ &+ t\partial_a^2 J_{\frac{1}{2}}\Big(-\frac{2v_\alpha v_\beta v_\gamma}{|v|^4}+\frac{v_\alpha}{|v|^2}\delta_{\gamma\beta}+\frac{v_\beta}{|v|^2}\delta_{\gamma\alpha}\Big)+t\partial_a^3 J_{\frac{1}{2}}\frac{v_\alpha v_\beta v_\gamma}{|v|^3}\,.\end{aligned} \tag{D.31}$$

$$\begin{aligned}\partial^3_{y_\rho y_\alpha w_\rho}\tilde{J} =& s\partial_a J_0\frac{v_\alpha}{|v|}-t\frac{v_\alpha}{|v|}\Big\{\Big(\frac{m^4 b}{k^3}-\frac{3m^6a^2b}{k^5}\Big)\Big(2K_1(k)+kK_0(k)\Big)\\ &-\frac{m^6a^2b}{k^4}\Big(3K_0(k)+(k+\frac{2}{k})K_1(k)\Big)\Big\}\,.\end{aligned} \tag{D.32}$$

$$\partial^3_{y_\rho y_\alpha y_\beta}\tilde{J} =\Big\{\Big(\frac{1}{|v|}-\frac{(v_\beta)^2}{|v|^3}\Big)\delta_{\alpha\beta}-(1-\delta_{\alpha\beta})\frac{v_\alpha v_\beta}{|v|^3}\Big\}\Big(\partial_a J_{\frac{1}{2}}-st\partial_a J_0\Big)-st\frac{v_\alpha v_\beta}{|v|^2}\partial_a^2 J_0\,. \tag{D.33}$$

D.2 Numerical treatment of $J_{\frac{1}{2}}(a,b)$ and $\partial_a J_{\frac{1}{2}}(a,b)$

Although we have the recurrence relations Eqs. (4.39-4.41), we still need to compute $J_{\frac{1}{2}}(a,b)$ and $\partial_a J_{\frac{1}{2}}(a,b)$ in order to get the rest. This requires to evaluate the integrals $\int_0^{t_0} dt K_1(ma\cosh t)$ and $\int_0^{t_0} dt K_0(ma\cosh t)\cosh t$. In the region where ma is large enough, we can sample the inverses of the integrals with Chebyshev polynomials reasonable well. For the results shown in Chap. 4, we use a setup with a relative accuracy of $O(10^{-3})$. Nonetheless, these functions are not well approximated by polynomials while ma becomes small. Fortunately, one can compute the required integral analytically from the series expansion of the Bessel functions.

The numerical implementation of the Bessel functions of the first two orders admit series expansions of form [Nis, Eq. (10.31.1)]

$$\begin{aligned}K_0(x) &= \ln(x)\sum_{n\geq 0} a_n x^{2n}+\sum_{n\geq 0} b_n x^{2n}\,,\\ K_1(x) &= \ln(x)\sum_{n\geq 0} c_n x^{2n+1}+\sum_{n\geq -1} d_n x^{2n+1}\,.\end{aligned} \tag{D.34}$$

Therefore,

$$\begin{aligned}\int_0^{t_0} dt K_1(ma\cosh(t)) = \int_0^{\sinh t_0} du \Big[& \frac{1}{2}\ln(1+u^2)\sum_{n\geq 0} c_n (ma)^{2n+1}(1+u^2)^n \\ & + \sum_{n\geq 0}\Big(c_n \ln(ma)+d_n\Big)(ma)^{2n+1}(1+u^2)^n + \frac{1}{ma} d_{-1}\frac{1}{1+u^2}\Big] \\ = \Big[& \sum_{n\geq 0,k\leq n}\binom{n}{k}\frac{1}{2k+1}\Big(\frac{1}{2}c_n (ma)^{2n+1}u^{2k+1}\ln(1+u^2) \\ & + (c_n\ln(ma)+d_n)(ma)^{2n+1}u^{2k+1} - c_n F_{k+1}(u)\Big) \\ & + \frac{d_{-1}}{ma}\arctan(u)\Big]\Big|_{u=\sinh t_0},\end{aligned} \tag{D.35}$$

where the F_k's satisfy

$$\begin{aligned} & F_{k+1}(x) = \int_0^x du \frac{u^{2(k+1)}}{1+u^2}, \\ & F_{k+1}(x) + F_k(x) = \frac{1}{2k+1}x^{2k+1}, \\ & F_0(x) = \arctan(x), \\ & F_{k+1}(x) = (-1)^{k+1}\arctan(x) + \sum_{1\leq m\leq k+1}\frac{(-1)^{m+1}}{2(k-m+1)+1}x^{2(k-m+1)+1}. \end{aligned} \tag{D.36}$$

The sum of the terms that do not contain $\ln(1+u^2)$ in the first term in the bracket can thus be written as

$$\begin{aligned} & \sum_{n\geq 0,k\leq n}\frac{(-1)^k}{2k+1}\binom{n}{k}c_n (ma)^{2n+1}\arctan(u) \\ & + \sum_{s\geq 0}\Big[\sum_{n\geq s}\frac{1}{2s+1}\binom{n}{s}\big(d_n + c_n\ln(ma)\big)(ma)^{2n+1} - \sum_{n\geq k,k\geq s}\frac{1}{2k+1}\binom{n}{k} f_{n,s,k}(ma)^{2n+1}\Big]u^{2s+1}, \end{aligned} \tag{D.37}$$

with

$$f_{n,s,k} = \frac{(-1)^{k-s}}{2s+1}c_n. \tag{D.38}$$

We have similar expression for $\int_0^{t_0} dt K_0(ma\cosh(t))\cosh t$.

D.3 Expressions for the C^i's

We present the computational details of the coefficients C^i's defined in Eq. (4.49) in this section. We write the coefficients C^i's as

$$C^i = \bar{C}^i + \Delta C^i, \tag{D.39}$$

where $\bar{C}^i$ is the usual part and ΔC^i is the additional part (c.f. text in Sect. 4.1). If not specified, the sum over all integer winding numbers $n \in \mathbb{Z}^4$ is always taken.

Let $\rho \in \{0,1,2,3\}$ and $\alpha, \beta, \sigma, \lambda \neq \rho$.

D.3.1 The usual part

$$\bar{C}^{5;\rho}_{\beta} = -i\frac{m^2}{16\pi^2}\sum_n \frac{y^{[n]}_\beta y^{[n]}_\rho}{|y^{[n]}|} K_1(m|y^{[n]}|)\,, \tag{D.40}$$

$$\bar{C}^{4;\rho} = -i\frac{m}{16\pi^2}\sum_n \Big(\frac{m(y^{[n]}_\rho)^2}{|y^{[n]}|} K_1(m|y^{[n]}|) + K_0(m|y^{[n]}|)\Big)\,, \tag{D.41}$$

$$\bar{C}^{3;\rho}_{\rho} = i\frac{m}{16\pi^2}\sum_n \Big(K_0(m|y^{[n]}|) - \frac{m(y^{[n]}_\rho)^2}{|y^{[n]}|} K_1(m|y^{[n]}|)\Big)\,, \tag{D.42}$$

$$\bar{C}^{3;\rho}_{\beta} = \bar{C}^{5;\rho}_{\beta}\,, \tag{D.43}$$

$$\begin{aligned}\bar{C}^{2;\rho}_{\alpha\beta} =& \frac{i}{16\pi^2}\sum_n m y^{[n]}_\rho K_1(m|y^{[n]}|)\Big[\Big(\frac{1}{|y^{[n]}|} - \frac{(y^{[n]}_\beta)^2}{|y^{[n]}|^3}\Big)\delta_{\alpha\beta} - (1-\delta_{\alpha\beta})\frac{y^{[n]}_\alpha y^{[n]}_\beta}{|y^{[n]}|^3}\Big] \\ & - \frac{im^2}{16\pi^2}\sum_n \frac{y^{[n]}_\rho y^{[n]}_\alpha y^{[n]}_\beta}{|y^{[n]}|^2}\Big(K_0(m|y^{[n]}|) + \frac{1}{m|y^{[n]}|}K_1(m|y^{[n]}|)\Big)\,,\end{aligned} \tag{D.44}$$

$$\begin{aligned}\bar{C}^{2;\rho}_{\rho\beta} =& i\frac{m}{16\pi^2}\sum_n \frac{y^{[n]}_\beta}{|y^{[n]}|} K_1(m|y^{[n]}|) - i\frac{m}{16\pi^2}\sum_n \frac{y^{[n]}_\beta (y^{[n]}_\rho)^2}{|y^{[n]}|^3} K_1(m|y^{[n]}|) \\ & - i\frac{m^2}{16\pi^2}\sum_n \frac{y^{[n]}_\beta (y^{[n]}_\rho)^2}{|y^{[n]}|^2}\Big(K_0(m|y^{[n]}|) + \frac{1}{m|y^{[n]}|}K_1(m|y^{[n]}|)\Big)\,,\end{aligned} \tag{D.45}$$

$$\begin{aligned}\bar{C}^{1;\rho}_{\rho} =& -i\frac{m}{16\pi^2}\sum_n \Big(-\frac{y^{[n]}_\rho}{|y^{[n]}|} + \frac{(y^{[n]}_\rho)^3}{|y^{[n]}|^3}\Big) K_1(m|y^{(n)}|) \\ & - i\frac{m^2}{16\pi^2}\sum_n \frac{(y^{[n]}_\rho)^3}{|y^{[n]}|^2}\Big(K_0(m|y^{[n]}|) + \frac{1}{m|y^{[n]}|}K_1(m|y^{[n]}|)\Big)\,,\end{aligned} \tag{D.46}$$

$$\begin{aligned}\bar{C}^{1;\rho}_{\beta} =& -i\frac{m^2}{16\pi^2}\sum_n \frac{(y^{[n]}_\rho)^2 y^{[n]}_\beta}{|y^{[n]}|^2}\Big(K_0(m|y^{[n]}|) + \frac{2}{m|y^{[n]}|}K_1(m|y^{[n]}|)\Big) \\ & - i\frac{m}{16\pi^2}\sum_n \frac{y^{[n]}_\beta}{|y^{[n]}|} K_1(m|y^{[n]}|)\,.\end{aligned} \tag{D.47}$$

Also, we list the following quantities relevant for the computation discussed in Sect. 4.2 here for convenience as they are obtained directly from the results given so

far

$$
\begin{aligned}
\partial_{y^\nu}\bar{C}^{1;\rho}_{\sigma} =& -\frac{im^2}{16\pi^2}\sum_n\Big(\frac{(y^{[n]}_\rho)^2}{|y^{[n]}|^2}\delta_{\nu\sigma}+\frac{2y^{[n]}_\rho y^{(n)}_\sigma\delta_{\rho\nu}}{|y^{[n]}|^2}-\frac{2(y^{[n]}_\rho)^2y^{[n]}_\sigma y^{[n]}_\nu}{|y^{[n]}|^4}\Big)\\
&\times\Big(K_0(m|y^{[n]}|)+\frac{2}{m|y^{[n]}|}K_1(m|y^{[n]}|)\Big)\\
&+\frac{im^2}{16\pi^2}\sum_n\frac{(y^{[n]}_\rho)^2y^{[n]}_\sigma}{|y^{[n]}|^2}\Big[\frac{my^{[n]}_\nu}{|y^{[n]}|}K_1(m|y^{[n]}|)+\frac{2y^{[n]}_\nu}{m|y^{[n]}|^3}K_1(m|y^{[n]}|)\\
&+\frac{2y^{[n]}_\nu}{|y^{[n]}|^2}\Big(\frac{1}{m|y^{[n]}|}K_1(m|y^{[n]}|)+K_0(m|y^{[n]}|)\Big)\Big]\\
&-\frac{im}{16\pi^2}\sum_n\Big(\frac{1}{|y^{[n]}|}\delta_{\sigma\nu}-\frac{y^{[n]}_\nu y^{[n]}_\sigma}{|y^{[n]}|^3}\Big)K_1(m|y^{[n]}|)\\
&+\frac{im^2}{16\pi^2}\sum_n\frac{y^{[n]}_\sigma y^{[n]}_\nu}{|y^{[n]}|^2}\Big(K_0(m|y^{[n]}|)+\frac{1}{m|y^{[n]}|}K_1(m|y^{[n]}|)\Big),
\end{aligned}
\tag{D.48}
$$

$$
\begin{aligned}
\partial_{y^\nu}\bar{C}^{2;\rho}_{\sigma\lambda} =&\frac{i}{16\pi^2}\sum_n m\delta_{\rho\nu}\Big[(\frac{1}{|y^{[n]}|}-\frac{(y^{[n]}_\lambda)^2}{|y^{[n]}|^3})\delta_{\sigma\lambda}-(1-\delta_{\sigma\lambda})\frac{y^{[n]}_\sigma y^{[n]}_\lambda}{|y^{[n]}|^3}\Big]K_1(m|y^{[n]}|)\\
&+\frac{i}{16\pi^2}\sum_n my^{[n]}_\rho\Big\{\Big(-\frac{y^{[n]}_\nu}{|y^{[n]}|^3}-\frac{2y^{[n]}_\nu}{|y^{[n]}|^3}\delta_{\nu\lambda}+\frac{3y^{[n]}_\nu(y^{[n]}_\lambda)^2}{|y^{[n]}|^5}\Big)\delta_{\sigma\lambda}\\
&-(1-\delta_{\sigma\lambda})\Big[\frac{1}{|y^{[n]}|^3}(\delta_{\sigma\nu}y^{[n]}_\lambda+\delta_{\lambda\nu}y^{[n]}_\sigma)-\frac{3y^{[n]}_\sigma y^{[n]}_\lambda y^{[n]}_\nu}{|y^{[n]}|^5}\Big]\Big\}K_1(m|y^{[n]}|)\\
&-\frac{i}{16\pi^2}\sum_n m^2\frac{y^{[n]}_\rho y^{[n]}_\nu}{|y^{[n]}|}\Big[\Big(\frac{1}{|y^{[n]}|}-\frac{(y^{[n]}_\lambda)^2}{|y^{[n]}|^3}\Big)\delta_{\sigma\lambda}\\
&-(1-\delta_{\sigma\lambda})\frac{y^{[n]}_\sigma y^{[n]}_\lambda}{|y^{[n]}|^3}\Big]\Big(K_0(m|y^{[n]}|)+\frac{1}{m|y^{[n]}|}K_1(m|y^{[n]}|)\Big)\\
&-\frac{im^2}{16\pi^2}\sum_n\Big(\frac{y^{[n]}_\rho}{|y^{[n]}|^2}(\delta_{\sigma\nu}y^{[n]}_\lambda+\delta_{\lambda\nu}y^{[n]}_\sigma)+\frac{y^{[n]}_\sigma y^{[n]}_\lambda}{|y^{[n]}|^2}\delta_{\rho\nu}-\frac{2y^{[n]}_\rho y^{[n]}_\nu y^{[n]}_\sigma y^{[n]}_\lambda}{|y^{[n]}|^4}\Big)\\
&\times\Big(K_0(m|y^{[n]}|)+\frac{1}{m|y^{[n]}|}K_1(m|y^{[n]}|)\Big)\\
&+\frac{im^2}{16\pi^2}\sum_n\frac{my^{[n]}_\rho y^{[n]}_\sigma y^{[n]}_\lambda y^{[n]}_\nu}{|y^{[n]}|^3}\Big[K_1(m|y^{[n]}|)+\frac{1}{m^2|y^{[n]}|^2}K_1(m|y^{[n]}|)\\
&+\frac{1}{m|y^{[n]}|}\Big(K_0(m|y^{[n]}|)+\frac{1}{m|y^{[n]}|}K_1(m|y^{[n]}|)\Big)\Big].
\end{aligned}
\tag{D.49}
$$

D.3.2 The additional part

The additional part comes from the function I defined in Eq. (4.28), which appears due to the jump Eq. (4.3) introduced for fixing the coordinates. It thus introduces discontinuity.

Define

$$
Y\equiv\mathrm{sgn}(y^{[n_\rho+l]}_\rho-L_\rho/2)\,,\quad W\equiv\mathrm{sgn}(w^{[l]}_\rho-L_\rho/2)\,,
\tag{D.50}
$$

and we choose $\alpha, \beta \neq \rho$. We will give the expressions according to whether we have equality between Y and W. The functions J_α can be found in Appendix D.1.

Case $Y = W$

$$\Delta C_\beta^{5;\rho} = -\frac{imL_\rho}{32\pi^2}(Y+W)\Big(-\frac{1}{a^2}J_1\partial_{y_\beta}a + \frac{1}{a}\partial_{y_\beta}J_1\Big)\,. \tag{D.51}$$

$$\Delta C^{4;\rho} = \frac{imL_\rho}{32\pi^2}\frac{1}{a}(Y+W)\partial_{w_\rho}J_1\,. \tag{D.52}$$

$$\Delta C_\rho^{3;\rho} = -\Delta C_\rho^4\,, \quad \text{with } y \leftrightarrow w, \quad [n_\rho + l] \leftrightarrow [l]\,. \tag{D.53}$$

$$\Delta C_\beta^{3;\rho} = \Delta C_\beta^{5;\rho}\,. \tag{D.54}$$

$$\Delta C_{\rho\beta}^{2;\rho} = \frac{iL_\rho}{32\pi^2}\Big(-\frac{1}{a^2}\partial_{y_\beta}a\partial_{y_\rho}J_1 + \frac{1}{a}\partial^2_{y_\beta y_\rho}J_1\Big)(Y+W)\,. \tag{D.55}$$

$$\Delta C_{\alpha\beta}^{2;\rho} = \frac{iL_\rho}{32\pi^2}\Big(\frac{2}{a^3}(\partial_{y_\alpha}a\partial_{y_\beta}a)J_1 - \frac{1}{a^2}(\partial^2_{y_\alpha y_\beta}a)J_1 - \frac{1}{a^2}\partial_{\{y_\beta}a\partial_{y_\alpha\}}J_1 + \frac{1}{a}\partial^2_{y_\alpha y_\beta}J_1\Big)(Y+W)\,. \tag{D.56}$$

$$\Delta C_\alpha^{1;\rho} = -\Delta C_{\rho\alpha}^{2;\rho}\,, \quad \text{with } y \leftrightarrow w,\ [n_\rho + l] \leftrightarrow [l]\,. \tag{D.57}$$

$$\Delta C_\rho^{1;\rho} = -\frac{iL_\rho}{32\pi^2 a}(\partial^2_{y_\rho w_\rho}J_1)(Y+W)\,. \tag{D.58}$$

$$\begin{aligned}\partial_{y_\gamma}\Delta C_{\alpha\beta}^{2;\rho} =& \frac{iL_\rho}{32\pi^2}(Y+W)\Big(-\frac{6}{a^4}(\partial_{y_\gamma}a\partial_{y_\beta}a\partial_{y_\alpha}a)J_1 + \frac{2}{a^3}(\partial^2_{y_\gamma y_\beta}a\partial_{y_\alpha}a)J_1 + \frac{2}{a^3}(\partial_{y_\beta}a\partial^2_{y_\alpha y_\gamma}a)J_1\\ &+ \frac{2}{a^3}(\partial_{y_\alpha}a\partial_{y_\beta}a)\partial_{y_\gamma}J_1 + \frac{2}{a^3}(\partial_{y_\gamma}a\partial^2_{y_\alpha y_\beta}a)J_1 - \frac{1}{a^2}(\partial^3_{y_\alpha y_\beta y_\gamma}a)J_1 - \frac{1}{a^2}\partial^2_{y_\alpha y_\beta}a\partial_{y_\gamma}J_1\\ &+ \frac{2}{a^3}\partial_{y_\gamma}a\partial_{\{y_\beta}a\partial_{y_\alpha\}}J_1 - \frac{1}{a^2}(\partial_{y_\gamma}\partial_{\{y_\beta}a)\partial_{y_\alpha\}}J_1 - \frac{1}{a^2}\partial_{\{y_\beta}a\partial_{y_\alpha\}}\partial_{y_\gamma}J_1\\ &- \frac{1}{a^2}\partial_{y_\gamma}a\partial^2_{y_\alpha y_\beta}J_1 + \frac{1}{a}\partial^3_{y_\alpha y_\beta y_\gamma}J_1\Big)\,.\end{aligned} \tag{D.59}$$

$$\begin{aligned}\partial_{y_\gamma}\Delta C_\beta^{1;\rho} =& -\frac{iL_\rho}{32\pi^2}\Big(\frac{2}{a^3}(\partial_{y_\gamma}a\partial_{y_\beta}a)\partial_{w_\rho}J_1 - \frac{1}{a^2}\partial^2_{y_\gamma y_\beta}a\partial_{w_\rho}J_1\\ &- \frac{1}{a^2}\partial_{y_\beta}a\partial_{y_\gamma w_\rho}J_1 - \frac{1}{a^2}\partial_{y_\gamma}a\partial^2_{y_\beta w_\rho}J_1 + \frac{1}{a}\partial^3_{y_\gamma w_\rho y_\beta}J_1\Big)(Y+W)\,.\end{aligned} \tag{D.60}$$

Case $Y \neq W$

With $\tilde{J}$ defined in Eq. (D.21), we have

$$\Delta C_\beta^{5;\rho} = \frac{imL_\rho}{16\pi^2}(\partial_{y_\beta}\tilde{J}\frac{1}{a} - \frac{1}{a^2}\tilde{J}\partial_{y_\beta}a)(1-YW) + \frac{imL_\rho}{32\pi^2}(Y-W)\Big(-\frac{1}{a^2}J_1\partial_{y_\beta}a + \frac{1}{a}\partial_{y_\beta}J_1\Big)\,. \tag{D.61}$$

$$\Delta C^{4;\rho} = -\frac{imL_\rho}{16\pi^2 a}\partial_{w_\rho}\tilde{J}(1-YW) - \frac{imL_\rho}{32\pi^2}\frac{1}{a}(Y-W)\partial_{w_\rho}J_1\,. \tag{D.62}$$

$$\Delta C^{3;\rho}_\rho = \frac{imL_\rho}{16\pi^2 a}\partial_{y_\rho}\tilde{J}(1-YW) + \frac{imL_\rho}{32\pi^2}\frac{1}{a}(Y-W)\partial_{y_\rho}J_1\,. \tag{D.63}$$

$$\Delta C^{3;\rho}_\beta = \Delta C^5_\beta\,. \tag{D.64}$$

$$\begin{aligned}\Delta C^{2;\rho}_{\alpha\beta} =& -\frac{iL_\rho}{16\pi^2}\Big(\frac{2}{a^3}(\partial_{y_\alpha}a)(\partial_{y_\beta}a)\tilde{J} - \frac{1}{a^2}(\partial^2_{y_\alpha y_\beta}a)\tilde{J} - \frac{1}{a^2}\partial_{\{y_\beta}a\partial_{y_\alpha\}}\tilde{J} + \frac{1}{a}\partial^2_{y_\alpha y_\beta}\tilde{J}\Big)(1-YW)\\ &-\frac{iL_\rho}{32\pi^2}\Big(\frac{2}{a^3}(\partial_{y_\alpha}a\partial_\beta a)J_1 - \frac{1}{a^2}(\partial^2_{y_\alpha y_\beta}a)J_1 - \frac{1}{a^2}(\partial_{\{y_\beta}a)(\partial_{y_\alpha\}}J_1) + \frac{1}{a}\partial^2_{y_\alpha y_\beta}J_1\Big)(Y-W)\,.\end{aligned} \tag{D.65}$$

$$\begin{aligned}\Delta C^{2;\rho}_{\rho\beta} =& -\frac{iL_\rho}{16\pi^2}\Big(-\frac{1}{a^2}\partial_{y_\beta}a\partial_{y_\rho}\tilde{J} + \frac{1}{a}\partial^2_{y_\beta y_\rho}\tilde{J}\Big)(1-YW)\\ &-\frac{iL_\rho}{32\pi^2}\Big(-\frac{1}{a^2}\partial_{y_\beta}a\partial_{y_\rho}J_1 + \frac{1}{a}\partial^2_{y_\beta y_\rho}J_1\Big)(Y-W)\,.\end{aligned} \tag{D.66}$$

$$\begin{aligned}\Delta C^{1;\rho}_\alpha =& \frac{iL_\rho}{16\pi^2}\Big(\frac{1}{a}\partial^2_{y_\alpha w_\rho}\tilde{J} - \frac{1}{a^2}\partial_{y_\alpha}a\partial_{w_\rho}\tilde{J}\Big)(1-YW)\\ &+\frac{iL_\rho}{32\pi^2}\Big(-\frac{1}{a^2}\partial_{y_\beta}a\partial_{w_\rho}J_1 + \frac{1}{a}\partial^2_{y_\beta w_\rho}J_1\Big)(Y-W)\,.\end{aligned} \tag{D.67}$$

$$\Delta C^{1;\rho}_\rho = \frac{iL_\rho}{16\pi^2 a}\partial^2_{y_\rho w_\rho}\tilde{J}(1-YW) + \frac{iL_\rho}{32\pi^2 a}\partial^2_{y_\rho w_\rho}J_1(Y-W)\,. \tag{D.68}$$

$$\begin{aligned}\partial_{y_\gamma}\Delta C^{2;\rho}_{\alpha\beta} =& -\frac{iL_\rho}{16\pi^2}(1-YW)\Big(-\frac{6}{a^4}(\partial_{y_\gamma}a\partial_{y_\beta}a\partial_{y_\alpha}a)\tilde{J} + \frac{2}{a^3}(\partial^2_{y_\alpha y_\gamma}a\partial_{y_\beta}a)\tilde{J}\\ &+\frac{2}{a^3}(\partial^2_{y_\beta y_\gamma}a\partial_{y_\alpha}a)\tilde{J} + \frac{2}{a^3}\partial_{y_\alpha}a\partial_{y_\beta}a\partial_{y_\gamma}\tilde{J} + (\frac{2}{a^3}\partial_{y_\gamma}a\partial^2_{y_\alpha y_\beta}a)\tilde{J} - \frac{1}{a^2}(\partial^3_{y_\alpha y_\beta y_\gamma}a)\tilde{J}\\ &-\frac{1}{a^2}\partial^2_{y_\alpha y_\beta}a\partial_{y_\gamma}\tilde{J} + \frac{2}{a^3}\partial_{y_\gamma}a\partial_{\{y_\beta}a\partial_{y_\beta\}}\tilde{J} - \frac{1}{a^2}\partial_{\{y_\beta}\partial_{y_\gamma}a\partial_{y_\alpha\}}\tilde{J}\\ &-\frac{1}{a^2}\partial_{\{y_\beta}a\partial_{y_\alpha\}}\partial_{y_\gamma}\tilde{J} - \frac{1}{a^2}\partial_{y_\gamma}a\partial^2_{y_\alpha y_\beta}\tilde{J} + \frac{1}{a}\partial^3_{y_\gamma y_\beta y_\alpha}\tilde{J}\Big)\\ &-\frac{iL_\rho}{32\pi^2}(Y-W)\Big(-\frac{6}{a^4}(\partial_{y_\gamma}a\partial_{y_\alpha}a\partial_{y_\beta}a)J_1\\ &+\frac{2}{a^3}(\partial^2_{y_\gamma y_\alpha}a\partial_{y_\beta}a)J_1 + \frac{2}{a^3}(\partial^2_{y_\gamma y_\beta}a\partial_{y_\alpha}a)J_1 + \frac{2}{a^3}(\partial_{y_\alpha}a\partial_{y_\beta}a\partial_{y_\gamma})J_1 + \frac{2}{a^3}(\partial_{y_\gamma}a\partial^2_{y_\alpha y_\beta}a)J_1\\ &-\frac{1}{a^2}(\partial^3_{y_\alpha y_\beta y_\gamma}a)J_1 - \frac{1}{a^2}\partial^2_{y_\alpha y_\beta}a\partial_{y_\gamma}J_1 + \frac{2}{a^3}\partial_{y_\gamma}a\partial_{\{y_\beta}a\partial_{y_\alpha\}}J_1\\ &-\frac{1}{a^2}\partial_{\{y_\beta}\partial_{y_\gamma}a\partial_{y_\alpha\}}J_1 - \frac{1}{a^2}\partial_{\{y_\beta}a\partial_{y_\alpha\}}\partial_{y_\gamma}J_1 - \frac{1}{a^2}\partial_{y_\gamma}a\partial^2_{y_\alpha y_\beta}J_1 + \frac{1}{a}\partial^3_{y_\alpha y_\beta y_\gamma}J_1\Big)\,.\end{aligned} \tag{D.69}$$

$$\begin{aligned}\partial_{y_\gamma}\Delta C_\alpha^{1;\rho} =& \frac{iL_\rho}{16\pi^2}(1-YW)\Big(\frac{1}{a}\partial^3_{y_\gamma y_\alpha w_\rho}\tilde{J} - \frac{1}{a^2}\partial_{y_\gamma}a\partial^2_{y_\alpha w_\rho}\tilde{J} + \frac{2}{a^3}\partial_{y_\gamma}a\partial_{y_\alpha}a\partial_{w_\rho}\tilde{J} \\ & - \frac{1}{a^2}\partial^2_{y_\gamma y_\alpha}a\partial_{w_\rho}\tilde{J} - \frac{1}{a^2}\partial_{y_\alpha}a\partial^2_{y_\gamma w_\rho}\tilde{J}\Big) \\ & + \frac{iL_\rho}{32\pi^2}(Y-W)\Big(\frac{2}{a^3}\partial_{y_\gamma}a\partial_{y_\beta}a\partial_{w_\rho}J_1 - \frac{1}{a^2}\partial^2_{y_\gamma y_\beta}a\partial_{w_\rho}J_1 - \frac{1}{a^2}\partial_{y_\beta}a\partial^2_{y_\gamma w_\rho}J_1 \\ & - \frac{1}{a^2}\partial_{y_\gamma}a\partial^2_{y_\beta w_\rho}J_1 + \frac{1}{a}\partial^3_{y_\gamma y_\beta w_\rho}J_1\Big)\,.\end{aligned} \tag{D.70}$$

D.4 Case with anti-periodic boundary condition in the time-direction

In lattice computations, periodic boundary conditions in the spatial directions and anti-periodic boundary condition in the time-direction are often used for fermions. Compared to the established results in Sect. 4.1, this essentially requires to add a phase of -1 when the temporal component of the winding number is odd. As for the jump introduced due to the mapping the between lattice coordinates and the real world ones [Eq. (4.3)], we will see that nothing has to be changed at this level. The same notations as in Sect. 4.1 will be used.

The propagator $S(x)$ in finite-volume under anti-periodic boundary condition reads

$$S^{\mathrm{L}}(x) = \sum_{n\in\mathbb{Z}^4}\Big[S\big(x+\mathfrak{n}^+\mathbf{L}\big) - S\big(x+\mathfrak{n}^-\mathbf{L}\big)\Big]\,, \tag{D.71}$$

where $\mathfrak{n}^+ = \mathrm{diag}(2n_0, n_1, n_2, n_3)$, $\mathfrak{n}^- = \mathrm{diag}(2n_0+1, n_1, n_2, n_3)$, $\mathbf{L} = (L_0, L_1, L_2, L_3)^\intercal$ and 0 indicates the temporal direction. To simplify the notation, we suppose that $L_0 = L_1 = L_2 = L_3 = L$ in the following.

The Poisson summation formula allows us to write

$$S^{\mathrm{L}}(x) = \sum_{k\in\frac{\pi}{L}\mathbb{Z}\times\left(\frac{2\pi}{L}\mathbb{Z}\right)^3}\frac{1}{2L^8}\tilde{T}(k)e^{ikx}\,, \tag{D.72}$$

where $\tilde{T}$ is the Fourier transform in infinite-volume of

$$T(x) \equiv S(x) - S\big(x+L_0\hat{0}\big)\,. \tag{D.73}$$

One can check that, for $p = (p_0, \vec{p}) \in \frac{\pi}{L}\mathbb{Z}\times\left(\frac{2\pi}{L}\mathbb{Z}\right)^3$ with $p_0 = \frac{n\pi}{L}$,

$$\tilde{T}(p) = \Big(1-(-1)^n\Big)\tilde{S}(p) = \Big(1-\cos p_0 L\Big)\tilde{S}(p)\,. \tag{D.74}$$

Analogous to Eq. (4.15), for a $2L$-periodic function in 1-dimension $f:[0,2L]\to\mathbb{R}$ we have,

$$\begin{aligned}\int_{u=0}^{L}[u]f(u) =& \frac{1}{2L}\sum_{p\in\frac{\pi}{L}\mathbb{Z}}\Big(\int_0^L u\hat{f}(p)e^{ipu} - L\int_{L/2}^{L}\hat{f}(p)e^{ipu}\Big) \\ =& \frac{1}{2L}\sum_{p\in\frac{\pi}{L}\mathbb{Z}^*}\frac{\hat{f}(p)}{p^2}(1-\cos(pL)) + \frac{1}{2}\sum_{p\in\frac{\pi}{L}\mathbb{Z}^*}\frac{1}{ip}\hat{f}(p)e^{ip\frac{L}{2}}\,,\end{aligned} \tag{D.75}$$

where $\hat{f}$ is the Fourier transform of f (in a box of size $2L$).

It is then straightforward to get the anti-periodic-boundary-condition version of Eq. (4.17). For $\rho \neq 0$, the expressions derived in Sect. 4.1 remain valid, whereas for $\rho = 0$,

$$\begin{aligned}\int_z [z_\rho] e^{i(p-q)z} =& -\frac{1}{2} L^3 \delta_{(p-q)_\perp,\vec{0}} \frac{iL_\rho}{(p-q)_\rho} \exp\left(\frac{i(p-q)_\rho L_\rho}{2}\right) \\ &+ \frac{1}{2} L^3 \delta_{(p-q)_\perp,\vec{0}} \frac{1}{(p-q)_\rho^2} \Big[1 - \exp\left(i(p-q)_\rho L_\rho\right)\Big] .\end{aligned} \tag{D.76}$$

And thus the most important term Eq. (4.18) reads in this case

$$\begin{aligned}F_{\rho\sigma}(y,w) =& \frac{1}{(2L^4)^2} \sum_{p,q \in \frac{\pi}{L}\mathbb{Z} \times \left(\frac{2\pi}{L}\mathbb{Z}\right)^3} e^{iqy - ipw} \tilde{T}(q) \gamma_\sigma \tilde{T}(p) \int_z [z_\rho] e^{i(p-q)z} \\ =& \frac{1}{8L^4} \sum_{p_\rho, q_\rho \in \frac{\pi}{L}\mathbb{Z}, q_\perp \in \left(\frac{2\pi}{L}\mathbb{Z}\right)^3} \tilde{S}(q) \gamma_\sigma \tilde{S}(p_\rho \hat{\rho} + q) e^{iq(y-w) - ip_\rho w_\rho} \\ &\times \Big(1 - \cos q_\rho L\Big)\Big(1 - \cos(p_\rho + q_\rho)L\Big) \\ &\times \Big\{ -\frac{i}{p_\rho} \exp\left(\frac{ip_\rho L}{2}\right) + \frac{1}{p_\rho^2 L_\rho}\Big[1 - \exp\Big(ip_\rho L\Big)\Big]\Big\} .\end{aligned} \tag{D.77}$$

To have a non-vanishing contribution, q_ρ and p_ρ in the before-last line above should be respectively odd and even multiple of $\frac{\pi}{L}$. Thus, the second term in the brace in the last line of the equation does not contribute. Take into account the possible values for p and q which give non-vanishing contribution, we can rewrite the equation as

$$\begin{aligned}F_{\rho\sigma}(y,w) = -\frac{1}{4L^4} & \sum_{\substack{p_\rho \in \frac{2\pi}{L}\mathbb{Z}, \\ q \in \frac{\pi}{L}\mathbb{Z} \times \left(\frac{2\pi}{L}\mathbb{Z}\right)^3}} \tilde{S}(q) \gamma_\sigma \tilde{S}(p_\rho \hat{\rho} + q) e^{iq(y-w) - ip_\rho w_\rho} \\ &\times \Big(1 - \cos q_\rho L_\rho\Big) \frac{i}{p_\rho} \exp\left(\frac{ip_\rho L_\rho}{2}\right) .\end{aligned} \tag{D.78}$$

One should be able to follow the same steps in Sect. 4.1 further. After applying the Poisson summation formula, Eq. (4.23), one can notice that the $1 - \cos q_\rho L_\rho$ factor, which is the main difference compared to the all-periodic boundary condition case, just corrects the effect of the windings in the variable $y - w$ according to the anti-periodic boundary condition in time, i.e. one will pick up a relative sign depending on the number of windings in the time direction: an odd number of windings takes a minus sign and an even number of windings remains unchanged.

Appendix E

Complements for Sect. 4.2

In this appendix are defined some functions which are used in Sect. 4.2. The functions $C^{i\prime}$s are defined in Appendix D.3.

We denote

$$B^{\rho}_{\lambda\sigma} = C^{1;\rho}_{\sigma}\delta_{\lambda\rho} + C^{2;\rho}_{\sigma\lambda}(1-\delta_{\lambda\rho})\,. \tag{E.1}$$

It is important to recall that the scalar propagator G_m should be treated as a distribution as discussed in Sect. 3.2.1. In particular, one should not forget to apply Eq. (3.48) when encountering a second derivative of G_m and a δ-function will appear. Nonetheless, as argued at the end of Sect. 4.2.1, we can just treat the higher derivatives of G_m as usual functions and add back the extra δ-function at the end.

E.1 List of functions for the box class

E.1.1 $\tilde{I}_4$

$$\tilde{I}^{++++}_{4,\mu\nu\sigma\lambda}(x,y,z,w) = \partial_\mu G_m(x-y)\partial_\nu G_m(y-z)\partial_\sigma G_m(z-w)\partial_\lambda G_m(w-x)\,. \tag{E.2}$$

$$\tilde{I}^{----}_{4,\mu\nu\sigma\lambda}(x,y,z,w) = \partial_\nu G_m(x-y)\partial_\sigma G_m(y-z)\partial_\lambda G_m(z-w)\partial_\mu G_m(w-x)\,. \tag{E.3}$$

$$\tilde{I}^{+++-}_{4,\mu\nu\sigma\lambda}(x,y,z,w) = \partial_\mu G_m(x-y)\partial_\nu G_m(y-z)\partial^2_{\sigma\lambda} G_m(z-w) G_m(w-x)\,. \tag{E.4}$$

$$\tilde{I}^{++-+}_{4,\mu\nu\sigma\lambda}(x,y,z,w) = \partial_\mu G_m(x-y)\partial^2_{\nu\sigma} G_m(y-z) G_m(z-w)\partial_\lambda G_m(w-x)\,. \tag{E.5}$$

$$\tilde{I}^{+-++}_{4,\mu\nu\sigma\lambda}(x,y,z,w) = \partial^2_{\mu\nu} G_m(x-y) G_m(y-z)\partial_\sigma G_m(z-w)\partial_\lambda G_m(w-x)\,. \tag{E.6}$$

$$\tilde{I}^{-+++}_{4,\mu\nu\sigma\lambda}(x,y,z,w) = G_m(x-y)\partial_\nu G_m(y-z)\partial_\sigma G_m(z-w)\partial^2_{\lambda\mu} G_m(w-x)\,. \tag{E.7}$$

$$\tilde{I}^{---+}_{4,\mu\nu\sigma\lambda}(x,y,z,w) = \partial_\nu G_m(x-y)\partial_\sigma G_m(y-z) G_m(z-w)\partial^2_{\lambda\mu} G_m(w-x)\,. \tag{E.8}$$

$$\tilde{I}^{--+-}_{4,\mu\nu\sigma\lambda}(x,y,z,w) = \partial_\nu G_m(x-y) G_m(y-z)\partial^2_{\sigma\lambda} G_m(z-w)\partial_\mu G_m(w-x)\,. \tag{E.9}$$

$$\tilde{I}^{-+--}_{4,\mu\nu\sigma\lambda}(x,y,z,w) = G_m(x-y)\partial^2_{\nu\sigma} G_m(y-z)\partial_\lambda G_m(z-w)\partial_\mu G_m(w-x)\,. \tag{E.10}$$

$$\tilde{I}^{+---}_{4,\mu\nu\sigma\lambda}(x,y,z,w) = \partial^2_{\mu\nu} G_m(x-y)\partial_\sigma G_m(y-z)\partial_\lambda G_m(z-w) G_m(w-x)\,. \tag{E.11}$$

$$\tilde{I}^{++--}_{4,\mu\nu\sigma\lambda}(x,y,z,w) = \partial_\mu G_m(x-y)\partial^2_{\nu\sigma} G_m(y-z)\partial_\lambda G_m(z-w) G_m(w-x)\,. \tag{E.12}$$

$$\tilde{I}^{+--+}_{4,\mu\nu\sigma\lambda}(x,y,z,w) = \partial^2_{\mu\nu} G_m(x-y)\partial_\sigma G_m(y-z) G_m(z-w)\partial_\lambda G_m(w-x)\,. \tag{E.13}$$

$$\tilde{I}^{--++}_{4,\mu\nu\sigma\lambda}(x,y,z,w) = \partial_\nu G_m(x-y) G_m(y-z)\partial_\sigma G_m(z-w)\partial^2_{\lambda\mu} G_m(w-x)\,. \tag{E.14}$$

$$\tilde{I}^{-++-}_{4,\mu\nu\sigma\lambda}(x,y,z,w) = G_m(x-y)\partial_\nu G_m(y-z)\partial^2_{\sigma\lambda} G_m(z-w)\partial_\mu G_m(w-x)\,. \tag{E.15}$$

$$\tilde{I}^{+-+-}_{4,\mu\nu\sigma\lambda}(x,y,z,w) = \partial^2_{\mu\nu} G_m(x-y) G_m(y-z)\partial^2_{\sigma\lambda} G_m(z-w) G_m(w-x)\,. \tag{E.16}$$

$$\tilde{I}^{-+-+}_{4,\mu\nu\sigma\lambda}(x,y,z,w) = G_m(x-y)\partial^2_{\nu\sigma}G_m(y-z)G_m(z-w)\partial^2_{\lambda\mu}G_m(w-x)\,. \tag{E.17}$$

E.1.2 $i\hat{\Pi}^{4,1}$

The anti-symmetrization of the indices ρ and σ is implicitly applied everywhere in the expressions listed below.

$$i\hat{\Pi}^{4,1,++++}_{[\rho,\sigma]\mu\nu\lambda} = -2iC^{2;\rho}_{\nu\sigma}\partial_\mu G_m(x-y)\partial_\lambda G_m(w-x)\,. \tag{E.18}$$

$$i\hat{\Pi}^{4,1,----}_{[\rho,\sigma]\mu\nu\lambda} = -2iB^{\rho}_{\lambda\sigma}\partial_\nu G_m(x-y)\partial_\mu G_m(w-x)\,. \tag{E.19}$$

$$i\hat{\Pi}^{4,1,+++-}_{[\rho,\sigma]\mu\nu\lambda} = -2i\partial_{y^\nu}B^{\rho}_{\lambda\sigma}\partial_\mu G_m(x-y)G_m(w-x)\,. \tag{E.20}$$

$$i\hat{\Pi}^{4,1,++-+}_{[\rho,\sigma]\mu\nu\lambda} = -2iC^{2;\rho}_{\nu\sigma}\partial_\mu G_m(x-y)\partial_\lambda G_m(w-x)\,. \tag{E.21}$$

$$i\hat{\Pi}^{4,1,+-++}_{[\rho,\sigma]\mu\nu\lambda} = \frac{2i}{m}C^{3;\rho}_{\sigma}\partial^2_{\mu\nu}G_m(x-y)\partial_\lambda G_m(w-x)\,. \tag{E.22}$$

$$i\hat{\Pi}^{4,1,-+++}_{[\rho,\sigma]\mu\nu\lambda} = -2iC^{2;\rho}_{\nu\sigma}G_m(x-y)\partial^2_{\lambda\mu}G_m(w-x)\,. \tag{E.23}$$

$$i\hat{\Pi}^{4,1,---+}_{[\rho,\sigma]\mu\nu\lambda} = \frac{2i}{m}C^{3;\rho}_{\sigma}\partial_\nu G_m(x-y)\partial^2_{\lambda\mu}G_m(w-x)\,. \tag{E.24}$$

$$i\hat{\Pi}^{4,1,--+-}_{[\rho,\sigma]\mu\nu\lambda} = -2iB^{\rho}_{\lambda\sigma}\partial_\nu G_m(x-y)\partial_\mu G_m(w-x)\,. \tag{E.25}$$

$$i\hat{\Pi}^{4,1,-+--}_{[\rho,\sigma]\mu\nu\lambda} = -2i\partial_{y^\nu}B^{\rho}_{\lambda\sigma}G_m(x-y)\partial_\mu G_m(w-x)\,. \tag{E.26}$$

$$i\hat{\Pi}^{4,1,+---}_{[\rho,\sigma]\mu\nu\lambda} = -2iB^{\rho}_{\lambda\sigma}\partial^2_{\mu\nu}G_m(x-y)G_m(w-x)\,. \tag{E.27}$$

$$i\hat{\Pi}^{4,1,++--}_{[\rho,\sigma]\mu\nu\lambda} = -2i\partial_{y^\nu}B^{\rho}_{\lambda\sigma}\partial_\mu G_m(x-y)G_m(w-x)\,. \tag{E.28}$$

$$i\hat{\Pi}^{4,1,+--+}_{[\rho,\sigma]\mu\nu\lambda} = \frac{2i}{m}C^{3;\rho}_{\sigma}\partial^2_{\mu\nu}G_m(x-y)\partial_\lambda G_m(w-x)\,. \tag{E.29}$$

$$i\hat{\Pi}^{4,1,--++}_{[\rho,\sigma]\mu\nu\lambda} = \frac{2i}{m}C^{3;\rho}_{\sigma}\partial_\nu G_m(x-y)\partial^2_{\lambda\mu}G_m(w-x)\,. \tag{E.30}$$

$$i\hat{\Pi}^{4,1,-++-}_{[\rho,\sigma]\mu\nu\lambda} = -2i\partial_{y^\nu}B^{\rho}_{\lambda\sigma}G_m(x-y)\partial_\mu G_m(w-x)\,. \tag{E.31}$$

$$i\hat{\Pi}^{4,1,+-+-}_{[\rho,\sigma]\mu\nu\lambda} = -2iB^{\rho}_{\lambda\sigma}\partial^2_{\mu\nu}G_m(x-y)G_m(w-x)\,. \tag{E.32}$$

$$i\hat{\Pi}^{4,1,-+-+}_{[\rho,\sigma]\mu\nu\lambda} = -2iC^{2;\rho}_{\nu\sigma}G_m(x-y)\partial^2_{\lambda\mu}G_m(w-x)\,. \tag{E.33}$$

E.1.3 $\tilde{N}$

$$\tilde{N}^{++++}_{4,\mu\nu\sigma\lambda}(x,y,z,w) = 2\partial_\mu G_m(x-y)\partial_\lambda G_m(w-x)\Big(\partial^2_{\nu\sigma}\partial_{m^2}G_m(w-y)\Big)\,. \tag{E.34}$$

$$\tilde{N}^{----}_{4,\mu\nu\sigma\lambda}(x,y,z,w) = 2\partial_\nu G_m(x-y)\partial_\mu G_m(w-x)\Big(\partial^2_{\sigma\lambda}\partial_{m^2}G_m(w-y)\Big)\,. \tag{E.35}$$

$$\tilde{N}^{+++-}_{4,\mu\nu\sigma\lambda}(x,y,z,w) = 2\partial_\mu G_m(x-y)G_m(w-x)\Big(\partial^3_{\nu\sigma\lambda}\partial_{m^2}G_m(w-y)\Big)\,. \tag{E.36}$$

$$\tilde{N}^{++-+}_{4,\mu\nu\sigma\lambda}(x,y,z,w) = 2\partial_\mu G_m(x-y)\partial_\lambda G_m(w-x)\Big(\partial^2_{\nu\sigma}\partial_{m^2}G_m(w-y)\Big)\,. \tag{E.37}$$

$$\tilde{N}^{+-++}_{4,\mu\nu\sigma\lambda}(x,y,z,w) = 2\partial^2_{\mu\nu}G_m(x-y)\partial_\lambda G_m(w-x)\Big(\partial_\sigma\partial_{m^2}G_m(w-y)\Big)\,. \tag{E.38}$$

$$\tilde{N}^{-+++}_{4,\mu\nu\sigma\lambda}(x,y,z,w) = 2G_m(x-y)\partial^2_{\lambda\mu}G_m(w-x)\Big(\partial^2_{\nu\sigma}\partial_{m^2}G_m(w-y)\Big)\,. \tag{E.39}$$

$$\tilde{N}^{---+}_{4,\mu\nu\sigma\lambda}(x,y,z,w) = 2\partial_\nu G_m(x-y)\partial^2_{\lambda\mu}G_m(w-x)\Big(\partial_\sigma\partial_{m^2}G_m(w-y)\Big)\,. \tag{E.40}$$

$$\tilde{N}^{--+-}_{4,\mu\nu\sigma\lambda}(x,y,z,w) = 2\partial_\nu G_m(x-y)\partial_\mu G_m(w-x)\Big(\partial^2_{\sigma\lambda}\partial_{m^2}G_m(w-y)\Big)\,. \tag{E.41}$$

$$\tilde{N}^{-+--}_{4,\mu\nu\sigma\lambda}(x,y,z,w) = 2G_m(x-y)\partial_\mu G_m(w-x)\Big(\partial^3_{\nu\sigma\lambda}\partial_{m^2}G_m(w-y)\Big)\,. \tag{E.42}$$

$$\tilde{N}^{+---}_{4,\mu\nu\sigma\lambda}(x,y,z,w) = 2\partial^2_{\mu\nu}G_m(x-y)G_m(w-x)\Big(\partial^2_{\sigma\lambda}\partial_{m^2}G_m(w-y)\Big)\,. \tag{E.43}$$

$$\tilde{N}^{++--}_{4,\mu\nu\sigma\lambda}(x,y,z,w) = 2\partial_\mu G_m(x-y)G_m(w-x)\Big(\partial^3_{\nu\sigma\lambda}\partial_{m^2}G_m(w-y)\Big)\,. \tag{E.44}$$

$$\tilde{N}^{+--+}_{4,\mu\nu\sigma\lambda}(x,y,z,w) = 2\partial^2_{\mu\nu}G_m(x-y)\partial_\lambda G_m(w-x)\Big(\partial_\sigma\partial_{m^2}G_m(w-y)\Big)\,. \tag{E.45}$$

$$\tilde{N}^{--++}_{4,\mu\nu\sigma\lambda}(x,y,z,w) = 2\partial_\nu G_m(x-y)\partial^2_{\lambda\mu}G_m(w-x)\Big(\partial_\sigma\partial_{m^2}G_m(w-y)\Big)\,. \tag{E.46}$$

$$\tilde{N}^{-++-}_{4,\mu\nu\sigma\lambda}(x,y,z,w) = 2G_m(x-y)\partial_\mu G_m(w-x)\Big(\partial^3_{\nu\sigma\lambda}\partial_{m^2}G_m(w-y)\Big)\,. \tag{E.47}$$

$$\tilde{N}^{+-+-}_{4,\mu\nu\sigma\lambda}(x,y,z,w) = 2\partial_{\mu\nu}G_m(x-y)G_m(w-x)\Big(\partial^2_{\sigma\lambda}\partial_{m^2}G_m(w-y)\Big)\,. \tag{E.48}$$

$$\tilde{N}^{-+-+}_{4,\mu\nu\sigma\lambda}(x,y,z,w) = 2G_m(x-y)\partial^2_{\lambda\mu}G_m(w-x)\Big(\partial^2_{\nu\sigma}\partial_{m^2}G_m(w-y)\Big)\,. \tag{E.49}$$

E.2 List of functions for the triangle class

E.2.1 $\tilde{I}_3$

$$\tilde{I}^{++}_{3,\mu\nu}(x,y,w) = \partial_\mu G_m(x-y)\partial_\nu G_m(y-w)G_m(w-x)\,. \tag{E.50}$$

$$\tilde{I}^{--}_{3,\mu\nu}(x,y,w) = \partial_\nu G_m(x-y)G_m(y-w)\partial_\mu G_m(w-x)\,. \tag{E.51}$$

$$\tilde{I}^{-+}_{3,\mu\nu}(x,y,w) = G_m(x-y)\partial_\nu G_m(y-w)\partial_\mu G_m(w-x)\,. \tag{E.52}$$

$$\tilde{I}^{+-}_{3,\mu\nu}(x,y,w) = \partial^2_{\mu\nu}G_m(x-y)G_m(y-w)G_m(w-x)\,. \tag{E.53}$$

E.2.2 $i\hat{\Pi}^{3,j}$

Because of the δ-function and the z-weight factor,

$$i\hat{\Pi}^{3,1}_{[\rho,\sigma]\mu\nu\lambda} = 0\,. \tag{E.54}$$

For the other $i\hat{\Pi}^{3,j}$'s, we give their expressions below with the indices ρ and σ already anti-symmetrized.

$$\begin{aligned} i\hat{\Pi}^{3,2}_{[\rho,\sigma]\mu\nu\lambda} = -4x_\rho\Big(&\partial_\nu G_m(y-w)\partial_\lambda G_m(w-x)G_m(x-y)\\ &+\partial_\lambda G_m(y-w)G_m(w-x)\partial_\nu G_m(x-y)\\ &+G_m(y-w)\partial_\lambda G_m(w-x)\partial_\nu G_m(x-y)\\ &+\partial^2_{\nu\lambda}G_m(y-w)G_m(w-x)G_m(x-y)\Big)\,. \end{aligned} \tag{E.55}$$

$$i\hat{\Pi}^{3,3}_{[\rho,\sigma]\mu\nu\lambda} = i\hat{\Pi}^{3,2}_{\mu\leftrightarrow\nu}(x\leftrightarrow y)\,. \tag{E.56}$$

$$i\hat{\Pi}^{3,4}_{[\rho,\sigma]\mu\nu\lambda} = -8i\delta(x-y)\delta_{\mu\nu}\Big(-\frac{1}{m}C^{3;\rho}_{\sigma}\partial_{\lambda}G_m(w-y) + B^{\rho}_{\lambda\sigma}G_m(w-y)\Big)\,. \tag{E.57}$$

$$i\hat{\Pi}^{3,5}_{[\rho,\sigma]\mu\nu\lambda} = -8i\delta(x-w)\delta_{\mu\lambda}\Big(\frac{1}{m}C^{3;\rho}_{\sigma}\partial_{\nu}G_m(y-w) + C^{2;\rho}_{\nu\sigma}G_m(y-w)\Big)\,. \tag{E.58}$$

$$i\hat{\Pi}^{3,6}_{[\rho,\sigma]\mu\nu\lambda} = i\hat{\Pi}^{3,5}_{\mu\overset{\sim}{\leftrightarrow}\nu}(y \leftrightarrow x)\,. \tag{E.59}$$

Appendix F

Supplementary material for Chap. 6

F.1 Results from individual ensembles for Sect. 6.3

The results of each individual ensemble used in the analysis presented in Sect. 6.3 obtained with Method 2 are tabulated in Tab. F.1 for completeness. They can be found in the original publication Ref. [Cha+20].

F.1.1 The connected contribution

See Tab. F.1.

Label	$\lvert y\rvert_{\text{cut}}$ [fm]	a_μ^{data}	a_μ^{FSE}	a_μ^{tail}	a_μ^{conn}
U103	1.85	58.9(1.8)	14.3	13.3	86.5(1.8)(6.9)
H101	2.55	75.7(2.9)	6.9	2.6	85.2(2.9)(2.4)
B450	2.00	73.6(3.3)	7.6	9.4	90.3(3.3)(4.3)
H200	1.75	68.6(1.8)	13.7	13.6	95.8(1.8)(6.8)
N202	2.60	91.0(2.5)	3.8	1.9	96.7(2.5)(1.5)
N300	2.10	79.0(1.8)	7.1	6.2	92.3(1.8)(3.4)

TABLE F.1: Results for the connected contribution using Method 2 for the ensembles at $\mathrm{SU}(3)_f$-symmetric point. Here a_μ^{data} corresponds to the value using lattice data up to some linearly-interpolated value of $y = \lvert y\rvert_{\text{cut}}$, chosen to minimize the total error of a_μ^{conn}. a_μ^{FSE} is the cumulated finite size correction up to $\lvert y\rvert = \lvert y\rvert_{\text{cut}}$ and a_μ^{tail} is the contribution computed with the model from $\lvert y\rvert = \lvert y\rvert_{\text{cut}}$ to infinity. In the last column we give the FSE-corrected result, where the first error is statistical and the second is the systematic error due to the FSE and the tail correction, corresponding to 25% of their total.

F.1.2 The (2+2)-disconnected contribution

See Tab. F.2.

F.2 Results from individual ensembles for Sect. 6.4

We put the results of each individual ensemble used in the analysis presented in Sect. 6.4 in this appendix for completeness. They can be found in the original publication Ref. [Cha+21]. Note that these tabulated results are obtained after the treatments described in Sect. 6.4 being applied accordingly.

Label	a_μ^{data}	a_μ^{FSE}	$a_\mu^{\text{tail};\pi^0+\eta}$	$a_\mu^{\text{tail};\eta'}$	a_μ^{disc}
U103	−17.7(1.9)	−2.4	−30.0	4.11	−45.9(1.9)(7.1)
H101	−23.4(2.3)	−0.6	−30.0	4.11	−49.8(2.3)(6.6)
B450	−26.7(3.4)	−0.9	−28.4	4.11	−51.8(3.4)(6.3)
H200	−12.6(3.7)	−2.2	−28.2	4.14	−38.9(3.7)(6.6)
N202	−21.0(6.0)	−0.2	−28.2	4.14	−45.3(6.0)(6.1)
N300	−20.6(5.4)	−0.7	−24.7	4.01	−42.0(5.4)(5.4)

TABLE F.2: Finite-volume corrected disconnected contributions to a_μ^{hlbl} at the $\text{SU}(3)_\text{f}$-symmetric point. A breakdown of the FSE contributions to the total results are shown, again a 25% systematic to the total finite-size correction is used. The value of $|y|_{\text{cut}}$ was 1.2 fm for each ensemble.

F.2.1 Purely light-quark contribution to the leading topologies

See Tab. F.3.

Ensemble	Connected$\times 10^{11}$	$(2+2)\times 10^{11}$	Sum$\times 10^{11}$
A653	64.5(1.0)	−31.8(2.8)	32.7(3.1)
A654	79.4(1.8)	−36.7(4.8)	42.6(5.3)
U103	59.3(0.9)	−22.1(4.3)	37.2(4.3)
H101	70.2(1.8)	−30.3(4.4)	39.9(4.8)
U102	66.5(1.2)	−23.6(2.5)	42.9(2.9)
H105	92.9(2.8)	−46.8(5.5)	46.1(6.0)
C101	127.7(5.6)	−62.2(6.6)	65.5(9.0)
B450	70.4(1.3)	−27.8(8.2)	42.6(8.3)
D450	144.5(11.9)	−84.8(14.5)	59.7(20.0)
H200	65.3(1.3)	−19.5(3.4)	45.8(3.5)
N202	83.2(2.0)	−28.5(3.0)	54.8(3.6)
N200	116.9(4.9)	−54.2(6.3)	62.7(7.9)
D200	151.7(9.6)	−80.4(13.4)	71.4(16.6)
N300	75.7(1.3)	−15.8(2.6)	59.9(2.9)

TABLE F.3: The two leading light-quark contributions to a_μ^{hlbl} for each gauge ensemble.

F.2.2 Strange quark contribution to the leading topologies

See Tab. F.4.

F.2.3 The $(3+1)_{\text{light}}$ contribution

See Tab. F.5.

F.3 Fitting results for the (3+1)-contribution

Listed are some representative fit forms that we have tried to described the tail truncated $(3+1)_{\text{light}}$ data.

Ensemble	Connected$\times 10^{11}$	$(2+2)\times 10^{11}$	Sum$\times 10^{11}$
A653	3.79(0.06)	−14.0(1.2)	−10.2(1.2)
A654	2.65(0.02)	−9.8(1.1)	−7.1(1.1)
U103	3.49(0.05)	−9.7(1.9)	−6.2(1.9)
H101	4.13(0.10)	−13.3(1.9)	−9.2(1.9)
H105	2.50(0.06)	−8.2(1.0)	−5.7(1.0)
C101	2.25(0.02)	−8.0(1.0)	−5.8(1.0)
B450	4.14(0.07)	−12.2(3.6)	−8.1(3.6)
H200	3.84(0.08)	−8.6(1.5)	−4.7(1.5)
N202	4.90(0.12)	−12.5(1.3)	−7.6(1.3)
N300	4.45(0.07)	−7.0(1.1)	−2.5(1.1)

TABLE F.4: Fully-connected strange-quark and the combined $(2+2)$ ls and ss contributions to a_μ^{hlbl}.

Ensemble	$\lvert y\rvert_{\mathrm{cut}}$[fm]	$a_\mu^{<}\times 10^{11}$	$a_\mu^{>}\times 10^{11}$	$a_\mu^{(3+1)}\times 10^{11}$
A654	1.47	−0.23(0.16)	0.00(0.11)	−0.23(0.20)
U102	1.17	−0.23(0.28)	0.00(0.16)	−0.23(0.34)
H105	1.28	0.61(0.58)	0.00(0.45)	0.61(0.79)
C101	1.43	−0.60(1.38)	0.00(1.01)	−0.60(1.83)
D450	1.37	0.64(1.61)	0.00(1.18)	0.64(2.14)
N203	1.01	0.19(0.48)	0.00(0.29)	0.19(0.59)
N200	1.32	0.01(0.65)	0.00(0.42)	0.01(0.82)
D200	1.50	−0.57(1.53)	0.00(1.32)	−0.57(2.21)

TABLE F.5: Results for $(3+1)_{\mathrm{light}}$ on each ensemble (using $w_{\mathrm{sys.}} = 120\%$), along with the choice of $\lvert y\rvert_{\mathrm{cut}}$ and the contributions to a_μ below and above the cut chosen according to the tail-truncation scheme described in the text.

- **Fit 0:** $A\Delta M^2$
- **Fit 2:** $(A+Ba)\Delta M^2$
- **Fit 23:** $A\Delta M^2 + Ba$
- **Fit 24:** $A\Delta M^2 + Ba^2$
- **Fit 25:** $(A+Ba^2)\Delta M^2$
- **Fit 26:** $A\Delta M^2 + Be^{-m_\pi L}$
- **Fit 28:** $A\Delta M^2 + Ba + Ce^{-m_\pi L}$

For the fitting, the value for a is taken in fm, $\Delta M^2 \equiv m_K^2 - m_\pi^2$ is in GeV^2 and $m_\pi L$ is dimensionless as it should be. The fitting results with different $w_{\mathrm{sys.}}$[1] to the full dataset are given in Tabs. F.6-F.8. The best-fit parameters are given in the order of appearance in the corresponding ansatz.

[1] See the text of Sect. 6.4.3.

Index	Parameters $\times 10^{11}$	$a_\mu \times 10^{11}$	χ^2/d.o.f.
0	-1.57(1.54)	-0.36(0.35)	0.21
2	4.47(11.37) -66.52(123.98)	1.02(2.60)	0.19
23	2.58(6.17) -4.36(6.27)	0.59(1.41)	0.16
24	1.83(5.00) -38.31(53.53)	0.42(1.14)	0.16
25	1.82(6.46) -403.18(745.76)	0.42(1.48)	0.19
26	0.95(4.00) -13.53(19.74)	0.22(0.91)	0.16
28	2.17(6.46) -2.52(10.63) -7.13(33.49)	0.50(1.48)	0.18

TABLE F.6: $w_{\text{sys.}} = 1$

Index	Parameters $\times 10^{11}$	$a_\mu \times 10^{11}$	χ^2/d.o.f.
0	-1.57(1.83)	-0.36(0.42)	0.36
2	9.74(13.42) -124.70(146.57)	2.23(3.07)	0.30
23	5.71(7.36) -7.63(7.47)	1.31(1.68)	0.25
24	4.59(5.94) -69.50(63.72)	1.05(1.36)	0.22
25	4.90(7.61) -772.36(881.90)	1.12(1.74)	0.29
26	1.90(4.70) -18.51(23.07)	0.43(1.08)	0.31
28	5.78(7.74) -7.94(12.65) 1.16(39.06)	1.32(1.77)	0.29

TABLE F.7: $w_{\text{sys.}} = 1.5$

Index	Parameters $\times 10^{11}$	$a_\mu \times 10^{11}$	χ^2/d.o.f.
0	-1.52(2.05)	-0.35(0.47)	0.38
2	9.89(14.90) -125.93(163.02)	2.26(3.41)	0.34
23	6.34(8.25) -8.20(8.35)	1.45(1.87)	0.28
24	5.12(6.65) -74.63(71.31)	1.17(1.52)	0.26
25	5.08(8.44) -789.14(981.15)	1.16(1.93)	0.34
26	1.98(5.19) -18.47(25.16)	0.45(1.19)	0.35
28	6.60(8.72) -9.25(14.13) 3.91(42.59)	1.51(2.00)	0.34

TABLE F.8: $w_{\text{sys.}} = 2$

Acronyms

$\alpha_{\mathbf{QED}}$ the fine structure constant.

a_μ the anomalous magnetic moment of the muon.

$a_\mu^{\mathbf{hlbl}}$ the Hadronic Light-by-Light contribution to the anomalous magnetic moment of the muon.

c.c. complex conjugate.

ChPT Chiral Perturbation Theory.

CLS Coordinated Lattice Simulations.

EFT effective field theory.

EOM equation of motion.

FSE finite-size effect.

GP Gegenbauer polynomial.

HLbL Hadronic Light-by-Light.

HMC Hybrid Monte Carlo.

HVP Hadronic Vacuum Polarization.

LQCD Lattice Quantum Chromodynamics.

MC Monte Carlo.

MCMC Markov-Chain Monte Carlo.

MD molecular dynamics.

PQChPT Partially-Quenched Chiral Perturbation Theory.

PQQCD Partially-Quenched Quantum Chromodynamics.

QCD Quantum Chromodynamics.

QED Quantum Electrodynamics.

QFT Quantum field theory.

RHMC Rational Monte Carlo.

SM Standard Model.

TFF transition form factor.

VEV vacuum expectation value.

VMD Vector-Meson Dominance.

Bibliography

[Aab+17] Morad Aaboud et al. "Evidence for light-by-light scattering in heavy-ion collisions with the ATLAS detector at the LHC". In: *Nature Phys.* 13.9 (2017), pp. 852–858. DOI: 10.1038/nphys4208. arXiv: 1702.01625 [hep-ex].

[Aad+19] Georges Aad et al. "Observation of light-by-light scattering in ultraperipheral Pb+Pb collisions with the ATLAS detector". In: *Phys. Rev. Lett.* 123.5 (2019), p. 052001. DOI: 10.1103/PhysRevLett.123.052001. arXiv: 1904.03536 [hep-ex].

[Aai+21] Roel Aaij et al. "Test of lepton universality in beauty-quark decays". In: (Mar. 2021). arXiv: 2103.11769 [hep-ex].

[Abe+19] M. Abe et al. "A New Approach for Measuring the Muon Anomalous Magnetic Moment and Electric Dipole Moment". In: *PTEP* 2019.5 (2019), p. 053C02. DOI: 10.1093/ptep/ptz030. arXiv: 1901.03047 [physics.ins-det].

[Abi+21] B. Abi et al. "Measurement of the Positive Muon Anomalous Magnetic Moment to 0.46 ppm". In: *Phys. Rev. Lett.* 126 (14 2021), p. 141801. DOI: 10.1103/PhysRevLett.126.141801.

[Adl69] Stephen L. Adler. "Axial-Vector Vertex in Spinor Electrodynamics". In: *Phys. Rev.* 177 (5 1969), pp. 2426–2438. DOI: 10.1103/PhysRev.177.2426.

[Adl81] Stephen L. Adler. "An Overrelaxation Method for the Monte Carlo Evaluation of the Partition Function for Multiquadratic Actions". In: *Phys. Rev. D* 23 (1981), p. 2901. DOI: 10.1103/PhysRevD.23.2901.

[Aoy+20] T. Aoyama et al. "The anomalous magnetic moment of the muon in the Standard Model". In: *Phys. Rept.* 887 (2020), pp. 1–166. DOI: 10.1016/j.physrep.2020.07.006. arXiv: 2006.04822 [hep-ph].

[Asm+16] Nils Asmussen et al. "Position-space approach to hadronic light-by-light scattering in the muon $g-2$ on the lattice". In: *PoS* LATTICE2016 (2016), p. 164. DOI: 10.22323/1.256.0164. arXiv: 1609.08454 [hep-lat].

[Asm+18] Nils Asmussen et al. "Exploratory studies for the position-space approach to hadronic light-by-light scattering in the muon $g-2$". In: *EPJ Web Conf.* 175 (2018). Ed. by M. Della Morte et al., p. 06023. DOI: 10.1051/epjconf/201817506023. arXiv: 1711.02466 [hep-lat].

[Asm+19] Nils Asmussen et al. "Developments in the position-space approach to the HLbL contribution to the muon $g-2$ on the lattice". In: *PoS* LATTICE2019 (2019), p. 195. DOI: 10.22323/1.363.0195. arXiv: 1911.05573 [hep-lat].

[Aub+20] Christopher Aubin et al. "Light quark vacuum polarization at the physical point and contribution to the muon $g-2$". In: *Phys. Rev.* D101.1 (2020), p. 014503. DOI: 10.1103/PhysRevD.101.014503. arXiv: 1905.09307 [hep-lat].

[BB88] Carlos A. Bertulani and Gerhard Baur. "Electromagnetic processes in relativistic heavy ion collisions". In: *Physics Reports* 163.5 (1988), pp. 299–408. ISSN: 0370-1573. DOI: https://doi.org/10.1016/0370-1573(88)90142-1.

[BCS10] Gunnar S. Bali, Sara Collins, and Andreas Schafer. "Effective noise reduction techniques for disconnected loops in Lattice QCD". In: *Comput. Phys. Commun.* 181 (2010), pp. 1570–1583. DOI: 10.1016/j.cpc.2010.05.008. arXiv: 0910.3970 [hep-lat].

[Bel+75] A. A. Belavin et al. "Pseudoparticle Solutions of the Yang-Mills Equations". In: *Phys. Lett. B* 59 (1975). Ed. by J. C. Taylor, pp. 85–87. DOI: 10.1016/0370-2693(75)90163-X.

[Ben+06] G. W. Bennett et al. "Final Report of the Muon E821 Anomalous Magnetic Moment Measurement at BNL". In: *Phys. Rev. D* 73 (2006), p. 072003. DOI: 10.1103/PhysRevD.73.072003. arXiv: hep-ex/0602035.

[BG14] Oliver Bar and Maarten Golterman. "Chiral perturbation theory for gradient flow observables". In: *Phys. Rev. D* 89.3 (2014). [Erratum: Phys.Rev.D 89, 099905 (2014)], p. 034505. DOI: 10.1103/PhysRevD.89.034505. arXiv: 1312.4999 [hep-lat].

[BG92] Claude W. Bernard and Maarten F. L. Golterman. "Chiral perturbation theory for the quenched approximation of QCD". In: *Phys. Rev. D* 46 (1992), pp. 853–857. DOI: 10.1103/PhysRevD.46.853. arXiv: hep-lat/9204007.

[BG94] Claude W. Bernard and Maarten F. L. Golterman. "Partially quenched gauge theories and an application to staggered fermions". In: *Phys. Rev. D* 49 (1994), pp. 486–494. DOI: 10.1103/PhysRevD.49.486. arXiv: hep-lat/9306005.

[Bha+06] Tanmoy Bhattacharya et al. "Improved bilinears in lattice QCD with non-degenerate quarks". In: *Phys. Rev. D* 73 (2006), p. 034504. DOI: 10.1103/PhysRevD.73.034504. arXiv: hep-lat/0511014.

[BHTRS19] Johan Bijnens, Nils Hermansson-Truedsson, and Antonio Rodríguez-Sánchez. "Short-distance constraints for the HLbL contribution to the muon anomalous magnetic moment". In: *Phys. Lett.* B798 (2019), p. 134994. DOI: 10.1016/j.physletb.2019.134994. arXiv: 1908.03331 [hep-ph].

[Bie+11] W. Bietenholz et al. "Flavour blindness and patterns of flavour symmetry breaking in lattice simulations of up, down and strange quarks". In: *Phys. Rev. D* 84 (2011), p. 054509. DOI: 10.1103/PhysRevD.84.054509. arXiv: 1102.5300 [hep-lat].

[BIS13] Thomas Blum, Taku Izubuchi, and Eigo Shintani. "New class of variance-reduction techniques using lattice symmetries". In: *Phys. Rev. D* 88.9 (2013), p. 094503. DOI: 10.1103/PhysRevD.88.094503. arXiv: 1208.4349 [hep-lat].

[BJ69] J. S. Bell and R. Jackiw. "A PCAC puzzle: $\pi^0 \to \gamma\gamma$ in the σ model". In: *Nuovo Cim. A* 60 (1969), pp. 47–61. DOI: 10.1007/BF02823296.

[BKS17] Mattia Bruno, Tomasz Korzec, and Stefan Schaefer. "Setting the scale for the CLS 2 + 1 flavor ensembles". In: *Phys. Rev. D* 95.7 (2017), p. 074504. DOI: 10.1103/PhysRevD.95.074504. arXiv: 1608.08900 [hep-lat].

[Blu03] T. Blum. "Lattice calculation of the lowest order hadronic contribution to the muon anomalous magnetic moment". In: *Phys. Rev. Lett.* 91 (2003), p. 052001. DOI: 10.1103/PhysRevLett.91.052001. arXiv: hep-lat/0212018.

[Blu+15] Thomas Blum et al. "Hadronic light-by-light scattering contribution to the muon anomalous magnetic moment from lattice QCD". In: *Phys. Rev. Lett.* 114.1 (2015), p. 012001. DOI: 10.1103/PhysRevLett.114.012001. arXiv: 1407.2923 [hep-lat].

[Blu+16] Thomas Blum et al. "Lattice Calculation of Hadronic Light-by-Light Contribution to the Muon Anomalous Magnetic Moment". In: *Phys. Rev. D* 93.1 (2016), p. 014503. DOI: 10.1103/PhysRevD.93.014503. arXiv: 1510.07100 [hep-lat].

[Blu+17] Thomas Blum et al. "Using infinite volume, continuum QED and lattice QCD for the hadronic light-by-light contribution to the muon anomalous magnetic moment". In: *Phys. Rev. D* 96.3 (2017), p. 034515. DOI: 10.1103/PhysRevD.96.034515. arXiv: 1705.01067 [hep-lat].

[Blu+18] T. Blum et al. "Calculation of the hadronic vacuum polarization contribution to the muon anomalous magnetic moment". In: *Phys. Rev. Lett.* 121.2 (2018), p. 022003. DOI: 10.1103/PhysRevLett.121.022003. arXiv: 1801.07224 [hep-lat].

[Blu+20] Thomas Blum et al. "Hadronic Light-by-Light Scattering Contribution to the Muon Anomalous Magnetic Moment from Lattice QCD". In: *Phys. Rev. Lett.* 124.13 (2020), p. 132002. DOI: 10.1103/PhysRevLett.124.132002. arXiv: 1911.08123 [hep-lat].

[BM11] David Bernecker and Harvey B. Meyer. "Vector Correlators in Lattice QCD: Methods and applications". In: *Eur. Phys. J. A* 47 (2011), p. 148. DOI: 10.1140/epja/i2011-11148-6. arXiv: 1107.4388 [hep-lat].

[Boc+85] Marco Bochicchio et al. "Chiral Symmetry on the Lattice with Wilson Fermions". In: *Nucl. Phys. B* 262 (1985), p. 331. DOI: 10.1016/0550-3213(85)90290-1.

[Bor+18] Sz. Borsanyi et al. "Hadronic vacuum polarization contribution to the anomalous magnetic moments of leptons from first principles". In: *Phys. Rev. Lett.* 121.2 (2018), p. 022002. DOI: 10.1103/PhysRevLett.121.022002. arXiv: 1711.04980 [hep-lat].

[Bor+21] Sz. Borsanyi et al. "Leading hadronic contribution to the muon magnetic moment from lattice QCD". In: *Nature* 593.7857 (2021), pp. 51–55. DOI: 10.1038/s41586-021-03418-1. arXiv: 2002.12347 [hep-lat].

[Boy+08] P. A. Boyle et al. "Use of stochastic sources for the lattice determination of light quark physics". In: *JHEP* 08 (2008), p. 086. DOI: 10.1088/1126-6708/2008/08/086. arXiv: 0804.1501 [hep-lat].

[BPP95] Johan Bijnens, Elisabetta Pallante, and Joaquim Prades. "Hadronic light by light contributions to the muon g-2 in the large N(c) limit". In: *Phys. Rev. Lett.* 75 (1995). [Erratum: Phys.Rev.Lett. 75, 3781 (1995)], pp. 1447–1450. DOI: 10.1103/PhysRevLett.75.1447. arXiv: hep-ph/9505251.

[BR16a] Johan Bijnens and Johan Relefors. "Connected, Disconnected and Strange Quark Contributions to HVP". In: *JHEP* 11 (2016), p. 086. DOI: 10.1007/JHEP11(2016)086. arXiv: 1609.01573 [hep-lat].

[BR16b] Johan Bijnens and Johan Relefors. "Pion light-by-light contributions to the muon $g-2$". In: *JHEP* 09 (2016), p. 113. DOI: 10.1007/JHEP09(2016)113. arXiv: 1608.01454 [hep-ph].

[BR68] Stanley J. Brodsky and Eduardo de Rafael. "Suggested Boson-Lepton Pair Couplings and the Anomalous Magnetic Moment of the Muon". In: *Phys. Rev.* 168 (5 1968), pp. 1620–1622. DOI: 10.1103/PhysRev.168.1620.

[Bru+15] Mattia Bruno et al. "Simulation of QCD with $N_f = 2 + 1$ flavors of non-perturbatively improved Wilson fermions". In: *JHEP* 02 (2015), p. 043. DOI: 10.1007/JHEP02(2015)043. arXiv: 1411.3982 [hep-lat].

[BS13] John Bulava and Stefan Schaefer. "Improvement of $N_f = 3$ lattice QCD with Wilson fermions and tree-level improved gauge action". In: *Nucl. Phys. B* 874 (2013), pp. 188–197. DOI: 10.1016/j.nuclphysb.2013.05.019. arXiv: 1304.7093 [hep-lat].

[BT68] W. A. Bardeen and Wu-Ki Tung. "Invariant Amplitudes for Photon Processes". In: *Phys. Rev.* 173 (5 1968), pp. 1423–1433. DOI: 10.1103/PhysRev.173.1423.

[C+] M. Cè et al. in preparation.

[Cap+99] Stefano Capitani et al. "Non-perturbative quark mass renormalization in quenched lattice QCD". In: *Nucl. Phys. B* 544 (1999). [Erratum: Nucl.Phys.B 582, 762–762 (2000)], pp. 669–698. DOI: 10.1016/S0550-3213(98)00857-8. arXiv: hep-lat/9810063.

[Cha+14] Bipasha Chakraborty et al. "Strange and charm quark contributions to the anomalous magnetic moment of the muon". In: *Phys. Rev. D* 89.11 (2014), p. 114501. DOI: 10.1103/PhysRevD.89.114501. arXiv: 1403.1778 [hep-lat].

[Cha+18] B. Chakraborty et al. "Strong-Isospin-Breaking Correction to the Muon Anomalous Magnetic Moment from Lattice QCD at the Physical Point". In: *Phys. Rev. Lett.* 120.15 (2018), p. 152001. DOI: 10.1103/PhysRevLett.120.152001. arXiv: 1710.11212 [hep-lat].

[Cha+20] En-Hung Chao et al. "Hadronic light-by-light contribution to $(g-2)_\mu$ from lattice QCD with SU(3) flavor symmetry". In: *Eur. Phys. J. C* 80.9 (2020), p. 869. DOI: 10.1140/epjc/s10052-020-08444-3. arXiv: 2006.16224 [hep-lat].

[Cha+21] En-Hung Chao et al. "Hadronic light-by-light contribution to $(g-2)_\mu$ from lattice QCD: a complete calculation". In: *Eur. Phys. J. C* 81.7 (2021), p. 651. DOI: 10.1140/epjc/s10052-021-09455-4. arXiv: 2104.02632 [hep-lat].

[Chi73] J. S. R. Chisholm. "Rational Approximants Defined from Double Power Series". In: *Mathematics of Computation* 27.124 (1973), pp. 841–848. ISSN: 00255718, 10886842.

[CHS19] Gilberto Colangelo, Martin Hoferichter, and Peter Stoffer. "Two-pion contribution to hadronic vacuum polarization". In: *JHEP* 02 (2019), p. 006. DOI: 10.1007/JHEP02(2019)006. arXiv: 1810.00007 [hep-ph].

[CK07] M. A. Clark and A. D. Kennedy. "Accelerating dynamical fermion computations using the rational hybrid Monte Carlo (RHMC) algorithm with multiple pseudofermion fields". In: *Phys. Rev. Lett.* 98 (2007), p. 051601. DOI: 10.1103/PhysRevLett.98.051601. arXiv: hep-lat/0608015.

[CKT80] K. G. Chetyrkin, A. L. Kataev, and F. V. Tkachov. "New Approach to Evaluation of Multiloop Feynman Integrals: The Gegenbauer Polynomial x Space Technique". In: *Nucl. Phys. B* 174 (1980), pp. 345–377. DOI: 10.1016/0550-3213(80)90289-8.

[CM82] N. Cabibbo and E. Marinari. "A New Method for Updating SU(N) Matrices in Computer Simulations of Gauge Theories". In: *Phys. Lett. B* 119 (1982), pp. 387–390. DOI: 10.1016/0370-2693(82)90696-7.

[CMK74] J. S. R. Chisholm, J. Mcewan, and Nicholas Kemmer. "Rational approximants defined from power series in N variables". In: *Proceedings of the Royal Society of London. A. Mathematical and Physical Sciences* 336.1607 (1974), pp. 421–452. DOI: 10.1098/rspa.1974.0028. eprint: https://royalsocietypublishing.org/doi/pdf/10.1098/rspa.1974.0028.

[Col+14a] Gilberto Colangelo et al. "Dispersive approach to hadronic light-by-light scattering". In: *JHEP* 09 (2014), p. 091. DOI: 10.1007/JHEP09(2014)091. arXiv: 1402.7081 [hep-ph].

[Col+14b] Gilberto Colangelo et al. "Remarks on higher-order hadronic corrections to the muon $g-2$". In: *Phys. Lett.* B735 (2014), pp. 90–91. DOI: 10.1016/j.physletb.2014.06.012. arXiv: 1403.7512 [hep-ph].

[Col+15] Gilberto Colangelo et al. "Dispersion relation for hadronic light-by-light scattering: theoretical foundations". In: *JHEP* 09 (2015), p. 074. DOI: 10.1007/JHEP09(2015)074. arXiv: 1506.01386 [hep-ph].

[Col+17] Gilberto Colangelo et al. "Dispersion relation for hadronic light-by-light scattering: two-pion contributions". In: *JHEP* 04 (2017), p. 161. DOI: 10.1007/JHEP04(2017)161. arXiv: 1702.07347 [hep-ph].

[Col+20] Gilberto Colangelo et al. "Longitudinal short-distance constraints for the hadronic light-by-light contribution to $(g-2)_\mu$ with large-N_c Regge models". In: *JHEP* 03 (2020), p. 101. DOI: 10.1007/JHEP03(2020)101. arXiv: 1910.13432 [hep-ph].

[Cre80] M. Creutz. "Monte Carlo Study of Quantized SU(2) Gauge Theory". In: *Phys. Rev. D* 21 (1980), pp. 2308–2315. DOI: 10.1103/PhysRevD.21.2308.

[Dal51] R H Dalitz. "On an Alternative Decay Process for the Neutral -Meson". In: *Proceedings of the Physical Society. Section A* 64.7 (1951), pp. 667–669. DOI: 10.1088/0370-1298/64/7/115.

[Dav+17] Michel Davier et al. "Reevaluation of the hadronic vacuum polarisation contributions to the Standard Model predictions of the muon $g-2$ and $\alpha(m_Z^2)$ using newest hadronic cross-section data". In: *Eur. Phys. J.* C77.12 (2017), p. 827. DOI: 10.1140/epjc/s10052-017-5161-6. arXiv: 1706.09436 [hep-ph].

[Dav+20a] M. Davier et al. "A new evaluation of the hadronic vacuum polarisation contributions to the muon anomalous magnetic moment and to $\boldsymbol{\alpha(m_Z^2)}$". In: *Eur. Phys. J.* C80.3 (2020). [Erratum: Eur. Phys. J. **C80**, 410 (2020)], p. 241. DOI: 10.1140/epjc/s10052-020-7792-2. arXiv: 1908.00921 [hep-ph].

[Dav+20b] C. T. H. Davies et al. "Hadronic-vacuum-polarization contribution to the muon's anomalous magnetic moment from four-flavor lattice QCD". In: *Phys. Rev.* D101.3 (2020), p. 034512. DOI: 10.1103/PhysRevD.101.034512. arXiv: 1902.04223 [hep-lat].

[DDPV02] Luigi Del Debbio, Haralambos Panagopoulos, and Ettore Vicari. "theta dependence of SU(N) gauge theories". In: *JHEP* 08 (2002), p. 044. DOI: 10.1088/1126-6708/2002/08/044. arXiv: hep-th/0204125.

[DHS21] Igor Danilkin, Martin Hoferichter, and Peter Stoffer. "A dispersive estimate of scalar contributions to hadronic light-by-light scattering". In: *Phys. Lett. B* 820 (2021), p. 136502. DOI: 10.1016/j.physletb.2021.136502. arXiv: 2105.01666 [hep-ph].

[DMJ10] Michele Della Morte and Andreas Juttner. "Quark disconnected diagrams in chiral perturbation theory". In: *JHEP* 11 (2010), p. 154. DOI: 10.1007/JHEP11(2010)154. arXiv: 1009.3783 [hep-lat].

[DTWL06] W. Detmold, B. C. Tiburzi, and Andre Walker-Loud. "Electromagnetic and spin polarisabilities in lattice QCD". In: *Phys. Rev. D* 73 (2006), p. 114505. DOI: 10.1103/PhysRevD.73.114505. arXiv: hep-lat/0603026.

[Dua+87] S. Duane et al. "Hybrid Monte Carlo". In: *Phys. Lett. B* 195 (1987), pp. 216–222. DOI: 10.1016/0370-2693(87)91197-X.

[DV17] Igor Danilkin and Marc Vanderhaeghen. "Light-by-light scattering sum rules in light of new data". In: *Phys. Rev.* D95.1 (2017), p. 014019. DOI: 10.1103/PhysRevD.95.014019. arXiv: 1611.04646 [hep-ph].

[Edm55] A. R. Edmonds. "Angular momentum in quantum mechanics". In: (Nov. 1955). DOI: 10.5170/CERN-1955-026.

[Efr79] B. Efron. "Bootstrap Methods: Another Look at the Jackknife". In: *The Annals of Statistics* 7.1 (1979), pp. 1 –26. DOI: 10.1214/aos/1176344552.

[Efr82] Bradley Efron. *The Jackknife, the bootstrap and other resampling plans*. CBMS-NSF regional conference series in applied mathematics. Lectures given at Bowling Green State Univ., June 1980. Philadelphia, PA: SIAM, 1982.

[EFW20] Gernot Eichmann, Christian S. Fischer, and Richard Williams. "Kaon-box contribution to the anomalous magnetic moment of the muon". In: *Phys. Rev.* D101.5 (2020), p. 054015. DOI: 10.1103/PhysRevD.101.054015. arXiv: 1910.06795 [hep-ph].

[Fer25] Enrico Fermi. "On the theory of collisions between atoms and electrically charged particles". In: *Nuovo Cim.* 2 (1925). Ed. by W. J. Marciano and S. White, pp. 143–158. DOI: 10.1007/BF02961914. arXiv: hep-th/0205086.

[FJ05] Phillipe de Forcrand and Oliver Jahn. "Monte Carlo overrelaxation for SU(N) gauge theories". In: *3rd International Workshop on Numerical Analysis and Lattice QCD*. Mar. 2005. arXiv: hep-lat/0503041.

[FKS98] T. Feldmann, P. Kroll, and B. Stech. "Mixing and decay constants of pseudoscalar mesons". In: *Phys. Rev. D* 58 (1998), p. 114006. DOI: 10.1103/PhysRevD.58.114006. arXiv: hep-ph/9802409.

[FM99] M. Foster and Christopher Michael. "Quark mass dependence of hadron masses from lattice QCD". In: *Phys. Rev. D* 59 (1999), p. 074503. DOI: 10.1103/PhysRevD.59.074503. arXiv: hep-lat/9810021.

[Fol+05] Justin Foley et al. "Practical all-to-all propagators for lattice QCD". In: *Comput. Phys. Commun.* 172 (2005), pp. 145–162. DOI: 10.1016/j.cpc.2005.06.008. arXiv: hep-lat/0505023.

[Fri82] D. Friedan. "A PROOF OF THE NIELSEN-NINOMIYA THEOREM". In: *Commun. Math. Phys.* 85 (1982), pp. 481–490. DOI: 10.1007/BF01403500.

[FSS96] L. Frappat, P. Sorba, and A. Sciarrino. "Dictionary on Lie superalgebras". In: (July 1996). arXiv: hep-th/9607161.

[G+18] Antoine Gérardin et al. "Hadronic light-by-light scattering amplitudes from lattice QCD versus dispersive sum rules". In: *Phys. Rev. D* 98.7 (2018), p. 074501. DOI: 10.1103/PhysRevD.98.074501. arXiv: 1712.00421 [hep-lat].

[G+19] Antoine Gérardin et al. "The leading hadronic contribution to $(g-2)_\mu$ from lattice QCD with $N_f = 2+1$ flavours of O(a) improved Wilson quarks". In: *Phys. Rev.* D100.1 (2019), p. 014510. DOI: 10.1103/PhysRevD.100.014510. arXiv: 1904.03120 [hep-lat].

[Gam+20] P. Gambino et al. "Challenges in semileptonic B decays". In: *Eur. Phys. J. C* 80.10 (2020), p. 966. DOI: 10.1140/epjc/s10052-020-08490-x. arXiv: 2006.07287 [hep-ph].

[GHM19] Antoine Gerardin, Tim Harris, and Harvey B. Meyer. "Nonperturbative renormalization and $O(a)$-improvement of the nonsinglet vector current with $N_f = 2+1$ Wilson fermions and tree-level Symanzik improved gauge action". In: *Phys. Rev. D* 99.1 (2019), p. 014519. DOI: 10.1103/PhysRevD.99.014519. arXiv: 1811.08209 [hep-lat].

[Giu+19a] D. Giusti et al. "Electromagnetic and strong isospin-breaking corrections to the muon $g-2$ from Lattice QCD+QED". In: *Phys. Rev.* D99.11 (2019), p. 114502. DOI: 10.1103/PhysRevD.99.114502. arXiv: 1901.10462 [hep-lat].

[Giu+19b] Leonardo Giusti et al. "Frequency-splitting estimators of single-propagator traces". In: *Eur. Phys. J. C* 79.7 (2019), p. 586. DOI: 10.1140/epjc/s10052-019-7049-0. arXiv: 1903.10447 [hep-lat].

[GL09] Leonardo Giusti and Martin Luscher. "Chiral symmetry breaking and the Banks-Casher relation in lattice QCD with Wilson quarks". In: *JHEP* 03 (2009), p. 013. DOI: 10.1088/1126-6708/2009/03/013. arXiv: 0812.3638 [hep-lat].

[GL10] Christof Gattringer and Christian B. Lang. *Quantum chromodynamics on the lattice*. Vol. 788. Berlin: Springer, 2010. ISBN: 978-3-642-01849-7, 978-3-642-01850-3. DOI: 10.1007/978-3-642-01850-3.

[GL84] J. Gasser and H. Leutwyler. "Chiral Perturbation Theory to One Loop". In: *Annals Phys.* 158 (1984), p. 142. DOI: 10.1016/0003-4916(84)90242-2.

[GL85] J. Gasser and H. Leutwyler. "Chiral perturbation theory: Expansions in the mass of the strange quark". In: *Nuclear Physics B* 250.1 (1985), pp. 465–516. ISSN: 0550-3213. DOI: https://doi.org/10.1016/0550-3213(85)90492-4.

[GMN19] Antoine Gérardin, Harvey B. Meyer, and Andreas Nyffeler. "Lattice calculation of the pion transition form factor with $N_f = 2 + 1$ Wilson quarks". In: *Phys. Rev.* D100.3 (2019), p. 034520. DOI: 10.1103/PhysRevD.100.034520. arXiv: 1903.09471 [hep-lat].

[Gol09] Maarten Golterman. "Applications of chiral perturbation theory to lattice QCD". In: *Les Houches Summer School: Session 93: Modern perspectives in lattice QCD: Quantum field theory and high performance computing*. Dec. 2009. arXiv: 0912.4042 [hep-lat].

[Gre+16] Jeremy Green et al. "Direct calculation of hadronic light-by-light scattering". In: *PoS* LATTICE2015 (2016), p. 109. arXiv: 1510.08384 [hep-lat].

[GS19] D. Giusti and S. Simula. "Lepton anomalous magnetic moments in Lattice QCD+QED". In: *PoS* LATTICE2019 (2019), p. 104. DOI: 10.22323/1.363.0104. arXiv: 1910.03874 [hep-lat].

[GW82] Paul H. Ginsparg and Kenneth G. Wilson. "A remnant of chiral symmetry on the lattice". In: *Phys. Rev. D* 25 (10 1982), pp. 2649–2657. DOI: 10.1103/PhysRevD.25.2649.

[Has01] Martin Hasenbusch. "Speeding up the hybrid Monte Carlo algorithm for dynamical fermions". In: *Phys. Lett. B* 519 (2001), pp. 177–182. DOI: 10.1016/S0370-2693(01)01102-9. arXiv: hep-lat/0107019.

[Has70] W. K. Hastings. "Monte Carlo Sampling Methods Using Markov Chains and Their Applications". In: *Biometrika* 57 (1970), pp. 97–109. DOI: 10.1093/biomet/57.1.97.

[Hay+06] Masashi Hayakawa et al. "Hadronic light-by-light scattering contribution to the muon g-2 from lattice QCD: Methodology". In: *PoS* LAT2005 (2006). Ed. by Christopher Michael, p. 353. DOI: 10.22323/1.020.0353. arXiv: hep-lat/0509016.

[HHK19] Martin Hoferichter, Bai-Long Hoid, and Bastian Kubis. "Three-pion contribution to hadronic vacuum polarization". In: *JHEP* 08 (2019), p. 137. DOI: 10.1007/JHEP08(2019)137. arXiv: 1907.01556 [hep-ph].

[HJ03] M. Hasenbusch and K. Jansen. "Speeding up lattice QCD simulations with clover improved Wilson fermions". In: *Nucl. Phys. B* 659 (2003), pp. 299–320. DOI: 10.1016/S0550-3213(03)00227-X. arXiv: hep-lat/0211042.

[HKS95] M. Hayakawa, T. Kinoshita, and A. I. Sanda. "Hadronic light by light scattering effect on muon g-2". In: *Phys. Rev. Lett.* 75 (1995), pp. 790–793. DOI: 10.1103/PhysRevLett.75.790. arXiv: hep-ph/9503463.

[Hof+18a] Martin Hoferichter et al. "Dispersion relation for hadronic light-by-light scattering: pion pole". In: *JHEP* 10 (2018), p. 141. DOI: 10.1007/JHEP10(2018)141. arXiv: 1808.04823 [hep-ph].

[Hof+18b] Martin Hoferichter et al. "Pion-pole contribution to hadronic light-by-light scattering in the anomalous magnetic moment of the muon". In: *Phys. Rev. Lett.* 121.11 (2018), p. 112002. DOI: 10.1103/PhysRevLett.121.112002. arXiv: 1805.01471 [hep-ph].

[HPR08] C. Hanhart, J. R. Pelaez, and G. Rios. "Quark mass dependence of the rho and sigma from dispersion relations and Chiral Perturbation Theory". In: *Phys. Rev. Lett.* 100 (2008), p. 152001. DOI: 10.1103/PhysRevLett.100.152001. arXiv: 0801.2871 [hep-ph].

[HPR14] C. Hanhart, J. R. Pelaez, and G. Rios. "Remarks on pole trajectories for resonances". In: *Phys. Lett. B* 739 (2014), pp. 375–382. DOI: 10.1016/j.physletb.2014.11.011. arXiv: 1407.7452 [hep-ph].

[HU08] Masashi Hayakawa and Shunpei Uno. "QED in finite volume and finite size scaling effect on electromagnetic properties of hadrons". In: *Prog. Theor. Phys.* 120 (2008), pp. 413–441. DOI: 10.1143/PTP.120.413. arXiv: 0804.2044 [hep-ph].

[Iwa83] Y. Iwasaki. "Renormalization Group Analysis of Lattice Theories and Improved Lattice Action. II. Four-dimensional non-Abelian SU(N) gauge model". In: (Dec. 1983). arXiv: 1111.7054 [hep-lat].

[Jeg17] Friedrich Jegerlehner. "The Anomalous Magnetic Moment of the Muon". In: *Springer Tracts Mod. Phys.* 274 (2017), pp. 1–693. DOI: 10.1007/978-3-319-63577-4.

[JMU08] K. Jansen, Christopher Michael, and C. Urbach. "The η' meson from lattice QCD". In: *Eur. Phys. J. C* 58 (2008), pp. 261–269. DOI: 10.1140/epjc/s10052-008-0764-6. arXiv: 0804.3871 [hep-lat].

[JN09] Fred Jegerlehner and Andreas Nyffeler. "The Muon g-2". In: *Phys. Rept.* 477 (2009), pp. 1–110. DOI: 10.1016/j.physrep.2009.04.003. arXiv: 0902.3360 [hep-ph].

[Jon76] R.Hughes Jones. "General rational approximants in N-variables". In: *Journal of Approximation Theory* 16.3 (1976), pp. 201–233. ISSN: 0021-9045. DOI: https://doi.org/10.1016/0021-9045(76)90050-2.

[KHS99] A. D. Kennedy, Ivan Horvath, and Stefan Sint. "A New exact method for dynamical fermion computations with nonlocal actions". In: *Nucl. Phys. B Proc. Suppl.* 73 (1999). Ed. by Thomas A. DeGrand et al., pp. 834–836. DOI: 10.1016/S0920-5632(99)85217-7. arXiv: hep-lat/9809092.

[KL00] Roland Kaiser and H. Leutwyler. "Large N(c) in chiral perturbation theory". In: *Eur. Phys. J. C* 17 (2000), pp. 623–649. DOI: 10.1007/s100520000499. arXiv: hep-ph/0007101.

[KN02] Marc Knecht and Andreas Nyffeler. "Hadronic light by light corrections to the muon g-2: The Pion pole contribution". In: *Phys. Rev. D* 65 (2002), p. 073034. DOI: 10.1103/PhysRevD.65.073034. arXiv: hep-ph/0111058.

[Kne+18] M. Knecht et al. "Scalar meson contributions to a_μ from hadronic light-by-light scattering". In: *Phys. Lett.* B787 (2018), pp. 111–123. DOI: 10.1016/j.physletb.2018.10.048. arXiv: 1808.03848 [hep-ph].

[KNO85] T. Kinoshita, B. Niić, and Y. Okamoto. "Hadronic contributions to the anomalous magnetic moment of the muon". In: *Phys. Rev. D* 31 (8 1985), pp. 2108–2119. DOI: 10.1103/PhysRevD.31.2108.

[KNT18] Alexander Keshavarzi, Daisuke Nomura, and Thomas Teubner. "Muon $g-2$ and $\alpha(M_Z^2)$: a new data-based analysis". In: *Phys. Rev.* D97.11 (2018), p. 114025. DOI: 10.1103/PhysRevD.97.114025. arXiv: 1802.02995 [hep-ph].

[KNT20] Alexander Keshavarzi, Daisuke Nomura, and Thomas Teubner. "The $g-2$ of charged leptons, $\alpha(M_Z^2)$ and the hyperfine splitting of muonium". In: *Phys. Rev.* D101 (2020), p. 014029. DOI: 10.1103/PhysRevD.101.014029. arXiv: 1911.00367 [hep-ph].

[KP85] A. D. Kennedy and B. J. Pendleton. "Improved Heat Bath Method for Monte Carlo Calculations in Lattice Gauge Theories". In: *Phys. Lett. B* 156 (1985), pp. 393–399. DOI: 10.1016/0370-2693(85)91632-6.

[Kur+14] Alexander Kurz et al. "Hadronic contribution to the muon anomalous magnetic moment to next-to-next-to-leading order". In: *Phys. Lett.* B734 (2014), pp. 144–147. DOI: 10.1016/j.physletb.2014.05.043. arXiv: 1403.6400 [hep-ph].

[LÏ0] Martin Lüscher. "Properties and uses of the Wilson flow in lattice QCD". In: *JHEP* 08 (2010). [Erratum: JHEP 03, 092 (2014)], p. 071. DOI: 10.1007/JHEP08(2010)071. arXiv: 1006.4518 [hep-lat].

[Lar+11] I. Larin et al. "A New Measurement of the π^0 Radiative Decay Width". In: *Phys. Rev. Lett.* 106 (2011), p. 162303. DOI: 10.1103/PhysRevLett.106.162303. arXiv: 1009.1681 [nucl-ex].

[Lar+20] I. Larin et al. "Precision measurement of the neutral pion lifetime". In: *Science* 368.6490 (2020), pp. 506–509. DOI: 10.1126/science.aay6641.

[LB80] G. Peter Lepage and Stanley J. Brodsky. "Exclusive processes in perturbative quantum chromodynamics". In: *Phys. Rev. D* 22 (9 1980), pp. 2157–2198. DOI: 10.1103/PhysRevD.22.2157.

[LP08] Martin Luscher and Filippo Palombi. "Fluctuations and reweighting of the quark determinant on large lattices". In: *PoS* LATTICE2008 (2008). Ed. by Christopher Aubin et al., p. 049. DOI: 10.22323/1.066.0049. arXiv: 0810.0946 [hep-lat].

[LPd72] B.E. Lautrup, A. Peterman, and E. de Rafael. "Recent developments in the comparison between theory and experiments in quantum electrodynamics". In: *Physics Reports* 3.4 (1972), pp. 193–259. ISSN: 0370-1573. DOI: https://doi.org/10.1016/0370-1573(72)90011-7.

[LR68] B. E. Lautrup and E. de Rafael. "Calculation of the Sixth-Order Contribution from the Fourth-Order Vacuum Polarization to the Difference of the Anomalous Magnetic Moments of Muon and Electron". In: *Phys. Rev.* 174 (5 1968), pp. 1835–1842. DOI: 10.1103/PhysRev.174.1835.

[LS11] Martin Luscher and Stefan Schaefer. "Lattice QCD without topology barriers". In: *JHEP* 07 (2011), p. 036. DOI: 10.1007/JHEP07(2011)036. arXiv: 1105.4749 [hep-lat].

[LS13] Martin Luscher and Stefan Schaefer. "Lattice QCD with open boundary conditions and twisted-mass reweighting". In: *Comput. Phys. Commun.* 184 (2013), pp. 519–528. DOI: 10.1016/j.cpc.2012.10.003. arXiv: 1206.2809 [hep-lat].

[Lus04] Martin Luscher. "Solution of the Dirac equation in lattice QCD using a domain decomposition method". In: *Comput. Phys. Commun.* 156 (2004), pp. 209–220. DOI: 10.1016/S0010-4655(03)00486-7. arXiv: hep-lat/0310048.

[Lus07] Martin Luscher. "Local coherence and deflation of the low quark modes in lattice QCD". In: *JHEP* 07 (2007), p. 081. DOI: 10.1088/1126-6708/2007/07/081. arXiv: 0706.2298 [hep-lat].

[Lus10a] Martin Luscher. "Computational Strategies in Lattice QCD". In: *Les Houches Summer School: Session 93: Modern perspectives in lattice QCD: Quantum field theory and high performance computing*. Feb. 2010. arXiv: 1002.4232 [hep-lat].

[Lus10b] Martin Luscher. "Trivializing maps, the Wilson flow and the HMC algorithm". In: *Commun. Math. Phys.* 293 (2010), pp. 899–919. DOI: 10.1007/s00220-009-0953-7. arXiv: 0907.5491 [hep-lat].

[Lus82] M. Luscher. "Topology of Lattice Gauge Fields". In: *Commun. Math. Phys.* 85 (1982), p. 39. DOI: 10.1007/BF02029132.

[Lus+96] Martin Luscher et al. "Chiral symmetry and O(a) improvement in lattice QCD". In: *Nucl. Phys. B* 478 (1996), pp. 365–400. DOI: 10.1016/0550-3213(96)00378-1. arXiv: hep-lat/9605038.

[Lus+97] Martin Luscher et al. "Nonperturbative O(a) improvement of lattice QCD". In: *Nucl. Phys. B* 491 (1997), pp. 323–343. DOI: 10.1016/S0550-3213(97)00080-1. arXiv: hep-lat/9609035.

[LW85] M. Luscher and P. Weisz. "On-Shell Improved Lattice Gauge Theories". In: *Commun. Math. Phys.* 97 (1985). [Erratum: Commun.Math.Phys. 98, 433 (1985)], p. 59. DOI: 10.1007/BF01206178.

[LW96] M. Luscher and P. Weisz. "O(a) improvement of the axial current in lattice QCD to one loop order of perturbation theory". In: *Nucl. Phys. B* 479 (1996), pp. 429–458. DOI: 10.1016/0550-3213(96)00448-8. arXiv: hep-lat/9606016.

[Met+53] N. Metropolis et al. "Equation of state calculations by fast computing machines". In: *J. Chem. Phys.* 21 (1953), pp. 1087–1092. DOI: 10.1063/1.1699114.

[MK33] L. Meitner and H. Kösters. "Über die Streuung kurzwelliger γ-Strahlen". In: *Z. Phys.* 84.3-4 (1933), pp. 137–144. DOI: 10.1007/BF01333827.

[MM06] C. McNeile and Christopher Michael. "Decay width of light quark hybrid meson from the lattice". In: *Phys. Rev. D* 73 (2006), p. 074506. DOI: 10.1103/PhysRevD.73.074506. arXiv: hep-lat/0603007.

[Mor+11] Colin Morningstar et al. "Improved stochastic estimation of quark propagation with Laplacian Heaviside smearing in lattice QCD". In: *Phys. Rev. D* 83 (2011), p. 114505. DOI: 10.1103/PhysRevD.83.114505. arXiv: 1104.3870 [hep-lat].

[MP04] Colin Morningstar and Mike J. Peardon. "Analytic smearing of SU(3) link variables in lattice QCD". In: *Phys. Rev. D* 69 (2004), p. 054501. DOI: 10.1103/PhysRevD.69.054501. arXiv: hep-lat/0311018.

[MS20] Daniel Mohler and Stefan Schaefer. "Remarks on strange-quark simulations with Wilson fermions". In: *Phys. Rev. D* 102.7 (2020), p. 074506. DOI: 10.1103/PhysRevD.102.074506. arXiv: 2003.13359 [hep-lat].

[MSP15] Pere Masjuan and Pablo Sanchez-Puertas. "Phenomenology of bivariate approximants: the $\pi^0 \to e^+e^-$ case and its impact on the electron and muon g-2". In: (Apr. 2015). arXiv: 1504.07001 [hep-ph].

[MSP17] Pere Masjuan and Pablo Sánchez-Puertas. "Pseudoscalar-pole contribution to the $(g_\mu - 2)$: a rational approach". In: *Phys. Rev.* D95.5 (2017), p. 054026. DOI: 10.1103/PhysRevD.95.054026. arXiv: 1701.05829 [hep-ph].

[MV04] Kirill Melnikov and Arkady Vainshtein. "Hadronic light-by-light scattering contribution to the muon anomalous magnetic moment revisited". In: *Phys. Rev.* D70 (2004), p. 113006. DOI: 10.1103/PhysRevD.70.113006. arXiv: hep-ph/0312226 [hep-ph].

[MW19] Harvey B. Meyer and Hartmut Wittig. "Lattice QCD and the anomalous magnetic moment of the muon". In: *Prog. Part. Nucl. Phys.* 104 (2019), pp. 46–96. DOI: 10.1016/j.ppnp.2018.09.001. arXiv: 1807.09370 [hep-lat].

[Neu98a] Herbert Neuberger. "Exactly massless quarks on the lattice". In: *Phys. Lett. B* 417 (1998), pp. 141–144. DOI: 10.1016/S0370-2693(97)01368-3. arXiv: hep-lat/9707022.

[Neu98b] Herbert Neuberger. "More about exactly massless quarks on the lattice". In: *Phys. Lett. B* 427 (1998), pp. 353–355. DOI: 10.1016/S0370-2693(98)00355-4. arXiv: hep-lat/9801031.

[Nic78] B. G. Nickel. "Evaluation of Simple Feynman Graphs". In: *J. Math. Phys.* 19 (1978), pp. 542–548. DOI: 10.1063/1.523697.

[Nic80a] H. Nicolai. "Supersymmetry and Functional Integration Measures". In: *Nucl. Phys. B* 176 (1980), pp. 419–428. DOI: 10.1016/0550-3213(80)90460-5.

[Nic80b] Hermann Nicolai. "On a New Characterization of Scalar Supersymmetric Theories". In: *Phys. Lett. B* 89 (1980), p. 341. DOI: 10.1016/0370-2693(80)90138-0.

[Nis] *NIST Digital Library of Mathematical Functions*. http://dlmf.nist.gov/, Release 1.1.2 of 2021-06-15. F. W. J. Olver, A. B. Olde Daalhuis, D. W. Lozier, B. I. Schneider, R. F. Boisvert, C. W. Clark, B. R. Miller, B. V. Saunders, H. S. Cohl, and M. A. McClain, eds.

[NN81a] H.B. Nielsen and M. Ninomiya. "A no-go theorem for regularizing chiral fermions". In: *Physics Letters B* 105.2 (1981), pp. 219–223. ISSN: 0370-2693. DOI: https://doi.org/10.1016/0370-2693(81)91026-1.

[NN81b] H.B. Nielsen and M. Ninomiya. "Absence of neutrinos on a lattice: (I). Proof by homotopy theory". In: *Nuclear Physics B* 185.1 (1981), pp. 20–40. ISSN: 0550-3213. DOI: https://doi.org/10.1016/0550-3213(81)90361-8.

[NN81c] H.B. Nielsen and M. Ninomiya. "Absence of neutrinos on a lattice: (II). Intuitive topological proof". In: *Nuclear Physics B* 193.1 (1981), pp. 173–194. ISSN: 0550-3213. DOI: https://doi.org/10.1016/0550-3213(81)90524-1.

[Nov+84] V. A. Novikov et al. "Use and Misuse of QCD Sum Rules, Factorization and Related Topics". In: *Nucl. Phys. B* 237 (1984), pp. 525–552. DOI: 10.1016/0550-3213(84)90006-3.

[NR83] V. A. Nesterenko and A. V. Radyushkin. "Comparison of the QCD Sum Rule Approach and Perturbative QCD Analysis for $\gamma^*\gamma^* \to \pi^0$ Process". In: *Sov. J. Nucl. Phys.* 38 (1983), p. 284.

[NRC02] A. A. Natale, C. G. Roldao, and J. P. V. Carneiro. "Two photon final states in peripheral heavy ion collisions". In: *Phys. Rev. C* 65 (2002), p. 014902. DOI: 10.1103/PhysRevC.65.014902. arXiv: nucl-th/0107034.

[Nyf09] Andreas Nyffeler. "Hadronic light-by-light scattering in the muon g-2: A New short-distance constraint on pion-exchange". In: *Phys. Rev. D* 79 (2009), p. 073012. DOI: 10.1103/PhysRevD.79.073012. arXiv: 0901.1172 [hep-ph].

[Nyf19] Andreas Nyffeler. "Hadronic light-by-light scattering in the muon g − 2". In: *EPJ Web Conf.* 218 (2019). Ed. by A. Denig and C. F. Redmer, p. 01001. DOI: 10.1051/epjconf/201921801001. arXiv: 1710.09742 [hep-ph].

[OMF03] I.P. Omelyan, I.M. Mryglod, and R. Folk. "Symplectic analytically integrable decomposition algorithms: classification, derivation, and application to molecular dynamics, quantum and celestial mechanics simulations". In: *Computer Physics Communications* 151.3 (2003), pp. 272–314. ISSN: 0010-4655. DOI: https://doi.org/10.1016/S0010-4655(02)00754-3.

[OS73] Konrad Osterwalder and Robert Schrader. "Axioms for Euclidean Green's Functions". In: *Commun. Math. Phys.* 31 (1973), pp. 83–112. DOI: 10.1007/BF01645738.

[Pat17] Agostino Patella. "QED Corrections to Hadronic Observables". In: *PoS* LATTICE2016 (2017), p. 020. DOI: 10.22323/1.256.0020. arXiv: 1702.03857 [hep-lat].

[PB79] G. Peter Lepage and Stanley J. Brodsky. "Exclusive processes in quantum chromodynamics: Evolution equations for hadronic wavefunctions and the form factors of mesons". In: *Physics Letters B* 87.4 (1979), pp. 359–365. ISSN: 0370-2693. DOI: https://doi.org/10.1016/0370-2693(79)90554-9.

[Pea+09] Michael Peardon et al. "A Novel quark-field creation operator construction for hadronic physics in lattice QCD". In: *Phys. Rev. D* 80 (2009), p. 054506. DOI: 10.1103/PhysRevD.80.054506. arXiv: 0905.2160 [hep-lat].

[PPR98] Santiago Peris, Michel Perrottet, and Eduardo de Rafael. "Matching long and short distances in large-Nc QCD". In: *Journal of High Energy Physics* 1998.05 (1998), pp. 011–011. DOI: 10.1088/1126-6708/1998/05/011.

[PPV12] Vladimir Pascalutsa, Vladyslav Pauk, and Marc Vanderhaeghen. "Light-by-light scattering sum rules constraining meson transition form factors". In: *Phys. Rev. D* 85 (2012), p. 116001. DOI: 10.1103/PhysRevD.85.116001. arXiv: 1204.0740 [hep-ph].

[Pre+07] William H. Press et al. *Numerical Recipes 3rd Edition: The Art of Scientific Computing*. 3rd ed. USA: Cambridge University Press, 2007. ISBN: 0521880688.

[Pri51] H. Primakoff. "Photo-Production of Neutral Mesons in Nuclear Electric Fields and the Mean Life of the Neutral Meson". In: *Phys. Rev.* 81 (5 1951), pp. 899–899. DOI: 10.1103/PhysRev.81.899.

[PRV09] Joaquim Prades, Eduardo de Rafael, and Arkady Vainshtein. "The Hadronic Light-by-Light Scattering Contribution to the Muon and Electron Anomalous Magnetic Moments". In: *Adv. Ser. Direct. High Energy Phys.* 20 (2009), pp. 303–317. DOI: 10.1142/9789814271844_0009. arXiv: 0901.0306 [hep-ph].

[PS86] A. Phillips and D. Stone. "Lattice Gauge Fields, Principal Bundles and the Calculation of Topological Charge". In: *Commun. Math. Phys.* 103 (1986), pp. 599–636. DOI: 10.1007/BF01211167.

[PV14] Vladyslav Pauk and Marc Vanderhaeghen. "Single meson contributions to the muon's anomalous magnetic moment". In: *Eur. Phys. J.* C74.8 (2014), p. 3008. DOI: 10.1140/epjc/s10052-014-3008-y. arXiv: 1401.0832 [hep-ph].

[Que49] M. H. Quenouille. "Problems in Plane Sampling". In: *The Annals of Mathematical Statistics* 20.3 (1949), pp. 355–375. ISSN: 00034851.

[RSP20] Pablo Roig and Pablo Sánchez-Puertas. "Axial-vector exchange contribution to the hadronic light-by-light piece of the muon anomalous magnetic moment". In: *Phys. Rev.* D101.7 (2020), p. 074019. DOI: 10.1103/PhysRevD.101.074019. arXiv: 1910.02881 [hep-ph].

[RVL97] T. van Ritbergen, J. A. M. Vermaseren, and S. A. Larin. "The Four loop beta function in quantum chromodynamics". In: *Phys. Lett. B* 400 (1997), pp. 379–384. DOI: 10.1016/S0370-2693(97)00370-5. arXiv: hep-ph/9701390.

[Saa03] Yousef Saad. *Iterative Methods for Sparse Linear Systems*. Second. Society for Industrial and Applied Mathematics, 2003. DOI: 10.1137/1.9780898718003. eprint: https://epubs.siam.org/doi/pdf/10.1137/1.9780898718003.

[Sak91] Andrei D Sakharov. "Violation of CP invariance, C asymmetry, and baryon asymmetry of the universe". In: *Soviet Physics Uspekhi* 34.5 (1991), pp. 392–393. DOI: 10.1070/pu1991v034n05abeh002497.

[Sch03] Stefan Scherer. "Introduction to chiral perturbation theory". In: *Adv. Nucl. Phys.* 27 (2003). Ed. by John W. Negele and E. W. Vogt, p. 277. arXiv: hep-ph/0210398.

[Sch14] Matthew D. Schwartz. *Quantum Field Theory and the Standard Model*. Cambridge University Press, Mar. 2014. ISBN: 978-1-107-03473-0, 978-1-107-03473-0.

[Sch48] Julian Schwinger. "On Quantum-Electrodynamics and the Magnetic Moment of the Electron". In: *Phys. Rev.* 73 (4 1948), pp. 416–417. DOI: 10.1103/PhysRev.73.416.

[Sch90] H. A. Schwarz. *Gesammelte Mathematische Abhandlungen*. Vol. 2. Springer Verlag, Berlin, 1890.

[SK19] Eigo Shintani and Yoshinobu Kuramashi. "Study of systematic uncertainties in hadronic vacuum polarization contribution to muon $g-2$ with 2+1 flavor lattice QCD". In: *Phys. Rev.* D100.3 (2019), p. 034517. DOI: 10.1103/PhysRevD.100.034517. arXiv: 1902.00885 [hep-lat].

[Som94] R. Sommer. "A New way to set the energy scale in lattice gauge theories and its applications to the static force and α_s in SU(2) Yang-Mills theory". In: *Nucl. Phys. B* 411 (1994), pp. 839–854. DOI: 10.1016/0550-3213(94)90473-1. arXiv: hep-lat/9310022.

[SS00] Stephen R. Sharpe and Noam Shoresh. "Physical results from unphysical simulations". In: *Phys. Rev. D* 62 (2000), p. 094503. DOI: 10.1103/PhysRevD.62.094503. arXiv: hep-lat/0006017.

[SS01] Stephen R. Sharpe and Noam Shoresh. "Partially quenched chiral perturbation theory without Φ_0". In: *Phys. Rev. D* 64 (2001), p. 114510. DOI: 10.1103/PhysRevD.64.114510. arXiv: hep-lat/0108003.

[SS96] Stefan Sint and Rainer Sommer. "The Running coupling from the QCD Schrodinger functional: A One loop analysis". In: *Nucl. Phys. B* 465 (1996), pp. 71–98. DOI: 10.1016/0550-3213(96)00020-X. arXiv: hep-lat/9508012.

[SSV11] Stefan Schaefer, Rainer Sommer, and Francesco Virotta. "Critical slowing down and error analysis in lattice QCD simulations". In: *Nucl. Phys. B* 845 (2011), pp. 93–119. DOI: 10.1016/j.nuclphysb.2010.11.020. arXiv: 1009.5228 [hep-lat].

[SW85] B. Sheikholeslami and R. Wohlert. "Improved Continuum Limit Lattice Action for QCD with Wilson Fermions". In: *Nucl. Phys. B* 259 (1985), p. 572. DOI: 10.1016/0550-3213(85)90002-1.

[SW92] J.C. Sexton and D.H. Weingarten. "Hamiltonian evolution for the hybrid Monte Carlo algorithm". In: *Nuclear Physics B* 380.3 (1992), pp. 665–677. ISSN: 0550-3213. DOI: https://doi.org/10.1016/0550-3213(92)90263-B.

[Sym83a] K. Symanzik. "Continuum limit and improved action in lattice theories: (I). Principles and ϕ^4 theory". In: *Nuclear Physics B* 226.1 (1983), pp. 187–204. ISSN: 0550-3213. DOI: https://doi.org/10.1016/0550-3213(83)90468-6.

[Sym83b] K. Symanzik. "Continuum limit and improved action in lattice theories: (II). O(N) non-linear sigma model in perturbation theory". In: *Nuclear Physics B* 226.1 (1983), pp. 205–227. ISSN: 0550-3213. DOI: https://doi.org/10.1016/0550-3213(83)90469-8.

[Tar75] R. Tarrach. "Invariant Amplitudes for Virtual Compton Scattering Off Polarized Nucleons Free from Kinematical Singularities, Zeros and Constraints". In: *Nuovo Cim. A* 28 (1975), p. 409. DOI: 10.1007/BF02894857.

[TD05] Doug Toussaint and C. T. H. Davies. "The Omega- and the strange quark mass". In: *Nucl. Phys. B Proc. Suppl.* 140 (2005). Ed. by Geoffrey T. Bodwin et al., pp. 234–236. DOI: 10.1016/j.nuclphysbps.2004.11.129. arXiv: hep-lat/0409129.

[Urb+06] C. Urbach et al. "HMC algorithm with multiple time scale integration and mass preconditioning". In: *Comput. Phys. Commun.* 174 (2006), pp. 87–98. DOI: 10.1016/j.cpc.2005.08.006. arXiv: hep-lat/0506011.

[Wat44] G. N. Watson. *A Treatise on the Theory of Bessel Functions*. Second. Cambridge University Press, Cambridge, England, 1944.

[Wei79] Steven Weinberg. "Phenomenological Lagrangians". In: *Physica A: Statistical Mechanics and its Applications* 96.1 (1979), pp. 327–340. ISSN: 0378-4371. DOI: https://doi.org/10.1016/0378-4371(79)90223-1.

[Whi84] C. Whitmer. "Overrelaxation Methods for Monte Carlo Simulations of Quadratic and Multiquadratic Actions". In: *Phys. Rev. D* 29 (1984), pp. 306–311. DOI: 10.1103/PhysRevD.29.306.

[Wil74] Kenneth G. Wilson. "Confinement of quarks". In: *Phys. Rev. D* 10 (8 1974), pp. 2445–2459. DOI: 10.1103/PhysRevD.10.2445.

[Wil99] Walter Wilcox. "Noise methods for flavor singlet quantities". In: *Interdisciplinary Workshop on Numerical Challenges in Lattice QCD*. Aug. 1999. arXiv: hep-lat/9911013.

[Wit79] Edward Witten. "Baryons in the 1/n Expansion". In: *Nucl. Phys. B* 160 (1979), pp. 57–115. DOI: 10.1016/0550-3213(79)90232-3.

[Wit83] Edward Witten. "Global Aspects of Current Algebra". In: *Nucl. Phys. B* 223 (1983), pp. 422–432. DOI: 10.1016/0550-3213(83)90063-9.

[Wol04] Ulli Wolff. "Monte Carlo errors with less errors". In: *Comput. Phys. Commun.* 156 (2004). [Erratum: Comput.Phys.Commun. 176, 383 (2007)], pp. 143–153. DOI: 10.1016/S0010-4655(03)00467-3. arXiv: hep-lat/0306017.

[WP81] D.H. Weingarten and D.N. Petcher. "Monte Carlo integration for lattice gauge theories with fermions". In: *Physics Letters B* 99.4 (1981), pp. 333–338. ISSN: 0370-2693. DOI: https://doi.org/10.1016/0370-2693(81)90112-X.

[WZ71] J. Wess and B. Zumino. "Consequences of anomalous Ward identities". In: *Phys. Lett. B* 37 (1971), pp. 95–97. DOI: 10.1016/0370-2693(71)90582-X.